Universidade de Aveiro Departamento de Geociências

2011

Luisa Joubert Chaves Pinto Ribeiro

Caracterização Petrológica e Geoquímica do Vulcanismo da Ilha de São Jorge, Açores

Petrologic and Geochemical Characterization of São Jorge Island Volcanism, Azores

Universidade de Aveiro Departamento de Geociências

2011

Luisa Joubert Chaves Pinto Ribeiro

Caracterização Petrológica e Geoquímica do Vulcanismo da Ilha de São Jorge, Açores

Petrologic and Geochemical Characterization of São Jorge Island Volcanism, Azores

Dissertação apresentada à Universidade de Aveiro para cumprimento dos requisitos necessários à obtenção do grau de Doutor em Geociências, realizada sob a orientação científica do Doutor Britaldo Normando Oliveira Rodrigues, Professor Catedrático do Departamento de Geociências da Universidade de Aveiro e da Doutora Zilda Terra Tavares de Melo de França, Professora Auxiliar com Agregação, do Departamento de Geociências da Universidade dos Açores

Apoio financeiro no âmbito dos trabalhos da Estrutura de Missão para a Extensão da Plataforma Continental na dependência do Ministério da Defesa Nacional.

Apoio financeiro da Universidade de Aveiro.

Apoio financeiro do Observatório Vulcanológico e Geotérmico dos Açores.

I dedicate this work to my son Luis

and to my nieces Mariana and Madalena.

o júri/the jury

Presidente/President

Prof. Doutor Victor José Babau Torres
Professor Catedrático da Universidade de Aveiro

Vogais/Members

Prof. Doutora Elizabeth Widom
Professora Titular da Miami University (Ohio)

Prof. Doutor José Francisco Horta Pacheco dos Santos
Professor Auxiliar da Universidade de Aveiro

Prof. Doutor Marceliano Lago San José
Professor Titular da Universidade de Zaragoza

Prof. Doutor Victor Hugo Lecoq Lacerda Forjaz
Professor Catedrático Jubilado da Universidade dos Açores

Prof. Doutor Fernando Joaquim Fernandes Tavares Rocha
Professor Catedrático da Universidade de Aveiro

Prof. Doutor Britaldo Normando Oliveira Rodrigues
Professor Catedrático da Universidade de Aveiro

Prof. Doutora Zilda Terra Tavares de Melo de França
Professora Auxiliar com Agregação da Universidade dos Açores

Acknowledgements

I should start to thank to my supervisors Professor Doutor Britaldo Rodrigues and Professora Doutora Zilda França who after accepting me as their student, have always enthusiastically support me throughout this project. A particular word of recognition must be address to Professora Zilda França that shared with me ideas, discussions, advice, friendship and, sometimes, her shoulder, encouraging me to go forward in some "dark" days.

I am very grateful to the EMEPC (the Task Group for the Extension of the Portuguese Continental Shelf) where I have been working for the last five years, and without which this study, probably, would have never be accomplished. The EMEPC gave this PhD project the main financial support, allowing the acquisition of most of the geochemical data in some of the best laboratories and the early presentation of the results in international conferences. Special thanks has to be addressed to Professor Doutor Manuel Pinto de Abreu, the head of EMEPC, that has always open the way for this project and has given me, when necessary, a different perspectives and critical opinions that inspired me to go forward. I would like to address many thanks and my appreciation for all colleagues at EMEPC (i.e. EMEPC@team) for the support during this work and in particular during the phases when I needed to be "isolated".

Thanks must also go to the Observatório Vulcanológico e Geotérmico dos Açores (OVGA) that has also financially supported this PhD project. This was achieved by the perseverance of Professor Doutor Victor Hugo Forjaz, the head of the OVGA, who has proposed me to do this project in São Jorge. His loyal friendship, continuous motivation, and intense discussions have always been productive and taught me important things in life.

I would like to show my gratitude the University of Aveiro for receiving me as a student and by giving support, particularly in the early stages of this project and during the acquisition of data to

this project, either in the University Library or in the laboratories associated with the Geosciences Department.

Fortunately, I had the chance to discuss some of the most important issues of this study with Professor Elisabeth Widom from Miami University and Professor Andrew Calvert from the USGS. To Elisabeth I thank the discussions of the isotopic data and the fruitful opportunity to share ideas and receive comments. To Andy I cannot forget the warm welcome to his laboratory where I had access to the best conditions. I acknowledge his availability and interest in the development of this work.

I have to thank João Fontiela by the help he gave during the weeks that we spend in the field and the hard work during sample preparation.

I have undoubtedly to thank some friends that during this period of my life, have given me their friendship, company and true advice, essential to daily life; so my special thanks goes to Fátima F.S. and family, especially Marta, to André F., to Nuno S.O., to Ana E.S.S.S. and to Duarte S.B.

Finally, yet importantly, I have to thank my family, in particular, to my uncles Jose and Isabel for their example, to my parents, Luis and Isabel and to my sister Maria for being always the support and comfort in my life.

Palavras chave: Açores; isótopos de Sr, Nd, Pb e Hf; heterogeneidades mantélicas; Geocronologia absoluta $^{40}Ar/^{39}Ar$.

Resumo

A ilha de São Jorge (38º 45' 24'' N - 28º 20' 44''W e 38º 33' 00'' N - 27º 44' 32'' W) é uma das nove ilhas do Arquipélago dos Açores que integram uma extensa e complexa estrutura, a Plataforma dos Açores, onde convergem as placas Americana, Eurasiática e Núbia que definem a junção tripla dos Açores. A ilha de São Jorge exibe características próprias, dentro do contexto açoriano, que evidenciam um vulcanismo fissural ao longo da direcção WNW-ESE, indicando uma importante interacção entre a actividade tectónica e a actividade vulcânica.

A conjunção entre dados de natureza vulcanoestratigráfica (Forjaz & Fernandes, 1975; and Madeira, 1998) e geocronológica, revelam que a formação da ilha deverá ter decorrido fundamentalmente durante duas fases vulcânicas distintas. Durante a primeira fase vulcânica, entre 1,31 e 1,21 Ma (Hildenbrand *et al*. 2008) ter-se-á formado o empilhamento lávico sobranceiro à Fajã de São João e, há cerca de 757 Ka, provavelmente, iniciou-se a segunda fase vulcânica que foi responsável pela edificação da restante parte da ilha e que se tem mantido activa até aos nossos dias. Durante a segunda fase vulcânica, no período compreendido entre os 757 e 543 ka, terá sido edificado o Complexo Vulcânico do Topo, constituindo a zona este da ilha; enquanto que a parte oeste, englobando o Complexo Vulcânico dos Rosais, deverá ter-se começado a formar à cerca 368 ka e mantido em actividade até, pelo menos, há aproximadamente 117 ka. Depois da edificação do Complexo Vulcânico dos Rosais a actividade

vulcânica parece ter migrado para a zona central da ilha o que conduziu à formação do Complexo Vulcânico das Manadas.

O vulcanismo em São Jorge é predominantemente alcalino, apresentando uma diversidade litológica que varia entre os basanitos/tefritos e os traquiandesitos basálticos. Apesar deste pequeno espectro litológico, as duas fases vulcânicas apresentam diferentes características mineralógicas, petrográficas e geoquímicas que deverão derivar de distintas condições petrogenéticas e taxas efusivas diversas e, consequentemente, de velocidades de crescimento dos empilhamentos lávicos distintos.

Durante a primeira fase vulcânica, em que a velocidade média de crescimento da ilha foi mais elevada (≈3.4 m/ka), as lavas apresentam-se ligeiramente menos alcalinas e mais enriquecidas em plagioclase. Tais factos sugerem a existência de uma câmara magmática, possivelmente, pouco profunda e bastante dinâmica, sob o empilhamento lávico da Fajã de São João, à qual estarão associados processos de cristalização fraccionada, segregação gravítica e acumulação.

A velocidade média de crescimento das sequências lávicas, durante a segunda fase vulcânica, foi mais baixa (≈1.9 m/ka) e as lavas apresentam uma composição, maioritariamente, alcalina sódica em que a paragénese é representada por fenocristais de olivina, piroxena, plagioclase e óxidos. As lavas são caracterizadas por um enriquecimento em elementos traço incompatíveis e terras raras leves mas evidenciam, para lavas geograficamente próximas, diferentes níveis de enriquecimento que poderão indicar pequenas heterogeneidades na fonte mantélica. Outros factores a considerar, que eventualmente contribuem para estas assimetrias, poderão ser: (1) a ocorrência de taxas de fusão ligeiramente mais elevadas, como observado nas lavas mais antigas dos complexos vulcânicos do Topo e Rosais; (2) a presença na fonte mantélica de granada e anfíbola residuais e/ou (3) a variação nas condições de fusão da fonte, tais como, a pressão.

As subtis diferenças geoquímicas acima referenciadas contrastam com as assinaturas isotópicas obtidas através dos isótopos de Sr-Nd-Pb-Hf, estando claramente impressas nas lavas dos vários complexos vulcânicos da ilha de São Jorge.

As lavas do Complexo Vulcânico do Topo e do flanco submarino, i.e. as lavas localizadas a este da falha da Ribeira Seca, amostram uma fonte mantélica com uma assinatura isotópica, que em termos de chumbo é semelhante à ilha Terceira. Por outro lado, as lavas dos complexos vulcânicos dos Rosais e das Manadas, i.e. as lavas do lado oeste de São Jorge, mostram que a

fonte mantélica se torna progressivamente mais diferenciada em termos de isótopos de chumbo, sobrepondo-se à assinatura isotópica da ilha do Faial. As duas assinaturas isotópicas de São Jorge, verificada pelos isótopos de chumbo, em conjugação com os outros três sistemas isotópicos (Sr-Nd-Hf), evidenciam a contribuição de três reservatórios/componentes mantélicos para a formação das composições observadas. Estes componentes mantélicos são (1) o Componente Comum, relacionado com a Plataforma dos Açores e a Crista Média Atlântica, (2) o Componente Este, com uma assinatura FOZO e, possivelmente, relacionado com o ponto quente dos Açores localizado sob a ilha Terceira, e (3) o Reservatório Oeste, semelhante ao encontrado sob a ilha do Faial, onde a litosfera poderá ter sido impregnada por um líquido magmático antigo e isolado no manto por mais de 2Ga. Neste contexto, parece poder-se concluir que as duas assinaturas isotópicas observadas reforçam a existência de pequenas heterogeneidades sob a Região dos Açores, como tem sido proposto, por alguns autores, para explicar a diversidade isotópica observada nas ilhas do Arquipélago.

Keywords: Azores; Sr, Nd, Pb and Hf isotopes; mantle heterogeneities; absolute geochronology $^{40}Ar/^{39}Ar$.

Abstract

The island of São Jorge (38º 45' 24'' N - 28º 20' 44''W and 38º 33' 00'' N - 27º 44' 32'' W) is one of the nine islands of the Azores Archipelago that is rooted in the Azores Plateau, a wide and complex region which encompasses the triple junction between the American, Eurasia and Nubia plates. São Jorge Island has grown by fissural volcanic activity along fractures with the regional WNW-ESE trend, unveiling the importance of the regional tectonics during volcanic activity.

The combination of the volcanostratigraphy (Forjaz & Fernandes, 1975; and Madeira, 1998) with geochronological data evidences that the island developed during two main volcanic phases. The first subaerial phase that occurred between 1.32 and 1.21 Ma ago (Hildenbrand *et al*. 2008) is recorded on the lava sequence forming the cliff at Fajã de São João, while the second phase started at 757 ka ago, is still active, and edified the rest of the island. This second phase edified the east side of the island that corresponds to Topo Volcanic Complex, in the period between 757 and 543 ka ago, while the west side named Rosais Volcanic Complex, started at 368 ka ago (Hildenbrand *et al*. 2008) and was still active at 117 ka ago. After the onset of Rosais, volcanic activity migrates to the center of São Jorge edifying Manadas Volcanic Complex.

The volcanism on São Jorge is dominantly alkaline, with a narrow lithological composition ranging between the basanites/tefrites through the basaltic trachyandesites, in spite of this the two volcanic phases show distinct mineralogical, petrographic and geochemical characteristics that should be related with different petrogenetic conditions and growth rates of the island.

During the first volcanic phase, growth rates are faster (≈3.4 m/ka), the lavas are slightly less alkaline and plagioclase-richer, pointing to the existence of a relative shallow and dynamic magma chamber where fractional crystallization associated with gravitational segregation and accumulation processes, produced the lavas of Fajã de São João sequence.

The average growth rates during the second volcanic phase are lower (≈1.9 m/ka) and the lavas are mainly alkaline sodic, with a mineralogy composed by olivine, pyroxene, plagioclase and oxide phenocrysts, in a crystalline groundmass. The lavas are characterized by enrichment in incompatible trace element and light REE, but show differences for close-spaced lavas that unveil, in some cases, slight different degrees of fertilization of the mantle source along the island. These differences might also result from higher degrees of partial melting, as observed in the early stages of Topo and Rosais volcanic complexes, of a mantle source with residual garnet and amphibole, and/or from changing melting conditions of the mantle source as pressure.

The subtle geochemical differences of the lavas contrast with the isotopic signatures, obtained from Sr-Nd-Pb-Hf isotopes, that São Jorge Island volcanism exhibit along its volcanic complexes. The lavas from Topo Volcanic Complex and from the submarine flank, i.e. the lavas located east of Ribeira Seca Fault, sample a mantle source with similar isotopic signature that, in terms of lead, overlaps Terceira Island. The lavas from Rosais and Manadas volcanic complexes, the western lavas, sample a mantle source that becomes progressively more distinct towards the west end of the island and that, in terms of lead isotopes, trends towards the isotopic composition of Faial Island. The two isotopic signatures of São Jorge, observed from the combination of lead isotopes with the other three systems, seem to result from the mixing of three distinct end-members. These end-members are (1) the common component related with the Azores Plateau and the MAR, (2) the eastern component with a FOZO signature and possibly related with the Azores plume located beneath Terceira, and (3) the western component, similar to Faial, where the lithosphere could have been entrained by an ancient magmatic liquid, isolated for a period longer than 2Ga. The two trends observed in the island reinforce the idea of small-scale mantle heterogeneities beneath the Azores region, as it has been proposed to explain the isotopic diversity observed in the Archipelago.

Contents

List of Figures

List of Tables

Chapter 1: Introduction

The study of ocean island lavas constitutes a major opportunity to study the composition and evolution of the upper mantle. Chemical data of major and, especially, of trace elements are an important tool that helps to decipher the composition of the mantle, its mineralogy, its compositional heterogeneities, and the melting conditions that generate the magmatic liquids. On the other hand, the isotopic composition of ocean island lavas helps to interpreted the mechanisms involve in the generation of the mantle because they allow to travel back in time and identify ancient processes.

The Azores Islands, in which São Jorge is included, are considered a natural laboratory to study mantelic and magmatic processes, not only for the fact of being formed by intraplate ocean island lavas with unusual and diverse composition, but also because of their complex tectonic setting and proximity to the Mid-Atlantic Ridge. In this sense, the origin of the Azores Archipelago and the evolution of the Azores Plateau, in which the islands are rooted, has been a matter of intense debate, at least, since the last quarter of the XX century. Several theories and models have been proposed to explain the formation and evolution of the Azores Plateau and of the islands, based on a continuous collection of geological, geochemical, geophysical and bathymetric data, used to study processes either at island-scale or at regional scale.

The present study is focused on the Island of São Jorge, located in the Central Island Group of the Archipelago and aims to identify and refine the volcanic growth of the island, the magmatic processes that originated the magmas in the mantle as well the characterization of the mantle beneath the island. With the data collected for this project and its analysis, this study pretends to contribute to the knowledge on the Azores and on the processes associated with its evolution.

In this sense in chapter two, is presented a geotectonic and geochemical introduction of the Azores Archipelago and of the Azores Plateau, in order to have an overview of the regional settings of São Jorge Island. The ages of the magnetic anomalies that cross the plateau and the

oldest ages of the islands, determined by absolute geochronology, are summarized in this chapter reflecting different temporal scales of the volcanic evolution of the Plateau.

In chapter three is presented a review of the most important data on São Jorge presented in earlier studies. This data comprises the main historic volcanic and seismic events, the tectonic setting, the volcanostratigraphy and the geochronological ages. The compilation of this information gives a good base for a detailed study of the island, but the information was review critically at the light of the most recent publications, as the case of recent geochronological data that changed considerably the knowledge of the early stages of formation of the island.

A comprehensive group of samples was collected on São Jorge main volcanic sequences of the three-volcanostratigraphic complexes and in other key locations of the island. In addition, the southeast flank of the island, which should correspond to the submarine prolongation of Topo Volcanic Complex, was sampled during the EMEPC\Açores\G3\2007 cruise, extending the characterization of the island to the offshore. On the samples showing less signs of alteration, what corresponded to a large set, geochemical, mineralogical, and isotopic analysis were performed as described in chapter four and detailed in the appendixes I and II.

Some of the isotopic analysis comprised the determination of the ages of the lavas using the $^{40}Ar/^{39}Ar$ method. The main objective of chapter five was to answer the question of when and how the island formed and to constrain temporally the evolution of São Jorge. Despite that during the preparation of this study another study was published with geochronological data on São Jorge, the results obtained improve and refine the temporal evolution of São Jorge and bring new and important constrains to volcanic activity in the island.

In chapter six is presented a petrographic characterization of the lavas in São Jorge. The observation under the microscope allow the identification of the most common minerals and textures that form São Jorge lavas and of less common mineral as biotite and amphibole, which were only present in few samples. The information obtained in chapter six was very useful for chapter seven where is presented the results on mineral chemistry analysis. The dependency of mineral composition to the conditions in which the minerals fractionate; i.e. pressure, temperature and oxygen fugacity (fO_2), allowed using the composition of the mineral to determine those conditions.

The geochemical characterization of the lavas and the analysis of major and trace element composition in terms of petrogenetic processes, is presented in chapter eight and nine, considering five lava groups, which correspond to the three volcanic complexes, Topo, Rosais and Manadas, to the lavas from Fajã de São João sequence and the submarine pillow lavas. Along these two chapters, the geochemical data are analyzed and modeled in order to interpret the magmatic processes responsible for magma generation and differentiation, the conditions in which the magmatic processes occurred (i.e. degree of partial melting, pressure and temperature) and the composition of the mantle source. At this point, and after the characterization on previous chapters of the lavas from Fajã de São João sequence, these lavas are treated separately because they evidence different temporal and genetic differences from the rest of the island.

Chapter ten focus on the isotopic composition of the lavas in São Jorge, which present a distinct signature in terms of Sr-Nd-Pb-Hf isotopes. In order to understand the meaning of the isotopic composition of the lavas and of the mantle beneath the island, several hypotheses are anticipated and analyzed, which consider the isotopic composition of other islands from the archipelago. In this analysis, several isotopic models are experimented with the objective to find a reasonable explanation for the compositions observed that satisfies the four isotopic systems.

In chapter eleven is presented a summary of all the data obtained or compiled in this study in order to put together the history of São Jorge, the main aspects that characterize the chemistry of the lavas and of the mantle source.

Chapter 2: Azores Regional Settings

2.1 Geographic Setting

The Azores Archipelago occupies a central position in the Atlantic Ocean between the longitudes 24 and 32°W and the latitudes 36 and 40°N. The archipelago is the most occidental region of Portugal and comprises nine islands, which are geographically distributed into three groups: the Oriental Island Group, formed by Santa Maria and São Miguel islands, the Occidental Island Group, which includes the islands of Flores and Corvo, and the Central Island Group that encompasses five islands, Terceira, Graciosa, Faial, Pico and São Jorge (Fig. 2.1).

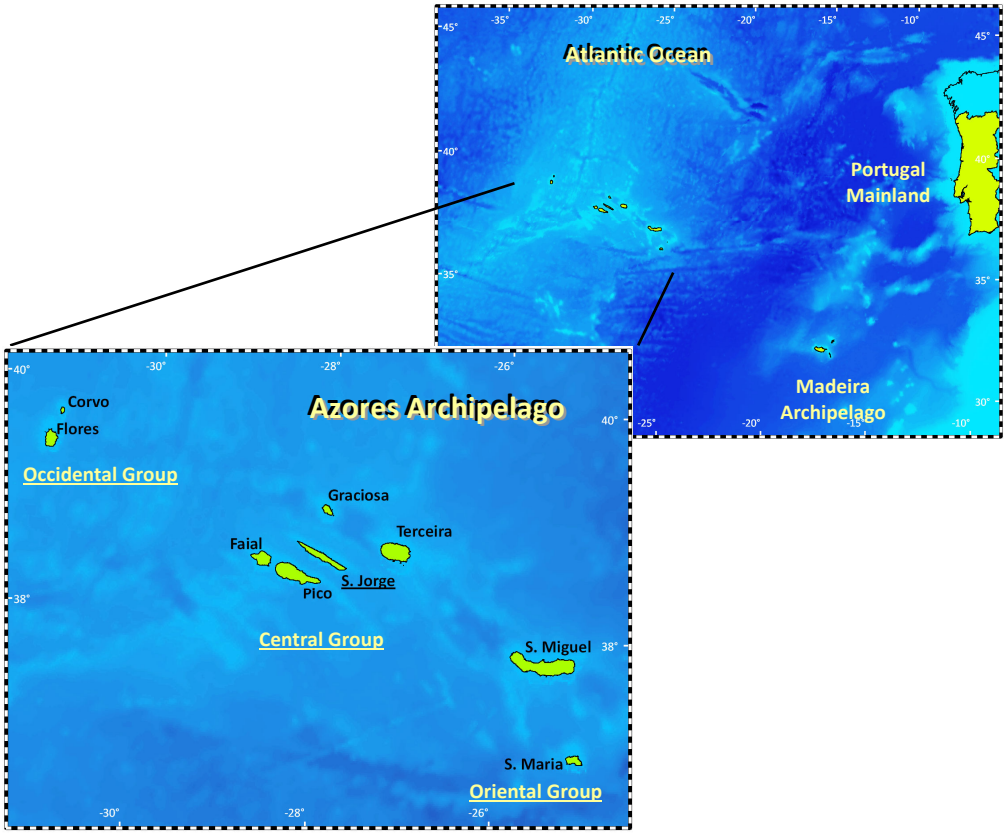

Fig. 2.1 – In this picture it is showed the localization of the Azores Archipelago, the most occidental region of Portugal and the geographic distribution of the Islands.

2.2 Geotectonic Setting

The Azores islands are the superficial expression of a much larger structure named Azores Plateau, with a triangular shape defined roughly by the 2000 m depth isobath. The approximate area the plateau is 5.8 million km^2 and the islands occupy only 0.05% of this area, what corresponds to 2333 km^2 (Nunes, 1991).

The Azores Plateau is a complex tectonic region that encompasses the triple junction between the American, Eurasia and Nubian plates. One of the most important structures in the region is the Mid-Atlantic Ridge (MAR), which crosses the plateau roughly in a north-south direction and separates the American Plate, where Flores and Corvo islands are located, from the other two plates where the rest of the islands are rooted (Fig. 2.2).

The East Azores Fracture Zone is another important structure that at approximately 37°N limits the Plateau. This south border represents a bathymetry droop from the edge of the Azores Plateau, at 2000 m, to approximately 3500 m depth.

The northeast boundary of the Plateau is defined by the Terceira Axis (Machado, 1957), which is a striking WNW-ESE feature that comprises a series of volcanic centers that correspond to the islands (Graciosa, Terceira and São Miguel) and seamounts (e.g. Banco D. João de Castro), separated from each other by deep a-magmatic basins (e.g. Hirondelle Basin). This structure at its most eastern tip meets with Azores-Gibraltar Fracture Zone that crosses the Atlantic. The limit between the Eurasian and Nubian Plates is well defined by this E-W fault characterized by pure dextral strike slip-movement (e.g. Jiménez-Mount *et al*., 2001).

The Mid-Atlantic Ridge is a well define structure crossing the Atlantic, however, in the Azores Region becomes shallower, losses some of its bathymetric definition and is necessary to recur to sediment distribution and magnetic anomalies to identify with precision the axis (Krause & Watkins, 1970; Searle, 1980). Along the Azores Plateau, from north to south, the MAR is offset by a series of transform faults as the North Azores Fracture Zone (39°25'N), Faial Fracture Zone (38°55'N), Açor Fracture Zone (38°23'N), Princess Alice Fracture Zone (38°00'N) and Pico Fracture Zone (37°30'N). These fracture zones split the MAR into segments, with approximately 50 to 60 km length (Luis *et al*., 1994), and due to their dextral strike-slip movement produces the displacement of segments and the rotation of the axis, from 7°N, north of the Plateau, to 10°N and 22°N, on the south side of the Plateau (Fig. 2.2).

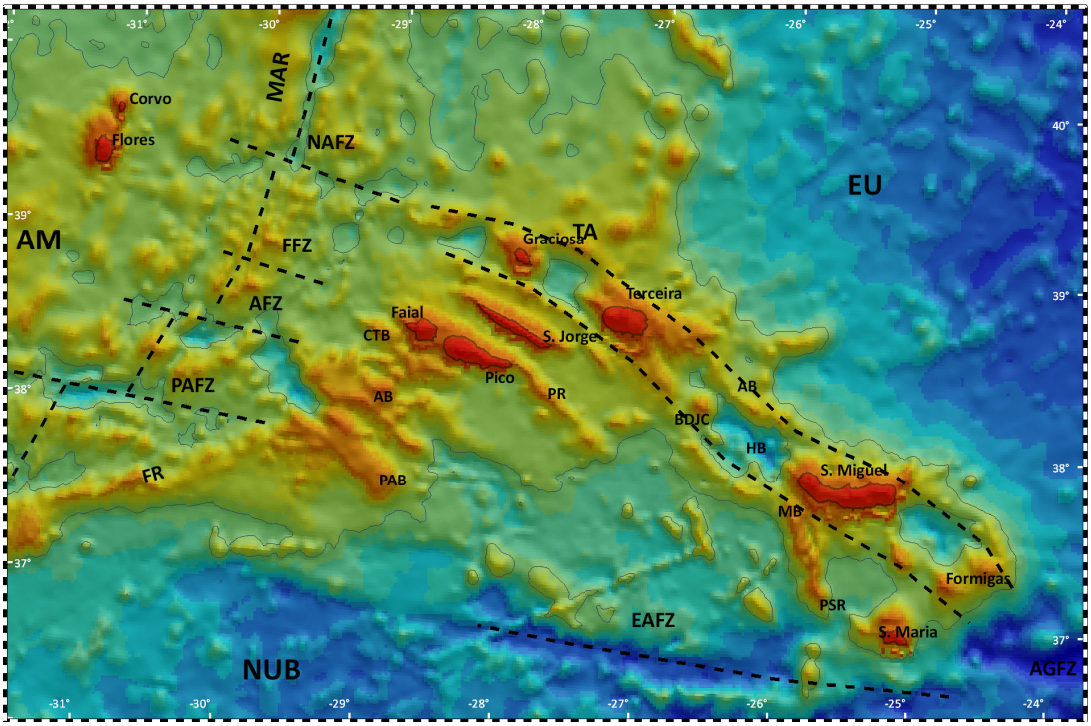

Fig. 2.2 – Bathymetric chart of the Azores Plateau (Smith & Sandwell, 1997) showing the main tectonic features described in the text. AM – American Plate; EU – Eurasian Plate; NUB – Nubian Plate; MAR – Mid-Atlantic Ridge; NAFZ – North Azores Fracture Zone; FFZ – Faial Fracture Zone; AFZ – Açor Fracture Zone; PAFZ – Princess Alice Fracture Zone; PFZ – Pico Fracture Zone; EAFZ – East Azores Fracture Zone; AGFZ – Azores-Gibraltar Fracture Zone; TA – Terceira Axis; PSR – Ponta Sul Ridge; MB – Monaco Bank; HB – Hirondelle Basin; DJCB – D. João de Castro Bank; AB – Alcatraz Bank; PR – Pico Ridge; CTB – Condor de Terra Bank; AB – Açor Bank; PAB – Princessa Alice Bank; FR – Faial Ridge.

East of the MAR, the contact between the Eurasian and Nubian plates is believed to be materialized by the Terceira Axis. Presently, the most accepted idea is that the confluence of the Mid-Atlantic Ridge and the Terceira Axis define the Azores Triple Junction, even though its location is not exactly defined. The role of this boundary has been discussed through several kinematic models explaining the Azores evolution, which, since the early 70's, progressively evolved with the acquisition of new data. The early model of Krause & Watkins, (1970) and the simplified model of McKenzie (1972) proposed that Terceira Axis is the third arm of a Rift-Rift-Rift triple junction, which evolved from a previous Rift-Fault-Fault system. This model was later reinforced by Searle (1980) and by Vogt & Jung (2004), the later interpreting the Terceira Axis (in this case Terceira Rift) as an ultraslow spreading centre with an average spreading rate of 2-4 mm/a.

Lourenço *et al*. (1998) prefers the idea that the triple junction is a distributed boundary in which the deformation is accommodated within the Plateau. The refinement of this tectonic interpretation presented by Lourenço (2007) proposes a tectono-magmatic model, in which the Terceira Axis is a focused deformation area accommodating the stress of the Azores Triple Junction. However, in the area of the Central Island Group, the deformation regime is partitioned over a large area constraint between Terceira-Graciosa and the region south of Condor Ridge (Fig. 2.3).

Other interpretations have been formulated to explain the triple junction and the role of the Terceira Axis. For example, Forjaz (1983) suggests the existence of an Azorean microplate limited by the East Azores Fracture Zone in the south, by the MAR in the west and by the North Azores Fracture Zone and the Terceira Axis in the north and northeast, whereas Ribeiro (1982) suggests that the Eurasian and Nubian plate boundary corresponds to a leaky-transform fault passing through São Jorge Channel and continuing south of São Miguel until meets the AGFZ in the Formigas area.

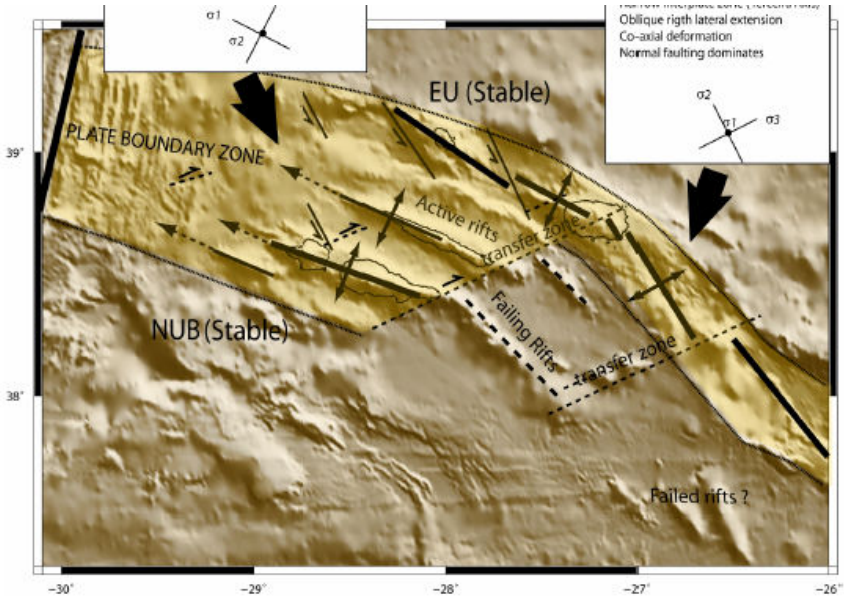

Fig. 2.3 – In this figures is presented the tectono-magmatic model proposed by Lourenço (2007), explaining the deformation patterns of the Azores Triple Junction

Another important structure in the Azores Plateau is anomalous shallow V-shape ridge that intersects the MAR south of the Plateau. This is a volcanic structure with two branches, the Faial

and Flores ridges, considered to result from a major thermal or magmatic event beneath the MAR (Cannat *et al*., 1999; Escartín *et al*., 2001; Gente *et al*., 2003).

The internal structure of the Plateau, east of the MAR, is characterized by several structures sub-parallel to the Terceira Axis striking 110-120°N, in the area of the Central Island Group, that bend towards a 140-150°N direction in the region of the Oriental Island Group. These structures correspond to major faults or to shallower areas where volcanic activity is concentrated.

The islands of the Central Island Group are aligned mainly along the 110-120°N direction, where volcanic activity edified linear volcanic ridges as Pico Ridge (PR) or São Jorge volcanic ridge (Lourenço, 1998). The 140-150°N direction is discrete in this region, nonetheless the eastward submarine prolongation of Pico ridge and the southeast flank of Terceira developed along this direction.

2.3 The Ages of the Azores

The models proposed to explain the development and evolution of the Azores Triple Junction and the Azores Plateau e.g. Krause & Watkins, (1970), Searle *et al.* (1980), Luis *et al*. (1994), Gente *et al*. (2003), which is intimately connected with the evolution of the North Atlantic and the plate boundary between the Eurasian, Nubian and American Plates, delivered important temporal constraints. Although these time constrains for the beginning of the formation of plateau are scarce and debatable, the few isochron ages provided by the magnetic anomalies give valuable information.

The early work of Searle (1980) proposes that the beginning of the construction of the Azores Plateau is marked by the oldest MAR isochron cut by the Azores Plateau (anomaly 20 or 21), which is about 50 Ma. However, Gente *et al.* (2003) presented a kinematic reconstruction for the development of the Plateau, which occurred between 20 and 7 Ma ago, considering the magnetic anomaly 13, with approximately 35 Ma (Fig. 2.4).

Recently Luis *et al*. (1994) presented a magnetic anomaly map covering both sides of the MAR with detail information up to anomaly 5. The magnetic anomaly 5, with 10 Ma, is symmetric in

both sides of the MAR and while in the eastern side passes beneath Faial Island and west of São Jorge and Graciosa islands, on the western side is located west of the islands of Corvo and Flores.

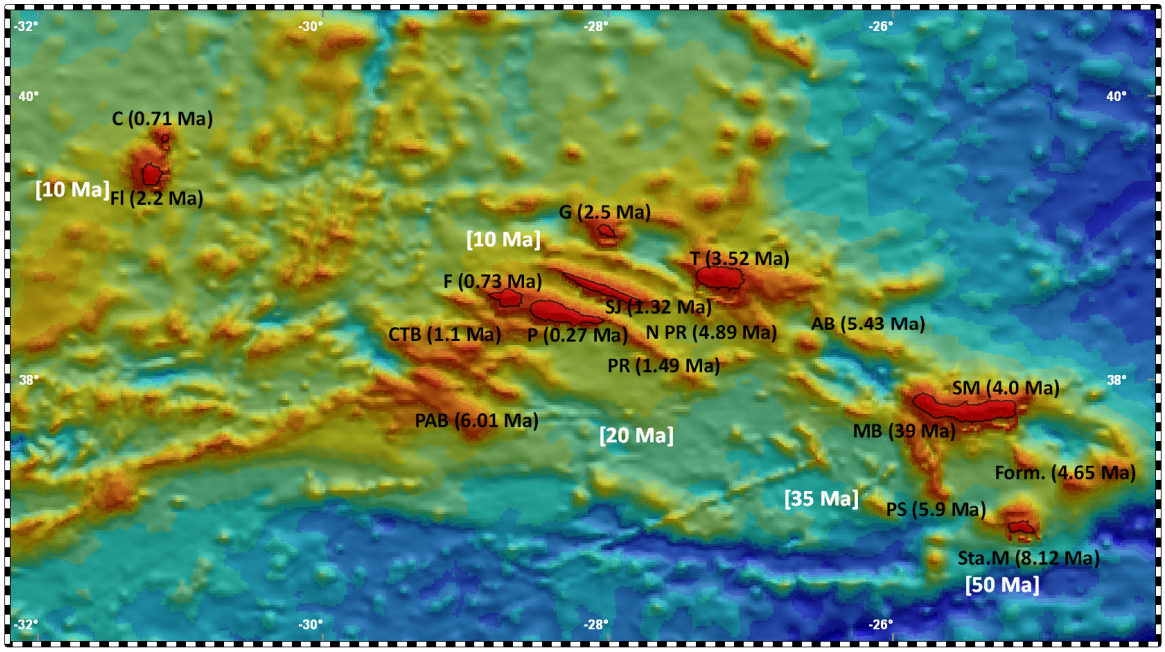

Fig. 2.4 – Bathymetric chart of the Azores Plateau (Smith & Sandwell, 1997) with the oldest geochronological ages of each island, the oldest ages of submarine reliefs (in black) and the ages of the magnetic anomalies [in white]. The geochronological ages are from Abdel-Monem *et al*. (1975), White *et al.* (1976), Feraud *et al*. (1980, 1984), Demand *et al*. (1982), Azevedo *et al*. (1991), Ferreira & Azevedo (1995), Beier (2006), França *et al*, (2006a) and Hildenbrand *et al*. (2008) and the data on the magnetic anomalies was adapted from Searle (1980), Luis *et al*. (1994) and Gente *et al*. (2003). For simplification, the names of the Islands have only the initial letter, for other the abbreviations see Fig. 2.2.

The absolute ages obtained on the lavas of the Azores Plateau and on the islands were determined using absolute geochronology methods. The oldest island in the Azores Archipelago is Santa Maria located near the eastern edge of the Plateau (Fig. 2.4). The isotopic ages on this island show that it was active in the time interval between 8.12 (Abdel-Monem *et al.*, 1975) and 3.2 Ma ago (Feraud *et al.*, 1984). In the same region, other ages were obtained as in Ponta Sul submarine ridge, located northwest of Santa Maria, with 5.9 Ma (Beier, 2006), and at Formigas Bank, situated northeast of Santa Maria, with 4.65 Ma (Abdel-Monem *et al.*, 1975).

The beginning of the subaerial volcanic activity in São Miguel Island is estimated to have stated, at its most eastern part, at 4.0 Ma (Abdel-Monem *et al.*, 1975). This age shows coeval volcanic

activity with Formigas Bank and is contemporaneous with the latest volcanic phase at Santa Maria.

At Monaco Bank, which is close to the south coast of São Miguel, it was found an age of 39 Ma (Beier, 2006), which is the oldest age found on any volcanic rock of the Azores Plateau. If so, Monaco Bank would be only 11 Ma younger than the maximum age predicted by Searle (1980) for the Azores Plateau, but it would be much older than the 20 Ma predicted by Gente *et al*. (2003) for the early stage of the construction of the Plateau.

The volcanic activity building up the Central Island Group presents younger ages than in the Oriental Island Group, reflecting a regional tendency for the westward migration of volcanism. On Terceira Island, the oldest know age is 3.52 Ma (Ferreira & Azevedo, 1995) while Graciosa has a maximum age of 2.5 Ma, according with Rb/Sr geochronological data of White *et al.* (1976). Currently, the oldest know age in Faial and Pico islands are 0.73 Ma (Feraud *et al.*, 1980) and 0.27 Ma (Demand *et al.*, 1982) respectively, evidencing the youth of the emerge part of the Pico Ridge when compared with the islands positioned on Terceira Axis. The age on the submarine part of Pico Ridge determined by Beier (2006), on the eastward submarine prolongation of this structure, is 1.49 Ma.

On São Jorge, Feraud *et al.* (1980) determined a maximum age of 0.55 Ma, nonetheless, recently Hildenbrand *et al.* (2008) doubled this age and showed that São Jorge began its emerge volcanic phase at 1.32 Ma.

The islands located west of the MAR were also dated and Flores seems to be older with a maximum age of 2.2 Ma (Azevedo *et al*., 1991) while Corvo could have approximately 1.5 Ma (França *et al*., 2006a). The comparison between the oldest known ages obtained on Flores, Corvo and Faial (0.73 Ma) and the age of the Plateau given by magnetic anomaly 5 (10 Ma), evidences that volcanism forming the islands is much younger than the plateau where they are rooted. This scenario, can be transposed to the rest of the Plateau where the islands and the submarine volcanic structures formed during much younger volcanic events that the underlying lithosphere.

Other ages where obtained by Beier (2006) on the submarine elevations of the Azores Plateau as in Alcatraz Bank with 5.43 Ma, located on the north border of Hirondelle basin, and in a structure situated North of Pico Ridge with 4.89 Ma. The seamounts located southwest of Faial Island, as

Princess Alice Bank yield ages of 6.01 and 5.51 Ma and Condor de Terra Bank yield and age of 1.10 Ma (Fig. 2.4).

Presently, the Azores Archipelago is volcanically active and about 26 historical eruption are reported on the Azores either subaerial, in São Miguel, Terceira, São Jorge, Faial and Pico, or submarine e.g. D. João de Castro Bank. The last volcanic eruption, also called Serreta Eruption, occurred at sea, 8.5 km west of Terceira Island, in 1998/2000 (Forjaz *et al.*, 2000, 2001).

2.4 General Geochemical Characterization

The Azores Plateau is a anomalously shallow morphology that due to the excess of magmatism/volcanism formed relatively thick lithosphere, with approximately 14 Km (Escartín *et al.*, 2001), and a positive gravity anomaly (Escartín *et al.*, 2001; Gente *et al.*, 2003) that contrast with normal oceanic lithosphere. The excess magmatism/volcanism has been interpret to have result from either a small thermal plume head that interacted with the MAR producing a geochemical anomaly along the MAR (Shilling 1975; White *et al.*, 1979; Cannat *et al.*, 1999; Dosso *et al.*, 1999) or from an anomalously volatile-enriched mantle, also called "wet-spot", which interacted with the MAR (Bonatti, 1990; Schilling *et al.*, 1980). This interaction is observed on the composition of the basalts along the ridge, which are enriched in incompatible trace elements and isotopic ratios when compared with the "normal" mid-ocean ridge basalts (N-MORB). The enrichment forms a long wave-length geochemical anomaly along the MAR with its maximum enrichment along the Azores Plateau as observed by Schilling (1975), White & Schilling (1978), Yu *et al*. (1997), Dosso *et al*. (1993, 1999) and Bourdon *et al*. (1996) among others.

In the Azores Plateau, at a regional scale, the geochemical and isotopic signature of the basalts (s.l.) is characterized by an enrich composition in incompatible trace elements and by high Sr and Pb and low Nd isotopic ratios, that are within the range of the ocean island basalts (OIB). Nonetheless, at a smaller scale, the Azores Archipelago has important intra/inter-island compositional variability, especially in the isotopic signature, that will be show along the text.

Essentially, the islands are formed by volcanic rocks with basaltic composition form but in some of the, e.g. São Miguel, Terceira, Graciosa, Faial, Flores and Corvo islands; due to magmatic differentiation processes, it is possible to find a wider lithological variability that can reach

trachytic compositions. Other less common lithologies have been reported in the Azores as the comenditic trachytes in São Miguel and Terceira (Schmincke & Weibel, 1972), the comendites and the pantellerites in Terceira (Schmincke, 1973). The alkaline signature of the lavas is predominant in all islands despite few punctual tendencies for transitional basalts, as for instance, in Furnas Volcanic Complex (São Miguel, Rodrigues *et al*., 1995), in Pico Island (França *et al.*, 1995), and in Terceira Island (Madureira, 2006).

Major element geochemistry depicts some specific characteristics of island as the sub-saturation and sodic nature of Santa Maria (White *et al*., 1979), the higher SiO_2 content and peralkaline nature of Terceira lavas (White *et al.*, 1979), the enrichment in K_2O (Schmincke & Weibel, 1972) and TiO_2 (Prytulak & Elliot, 2007) of São Miguel. The remaining islands of the Archipelago have similar characteristics regarding major element concentrations exhibiting undersaturated and alkaline compositions with the predominance of sodium over potassium (e.g. França 2000; França *et al.*, 2006, 2006a; Azevedo & Ferreira, 2006; Madureira, 2006; Beier, 2008). Also, geochemical data on submarine lavas published by White*, et al.* (1976), Schilling (1975) and, more recently, by Beier (2006) revealed that the compositional signature found on the islands propagates throughout the Azores Plateau, where there is a strong alkali enrichment. This enrichment, especially in K_2O, is stronger in the eastern side of the plateau near São Miguel, and decreases slightly westward towards the MAR and Terceira Axis, where some of the basalts display a transitional signature. These plateau transitional basalts are explained by Beier (2006) as variations in the melting conditions as for instance, higher degrees of partial melting and variations in the depth of melting, possible at shallow levels, but not by different source composition.

All the islands and the plateau lavas have enriched compositions in LREE relative to HREE[1] with $(La/Yb)n$[2] and $(La/Sm)n$ ratios that point to deep mantle melting process within the garnet stability field. In detail, the highest LREE/HREE ratios are found on São Miguel and Santa Maria islands (White *et al.*, 1979) as well as in the eastern region of the Plateau (Beier, 2006). The light and heavy REE ratios decrease in the Central and Occidental islands groups when compared with the Oriental Island Group, nonetheless, are indicative of a garnet-bearing mantle source.

[1] LREE – light rare earth element; HREE – means heavy rare earth element.
[2] "n" – normalized to chondritic ratios.

The concentrations in incompatible trace elements measured in the Azores basalts shows enrichment in those elements and relative similar patterns when plotted on a spider diagram. Even so, some of these concentrations are characteristic of an island, as for instance the LILE[3], Th, Hf, Nb, Ta and Sr enrichment in São Miguel, the Ba enrichment and Sr depletion in Terceira (White *et al*., 1979).

The Azores Archipelago is characterized by an uncommonly large isotopic diversity. The $^{87}Sr/^{86}Sr$ and $^{143}Nd/^{144}Nd$ isotopic ratios exhibit a negative correlation with extreme compositions particularly in São Miguel Island, where radiogenic Sr can reach up to 0.70509 (White *et al.*, 1976), while Nd is low and decreases from 0.513002 to 0.51262 (Turner *et al.*, 1997; Widom *et al.*, 1997). On the Pb-Pb bi-dimensional plots is where the Azores islands reveal more clearly their differences (e.g. Oversby, 1971; Davies *et al*., 1989; Turner *et al*., 1997; Widom *et al.*, 1997; Beier *et al.*, 2006; França *et al.*, 2006 and Elliot *et al*., 2007). São Miguel plots above the NHRL ranging between the MAR signature and very radiogenic $^{207}Pb/^{204}Pb$ and $^{208}Pb/^{204}Pb$, while Terceira extends from the MAR towards more radiogenic $^{206}Pb/^{204}Pb$ and Graciosa has variable $^{206}Pb/^{204}Pb$ for a given $^{207}Pb/^{204}Pb$. In Faial the $^{206}Pb/^{204}Pb$ ratios are the lowest values of the archipelago (≈18.637) and Flores Island shows a tendency to follow this signature. São Jorge and parts of Pico lie on the NHRL and overlap partially the isotopic field of the basalts from the adjacent MAR.

As described, the isotopic variability characterizing the basalts of the Azores is interpreted to be the reflex of a heterogeneous mantle source, what in conjunction with the distance between the islands, 40 to 100 km, evidences small-scale mantle heterogeneities. Isotopic diversity is also detected even at smaller scales on a single island, as in São Miguel, where the Sete Cidades Complex, building-up the west side of the island, is comparatively less radiogenic than Nordeste Complex, building-up the eastern side of São Miguel (e.g. Turner *et al.*, 1997; Widom *et al.*, 1997; Beier *et al.*, 2006 and Elliot *et al*., 2007).

Each isotopic array, Sr, Nd and particularly Pb, has been attributed to mixing between mantle components: one “enrich” mantle component with a specific composition that characterized each island and a depleted component related to the close presence of the MAR, which trends to the DMM mantle component defined by Zindler & Hart (1986).

[3] LILE stands for large-ion lithophile element.

The "enrich" component has been particularly well studied in São Miguel and Terceira islands. The extremely high $^{207}Pb/^{204}Pb$ and $^{208}Pb/^{204}Pb$ ratios in São Miguel and the radiogenic $^{206}Pb/^{204}Pb$ ratios in Terceira have been related with EMII and HIMU mantle components, respectively (Widom *et al*., 1997, Turner *et al*., 1997). The EMII components has high $^{87}Sr/^{86}Sr$ and low $^{143}Nd/^{144}Nd$ ratios and is considered to be associated with the presence of recycled sediments or subcontinental mantle lithosphere in the parent source of magmas, while a HIMU source is thought to represent recycled subducted oceanic crust and/or lithosphere (Zindler & Hart, 1986).

The $\delta^{18}O$ data from Widom & Farquhar (2003) is consistent with mixing between low $\delta^{18}O$ Azores plume source with a component of subducted, hydrothermally altered lower oceanic crust, and either minor recycled sediment or localized EMII-rich delaminated subcontinental lithospheric mantle. Other isotopic ratios as $^{187}Os/^{188}Os$ where determined for six Azorean islands and the extreme compositions corroborate the previous interpretation of a relative shallow EMII component interacting with a deep mantle component related with the Azores plume (Widom & Shirey, 1996). In addition, both Moreira *et al*. (1999) and Madureira *et al*. (2005) found, respectively, relative primitive He and Ne ratios on the lavas from Terceira and interpreted these results as primitive mantle contribution and evoked the role of a deep mantle plume, presently located beneath Terceira, in the generation of the Azores magmas.

Nonetheless, new Hf isotopic data (Elliot *et al.* 2007) combined with Nd isotopes showed that São Miguel Island defines a steeper slope in the εHf and εNd space than the mantle array. These argue for an enriched mantle component, which is an ancient melt from a garnet peridotite mantle source that was later subducted and isolated for approximately 3 Ga, before being intruded into oceanic mantle lithosphere. At the same time, Beier *et al.* (2007) combining Sr-Nd-Pb-Hf isotopes with trace element data from Nordeste Complex in São Miguel, considered that the subduction of oceanic crust containing small amounts (1-2%) of relatively evolved lavas derived from a subducted seamount, could reproduce the variability of isotopic and trace element ratios observed in the lavas.

Chapter 3: São Jorge Island: A Review

In this chapter it will be presented the island of São Jorge. The main morphologic, tectonic, geological, seismic and volcanic aspects, which characterize the island, will be progressively introduced in order to present a general overview that will serve as the base knowledge for the new data acquired for the present study. Most of the topics developed here review the data already presented by other authors that have focused their work in São Jorge. This is the case of the tectonic, volcanostratigraphic and geochronological studies from Forjaz *et al.*, (1970) Forjaz & Fernandez (1970, 1975), Feraud *et al.*, (1980), Madeira (1998), França (2000), França *et al.*, (2005) and Hildebrand *et al.* (2008) that have been progressively incrementing the knowledge on the island geology and temporal evolution. The seismic and volcanic events that occurred/or affected São Jorge since the early settlement of habitants in the island, in 1439, are also compiled and presented in this chapter.

3.1 Geographic Settings

São Jorge Island is one of the five islands forming the Central Island Group of the Azorean Archipelago occupying a position between the coordinates[4] 38º 45' 24'' N - 28º 20' 44''W and the coordinates 38º 33' 00'' N - 27º 44' 32'' W (Fig. 3.1).

The strategic geographic position of São Jorge on the Central Island Group consents, from any of its seacoasts, a privilege view of the other islands (Fig. 3.1). From the north coast, towards the

[4] Militar Chart of Portugal, Pages 14 to 20, at the scale 1:25 000 of Instituto Geográfico do Exército.

northeast is possible to see, at a distance of 60 km, Terceira Island and, looking north, Graciosa Island is at a distance of 40 km. On the west and southwest coasts, it is possible to see Faial Island, only 30 km away, and its closer neighbor Pico Island, which is just 18 km apart.

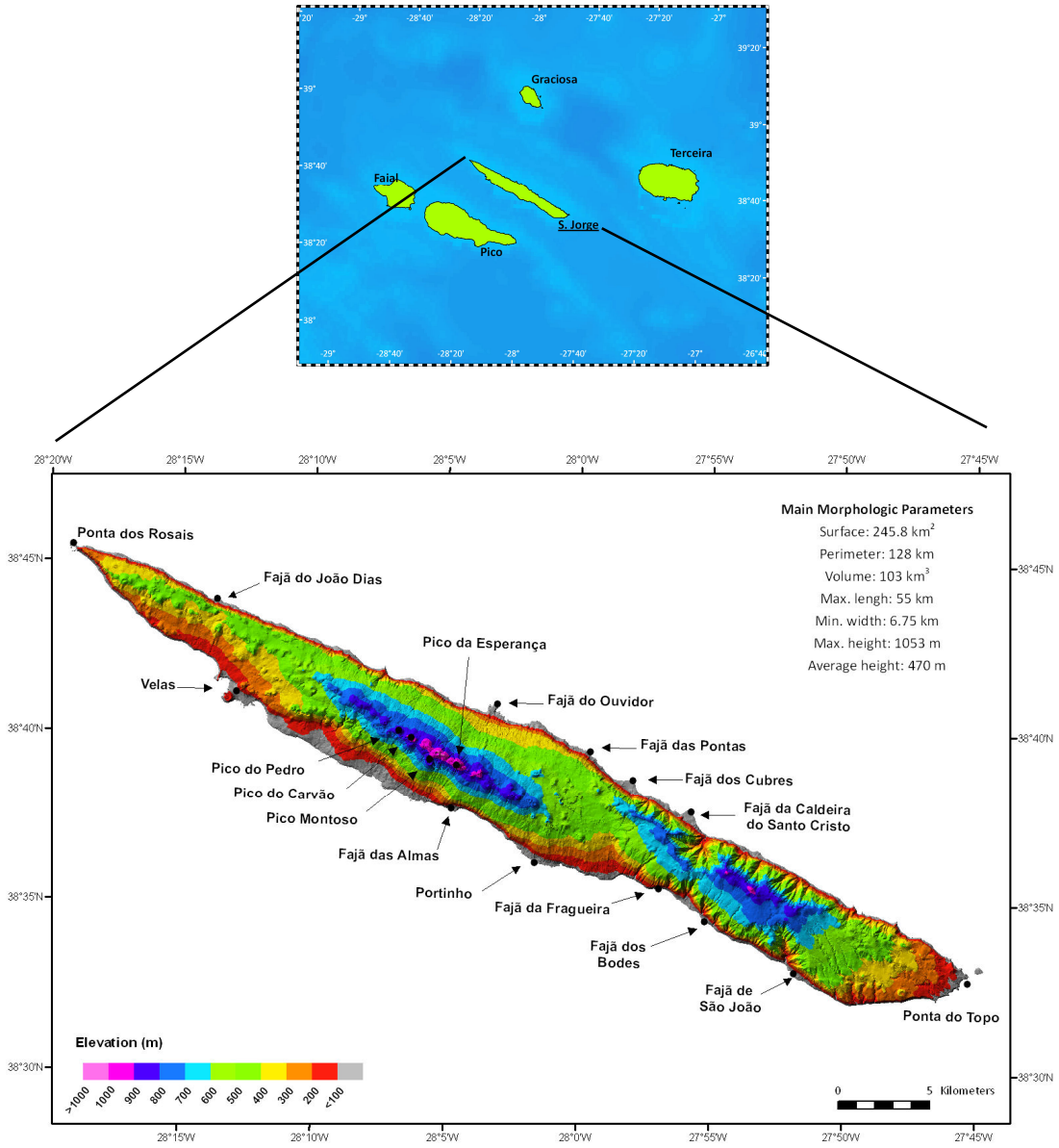

Fig. 3.1 – The upper map shows the geographic distribution of the islands forming the Central Island Group. The lower map shows the relief of São Jorge Island in intervals of 100 m. The locations in the map are mentioned in the text as well as the main morphologic parameters.

São Jorge Island is the fourth largest island of the Azores Archipelago with an area of 245.8 km^2. The island has a very elongated shape with a maximum length of 55 km between Ponta dos Rosais, on the west, and Ponta do Topo, on the east, and a maximum width is 6.75 km between

Fajã das Pontas, located on the north shore, and Portinho, on the south shore (Fig. 3.1). Its shape evidences an axial zone oriented with the direction 120°N, which is also the main alignment of this area of the Azores Plateau. This axial zone corresponds to the main volcanic direction that constructed the island by fissural volcanic activity and formed imposing volcanic piles of predominantly lava flows, frequently, alternating with pyroclastic deposits.

Administratively, São Jorge is divided into two municipalities: Calheta in the east with five parishes and Velas in the west with six parishes (Table 3.1). The population, mainly rural, is distributed by several localities surrounded by unpopulated pastureland; however, it can be observed a lager concentration and development of the villages situated along the south coast of the island (Fig. 3.2).

Table 3.1 – In this table are discriminated the municipalities and parishes of São Jorge Island with their respective areas. The population corresponds to the number of people living in each parish in 2001, according with the latest available data from CENSUS 2001 of the National Statistics Institution of Portugal (INE).

Municipality	Parish	Area (km^2)	Population
Velas	Manadas	11.2	400
	Norte Grande	31.85	688
	Rosais	24.23	820
	Santo Amaro	22.53	902
	Urzelina	13.69	866
	Velas	13.89	1929
Calheta	Calheta	18.81	1249
	Norte Pequeno	12.11	261
	Ribeira Seca	53.77	1105
	Santo Antão	32.34	921
	Topo	9.24	533

The number of habitants on São Jorge, in 2002, was 9522 and according with the National Statistics Institution of Portugal (INE) this number has been decreasing at a rate of 7% per year if we consider the 10219 habitants of the island in 1991. The decrease in population is a general tendency in the Azores region where in São Jorge only lives 4% of the population.

The average population density in São Jorge is relative low (39 habitants per km^2) when compared with the average of the Azores (104 habitants per km^2). Still, as can be observed in Fig. 3.2, the population density in Velas is high, with 139 habitants per km^2. As well, in Fig. 3.2 it is possible to observe that beside Velas, most of the populated parishes in São Jorge are Urzelina, Manadas and Calheta evidencing the tendency for people to concentrate in urban areas along the south coast.

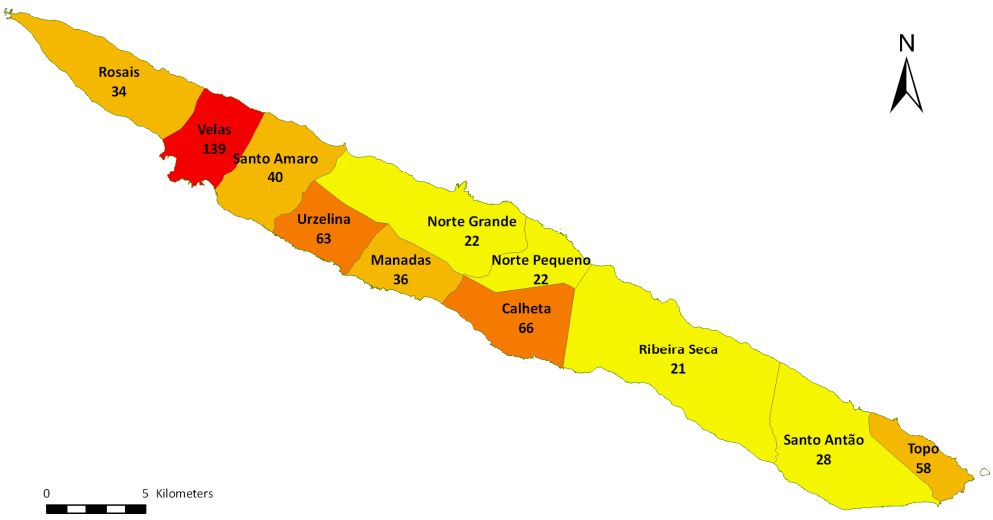

Fig. 3.2 – Map with the administrative distribution of parishes in São Jorge Island and their respective population density (number of habitants per km^2). Notice the higher densities in Velas, the capital, and on the parishes located on south shore of the island.

3.2 Geomorphologic Characterization

The morphology of São Jorge exhibits contrasting characteristics as the scarps that surround the island, the smoother topography on summit areas and the elevated peaks in the center of the island with altitudes higher than 900 m, e.g. Pico do Pedro with 901m, Pico Montoso with 945 m, Pico do Carvão with 956 m and, the highest, Pico da Esperança with 1053 m (Fig. 3.1).

Beside the fissural volcanic activity that constructed the island, other geologic processes as sea erosion, flank instability and tectonic structures modeled continuously São Jorge morphology. Sea erosion and flank instability should have been the main erosion agents shaping the coastline with a perimeter of ≈128 km. Nonetheless, the majority of the shorelines follow preferably the island main axis coinciding also with the regional tectonic setting; therefore, evidencing a close relationship between tectonics and erosion.

Because São Jorge was formed by fissural volcanic activity and shaped by erosion and tectonics, presents morphologic characteristics that contrast with other islands of the archipelago that have a central volcano edifice. The contrast are depicted in the diagram of Fig. 3.3 that distributes the

landmass of the islands by altitude intervals, and where São Jorge reveals a distinct profile from the neighbor islands of Faial, Pico and Terceira and of São Miguel. Most of the territory of São Jorge is located at an altitude between 300 and 600 m, while Faial, Terceira and São Miguel, with similar profiles, have most of their landmass bellow the 300 m. Pico Island with its highest point at 2351 m exhibits a different elevation profile, even so, approximately 50% of its landmass is bellow 400 m.

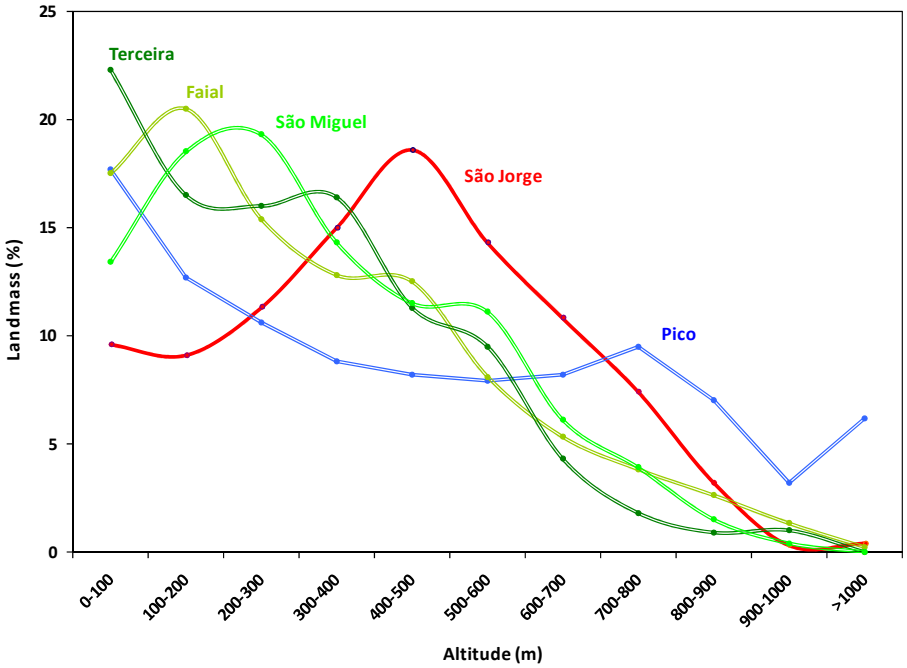

Fig. 3.3 – The diagram shows the distribution of the landmass of São Jorge, Faial, Terceira, São Miguel and Pico Islands with respect to their altitude. Data from CMMG, Azores University[5]

In detail, several morphological differences can be observed between the north and south coasts of São Jorge. The northern coast is characterized by having very steep and elevated coastal-cliffs, frequently with more than 400 m height and dipping more than 40°, while the southern coast is less inclined and usually less elevated.

The shoreline surrounding São Jorge is frequently disrupted by the locally called *fajãs*. The *fajãs* are relative flat platforms that assume a particular important role on the island since they are located at the base of the slopes and allow access to the sea (Fig. 3.4). The fajãs can be formed

[5] http://www.climaat.angra.uac.pt/

either by clastic deposits accumulated at the base of the slopes, due to flank instability, or by more recent lava flows that spread into the sea forming lava deltas. An important feature of the fajãs is that they protect the coastal cliffs from sea erosion and help to preserve (or fossilize) the older scarps. Examples of lavic fajãs are the lava deltas named Fajã do Ouvidor, on the north coast, and Fajã das Almas located on the south shore. Examples of detritic fajãs are Fajã da Caldeira do Santo Cristo and Fajã de São João (Fig. 3.1). The combination between both types of fajãs, lavic and detritic, is described by Borges (2003) at Fajã dos Cubres. The surface of this fajã is formed by a platform constituted by sediments progressively deposited during mass flows that overlay, at least partially, an older lava delta.

Fig. 3.4 – Picture of Fajã dos Cubres with the natural lagoon created by the interaction of the sediments and the sea. According with Borges (2003) this fajã was formed by the combination of a lava delta overlaid by clastic sediments.

A particularity of Fajã da Caldeira do Santo Cristo and Fajã dos Cubres is the existence of a natural lagoon in each fajã that results from a complex balance between the sea regime and the sediments forming the fajã (Fig. 3.4) and with the presence of an important and rare biodiversity (Borges, 2003).

On summit areas of the island, several morphologic differences are observed between the eastern, central and western parts of São Jorge. On the eastern side, the volcanic structures are smooth and present evidences for longer exposition to erosion and weathering process than in the western side where the volcanic cones are relatively well preserved. On the center of the island, the relief is more vigorous and the volcanic edifices maintain their original shape indicating their youth in comparison with the rest of the island. The transition between the eastern and central zones is located in the area south of Fajã das Pontas, where smother morphology forms a plateau at 600 m height with a saddle-like shape, as can be observed in Fig. 3.1.

The drainage system has modeled São Jorge landscape and in particular, the eastern side of the island where is better emplaced. In this area, the drainage system shows some hierarchy (Madeira, 1998) and the watersheds are visible on the morphology. On the western side, the drainage system is formed, mainly, by linear streams lacking hierarchy patterns and evidencing their youth relative to the eastern side.

3.3 Main Tectonic Structures

The tectonic study of São Jorge, presented by Madeira (1998), makes a review of the previous works of Forjaz and coworkers and adds new and important data to the knowledge and interpretation of the island tectonic setting. In view of that and since Madeira (1998) confirmed and included the data of the previous works, the tectonic description is mainly founded on this author work.

The geographic and morphologic characteristics of São Jorge demonstrate that the 120°N azimuth is the preferential direction that dominates São Jorge tectonic setting and, consequently, the fissural volcanism the constructed the island. When considered regionally, the island tectonic setting mimics the overall pattern of the morphological and structural features that dominates the Azores Plateau, in this sector, which concentrated volcanic activity and develop a linear volcanic ridge that emerged and formed the island (Lourenço, 1998)

Madeira (1998) showed that the 120°N direction corresponds presently to the dominant and active fault system to which most of the volcanic and tectonic structures are subordinated, nonetheless, a second family of faults, with a more discrete expression, follows the 150°N regional direction (Fig. 3.5). From tectonic markers on fault scarps and on volcanic structures it was inferred that the movement along the 120°N fault system is extensional oblique combined with a right lateral strike-slip component, while the 150°N faults have an oblique extensional behavior combined with a left lateral strike-slip component.

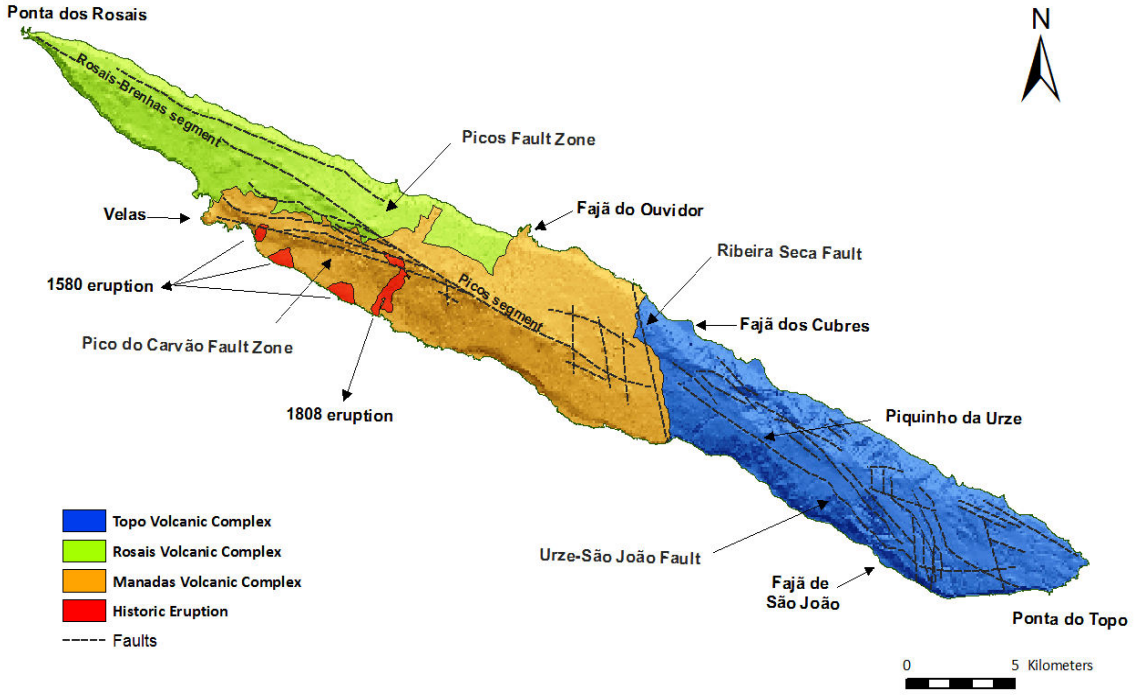

Fig. 3.5 – Map showing the three main stratigraphic units defined by Forjaz & Fernandez (1975): Topo, Rosais and Manadas volcanic complexes. The most recent lavas from Manadas Volcanic Complex correspond to the lavas of the 1580 and 1808 historical eruptions that affected the south side of the island. The faults on this map are adapted from Madeira (1998). The main faults are aligned with the 120°N and the 150°N direction, which corresponds to the regional tectonic setting.

The 150°N regional direction has a relative discrete expression on São Jorge and is visible on some tectonic and volcanic structures e.g. small-scale faults, oriented dikes or aligned volcanic cones. The Ribeira Seca Fault is the most significant structure from the 150°N fault system that crosses São Jorge (Fig. 3.5). Along this fault, initially inferred by Forjaz & Fernandes (1975), it is not possible to identify any structure, as for instance fault scarps, that could be directly related with a fault, however, evidences as the inconformity contact between distinct volcanic units and the northward displacement of the east side of the island, reinforces its existence.

As can be observed from Fig. 3.5, the Ribeira Seca Fault has a strong impact in the island dividing it into the east and west side and breaking the continuity between the structures located on each side. The inferred movement along Ribeira Seca Fault points to the combination of a left lateral strike-slip movement with a dip-slip component dipping west, and according with Madeira (1998), since the beginning of the edification of the island, Ribeira Seca Fault could have produced the northward displacement of the east side of São Jorge, in the order of 3 to 3.5 km, and the vertical slip of the west side of unknown lengthiness.

The 120°N faults on São Jorge exhibits a series of complex structures, segments and ramifications. In fact, this is the principal fault system that favored the ascension of magma to the surface and along which most of the volcanism occurred.

As mentioned, the 120°N faults system has no continuity between the east and west side of São Jorge. On the east side, the main fault is the Urze – São João Fault that exhibits a sinuous profile that varies between 120°N, 150°N and a E-W direction (Fig. 3.5).

On the western side, the main fault system follows predominantly the 120°N direction where several segments or deformation zones can be observed (Fig. 3.5). The Picos Fault Zone has 33 km and is subdivided into the Picos segment and the Rosais-Brenhas segment. The Pico do Carvão Fault Zone has an onshore extension of 12 km and presents a profile that bends from 120°N, near the connection point with Picos segment, towards a WNW-ESE direction, near Velas where it continues toward São Jorge-Pico Channel.

3.4 São Jorge volcanostratigraphy

The studies of Machado & Forjaz (1965) on São Jorge based on geomorphologic, tectonic and geologic evidences, predicted that three main volcanic phases progressively constructed the island. After this study, other works (Forjaz *et al.* 1970; and Forjaz & Fernandes, 1970; Forjaz *et al.*, 1990 and Madeira, 1998) refined the stratigraphy of São Jorge making small readjustment on the cartographic limits of each volcanic complex/stratigraphic unit.

The names of the stratigraphic units also suffer some changes as the case of Manadas Volcanic Complex. This unit defined by Machado & Forjaz (1968) was called Terreiros Volcanic Complex and then, in 1970 Forjaz *et al.* and Forjaz & Fernandes rename it to Manadas Volcanic Complex. Later, in 1990 Forjaz *et al.* rename it again to Terreiros Volcanic Complex. For the purpose of this work and for the homogeneity of terminology with of the most recent work of Madeira (1998) the names of the volcanic complexes that will be used are the ones defined by Forjaz & Fernandes (1970) for the Portuguese Geologic Chart: Topo Volcanic Complex, Rosais Volcanic Complex and Manadas Volcanic Complex.

As earlier mentioned, São Jorge Island grew progressively in three volcanic phases. The first phase emplaced Topo Volcanic Complex on the east side and then volcanic activity begins to migrate to the west and starts to edify Rosais Volcanic Complex. The subsequent displacement of volcanism towards the center of the island created a third stratigraphic unit named Manadas Volcanic Complex (Fig. 3.5).

The volcanic complexes comprise thick volcanic sequences formed by fault-controlled fissural volcanism, which more striking evidence is observed on the volcanic cones disposed along the main active faults. The morphologic characteristics of São Jorge expose continuously along the steep cliffs, forming the island coastline, the volcanic sequences formed predominantly by lava flows, which alternate frequently with pyroclastic deposits.

On several locations, the existence of the lavic or detritic fajãs facilitates the access to the base of the volcanic piles. In these cases and specifically in this work, the lava sequences at those locations will inherit the fajã name e.g. Fajã de São João lava sequence.

3.4.1 Topo Volcanic Complex

Topo Volcanic Complex was the first to emerge, forming the eastern side of the island comprised between the most eastern tip, Ponta do Topo, and Ribeira Seca Fault (Fig. 3.5). The contact between Topo and Manadas volcanic complexes, visible on the south coast, is an inconformity with Manadas lavas overlying old Topo products as pointed out by Madeira (1998).

The eastern side of São Jorge is, presently, largely eroded when compared with the rest of the island putting to evidence its older age. Evidences of erosion are present on summit areas where the morphology is smoother, along the coast with the steeper cliffs and on the fajãs, which are predominantly detritic. The cliffs are more pronounced along the north coast and are likely the combination of the tectonic activity along the 120°N direction and sea erosion. In addition, the left lateral strike-slip component of Ribeira Seca Fault produced the northward displacement of Topo Complex favoring erosion, which resulted on the present exposure of the axial zone of Topo complex (Madeira, 1998).

The products of volcanic activity, which developed thick volcanic piles, should have been mainly effusive due to the predominance of lava flows mainly of *aa* type over pyroclastic materials. The volcanic sequences are cut, frequently, by dikes oriented with the tectonic system and are more abundant at base of the slopes and on the exposed axial zone. In the periods between eruptions, soils had time to form and it is frequent to find thick reddish baked-soils interbedded with lava flows (França *et al.*, 2005).

In the most eastern part of the island, in the area of Topo village, the cliffs are formed by pyroclastic material, occasionally cut by dikes, what evidences a more explosive volcanism at this location (Fig. 3.6). In the summit areas, near Topo village, erosion has smoothed the topography and weathering has deeply altered the rocks producing a thick layer of soils (Fig. 3.7).

Fig. 3.6 – Outcrop of one of the sea cliffs of São Jorge located at its most eastern tip near Topo Village. These cliffs are mainly formed by pyroclastic deposits cut by dikes.

The most expressive fajãs on the north shore of Topo Volcanic Complex are the Fajã da Caldeira do Santo Cristo and Fajã dos Cubres, each one with a natural lagoon as presented in Fig. 3.8. These fajãs are at the base of impressive cliffs that can reach up to 500 m and are separated from each other approximately 3 km.

The lava sequence forming the cliff behind Fajã dos Cubres has approximately 500 m from sea level to its top at Norte Pequeno village. At the base of the Cubres sequence, lava flows evidencing effusive volcanism, are cut, frequently, by dikes; however, as the volcanic sequence grew, pyroclastic layers become more abundant and intrusions diminish. On the latter stages, volcanic activity, on Cubres sequence becomes again more effusive and the top of the sequence is formed mainly by lava flows with relative thin width.

Fig. 3.7 – Volcanic cones located on the eastern side of São Jorge near Topo village. Notice the smooth contour of the cones shaped by erosion, revealing a long period of exposure.

On the south shore of Topo Volcanic Complex one of the most prominent fajãs is the Fajã de São João that gives access to a lava flow pile with more than 400 m. The sequence is formed by the accumulation of relative thick lava flows frequently cut by dikes, which can reach metric width. Towards the top, the lava flows of São João sequence are more often interbedded with baked soils (Fig. 3.9) suggesting larger intervals between eruptions.

Fig. 3.8 – Picture taken from Fajã das Pontas towards the east. From here is visible the aspect of the northeast coast of São Jorge, with Fajã dos Cubres (first plane) and Fajã da Caldeira do Santo Cristo with their lagoons.

Fajã de São João sequence was considered a part of Topo Volcanic Complex (Forjaz & Fernandez, 1975; Madeira, 1998). Nevertheless, the lavas from this lava sequence exhibits different characteristics expressed by the presence of highly porphyritic lavas with large and well developed plagioclase phenocrysts. These porphyritic lavas of Fajã de São João occur as lava flows or dikes and can be considered as plagioclase cumulates (as will be detailed further ahead).

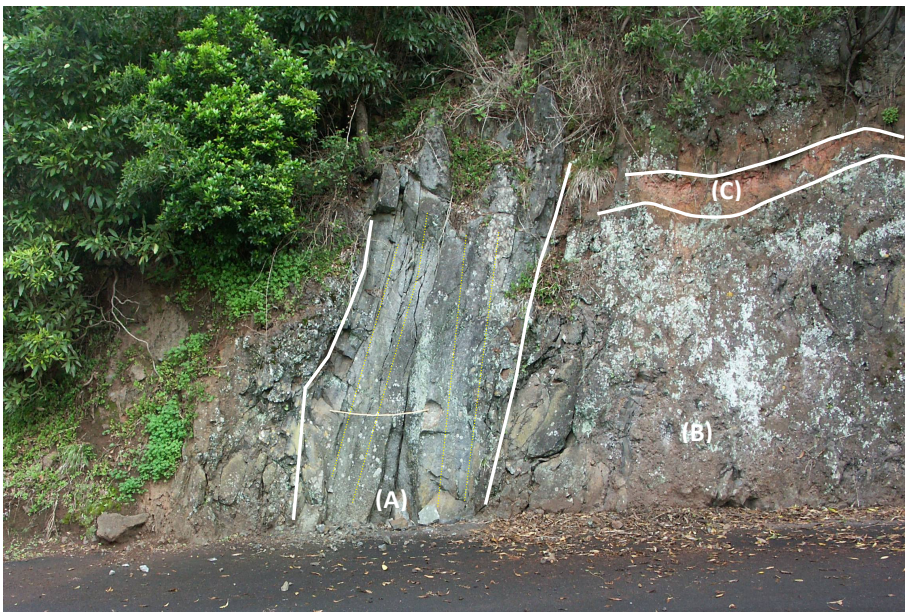

Fig. 3.9 – General aspect of an outcrop on São João lava sequence, which exhibits different characteristics from the remaining lava sequences on the island, as for instance the plagioclase-rich lavas. In the picture a metric and symmetric layered dike (A) cuts through a thick lava flow (B) topped by a baked soil (C).

3.4.2 Rosais Volcanic Complex

After the onset of Topo, volcanism migrates westward and begins the edification of Rosais Volcanic Complex that extends between Ribeira Seca Fault and Ponta dos Rosais (Fig. 3.5). The volcanic activity, which was predominantly effusive, also edified thick volcanic piles as in Topo Volcanic Complex.

Presently, the lava sequences outcrops along the strongly eroded coastal cliffs; however, on summit areas volcanic structures, e.g. scoria cones, are better preserved indicating their youth relative to Topo. The most expressive volcanic cones of Rosais are located between Velas and the area near Rosais lighthouse. Pico da Barroca, Pico do Tanoeiro, Pico dos Matinhos, Pico das Urzes, Pico da Velha and Monte Trigo are some of the Rosais cones that lay in the Rosais-Brenhas fault segment (Fig. 3.10).

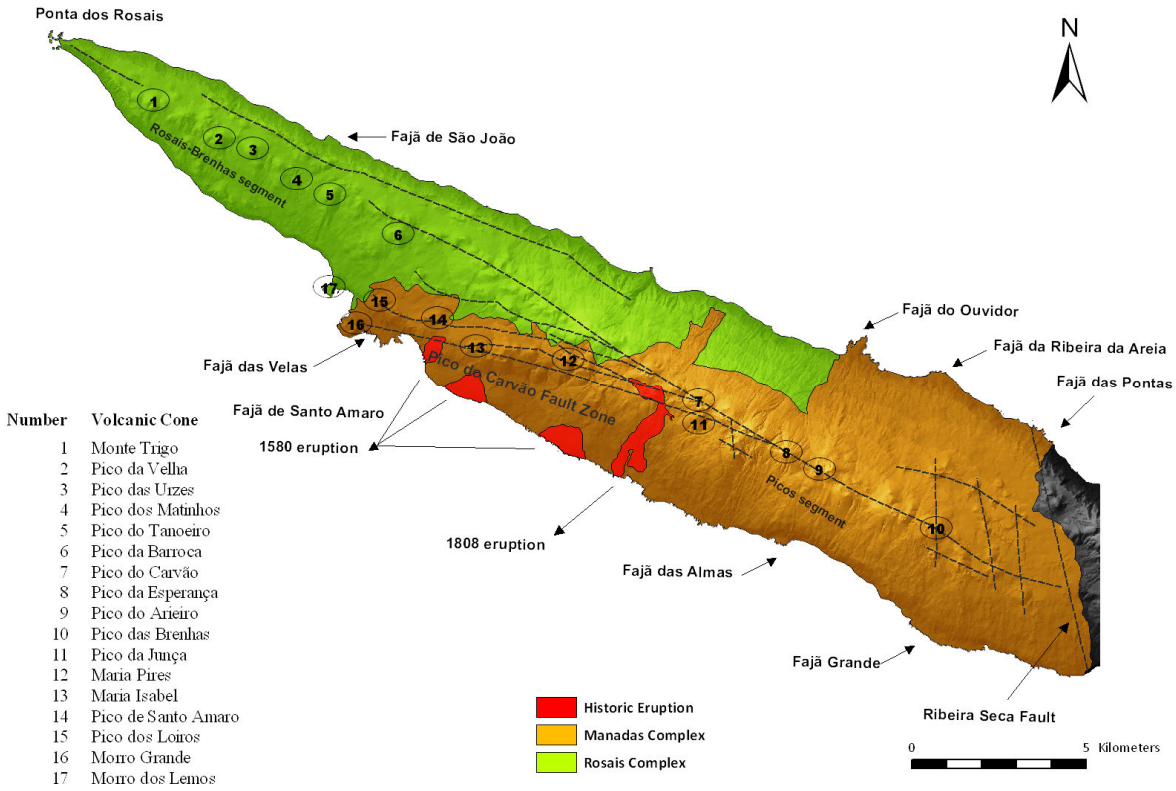

Fig. 3.10 – Detailed view of the geologic map of Rosais and Manadas Complexes (adapted from Madeira, 1998) with the principal faults, fajãs and the position of the volcanic cones.

The stratigraphic contact between Topo and Rosais volcanic complexes is not visible because it was covered by Manadas lavas; however, the contact between Manadas and Rosais is visible, especially, where the recent lavas cover the old coastline of Rosais. This is the case of the old Rosais coastline, which forms the cliff behind Fajã das Almas, located east of Manadas Village (Fig. 3.11). This cliff is an impressive vertical lava sequence, formed by thin lava flows sometimes interbedded with baked soils, that was shaped by erosion and latter covered by the lava flow that formed the fajã.

Fig. 3.11 – This picture was taken from Fajã das Almas looking southeast and shows a part of Rosais lava sequence forming the shore line behind Fajã das Almas. This lava sequence is located on the south shore of São Jorge and is formed by the pile up of relative thin lava flows.

Fig. 3.12 – Cliff located on Fajã do João Dias exhibiting several pyroclastic deposits cut by an intricate network of dikes that reveals a complex volcanic history.

Another important volcanic sequence from Rosais Volcanic Complex is located in the north shore close to Ponta dos Rosais, constituting the cliff behind Fajã do João Dias (Fig. 3.12). This cliff elevates from sea level to its summit at 450 m and exposes macro-scale structures with thick pyroclastic layers interbedded with lava flows and baked soils, decameter dikes, all exhibiting an intricate stratigraphic relation. At the base of the sequence, alternating layers of explosive material and vesicular lava flows are abundant.

3.4.3 Manadas Volcanic Complex

Manadas Volcanic Complex comprises the most recent volcanic events on São Jorge. During the onset of this complex, volcanic activity instead of continuing its migration westward, as it happened with Rosais, starts to focus on the center of the island.

Manadas is considered to be still volcanically active with the last two sub-aerial eruptions occurring during the year 1580 at Fajã da Queimada and the year 1808 at Urzelina (Fig. 3.10). More recently, a submarine eruption is believed to have occurred during the 1964 seismic crisis (Forjaz & Fernandez, 1975), probably in the offshore prolongation of Pico do Carvão Fault Zone (Madeira, 1998).

In this complex, recent lava flows are well conserved and some of them often cover older cliffs and reached sea level forming lava deltas at the base of the slopes. These structures are easily illustrated by the Fajã das Velas, Fajã das Almas, Fajã de Santo Amaro and Fajã Grande on the south shore, and Fajã do Ouvidor, Fajã da Ribeira da Areia and Fajã das Pontas on the north coast. These last three fajãs formed by lavas flows coming from the volcanic cones located on the summit of the island. Curiously, the degree of erosion of the three fajã seem to greater at Fajã das Pontas, the most eastern, and decreases towards Fajã Ouvidor, the most western, suggesting relative increase in age towards the east.

Because of the youth of these lavas flows, several volcanic structures are well preserved. This is the case of the dendritic pattern observed at Fajã do Ouvidor (Fig. 3.13), interpreted to arise from flow fronts repeatedly arrested by enhanced cooling and magma pressure subsequently causing new breakouts as explained by Mitchell *et al.* (2008).

The fault-controlled fissural volcanisms is more evident in Manadas Volcanic Complex with most of the volcanic cones disposed along the main faults crossing Manadas, as the 150°N fault family in the Ribeira Seca area. Also, along the two main WNW-ESE fault zones is evident the distribution of the volcanic cones. Following a east-west direction the Picos fault segment comprises Pico da Brenhas, Pico do Arieiro, Pico da Esperança and Pico do Carvão, while the Pico do Carvão Fault Zone, which bends towards Velas, encompasses Pico da Junça, Maria Pires, Maria Isabel, Pico de Santo Amaro, Pico dos Loiros and Morro Grande (Fig. 3.10).

The volcanic deposits and the eruptive centers preserved on Manadas Volcanic Complex reveals a wider diversity in eruptive styles than on the other complexes as for instance the hydromagmatic eruptions located near Velas.

The area of Velas is a privilege location where magmatic and hydromagmatic eruptions coincide (Fig. 3.14). The Pico dos Loiros cone was the first to erupt and during its activity has generated a thick lava flow, aa type, that covered the old Rosais cliff and formed Fajã das Velas. The tuff cones resulting from surtseyan eruptions, Morro dos Lemos and Morro Grande are located right next to Velas, began to form below sea level and at least until they emerge the volcanic activity should have been predominantly hydromagmatic. The products of this eruption formed hyaloclastite deposits evidencing the interaction of seawater with the magma (Cas & Wright, 1993). At Morro Grande, a small scoria cone that marks a change in eruption style from a hydromagmatic to strombolian phase.

Fig. 3.13 – The Fajã do Ouvidor is one of the most recent lava fajãs of São Jorge where it is possible to observe its dendritic morphology.

The presence of tuff rings in the axial part of the island evidences the occurrence of phreatomagmatic eruptions, which reveal the interaction of magma with groundwater from the island drainage system, as can be observed at Pico do Arieiro.

Pyroclastic flows (*nuées ardents*) of block and ash flow were described during the historic eruption of 1580 and 1808, nonetheless older deposits including surge deposits were found on the volcanic record of Manadas.

Fig. 3.14 – Picture of the volcanic cone Morro dos Lemos taken from the lavic Fajã das Velas. This cone was formed during a phreatomagmatic eruption. The depression observed on the center of the picture shows the contact between the lava from Pico dos Loiros and the products of the hydrovolcanic activity.

3.5 Previous Geochronological Data

The determination of the ages of the lavas on São Jorge Island, using geochronological methods in conjunction with the stratigraphy, allows to date the occurrence of volcanic events, to estimate the growth of the volcanic sequences and to constrains the different volcanic phases in which the island developed. Three studies presenting absolute geochronology data where presented before this study, which brought a new insight on the island evolution. These studies are presented in the next paragraphs.

3.5.1 Geochronological data from Feraud *et al.* (1980)

The first geochronological ages on São Jorge was obtained by Feraud *et al.* (1980) through K/Ar method on four lava flows as can be seen in Table 3.2. The maximum age obtained was 550±60 ka on a lava flow at the base of Fragueira volcanic pile. A second lava flow located west of Topo village delivered an age of 280±90 ka and another one, near Piquinho da Urze yield an age of 140±50 ka. The youngest age was obtained on a lava located ENE of Ribeira Seca village yielding an age of 110±70 ka (Fig. 3.15).

The three oldest ages obtained by Feraud *et al.* (1980) cover only the eastern side of the island where Topo Volcanic Complex outcrops. The 550 and 140 ka old lavas are a good constrain for the edification of the lava sequence at that location(≈1.6 m/ka), while the 280 ka old lava evidences coetaneous volcanic events on different locations of Topo Volcanic Complex. The youngest lava flow with 110±70 ka was collected near the contact between Manadas and Topo volcanic complexes however the error is too large with respect to the age, not allowing any conclusive interpretation.

3.5.2 ^{14}C data from Madeira (1998)

On recent volcanic deposits from Manadas Volcanic Complex (Fig. 3.10) charcoal and organic matter trapped on paleosoils and pyroclastic deposits was dated by Madeira (1998) using ^{14}C method.

The oldest volcanic event occurred at Pico da Esperança at 5310±80 BP and was followed by other 9 sub-aerial volcanic events on the area. The ages obtained are presented in Table 3.2 and in Fig. 3.15 where the historic eruptions that happened in the year 1580AD and the year 1808AD are also represented. According with this work, Madeira (1998) predicts a recurrent interval of eruptions between 200 and 300 years.

Table 3.2 – Compilation of the geochronological data on São Jorge Island. The table includes the K/Ar data from Feraud *et al.* (1980), the volcanic events dated by the ^{14}C method from Madeira (1998) and the K/Ar ages of Hildenbrand *et al.* (2008).

	Age	Location	MAP
Feraud *et al.* (1980)	550±60 ka	Fragueira volcanic pile (base)	
	280±90 ka	West of Topo village	
	140±50 ka	Piquinho da Urze	
	110±70 ka	ENE of Ribeira Seca	
Madeira (1998)	5310±80 BP	Deposit from Pico da Esperança eruption?	[2]
	3740±50 BP	Pyroclastic deposits located at Pico do Carvão	[4]
	2980±60 BP	Pyroclastic deposit located at Urzelina	[5]
	2880±60 BP	Pyroclastic deposit from Pico do Carvão or Pico Montoso eruption	[3]
	2530±60 BP	Deposit from Pico do Arieiro eruption	[1]
	1880±50 BP	Pyroclastic deposits located near Manadas Village	[3]
	1530±90 BP	Pyroclastic deposits located at Pico do Carvão	[4]
	1360±45 BP	Deposit from Pico Pinheiro eruption	[1]
	1120±45 BP	Deposit from Pico Montoso eruption	[3]
	700±70 BP	Pyroclastic deposits located at Pico do Carvão	[4]
Hildenbrand *et al.* (2008)	1323±21 ka	Fajã de São João volcanic sequence (base)	
	1207±17 ka	Fajã de São João volcanic sequence (top)	
	736±12 ka	Fajã dos Cubres volcanic sequence (base)	
	729±11 ka	Fajã dos Bodes volcanic sequence (base)	
	690±11 ka	Fajã dos Bodes volcanic sequence (top)	
	368±6 ka	Sequence located west of Fajã do Ouvidor (base)	
	268±6 ka	Sequence located at Velas (base)	

3.5.3 Geochronological Data from Hildenbrand *et al.* (2008)

Recently the study by Hildebrand *et al.* (2008) presented several new K/Ar ages on São Jorge covering volcanic sequences from Topo and Rosais volcanic complexes as exhibit in Fig. 3.15.

In fact, the lava sequence located on Fajã de São João, on the southeast shore of São Jorge, was formed during an early volcanic phase in a period constrained between 1323±21 ka and 1207±17 ka ago. This lava sequence, considered to belong to Topo Volcanic Complex, is much older than expected and shows that São Jorge began its sub-aerial volcanic activity much earlier than the 550 ka predicted by Feraud *et al.* (1980).

The other volcanic sequences dated by Hildebrand *et al.* (2008) on Topo Volcanic Complex present younger ages than Fajã de São João, as in Fajã dos Bodes with an age range between 729±11 and 690±11 ka and the base of Fajã dos Cubres with 736±12 ka.

The volcanism at Rosais Volcanic Complex was also dated at the base of the volcanic pile situated west of Fajã do Ouvidor yielding an age of 368±6 ka. Presently, this is the oldest age constraining the volcanic events forming the lavas of Rosais Volcanic Complex. A second lava collected at Velas village, also from Rosais Volcanic Complex, was dated yielding an age of 268±6 ka.

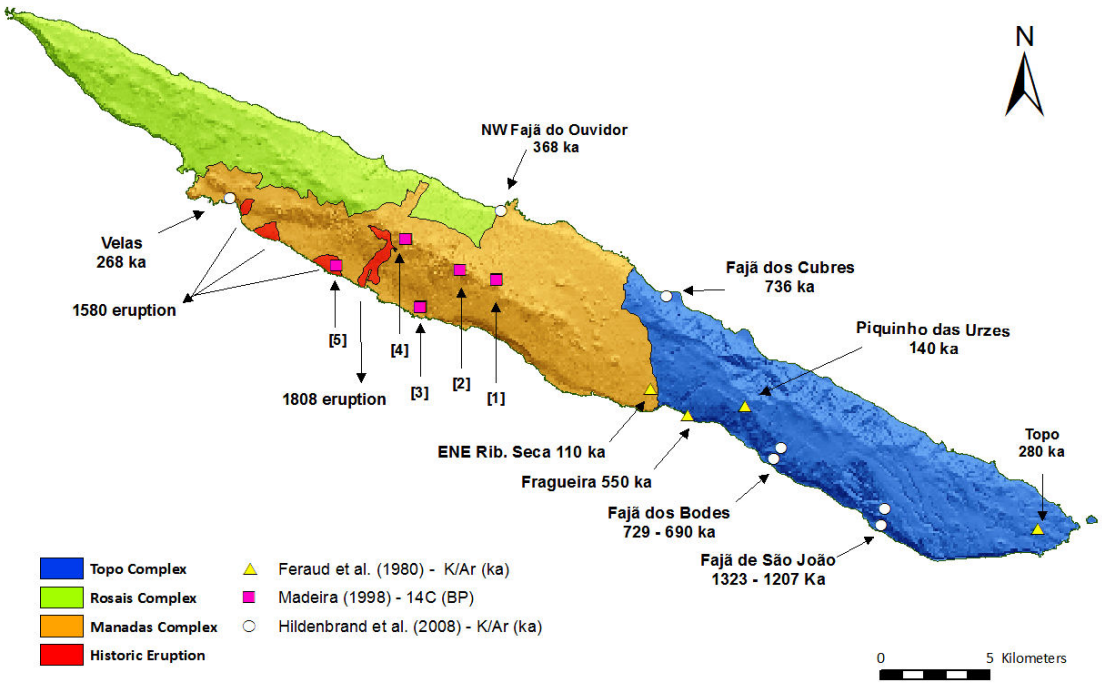

Fig. 3.15 – Map of São Jorge Island showing the geochronological data previous to this work. The ages presented are from Feraud *et al.* (1980), Madeira (1998) and Hildenbrand *et al.* (2008). The data from Madeira (1998) is referenced by location and the ages are presented in Table 3.2, where all the geochronological data is compiled.

3.6 The Historical Eruptions of São Jorge Island

As earlier mentioned, two subaerial eruptions occurred in São Jorge Island after the settlement of the first habitants probably in 1439. These eruptions were observed and described by the local

population, which lives were strongly affected by these events, and were also testified by the populations of the neighbor's islands.

After a series of strong seismic events, the 1580 historic eruption began on the 29th of April on a volcanic cone behind Fajã Estevão da Silveira, located on the south side of São Jorge. This strombolian eruption evolved and a few days later, on the 3rd of May, two vents were ejecting burning gases, bombs and fine pyroclastic material, locally called *bagacinas*. In the afternoon of that day, two lava flows began do form and move down hill reaching the sea and enlarging the fajã. At night, another effusive event starts on a vent located on the back of Fajã da Queimada, which is closer to Velas.

A particularity of the 1580 eruption is that several vents were active and that the lava sources appear in an east–west direction, producing five main lava flows, which reached the sea at Fajã de Santo Amaro, Fajã da Queimada, Fajã da Ribeira de Almeida and Fajã da Queimada Brava, the later with two lava flows (see Fig. 3.10). Another particularity of the 1580 historical eruption was the occurrence of an explosive phase that generated at least one pyroclastic flow or nuée ardent, as compiled in Forjaz *et al.* (2008).

The 1808 eruption in São Jorge Island began on the 1st day of May on a volcanic cone behind the village of Urzelina. This eruption was preceded by intense seismic activity and by volcanic tremor scaring the habitants. From the first to the third day, volcanic activity decreased but then two more vents formed with strombolian activity. After May 10th volcanism becomes more active and a lava flow began to move south towards Urzelina village and reached the sea (Fig. 3.16). This lava flow, named *Mistério da Urzelina*, destroyed a great part of the village and buried almost completely the church of São Mateus. The most devastating event occurred in the 17th of May with a pyroclastic flow that killed thirty-seven people. After the 5th of June the lava flow stopped and, until the first week of July, the eruption ejected mainly fine pyroclastic material (Forjaz *et al.*, 2008).

A third volcanic eruption is suspected to have occurred offshore at the western end of São Jorge, during the seismic crisis of 1964, in which was described the occurrence of volcanic tremor and of a strong sulfurous smell. However, in the next day the seismic activity deceases considerably and the habitants of São Jorge felt no more phenomena (Forjaz *et al.*, 2008).

Fig. 3.16 – Aerial picture of the lava flow produced by the 1808 historical eruption taken in 1970. Courtesy of VH Forjaz.

The volcanic events dated with ^{14}C by Madeira (1998) together with the historical eruptions are presented in the diagram of Fig. 3.17, where they are positioned relative to their distance to Ponta dos Rosais, the west end of the island. The average period between eruptions is close to 425 years, but this recurrence value should be considered as a maximum because it is probable that more volcanic events happened. In fact, as mentioned earlier, Madeira (1998) predicted a recurrent period of 200 to 300 years.

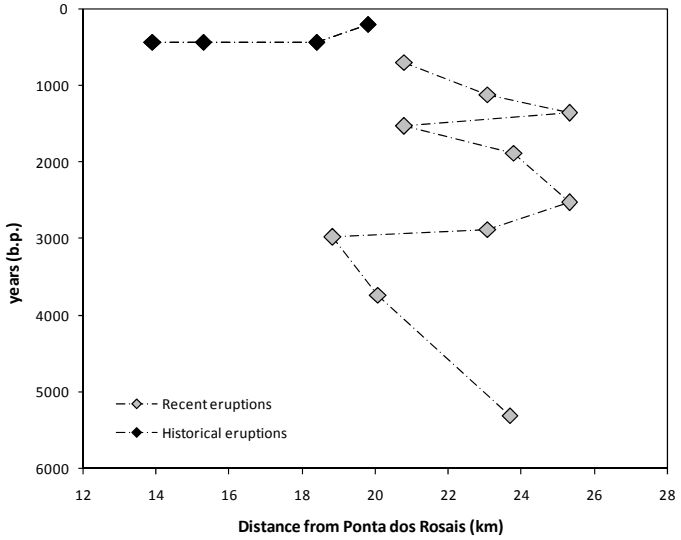

Fig. 3.17 – Spatial and temporal distribution of the more recent volcanic events known in São Jorge. The data of the recent eruptions are from Madeira (1998).

All the considered eruptions occurred in a restricted area with 15 km length, and seem to temporally oscillate between an east-west direction. In addition, these eruptions affected essentially the south side of the island, what in conjunction with field observations indicates that this is one of the most hazardous areas of São Jorge. The volcanic record shows that the eruptive style in São Jorge is principally strombolian, producing lava flows and fine tephra. Nonetheless, the geologic record and the observations during the two historic eruptions points to the occurrence of violent and destructive events with the formation of pyroclastic flows. The possibility of a new eruption in São Jorge with this characteristic affecting the south side of the island, which is, presently, the area that encompasses the most populated parishes should be taken into consideration by the authorities responsible by the volcanic risk, in this case the Civil Protection.

3.7 Significant Historical Seismic Events of São Jorge Island

The distribution of the Azores Islands near the Mid-Atlantic Ridge in a complex tectonic and volcanic active environment is the principal cause for recurrent seismic activity as showed in Fig. 3.18.

The description of the seismic events started with the settlement of the islands probably in 1439, allowing a continuous record of all the macroseismicity as well as their human and material consequences. These descriptions continued to be very important, even after the installation of the seismic network in 1902, because only after 1975 the instrumental data was considered acceptable (Nunes, 1991). The information regarding the historical seismicity of the Azores is distributed throughout several databases as recognized by Carvalho *et al.* (2001):

- The Azores University catalog that covers the period between 1980 and 1998 (Nunes *et al.,* 2000);
- The catalog developed by Costa Nunes (1986) considering the period 1917 to 1979;
- The Seismological Bulletin of the Azores (SIVISA, 1998) with the data from the 1998 Faial earthquake;

- The international catalog from the North Atlantic Region covering the period between 1951 and 1995;
- The Azores University Catalog that was later modified by Nunes and co-workers (2004) and converted to the Seismic Catalog of The Azores Region, compiling the events occurred between 1850 and 1998.

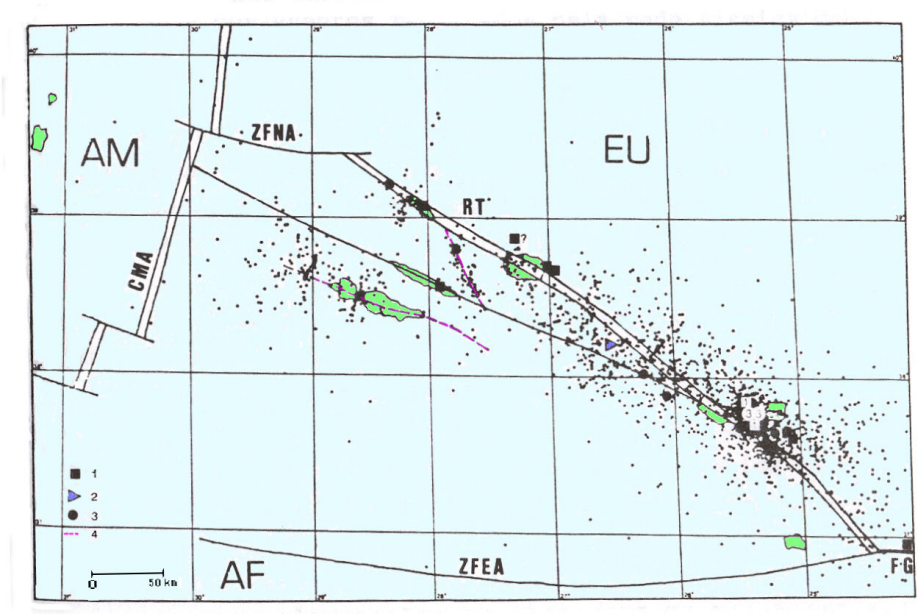

Fig. 3.18 – In this image are represented the main regional tectonic features of the Azores Region and the seismic activity occurred between 1980 and 1989 with intensity higher than 4. The earthquakes are focused along the main faults showed in the map, in which is also displayed the fault responsible for the 1980 earthquake, of January 1st (adapted from Nunes, 1991).

The seismic activity in the Azores is described as being concentrated in seismic crises with hundreds of microearthquakes typically with low magnitude (3 or less; França *et al.*, 2009), or by violent earthquakes, as for instance the 1757 earthquake, felt mainly in the Central Island Group (Machado, 1949). It is noteworthy that, even though most earthquakes have an important tectonic origin sometimes they are connected to volcanic events, as for instance the Capelinhos eruption in 1957/8.

More recent studies, analyzing the focal mechanisms of the Azores earthquakes points to relative shallow focal depths, less than 10 km (Borges *et al.*, 2007) with a tectonic behavior, in the Central Island Group, that corresponds to normal faulting with a horizontal tension axis trending NE-SW. The analysis and modeling of the historical and measured earthquakes considering their location

as well their distribution allowed Carvalho *et al.* (2001) to produce a seismic hazard map. The map points to the areas located west of the Central Island Group and between Terceira and São Miguel islands as the highest hazard zones (Fig. 3.19).

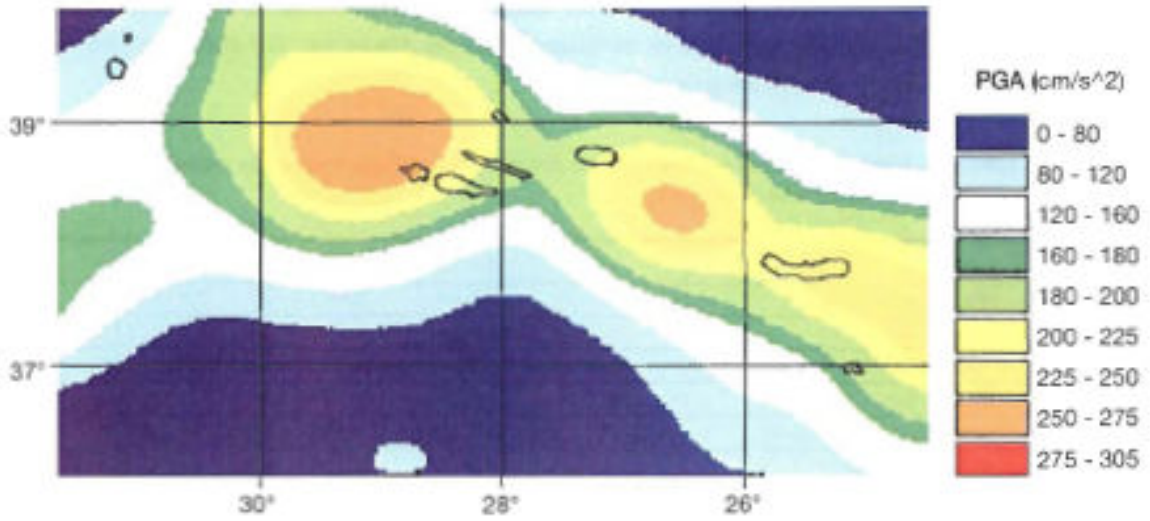

Fig. 3.19 – Hazard map for the Azores Archipelago using a semi-zonified source methodology (after Carvalho *et al.*, 2001). Mean PGA (peak group acceleration) values, exceedance probability of 10% in 50 years. The most hazardous seismic areas are located between Terceira and São Miguel islands an west of the Central Island Group.

The flowing paragraphs resume the most important seismic events felt in São Jorge, enlisting also the seismic crises and the strongest earthquakes, with epicenters located in other islands of the Central Island Group, affecting inevitably São Jorge.

According to Nunes (1991), São Jorge Island has "a peculiar seismic history characterized by long quiet epochs interrupted by periods with strong activity and/or by single violent events." From the epochs with seismic activity, it is important to mention the 1757 earthquake, considered the most violent historical event in the Azores (Machado, 1949) and the seismic crisis of 1964, which could be related with a submarine volcanic eruption (Machado & Forjaz, 1965; França *et al*., 2009)

The 1757 earthquake occurred on the night of the 9th of July of 1757 lasting 2 minutes. This was the most violent seismic event of the Azores with the epicenter located on the south coast of São Jorge between Calheta and Topo villages, and it was probably felt with Intensity XI on the Modified Mercalli Scale (MM). This event was felt strongly in Pico, Faial and Terceira islands, (Table 3.3) and Machado (1949) estimated its magnitude as a 7.4 earthquake in the Richter Scale.

The effects of this event devastated São Jorge with an aftermath of 1000 deaths (20% of the population at the time). On Pico Island the earthquake produced 11 deaths, as well the destruction of houses and churches.

Table 3.3 – Synthesis of the data regarding the 9th of July of 1757 earthquake (after Machado, 1949)

Island	Village	Distance from epicenter (km)	Intensity (Mercalli, 1931)
São Jorge	Fajã dos Vimes	3	XI
	Fajã de São João	6	X a XI
	Fajã dos Cubres	8	X a XI
	Calheta	9	X a XI
	Topo	13	X
	Velas	27	VIII (?)
Pico	Piedade	21	IX
Terceira	Angra	61	VI a VII
	Porto Judeu	70	VI
Faial	Horta	62	VI (?)
São Miguel		225 (?)	III (??)
Santa Maria		300 (?)	III (??)

During the seismic crises of 1926 in Faial, a strong seismic event occurred on the 31 of August with the epicenter located in the Faial-Pico Channel. This event had an Intensity of X (MM) and was felt on its neighbor's islands: São Jorge (Intensity V), Graciosa (Intensity III) and Terceira (Intensity III and IV), (Agostinho, 1927).

A strong and lasting seismic crisis affected the Central Island Group during Capelinhos volcanic eruption. This eruption occurred between September 1957 and October 1958 and was accompanied by an intense seismic activity that was more pronounced during two periods. The first, occurred in the previous days of the eruption, between the 16th and 27th of September of 1957. Approximately 200 events were felt with a maximum intensity of V (MM). The epicenters located on the east part of the island progressively moved westward and were overcome by the volcanic tremor (Machado, 1958 *in* Forjaz, 1997). On the 27th of September the volcanic eruption begins. This period is characterized by the submarine volcanic activity occurring only two effusive events on the 23rd and 24th of April. The second seismic crisis precedes the second eruptive phase characterized by strombolian and effusive eruptions. This second crisis begins violently on the 12th of May with approximately 450 events felt in the first days. This crisis lasts until June with more

than 580 seismic events. The strongest epicenters were localized in three different locations on Faial: (1) on Praia do Norte were it was felt with Intensity X (MM) producing large movements along faults (França *et al.*, 2009); (2) on the south side of the Caldeira were the events had Intensity X, producing also movement along faults and on (3) Espalhafatos village where the events were felt with Intensity VII and VIII (MM). The strongest earthquakes during the two main phases were also felt strongly in Pico (Intensity III and IV) and in São Jorge (Intensity III).

The 1964 seismic crisis of São Jorge was one of the most important seismic crises of the island with more than 500 events, affecting also the rest of the Central Island Group, as explained by Machado & Forjaz (1965) and Machado (1973). The seismic crises itself starts on the 15th of February with a violent earthquake (Intensity VI in Urzelina) followed by 179 events on the first 24 hours. With the evolution of the crisis (Table 3.4), the epicenters tend to move westward towards Rosais culminating with an earthquake, on the 21st of February in Rosais, with intensity VIII (MM) (Fig. 3.20).

Table 3.4– Chronology of the main events of the 1964 seismic crises of São Jorge, felt on the Central Island Group.

Day	Local/Event	Intensity
21/Ago/1963	Earthquake in the São Jorge-Pico Channel	V a VI
13 e 14/Dez/1963	Continuous tremor	
29/Jan e 1/Fev/1964	Break of the telegraphic cables	
14/Fev/1964	Continuous tremor	
Beginning of the seismic crises of February of 1964		
15	Urzelina	VI
16	Urzelina	VI
17	Manadas	VI
	Graciosa Island	II
18	Rosais	VII
19	Rosais	VII
	Pico Island	IV – V
	Faial Island	IV
20	Velas	VI
21	Rosais	VIII
22	Velas	III
23	Rosais	IV – V
24	Velas	III
	Terceira Island	I – II
25	No record	

Additionally, both publications on the 1964 seismic crises, proposes that the crisis is related with a submarine volcanic episode offshore Velas. In the months preceding the crisis (Table 3.4), it was felt a great instability with a strong earthquake on the 21st of August of 1963. The epicenter was localized on the São Jorge-Pico Channel with an Intensity V to VI (MM). Afterwards the Horta seismometer record a continuous tremor frequently found during magma ascent. Latter on between the 29th of February and the 1st of March of 1964, two submarine cables were broken in the margins of São Jorge Channel.

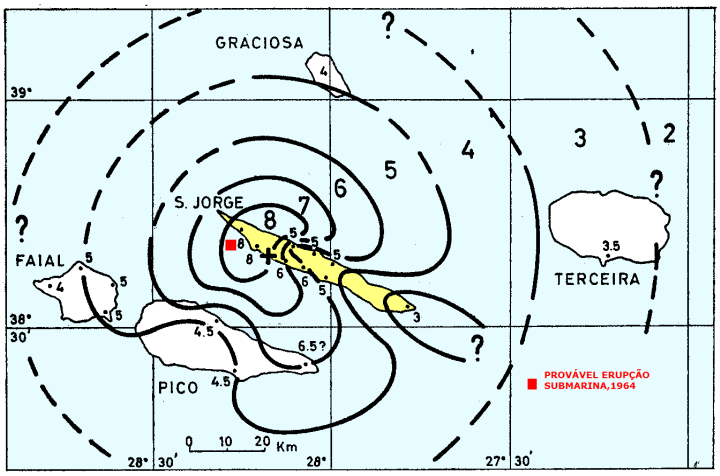

Fig. 3.20– Isoseismic map of the 21st of February of 1964 earthquake (after Machado & Forjaz, 1965) with the probable location of the suspected volcanic eruption associated with the seismic crisis.

The Pico seismic crisis of 1973/74 started on the 11th of October of 1973, with the majority of the epicenters located on Pico Islands but affecting also São Jorge (Forjaz *et al*., 1974; Machado *et al.,* 1974). The origin of this crisis was related, according with Nunes *et al.* (1997), with the Pico stratovolcano radial faults and the alignment of the epicenters along a NNW-SSE direction. This crisis main characteristic was the succession of periods of strong activity with periods of silence. The strongest earthquakes occurred on the 1st, 18th and 23rd of November and on the 10th of December (Table 3.5). In particular, the 23rd of November earthquake was the most violent. The epicenter was situated in Santo Antonio Village, on Pico, and its maximum Intensity was VII/VIII (MM) and magnitude 5.8 on the Richter Scale (França *et al.*, 2009). On São Jorge, this event was felt with Intensity V and was recorded on seismometers located in Portugal Mainland, Lisbon, Coimbra and Porto. During the three months that the crises lasted a total of 724 events were recorded on Horta seismometer, and from these 377 were felt by the population.

Table 3.5 – Chronology of the main events occurred on the 1973 seismic crisis, and their Intensity (MM).

Event day	Local	Intensity
1/Nov	Pico	IV a V
18/Nov	Pico	V a VI
23/Nov	Pico	VII – VIII
	São Jorge	V
	Faial	VII
	Graciosa	III
	Terceira	IV
10/Dez	Pico	V a VI

The Terceira 1980 earthquake occurred on the 1st of January and it is considered as one of the most violent event of the XX century in the Azores, reaching a magnitude of 7.2 (Richter Scale) or XVIII – IX Intensity (MM) (Oliveira *et al.*, 1982). The epicenter was localized at sea on the channel between Terceira, São Jorge and Graciosa. The aftermath of this earthquake was 61 deaths and 400 injured and large property damage in Terceira, São Jorge and Graciosa (Borges *et al.*, 2007). On the days after the earthquake, it was installed a seismic portable network that recorded 400 aftershocks of the main event (Hirn *et al.*, 1980), 100 of which were localized with precision. The projection of the epicenters on a regional map (Fig. 3.21), shows that the earthquakes plot along a 150°N direction on an area with 40 km long and 6 km width, and at a depth of 14 km. (Hirn *et al.*, 1980). The study of the focal mechanism, of its aftershocks, and of epicenters spatial distribution, points to the source of this event localized on a vertical fault with a 150°N direction and with a left strike-slip movement (Hirn *et al.*, 1980).

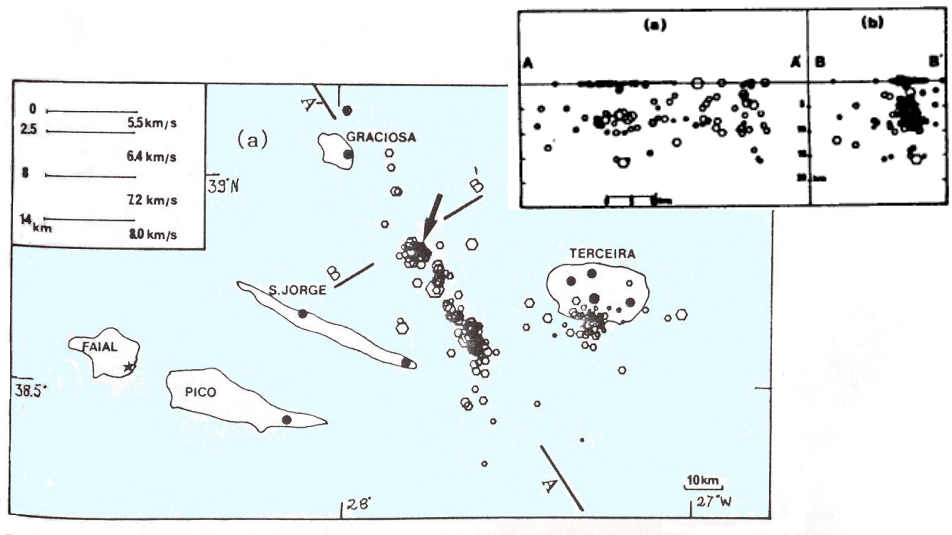

Fig. 3.21 – Map with the location of the epicenters of the 1980 earthquake and replicas that followed the main event (Hirn *et al.*, 1980).

The 1998 Faial earthquake had his epicenter located at sea, approximately 10 Km NE of the island on a region considered to be hazardous (Carvalho *et al.*, 2001). The earthquake was felt in Faial with Intensity VIII/IX and the seismometers measure an intensity of 6 (Oliveira *et al.,* 1998). The aftermath of this violent event was 8 deaths, more than one hundred people injured and large property damage mainly in Faial (Madeira *et al.*, 1998), although property damage was also reported in Pico (Nunes *et al.,* 1998; França, 2000). The earthquake was strongly felt in its neighbor's islands of Graciosa, Terceira and São Jorge. On the last one, the earthquake was felt mostly in the Rosais area with intensity V (Fig. 3.22). The analysis of the epicenter and of the more than ten thousand aftershocks events in three months (Oliveira *et al.,* 1998), located the origin of this crises on a family of faults with a NNW-SSE direction. These faults with a left lateral strike-slip motion, produced deformation on Faial Island that resulted on fractures opening along the two main tectonic orientations: WNW-ESE and NNW-SSE.

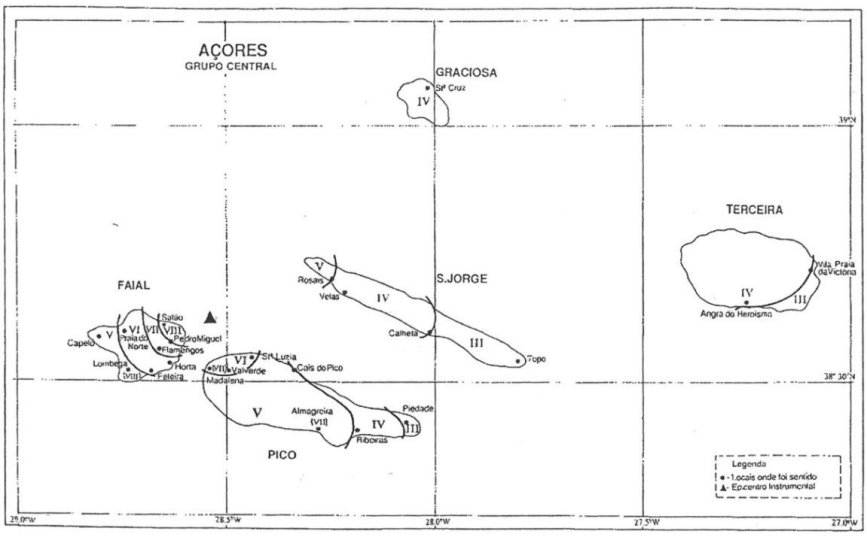

Fig. 3.22 – Map with the distribution of Intensity of the 1998 earthquake on the Central Island Group (after Costa Nunes *et al.*, 1998)

Chapter 4: Sampling New Data in São Jorge

4.1 Introduction

To achieve the main goals of this study it was required an extensive sampling of São Jorge Island that covered the three main complexes described in the previous chapter: Topo, Rosais and Manadas. The first samples were recovered during the field work that took place between the 26 of November and the 8 of December of 2004.

A second sampling opportunity on São Jorge occurred in 2007. At this time, samples from the submarine southeast flank of the island were sampled during the EMEPC\Açores\G3\2007 cruise as will be described below.

The two sampling phases on São Jorge covered a part of the lavas erupted during the subaerial and the submarine growth of the island. Due to the intrinsic characteristics of each lava group and of the sampling phases, the procedures will be described separately.

4.2 The Subaerial Samples

As mentioned, the onshore samples were recovered during the field work that took place between the 26 of November and the 8 of December of 2004. In spite of the great outcrop exposure in São Jorge, mainly along the coastal scarps, accessibility to the lava sequences was limited by the geomorphologic characteristics of the island, as can be appreciated from the previous morphologic description. The steepness of the cliffs on one hand and the vegetation and soil cover in summit areas on the other, were limitative of the number of quality samples in some locations. Despite this a total of 110 samples were collected from diverse volcanic structures (e.g.

dikes, lava flows and lava sequences) with an extensive geographical coverage in key location along the island.

The stratigraphic position of the lavas was a major concern due to the fact that one of the main purposes of this study was to obtain a detail geochemical characterization of the lava sequences and of the volcanic complexes, and also to obtain geochronological data.

Observation and description of hand sample was very important during fieldwork to distinguish the samples and if possible a pattern in the island. This was the case in Fajã de São João sequence, which showed distinct petrographic characteristics from the remaining lavas observed. Therefore, a considerable high number of samples were collected at this sequence.

During sample preparation for lithogeochemistry analyses, a major concern was to exclude samples with signs of alteration. The observation of the hand samples and the petrographic observation of the thin sections excluded several samples from chemical analyses (e.g. SJ4, SJ6, SJ11, SJ81, SJ96, SJ100 and SJ108). Another criterion used to choose the samples was their spatial distribution in order to cover most of the island and represent the most important volcanic sequences and the volcanic complexes. So, from the initial set, a group of 91 samples were selected to be analyzed for major and trace elements (see APPENDIX I). In the map of Fig. 4.1 it is displayed the geographical position of the samples that went through the geochemical analysis, which comprehends 18 lavas from Fajã de São João volcanic sequence, 36 from Topo Volcanic Complex, 18 from Rosais Volcanic Complex and 19 from Manadas Volcanic Complex.

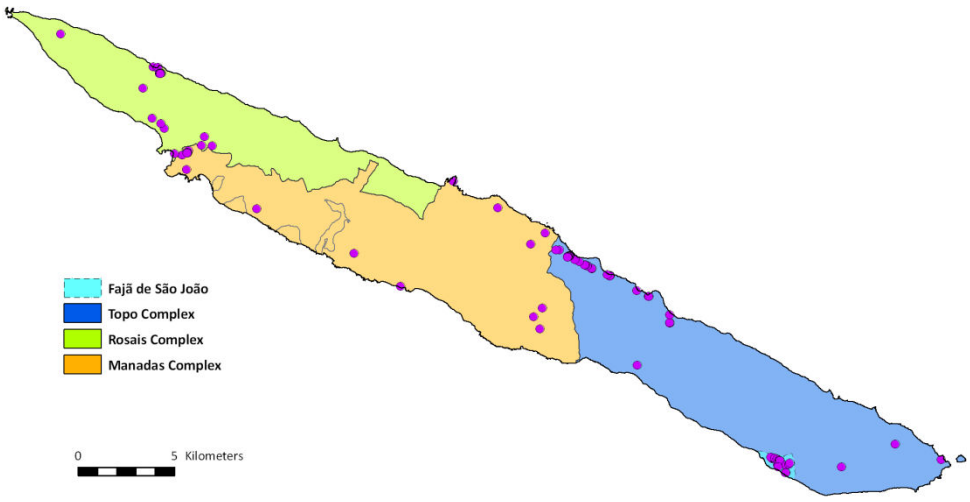

Fig. 4.1 – Localization of the samples collected during the first sampling phase in São Jorge that were analyzed for major and trace elements.

In order to obtain additional data for a more detail characterization of São Jorge, three smaller subsets of samples were created:

- The first subset, with 14 samples, was chosen to be analyzed for Sr, Nd, Pb and Hf isotopes (Fig. 4.2A, see APPENDIX I);
- A second subset of 12 lavas was used for obtaining the ages of the samples through the $^{40}Ar/^{39}Ar$ method (Fig. 4.2B, see APPENDIX I). These samples were chosen considering their good quality i.e. low degree of alteration, the mineralogy observed on the lavas matrix, the position of the lava inside the lava sequence, which required a tight stratigraphic control and their position on the volcanic complex defined by the volcanostratigraphy.
- The third group of samples formed by 15 polished thin sections was used in the ion-microprobe to analyze the mineral phases of the lavas (see APPENDIX II).

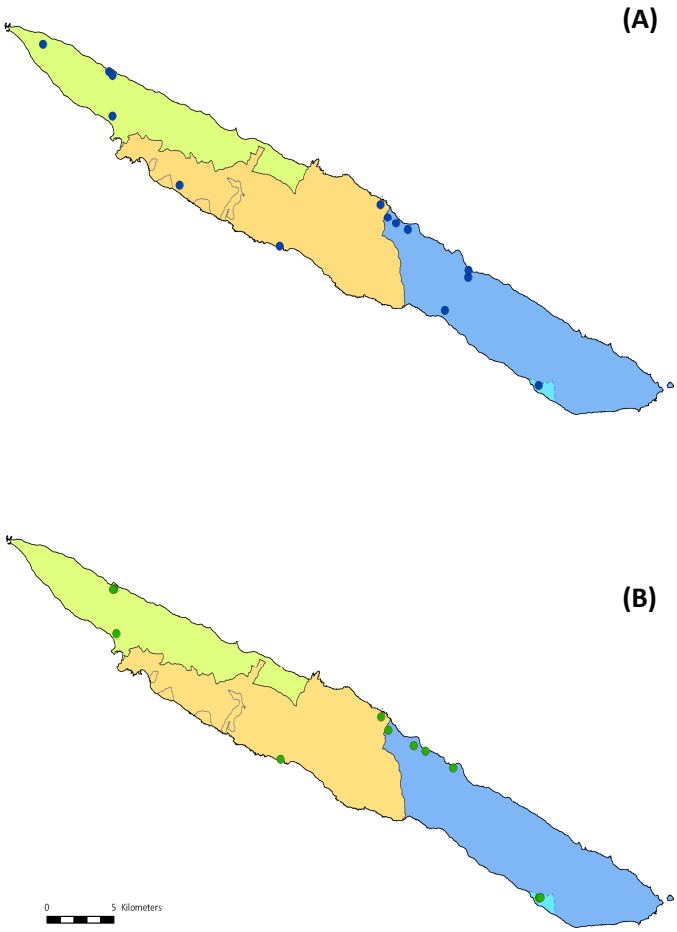

Fig. 4.2 – São Jorge map with the localization of the samples that went though (A) Sr-Nd-Pb-Hf isotopic analysis and through (B) $^{40}Ar/^{39}Ar$ analysis. See legend of Fig. 4.1 for color code of the volcanostratigraphy.

4.3 The Submarine Samples

The second sampling phase has constituted a major opportunity for collecting samples on São Jorge Island southeast submarine flank. During the EMEPC\Açores\G3\2007 cruise, which will be described below, a dredging operation took place on the southeast flank of the island (Fig. 4.3), at a depth of approximately 1200 m depth, and a total of 28 samples, with volcanic and sedimentary nature were recovered.

The volcanic samples, which are included in the present work, were mainly pillow lavas and their description is presented further ahead on the petrography chapter. These pillow lavas went through the same geochemical and isotopic analyses as the onshore samples. Overall, nine samples were analyzed for whole rock geochemistry and from these, only, five where chosen for radiogenic isotope analysis (Sr, Nd, Pb and Hf). The petrographic observation showed that, in general, all pillow lavas shared similar characteristics and only one was used to mineral chemistry by ion-microprobe.

4.3.1 The EMEPC\Açores\G3\2007 Cruise

The EMEPC\Açores\G3\2007 cruise was carried out in the scope of the Portuguese Extension Shelf Project on board of the S.V. Kommandor Jack. This was a two LEG multidisciplinary cruise, comprising research areas as geology, geophysics, geochemistry, hydrography, macro and microbiology, environmental chemistry and oceanography, although it's main objective was to collect volcanic samples on the seafloor of the Azores Region.

During the LEG1 (Fig. 4.3), several dredge operations were carried out on the Azores Archipelago near the islands of the Central Island Group and between these and São Miguel Island. The dredging site D1 covered the flank of São Jorge Island situated at the end of São Jorge – Pico Channel and southeast of Fajã de São João (27º48.0'W, 38º29.0'N). This dredging location on São Jorge flank is an elevation with a positive magnetic anomaly, where it was possible to dredge 28 samples of volcanic and sedimentary nature.

The volcanic rocks recovered are mainly pillow lavas as exhibited in Fig. 4.4. The sedimentary rocks collected on São Jorge flank were mainly consolidated volcaniclastic breccias and bioclastic

limestones. Breccias, as in Fig. 4.5, are formed by clasts essentially with volcanic origin, presenting variable dimension (<3 cm), and alteration state. The fragments are agglutinated mainly by limestone or by argilitic cement frequently exhibiting iron oxides. The bioclasts are mostly made of shells, shell fragments and corals that can be coarse reaching 1 cm in size, and are cemented by limestone (Fig. 4.6). The presence of limestone in the Azores has been described previously on samples dredge in the Azores Region (e.g. Beier, 2006).

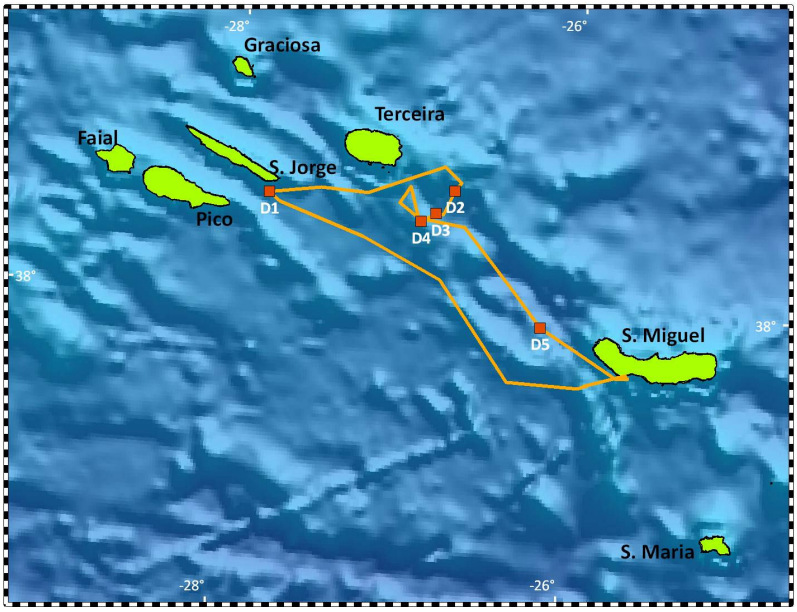

Fig. 4.3 – LEG1 track of the EMEPC\Açores\G3\2007 cruise showing the dredging locations. Dredging operation D1 took place at approximately 6.5 Km from the southeast coast of São Jorge at a depth of 1200 m.

Fig. 4.4 – Picture of a volcanic sample dredge on São Jorge flank. The sample is fresh presenting a dark grey color and small plagioclase phenocrysts were identified (2-3 mm).

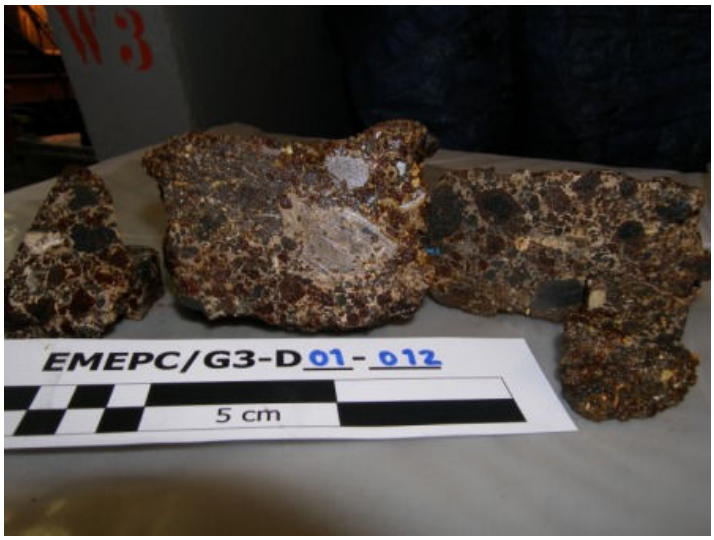

Fig. 4.5 – In this picture is showed one of the volcaniclastic breccias collected offshore São Jorge. This sample is composed by sub-rounded to angular volcanic clasts of variable size (< 2 cm). The clasts present variable colors, from dark grey to orange-brown showing different alteration states. The cement joining the clast is light yellow and is made of limestone.

Fig. 4.6 – Sedimentary rock collected on São Jorge submarine flank formed by relatively fine bioclastic material and limestone. At this scale of observation volcanic material is absent.

Chapter 5: New Geochronological Data: $^{40}Ar/^{39}Ar$ ages

In this study, one of the main objectives was to obtain new geochronological data on São Jorge, lavas in order to date the lavas and temporally constraint its volcanostratigraphy. As a result, we present twelve $^{40}Ar/^{39}Ar$ ages on lavas from the three main volcanic complexes and from Fajã de São João lava sequence (Ribeiro *et al*., 2010). These ages allow to estimate the growth rate of the volcanic sequences and to predict the time interval in which they were active. The interpretation of the new data in conjunction with the results of former geochronological studies and the volcanostratigraphy (chapter 3), will give, hopefully, a new insight into the development of São Jorge.

5.1 Stratigraphic Position of the Dated Lavas

In the next paragraphs is presented the stratigraphic position of the samples dated by $^{40}Ar/^{39}Ar$ method. Several conditions or constrains in the choice of the samples had to be taken into consideration so the ages could be interpreted correctly.

The general east-west age progression of volcanism as predicted by the volcanostratigraphy was the first essential condition in the choice of the samples used to geochronology. A second constrain was the stratigraphic control, in order to limit temporally the volcanic events. In this sense, it was given preference, when possible, to the lavas located at the base and top of the volcanic piles. Additionally, it was necessary that the lavas were not weathered and the presented good petrographic characteristics.

The previous conditions were relatively easy to apply to the lava sequences of Topo and Rosais volcanic complexes, however, Manadas Volcanic Complex showed different characteristics. In Manadas, because is the most hazardous area in São Jorge, it was considered important to date the lavic fajãs, since these lava flows cover the shorelines in the same way as the historical eruptions did.

From the application of these conditions to the lavas, it was possible to obtain twelve new $^{40}Ar/^{39}Ar$ ages on São Jorge. The samples chosen were collected on:

- Fajã de São João sequence, where two lavas were analyzed for argon. These lavas were sampled on intermediate levels on the lava pile at 220 and 290 m height.
- The north coast of São Jorge, where the axial zone of Topo Volcanic Complex outcrops. The samples were collected at the base of the lava piles on Fajã da Caldeira do Santo Cristo, on the road between Fajã da Caldeira do Santo Cristo and Fajã dos Cubres and at the base and top (≈ 410 m height) of Fajã dos Cubres.
- Two locations at Rosais Volcanic Complex. The dated samples were recovered on a lava flow located on the road between Velas Village and Rosais Village and at Fajã do João Dias lava sequence on two lavas flows and one dike. Due to the degree of alteration of the lavas located at the base of Fajã do João Dias sequence, it was only possible to analyze two lava flows outcropping at 185 and 225 m height, therefore occupying a high stratigraphic position in this sequence.
- On Manadas Volcanic Complex, lavas were collected on a recent lava delta located on the north shore of São Jorge, named Fajã da Pontas, and on the lava flow forming Fajã das Almas, located on the south shore of the island.

5.2 The New $^{40}Ar/^{39}Ar$ Ages on São Jorge

Here we present the new $^{40}Ar/^{39}Ar$ ages obtained on the lavas of São Jorge Island, which are displayed also in Fig. 5.1:

- The $^{40}Ar/^{39}Ar$ ages on intermediate levels of Fajã de São João sequence are 1309.8±3.5 ka and 1284.0±4.8 ka old. These ages confirm that lavas from Fajã de São João sequence are within the interval determined by Hildenbrand *et al.* (2008). In addition, will allow a tighter constrain on the evolution of the sequence.
- The lavas located at Fajã da Caldeira do Santo Cristo and on the road from this fajã to Fajã dos Cubres yield ages of 756.8±5.0 ka and 743.3±4.0 ka, respectively, and are slight older than the ages obtain by Hildenbrand *et al.* (2008) on Fajã dos Cubres, which is 736 ka old.
- The base and the top of the volcanic sequence at Fajã dos Cubres, with more than 400 m height, are constrained between 730.2±4.0 ka and 543.3±4.3 ka. The stratigraphic position of the youngest lavas of this sequence (543 ka old) provides an important limit for the end of volcanic activity at this location.
- On Rosais Complex north cliff, the analysis on the lavas from Fajã do João Dias sequence delivered ages on the two lava flows of 270.1±2.5 and 218.8±3.3 ka respectively, and on the dike, intercepting the younger lava, it was obtained 215.0±2.5 ka. These ages on Fajã do João Dias sequence are the first to be obtained in this region of Rosais Volcanic Complex and their position on the lava sequence suggests that volcanic activity must have started earlier.
- In the vicinity of Velas Village, the lava flow analyzed shows that Rosais was active at 116.6±2.0 ka ago.
- On the youngest volcanic complex, Manadas, the lava flow forming Fajã das Pontas has an age of 2.9±10.3 ka, while in Fajã das Almas the lava flow delivered an age of 0.5 ± 6.9 ka ago. The error associated with these two ages is considerably high, not allowing a precise dating. However, the stratigraphic position of these lavas, which correspond to two relatively well preserved Fajãs, associated with the age obtained evidence the youth of these lavas.

One of the most important implications that result from geochronological data is related with the interpretation of Fajã de São João sequence and the beginning of the subaerial volcanism in São Jorge. During fieldwork, several important petrographic and lithological differences were observed in Fajã de São João lava sequence when compared with the rest of the island. Later, the work from Hildenbrand *et al.* (2008), published during the preparation of this study, showed that Fajã de São João lava sequence corresponds to an older volcanic event in São Jorge. The conjunction of this data by itself suggests that this lava sequence should be treated separately

from Topo Volcanic Complex, nonetheless mineral chemistry data and geochemical data will be analyzed in the forthcoming chapters and will reinforce (or not) the previous observations.

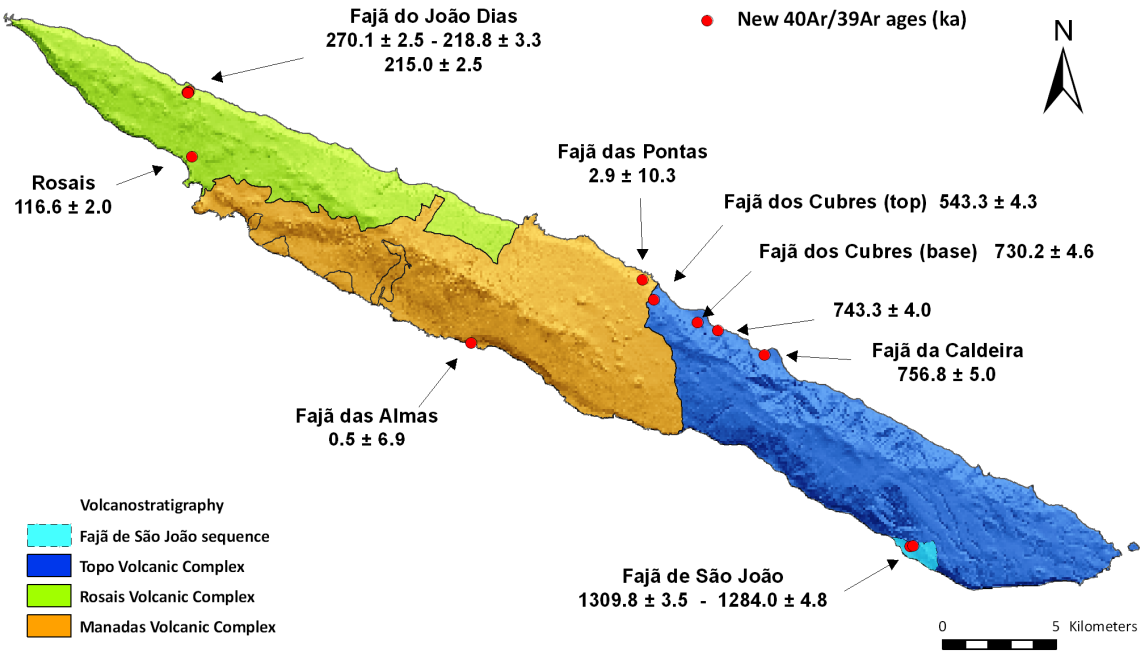

Fig. 5.1 – In this picture is presented the geologic map of São Jorge Island showing the location and the new $^{40}Ar/^{39}Ar$ ages. (see APPENDIX I.C and I.D)

5.3 Growth Rates of the Volcanic Sequences in São Jorge

With the new geochronological data and the position of the lavas on the lava piles, is possible to estimated average construction rate of several lava sequences on São Jorge.

The base and the top of Fajã de São João lava sequence, with 400 m height, were temporally constrained by Hildenbrand *et al.* (2008) between 1323 and 1207 ka ago. For this period, it is possible to estimate the average growth rate of the volcanic sequence, which is 3.4 meters per thousand years (m/ka). However, using the lavas dated in this study, within the 1310 and 1284 ka interval located at 220 and 290m height respectively, it is possible to obtain a better constrain on the growth rates at intermediate levels on the sequence. Therefore, in the time period between 1323 and 1310 ka the sequence grew at a rate of 6.1 m/ka, in the interval between 1310 and 1284

ka the average growth rate reduces to 2.7 m/ka and, finally, in the interval between 1284 and 1207 ka the growth rate diminishes to 1.4 m/ka. These estimates seem to be congruent with the observations during fieldwork, where it was observed an increasing number of baked soils alternating with lava flows towards the higher stratigraphic levels of the lava pile, pointing to longer interruptions of volcanic activity.

In the case of the 410 m height lava sequence of Fajã dos Cubres, temporally constrained in this study, between 730 and 543 ka, it is obtained an average growth rate of 1.9 m/ka. This value is lower than the estimates for Fajã de São João and due to the inexistence of geochronological data at intermediate stratigraphic levels, it is not possible to control growth rate variations, however, as in Fajã de São João is most likely that during the early volcanic stages growth rates were higher.

At Fajã do João Dias, located on the northwest coast of Rosais Volcanic Complex, the dated lava flows collected on intermediate levels on the lava pile, at 185 and 225 m height with 270 and 219 ka respectively, delivered a relative low growth rate of 0.8 m/ka. Nonetheless, the oldest lava dated in Fajã do João Dias is located at 185 m above sea level, thus is expected that volcanism at the base of the volcanic pile started sometime earlier. For the prediction of the beginning of the sub-aerial volcanism at Fajã de João Dias sequence it was used the previous growth rates of 3.4 m/ka, for Fajã de São João, and of 1.9 m/ka, of Fajã dos Cubres. As a result, it is possible to estimate that the sub-aerial volcanism at Fajã do João Dias started in the interval between 325 and 367 ka ago.

If the maximum age of the predicted interval is corrected, i.e. 367 ka, then volcanic activity at Fajã do João Dias should have started at the same time than the volcanic sequence near Fajã do Ouvidor, which was dated from 368 ka ago (Hildenbrand *et al*., 2008). If this prediction is correct, than volcanic activity in Rosais Volcanic Complex can be considered coeval at the two locations. Otherwise, since it is assumed that volcanic activity in São Jorge migrates westward and considering that Fajã do Ouvidor is located several km east of Fajã do João Dias, than the 325 ka should be a more appropriate age for the beginning of volcanism at Fajã do João Dias. Nonetheless, there is a strong possibility for coeval volcanism in Rosais Volcanic Complex. Both interpretations are possible and have implications on the evolution and growth of the island. However, only with additional information would be possible to test which is the most correct.

5.4 Time Constrains on São Jorge Evolution

The early stratigraphic and geomorphologic works on São Jorge (Forjaz & Fernandes, 1975; Madeira, 1998) consider Fajã de São João sequence as a part of Topo Volcanic Complex, however, the geochronological data demonstrates that Fajã de São João was edified over a time period between 1321 and 1207 ka ago (Hildebrand *et al.*, 2008). Thus, at the light of this new data Fajã de São João lava sequence should have been the first sub-aerial volcanic phase on São Jorge.

The oldest age obtained in São Jorge, outside Fajã de São João lava sequence, is the 757 ka old lava flow outcropping at the base of Fajã da Caldeira do Santo Cristo lava sequence (from now Fajã da Caldeira), which belongs to Topo Volcanic Complex. The 450 ka gap between both ages could be interpret as a non-volcanic period as pointed out by Hildenbrand *et al.* (2008). Yet, it should be taken to consideration that (1) this estimate concerns only the sub-aerial volcanism, (2) erosion process in São Jorge are very efficient and could have removed part of the volcanic record of Fajã de São João and, finally, (3) that Topo lavas could have cover a part of Fajã de São João younger volcanic events. Accordingly, the estimate of 450ka for the non-volcanic phase should be considered as a maximum time interval.

The 757ka old lava, located at the base of Fajã da Caldeira, could be considered as an early event of the second volcanic phase that formed the three volcanic complexes, Topo, Rosais and Manadas, and is still active.

This second volcanic phase begins with the construction of Topo Volcanic Complex that forms the eastern side of São Jorge. The lavas located stratigraphically at the base of Topo lava piles, along its north shore, on Fajã da Caldeira, on the road between Fajã da Caldeira and Fajã dos Cubres and at Fajã dos Cubres are dated from 757, 743 and 730 ka respectively. Despite the small age difference between the lavas, the age progression seems to evidence a continuous westward migration of the volcanic activity and suggest favorable conditions for abundant magma supply.

Topo Volcanic Complex also grew vertically forming volcanic piles with more than 400 m height as for instance, the lava sequence of Fajã do Cubres temporally constrained, in this study, in a period between 730 and 543 ka ago. Other geochronological data on Topo Volcanic Complex, as the ages on Fajã dos Bodes lava sequence (729 and 690 Ka ago; Hildenbrand *et al.,* 2008), and the age at base of Fragueira lava sequence (550 ka; Feraud *et al.*, 1980), are within the time interval of Fajã dos Cubres. This suggests that the main volcanic activity in Topo Volcanic Complex occurred in the

period between 757 and 543 ka ago. Nonetheless, volcanism continued on Topo Volcanic Complex as evidenced by the lavas stratigraphically positioned on the summit of volcanic structures, at Piquinho da Urze with 140 Ka (Feraud *et al.*, 1980) and at the eastern end of the island on Topo Village with 280 ka ago (Feraud *et al.*, 1980). The younger age of both lavas when compared to the 543 ka old lava at the top of Fajã dos Cubres sequence and their relative stratigraphic position suggests that volcanic activity in Topo diminishes in intensity in these latter stages.

The Rosais Volcanic Complex, spatially located west of Topo and west of Ribeira Seca Fault, was the second to form, what is consensual with the regional westward migration of volcanism. Its earliest known volcanic activity was identified on a lava flow at the base of the lava sequence near Fajã do Ouvidor dated from 368 ka (Hildenbrand *et al.*, 2008). The time interval of 175 ka between this lava flow, at the base of Rosais lava pile, and the lava flow at the top of Fajã dos Cubres sequence (543 ka) and the lack of more temporal constraints, suggests a scenario of reduced sub-aerial volcanic activity between Topo and Rosais volcanic complexes or in alternative could point to a non-volcanic period.

The new $^{40}Ar/^{39}Ar$ data from Rosais Volcanic Complex shows that the western end of the island at Fajã do João Dias was active between 270 and 215 ka ago. However, the high stratigraphic position of the dated lavas (more than 185 m asl) suggest that volcanic activity at this sequence should have started some time earlier, possibly in the time period between 325 and 367 ka ago. An important aspect that Rosais geochronological data evidences is that volcanic activity in the western side of Rosais is much older than expected. In addition, despite the expected westward progression of volcanism, on Rosais Volcanic Complex, volcanism seems to be coeval on several locations, as at the base of the cliff at Fajã do Ouvidor (368 ka, Hildenbrand *et al.*, 2008) and at the base of Fajã do João Dias (325-367 ka). In addition, at Fajã do João Dias lava sequence (215-270 ka) and at the base of the lava sequence at Velas Village (268 ka, Hildenbrand *et al.*, 2008) volcanic activity was contemporaneous.

The youngest volcanic event dated on Rosais has 117 ka and occurred west of Velas village. This lava was collected at a height of 160 m asl and was originated by one of the nearby volcanic cones which indicates a relative high stratigraphic position, however, the fact that several lavas pile-up above this lavas and that other geographically-closed well preserved volcanic structures are observed suggest that Rosais was active for some time after.

The absence of $^{40}Ar/^{39}Ar$ data on Rosais volcanic events younger than 117 ka and the fact that a part of this complex is cover by Manadas lavas, gives no tight time constrains for end of Rosais volcanic activity and the beginning of the build-up of Manadas Volcanic Complex. However, during the edification of Manadas Complex, volcanism beings to concentrate in the central part of São Jorge, between Velas Village and Ribeira Seca Fault. Manadas Volcanic Complex is considered to be active with the last two historic eruptions occurring in 1580 and 1808 A.D. Nonetheless, volcanic activity can be tracked backwards from the $^{40}Ar/^{39}Ar$ dating of Fajã das Pontas with 2.9 ka and the ^{14}C dating of Madeira (1998), which reports 10 sub-aerial volcanic events ranging between 5310 and 700 years B.P.

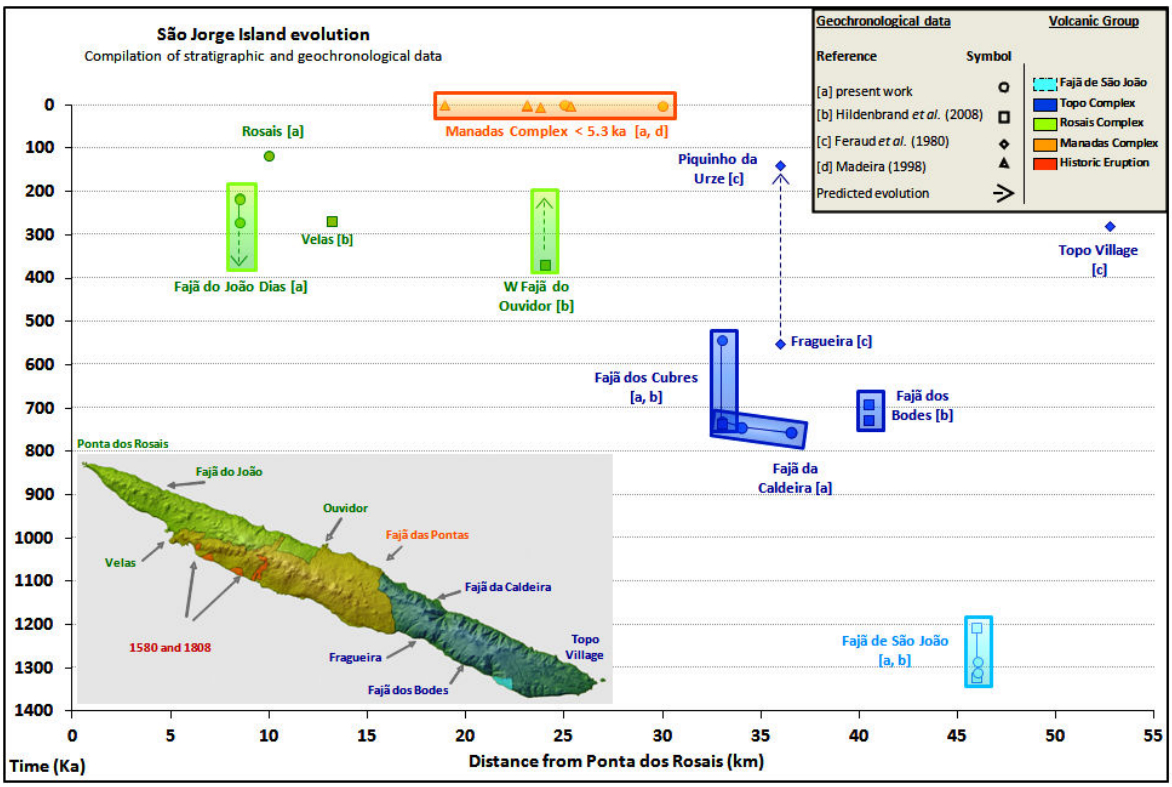

Fig. 5.2 – Time evolution of São Jorge volcanic sequences combining the new $^{40}Ar/^{39}Ar$ results (circles) with the previous geochronological data from Feraud *et al.* (1980) blue diamonds, Madeira (1998) orange triangles and Hildenbrand *et al.* (2008) squares. The age progression shows the early volcanic stage of Fajã de São João lava sequence (light blue) that followed by a second volcanic phase where Topo (dark blue), Rosais (green) and Manadas (orange) volcanic complexes developed.

Chapter 6: General Petrographic Characteristics of São Jorge

6.1 Introduction

The observation under petrographic microscope of volcanic rocks allows a characterization of their textural and mineralogical variability, which is dependent on the composition, evolution and physical conditions of the magmatic liquids. The two main aspects that have to be look for are texture that focus on minerals size, shape and arrangement, and mineralogy that is more dependent on the chemical composition of the magma (Best & Christiansen, 2001).

The volcanic rocks, on the scope of this work, outcrop mainly as lavas flows and dikes displaying porphyric textures with a well-developed phenocryst phase immersed in a microcrystalline matrix. In general, the phenocryst assemblage is formed by olivine, pyroxene, plagioclase and Fe-Ti rich oxides, whereas the microcrystalline matrix has a similar composition.

It was not possible to make a clear petrographic distinction between the lavas from the three main volcanic complexes with the exception of the lavas from Fajã de São João sequence and the pillow lavas from the submarine flank, which display distinctive characteristics from the remaining lavas and are described separately as special cases.

In this sense, a general textural and mineralogical characterization of Fajã de São João lavas is presented here and is completed with several petrographic details with petrogenetic interest, as for instance the occurrence minor hydrous mineral phases as kaersutite and biotite.

6.2 Main petrographic characteristics

The textures observed in São Jorge lavas can range between microcrystalline, with no phenocrysts, and porphyritic with a variable amount of large crystals.

The porphyric lavas, as for instance in Fig. 6.1 are, usually, formed by well-developed crystals embedded in a microcrystalline matrix where, locally, intergranular or glomeroporphyric textures can be found (Fig. 6.2). Commonly, lavas are vesicular exhibiting a great variability on shape and size of vesicles. Other features as trachytic textures characterized by plagioclase microlites orientated along flow direction, as in Fig. 6.3 were also observed.

The variation observed on the amount and size of phenocrysts in porphyric rocks suggests that the liquids, during magma crystallization, went through non-uniform physical conditions. Usually, this texture points at least to two different crystallization stages; an initial stage at high temperature and with small cooling rates, where crystals nucleate and grow during a specific amount of time (Bard, 1986; Best & Christiansen, 2001); and a second stage where rapid undercooling allows only matrix formation.

Changes on the physical conditions during phenocrysts growth, as for instance, the decrease in pressure, sudden temperature variations or even liquid composition change, can be subtle but are often recorded on crystals (Bard, 1986; Best & Christiansen, 2001). Features as dissolution of crystals, reabsorption patterns, corrosion gulfs or even zoning are observed frequently and account for these changes.

The narrow lithological variability and the silica undersaturation nature of the lavas (total alkalis vs. silica diagram that is presented further ahead in chapter 8) are reflected on their mineralogical assemblage composed mainly by olivine, pyroxene, plagioclase and Ti-Fe oxides. Other rare mineral phases, considered minor, as kaersutite and biotite are identified and discussed bellow.

Olivine is present in almost all lavas from São Jorge, either on the phenocrysts phase, the matrix or both. On the phenocrysts phase, usually, olivine crystals are well developed and exhibit euhedral to subeuhedral crystals. Compositional zoning can be found in some crystals rims showing chemical variations during final mineral fractionation. Disequilibrium between olivine and the magmatic liquid is often observed in olivines corroded and embayed to more anhedral

shapes. This observation points to an early crystallization of olivine that later enters in disequilibrium as liquid compositions evolves.

Olivine with kink bands was also found in some Topo lavas as showed in Fig. 6.1. Kink bands result from crystal deformation along slip planes, induced by plastic flow (Ave'Lallemant & Carter, 1970) probably during transport of the already crystallized minerals to more shallow levels. Most olivine minerals are fresh but olivine alteration was observed on several minerals contours or along fractures in the form of iddingsite (Fig. 6.4). Less frequently, iddingsite deeply alters olivine producing a complete replacement of the original crystal.

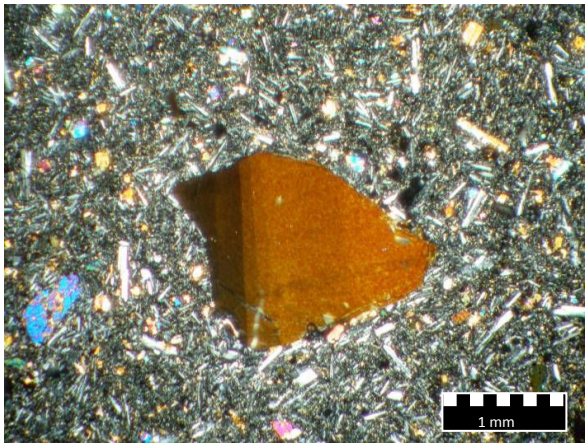

Fig. 6.1 – Basaltic rock with porphyritic texture exhibiting an olivine crystal with ondulatory extinction (kink bands). Matrix assemblage is made of plagioclase, olivine, pyroxene and oxide microphenocrysts (cross-polarized light).

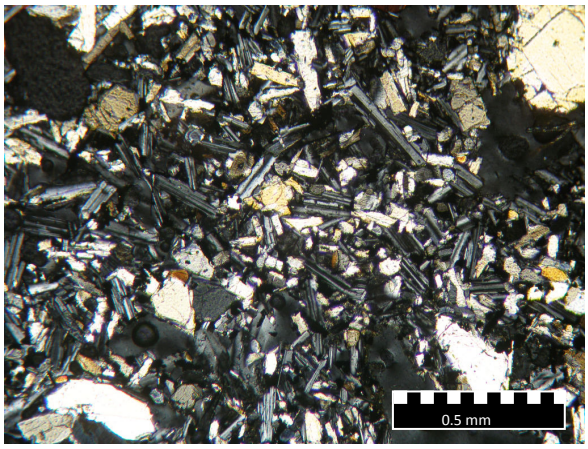

Fig. 6.2 – Intergranular texture observed in several porphyric basaltic rocks. Plagioclase minerals are interlocked with pyroxene and Fe-Ti oxides in the presence olivine. (Cross-polarized light))

In most lavas observed in São Jorge, pyroxene with augitic composition, is an important mineral in the phenocryst phase and/or in the matrix. They can appear as euhedral to anhedral shape crystals showing, in many cases, oxide inclusions and corroded rims evidencing disequilibrium between the mineral and the magmatic liquid. In pyroxene, corroded rims are attributed to dissolution process under low pressure and undersaturation of the magma (Best & Christiansen, 2001).

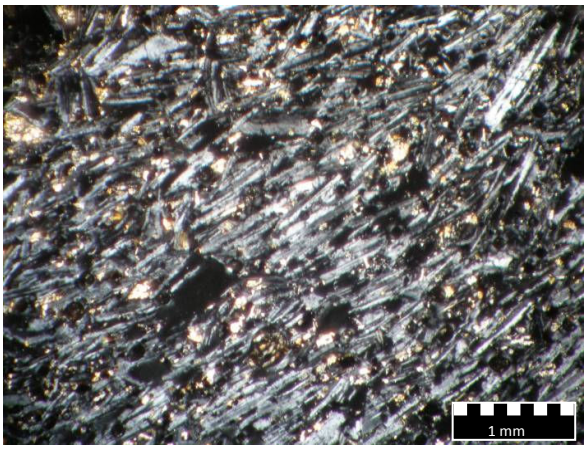

Fig. 6.3 – General aspect of the trachytic texture observed in São Jorge lavas. Plagioclase crystals are aligned according with flux direction (cross-polarized light).

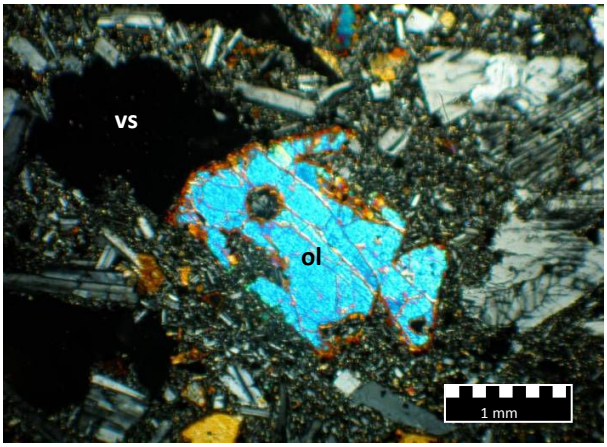

Fig. 6.4 – Lava with porphyritic texture presenting also large vesicles (vs) where an anhedral olivine (ol) phenocryst shows alteration to iddingsite along the corroded rims and embayed fractures (cross-polarized light).

Zoning on the pyroxenes is commonly observe under cross-polarize light (Fig. 6.5), manifesting small variations on mineral composition. Zoning can be complex appearing sectorial or concentric and suggesting a great sensibility of these mineral to the magmatic conditions. Pyroxenes when present in the phenocrystaline phase should be one of the first to fractionate. On the matrix,

pyroxene usually is not the dominant mineral but appears as prismatic microcrystals developing interstitial textures along with plagioclase and oxides.

Pyroxene crystals with green cores surrounded by lighter colored rims have been found in few lavas from Rosais Volcanic Complex (Fig. 6.6). The green pyroxenes have been described in other oceanic islands with alkaline signature as having distinct chemical composition that resulted from fractionation at high pressures (Dobosi & Fodor, 1992; Mata, 1996). However, on the Azores and particularly on Terceira Island, it was suggest that these green pyroxene cores result from mixing of magmas with different degrees of evolution (Madureira, 2006).

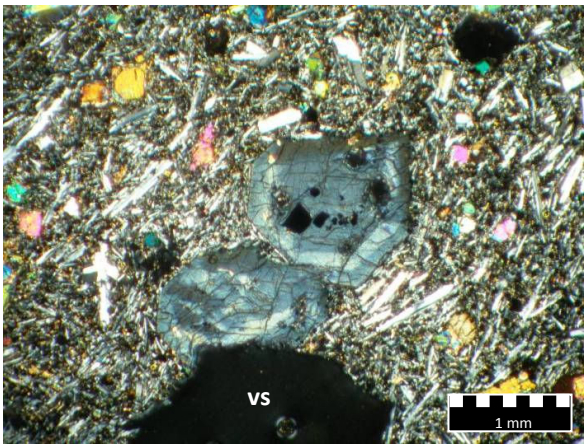

Fig. 6.5 – Porphyric lava with vesicles (vs) and pyroxene crystals with subeuhedral shape and chemical zoning. Microphenocrysts of plagioclase are aligned along a NE-SW direction and are accompanied by olivine and pyroxene. Fe-Ti rich oxides are present in the matrix and inside the pyroxene (cross-polarized light).

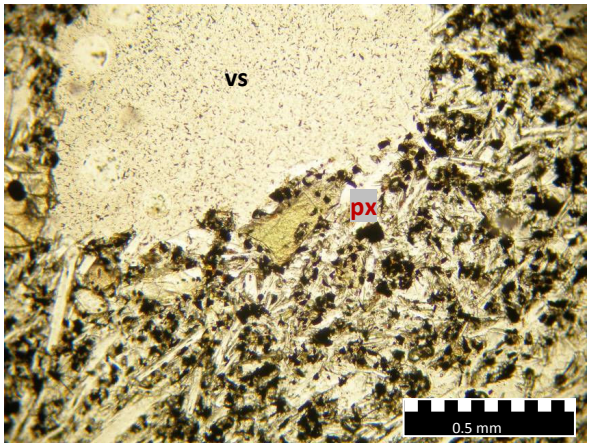

Fig. 6.6 – Small and anhedral green pyroxene (px) crystal located on the rim of a large vesicle (vs). These pyroxenes are usually interpret as being formed at high pressure (plane polarized light; see text for description)

Plagioclase is very abundant and an important mineral phase during fractionation process on São Jorge Island. Their size range is quite variable and crystals may reach more than 5 mm long in thin sections. In addition, their shape is often subeuhedral to euhedral exhibiting prismatic or basal sections.

In the phenocrysts observed is common to find Carlsbad and Carlsbad albite twinning, sometimes intergrowth and frequently complex growth histories as oscillatory zoning (Fig. 6.7), multiple reabsorption surfaces, characterized by rounded edges and truncation of growth surfaces (Zellmer *et al.*, 2003), and partial reabsorption surfaces as in Fig. 6.8. Complex plagioclase growth has commonly been attributed to processes that take place in magma chambers or during magma ascent, as crystals experience fluctuations in pressure, in temperature and in water saturation. As a result, repeated dissolution and overgrowth produces the observed textures (Zellmer *et al.*, 2003). On the matrix prismatic plagioclase microlites are dominant in the majority of the samples along with Fe-Ti oxides.

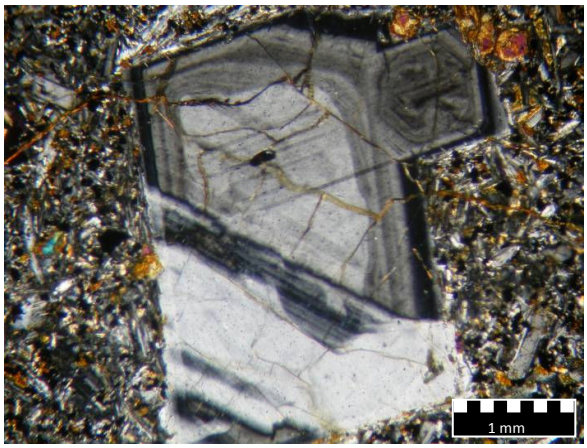

Fig. 6.7 – Large plagioclase crystal exhibiting oscillatory zoning (cross-polarized light). See text for description.

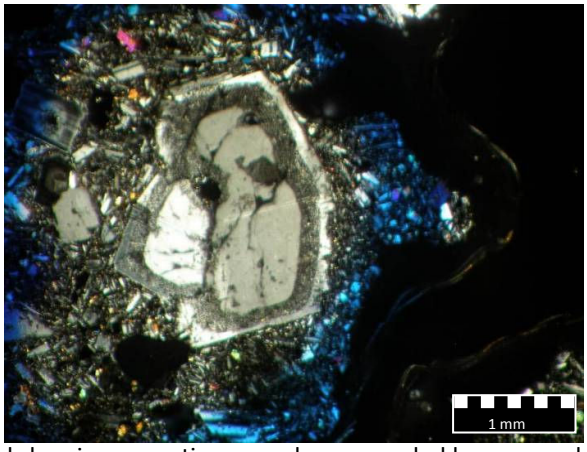

Fig. 6.8 – Plagioclase crystal showing a reaction aureole surrounded by a normal rim. The aureole suggests a period of disequilibrium between the mineral and the liquid followed by a new phase of plagioclase crystallization (cross-polarized light).

The abundant opaque minerals observed in São Jorge lavas are mainly Fe-Ti rich oxides. They may occur as euhedral phenocryst, small inclusions on phenocrysts or as a component of the microcrystalline matrix. In several locations, as for instance on vesicle rims, Fe-Ti oxides present feathery crystals possible due to faster cooling of the liquid in that location (Fig. 6.9). Oxides also appear in some peculiar situations, as for instance, surrounding amphibole crystals forming thick coronas.

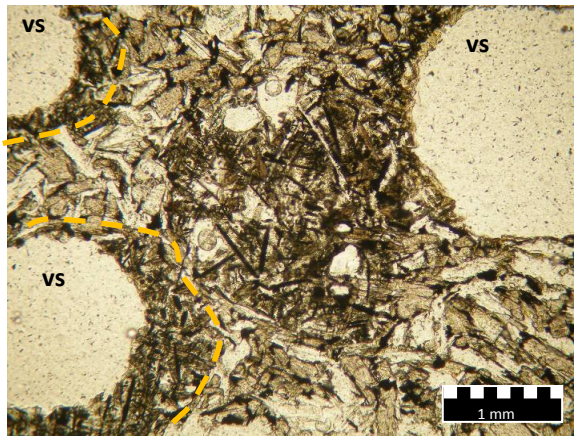

Fig. 6.9 – In this picture it is showed the textures formed by a rapid decrease in temperature of the magmatic liquid. The cooling is faster near vesicles, which affects crystal morphology. These crystals are smaller and oxides exhibit feathery shape. Dash line surrounds quenched areas.

6.3 Special cases

6.3.1 Fajã de São João lava sequence

Almost all samples recovered at Fajã de São João lava sequence present distinctive characteristics from all other rocks in São Jorge. On hand sample, plagioclase is the dominant mineral sometimes corresponding to almost 50% of the volume and with crystals reaching more than 1 cm long. These porphyritic lavas of Fajã de São João lava sequence occur as lava flows or dikes and can be consider as plagioclase cumulates. An example of these plagioclase-rich lavas is found on one dike with metric width and internal symmetric structure presented previously in Fig. 3.9. From the wall towards the centre, the dike exhibits different layers, where vertical flow markers, as for instance

vesicles, flux lamination and oriented plagioclase crystals, point to flux direction (Fig. 6.10). The distribution of the plagioclase crystals on the dike is asymmetric: closer to the wall plagioclase is less abundant and crystals are aligned with flux direction, however, on the center the lava is extremely enriched in plagioclase (Fig. 6.11). The dike internal structure can be attributed to flowage segregation of magma flux on conduits where grain-dispersive pressures push crystals into the interior of the flowing magma and away from the conduit wall where there are strong velocity gradients (Best & Christiansen, 2001).

Under the microscope, the textures vary between microporphyric in some lavas to strongly porphyric on another's or even trachytic for the most evolved lithotypes (Fig. 6.3). The porphyritic lavas are characterized by a mineral assemblage with well-developed plagioclase, scarce olivine and almost absent pyroxene.

Fig. 6.10 – As mentioned in the text the dike, from São João sequence, presents an internal symmetric structure, from the wall towards the centre with layers displaying vertical flow markers, as vesicles, flux lamination and oriented plagioclase crystals. Here is showed a detail of the different flow layers of the dike. Notice the aphyric texture closer to the wall (left side) and the concentration of plagioclase on a central layer of the dike (right side). On the center, layers with vesicles alternate with more aphyric ones.

Many plagioclase crystals exhibit euhedral to subeuhedral shape with normal Carlsbad or Carlsbad-albite twinning or, anhedral shape due to a complex growth where oscillatory zoning is common (Fig. 6.7). Corrosion gulfs are frequent shaping these crystals rims. Olivine crystals are scarce but when present normally show euhedral shapes. Frequently olivine has signs of alteration to iddingsite along the rims and fractures.

The observed mineralogy points to an early growth of the large plagioclase phenocrysts and the few olivines are a latter mineral phase immersed in the groundmass. The matrix of these lavas is mainly microporphyric displaying very often trachytic textures and vesicles. Oxides are also very abundant in the matrix, while olivine and pyroxene can be considered minor.

Fig. 6.11 – Detail view of the centre of the plagioclase-rich dike where the plagioclases crystals are concentrated in higher proportions due to flowage segregation.

6.3.2 Submarine lavas from São Jorge flank

Submarine lavas recovered in São Jorge southeast flank during EMEPC\Açores\G3\2007 cruise, were mainly pillow lavas that cooled quickly when in contact with seawater.

On hand sample observation, as presented earlier in Fig. 4.4, lavas present a thin alteration cap but are fresh on the inside. At this scale, plagioclase seems to be the dominant mineral phase and in some samples can be associated with olivine and/or pyroxene.

The common presence of abundant plagioclase phenocrysts in São Jorge submarine flank is also a characteristic found in many lavas on-shore, in particular, on Fajã de São João lava sequence, just 8 km northwest of the dredging location. The presence and abundance of plagioclase fractionation could be pointed as a major process during magma differentiation in São Jorge.

Under the microscope, the lavas are mainly porphyritic and vesicular with cryptocrystalline matrix (Fig. 6.12), although glass was also observed in some samples as in Fig. 6.13. The amount, size and shape of vesicles are variable and depend on the amount of gas trapped in the lava. Although the

lavas are considered fresh, the interaction between the lava and the seawater is beginning to fill the vesicles with secondary minerals as for instance calcite.

The phenocrysts observed in the lavas are mainly plagioclase, olivine and oxides. Although these minerals present, in general, the same characteristics as in the lavas previously described, their proportion and development may vary from sample to sample.

Olivine in the phenocryst phase can present variable size, shape and habit depending on the cooling process. The more developed olivines can have euhedral habit, concave fractures and occasionally there are skeletal olivines due to quenching (Fig. 6.14). Small oxide inclusions are very common in these olivines. Smaller or less developed olivine phenocrysts are sometimes grouped in clusters (Fig. 6.12).

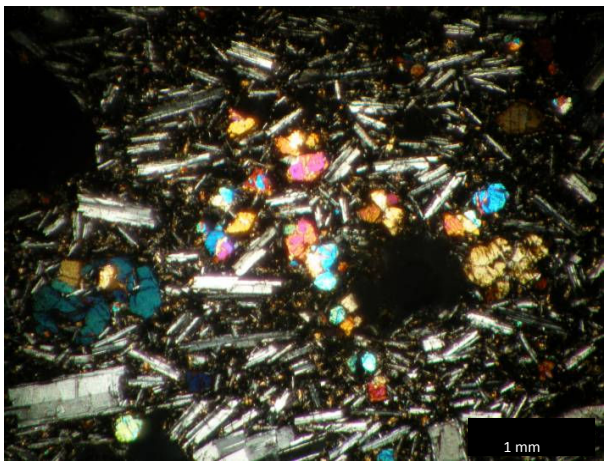

Fig. 6.12 – General aspect of the lavas from São Jorge submarine flank. Olivine phenocrysts appear frequently clustered while plagioclase is prismatic (cross-polarized light).

Plagioclase crystals are also observed in the phenocrysts phase. The most developed crystals have a prismatic habit, frequently with typical twinning although few other prismatic phenocrysts display compositional zoning. The plagioclases can have corrosion gulfs, fractures and oxide inclusions. It is also common to have intergrowth between plagioclase crystals or between plagioclase and olivine. Smaller plagioclase crystals or microphenocrysts, are prismatic and can be locally oriented giving a fluidal texture.

Oxides occur mainly inside olivine and plagioclase phenocrysts or in the matrix and rarely as single phenocrysts. Inside a large olivine crystal, oxides occur often near the rims although it can be

found in the core. In the matrix oxides occur as microphenocrysts and in some samples it was found with feathery habit.

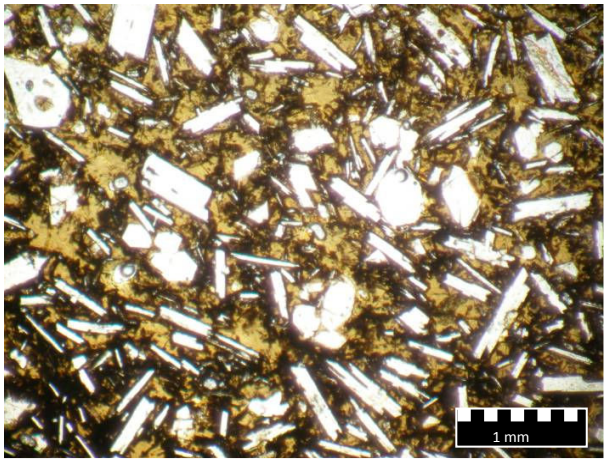

Fig. 6.13 – In this picture it is showed the general petrographic aspect of one of the submarine pillow lavas. This lavas presents phenocrysts of olivine and plagioclase (with prismatic habit) embed in a light brown glass matrix (plane polarized light).

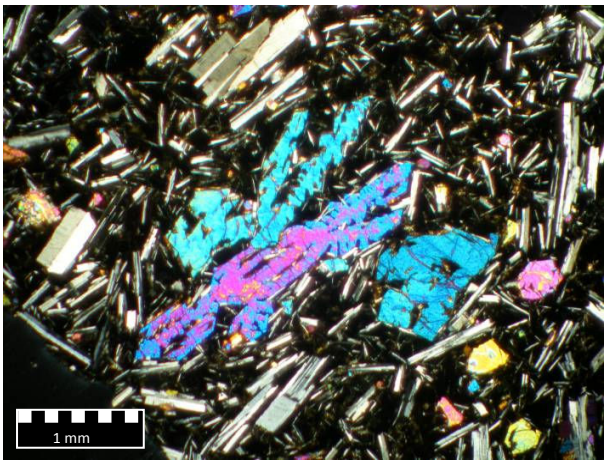

Fig. 6.14 – Microphotograph illustrating the submarine lavas of São Jorge. A skeletal olivine crystal is surrounded by smaller prismatic plagioclase crystal immerse in a very fine-grain matrix (cross-polarized light).

The relations between the different minerals suggest an early crystallization of the more developed olivines and oxides followed by plagioclase.

The groundmass or matrix is usually microporhyric formed by small plagioclase, olivine and oxide crystals. Cryptocrystalline textures in the matrix were also observed as the outcome of rapid undercooling as the superheated magmas reach the seafloor (Best & Christiansen, 2001).

The lavas recovered are relatively fresh and do not show evidences of alteration with the exception of some olivine oxidation in the rims and in fractures crossing the crystals and tiny secondary mineral in few vesicles.

6.3.3 Hydrous mineral phases

Hydrous minerals as kaersutite and biotite were also identified in São Jorge lavas. Although minor, their occurrence reflects the presence of water in the silicate melt. In fact, experimental data (Nicholis & Rutherford, 2004) points to the presence of at least 3% of H_2O dissolved in the melt to fractionate this mineral. The physical conditions of the system as pressure, temperature and oxygen fugacity need also to be adequate to stabilize these minerals.

On the Azores, kaersutite was observed recently in Pico (França, 2000) and in São Miguel islands (Beier *et al*., 2006). In São Miguel, the presence of kaersutite, which do not present internal zoning, was interpreted along with the lava mineralogical assemblage as the result of decompression during magma ascent.

In São Jorge, kaersutite occurs in different environments, as xenocrysts with reaction coronas on a hawaiitic lava of Fajã das Alma (SJ107)), on a tefrite lava from Fajã do Ouvidor (SJ98) and as a phenocryst on a nodule found inside a lava located near Velas Village (SJ32).

In the nodule, this mineral is characterized by a coarse-grain texture with the predominance of pyroxene accompanied by olivine and oxides. The groundmass is made of pyroxene, olivine, oxides, and minor plagioclase presenting locally mosaic texture. Kaersutite is present as anhedral crystals associated with pyroxene and small oxides (Fig. 6.15). The closed relation observed between the pyroxene, oxides and the kaersutite, suggest that kaersutite in the nodule was not under stable conditions.

On the lavas from Fajã das Alma, kaersutite exhibits thick reaction rims of opaque minerals usually ascribed as magnetite, as in Fig. 6.16 (Deer *et al*., 1992; Gribble & Hall, 1992; Nicholis & Rutherford, 2004). Considering that the kaersutite might have formed at deeper levels, its presence in a hawaiitic lava with reaction coronas suggests that they are xenocrysts, brought to the surface by host magmas.

It was proposed that the magnetite coronas result from decompression during magma ascent (Beier *et al*., 2006). However new experimental data points to decompression as producing dissolution of the crystals but because of high diffusive rates, material is transported away from the crystal rim and coronas do not develop (Nicholis & Rutherford, 2004). In fact, according with Nicholis & Rutherford (2004) study, coronas should form already at shallow depths on conditions outside the amphibole stability field, which suppress the diffusion and transport of the breakdown materials away from the rims, and enhance the conditions for the development of the coronas. The breakdown of kaersutite, found in Fig. 6.17, could be a more advance stage, because the corona is surrounding not only the amphibole but also an intergrowth of oxides and plagioclase. Therefore the presence of amphibole with coronas suggest some time of residence of the lavas at shallow level.

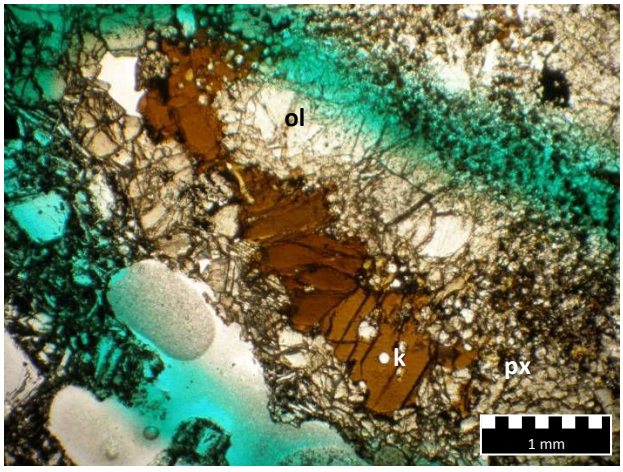

Fig. 6.15 – Large brown kaersutite crystal (k) located on a nodule. The amphibole is surrounded by a mosaic of light brown pyroxene. The transparent olivine (ol) crystal is located next to the amphibole (plane polarized light).

Biotite crystals are uncommon on volcanic basaltic rocks because biotite is not stable at very shallow levels (P>1bar *in* Best, 1982; Deer *et al*., 1992). However, experimental studies on biotite (Best, 1982) showed that for much faster drops in pressure than in temperature, as it happens during eruptions, the system falls below the solidus before leaving the biotite stability field. Because it is unstable and cannot be reabsorbed into any melt, biotite is decomposed in a solid-state system into anhydrous phases as Fe-Ti oxides, magnesium pyroxene and K-feldspar (Best, 1982).

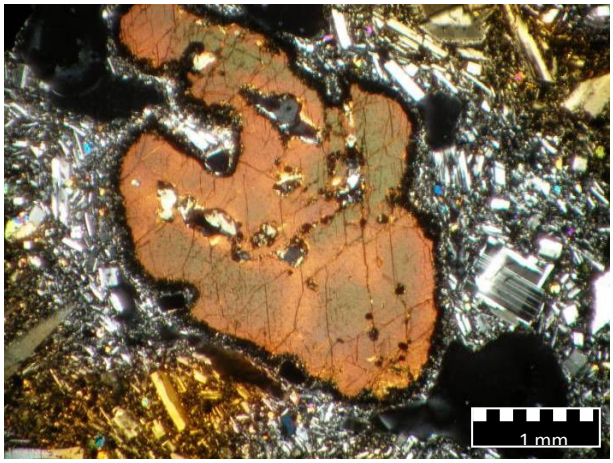

Fig. 6.16 – Hawaiite lava displaying large and anhedral kaersutite crystal surrounded by a reaction corona of reaction made of Fe-Ti oxides (cross-polarized light).

The biotite crystals observed in samples from Topo Volcanic Complex, appear as microcrystals of anhedral shape and undefined rims showing evidences of disequilibrium. The close relation found with feldspar microlites in the presence of abundant oxides, suggest that these minerals are being decomposed (Fig. 6.18). The observations also suggest that lava was rapidly brought to the surface allowing the preservation of these small crystals

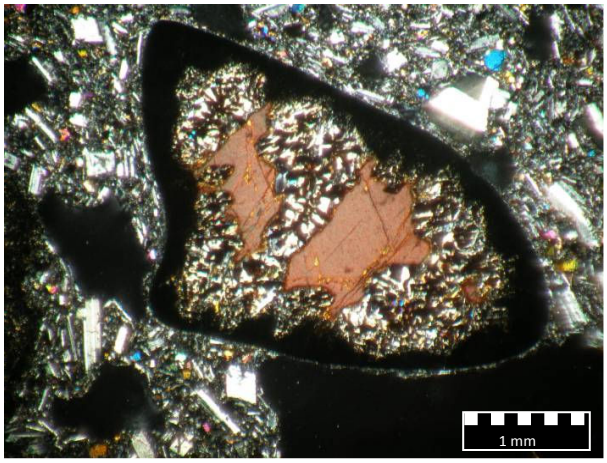

Fig. 6.17 – Kaersutite crystal surrounded by an intergrowth of oxides and plagioclase, all inside a Fe-Ti oxide rich reaction corona (cross-polarized light).

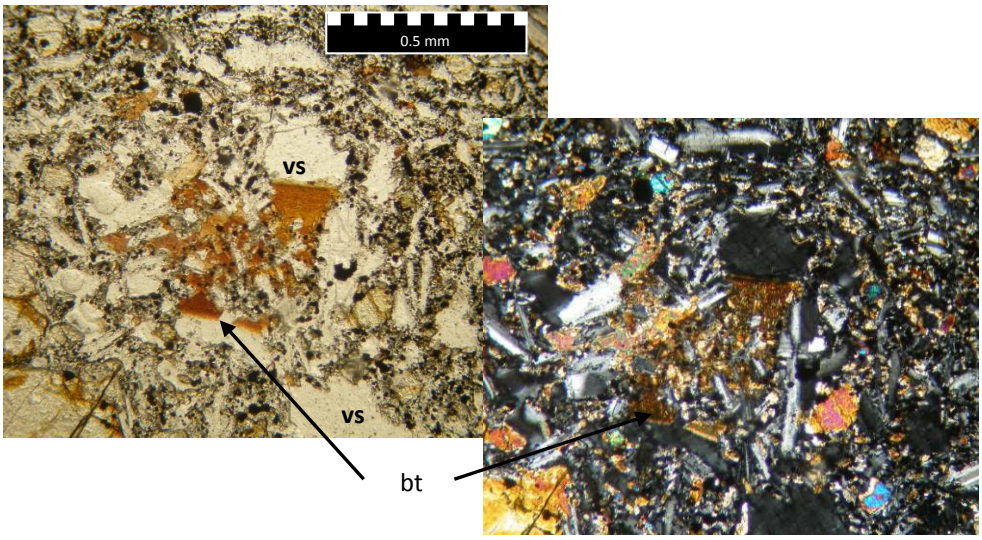

Fig. 6.18 – Biotite (bt) is present as small anhedral crystals and displays a typical speckled effect under cross-polarized light. On this lava, biotite is associated with plagioclase and small Fe-Ti oxides. Biotite is showed under normal light on the left and under cross-polarized light on the right (10x).

Chapter 7: Mineral Chemistry: Characterization and Geothermobarometry

7.1 Olivine

As mentioned in the petrography (chapter 6), olivine is ubiquitous in most São Jorge lavas and is present on the phenocryst phase as well on the matrix. According with the textural aspects most of the observed olivines, on the scope of this work, should have been one of the first minerals to crystallize from the melt, however, olivines with kinkbands and on nodules were also observed.

The chemical composition of olivine is constrained between two endmembers of a solid solution, Forsterite (Mg_2SiO_4) and Fayalite (Fe_2SiO_4), with a complete diadochy between Mg^{2+} and Fe^{2+} (Deer *et al.*, 1992). The replacement in the olivine structure by Mn^{2+}, Ni^{2+} and Ca^{2+} is frequent during magmatic evolution processes, which are good tools to characterize some of those processes.

The composition of the olivine is very sensitive to the composition of the magmatic liquid, and during its growth, variations on liquid composition are record along the crystals. When olivine is first separated from the liquid of a given composition is usually richer in Mg, than those of later crystallization, leaving Fe^{2+} concentrated in the residual liquid (Deer *et al.*, 1992). As consequence olivines can exhibit large intra-crystal compositional variation between the core and rim with respect to forsterite (Fo), having rims more depleted in Mg. In addition, the olivine in the matrix should be more enrich in Fe than the phenocrysts, although it could be observed some overlap depending on the time when matrix began to form. This seems to be the case of the majority of the olivines analyzed on São Jorge lavas, as can be observed in Table 7.1.

Compositional variation between core and the rim in olivines can also be perceptible among other elements as NiO and CaO. Usually, Ni is positively correlated with Mg and its concentration is

expected to be greater in olivine cores, decreasing towards the rims during crystal fractionation process as reflected in Fig. 7.1A).

In São Jorge, olivines can reach a maximum concentration in NiO of 0.29% (APPENDIX II.A), which is a lower value than the concentration of NiO of Terceira olivines (NiO<0.34, Madureira, 2006), but a higher concentration when compared with the NiO content in Pico olivines (NiO<0.24; França, 2000).

Table 7.1 – Core-rim and matrix composition of olivines of several lavas is presented in terms of Fo content. As expected the olivines cores are enriched in MgO.

	Fo (%)		
Lava	**Core**	**Rim**	**Matrix**
SJ29	83.9	74.4	61.9
SJ55	78.8	58.9	74.9-48.3
SJ77	80.2	69.4	74.9-65.3
SJ91	78.2	66.4	58.2
D17	82.8	75.7	71.4-68.3

The compositional zoning observed in terms of Ca shows that this element increases as the percentage of the forsteritic molecule decreases. Consequently, the olivine rims and crystals in the matrix are enriched in CaO in comparison with olivine cores (Fig. 7.1B). Overall, the concentration in CaO presents a wide range (0.12 and 0.47 %) with some samples having more than 0.40% of CaO. Comparing the values with Terceira Island where olivines have at most 0.38% of CaO, São Jorge is slightly more enriched.

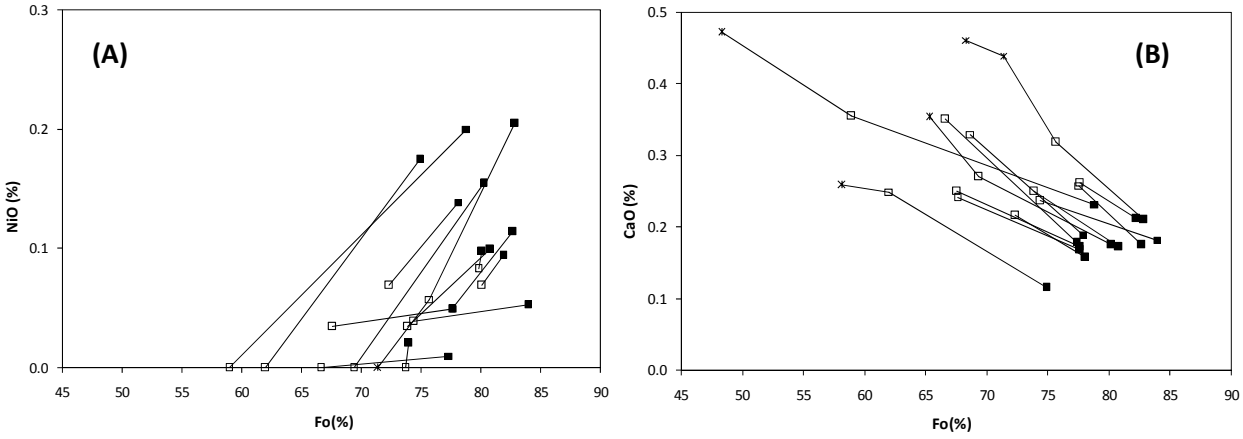

Fig. 7.1 – Diagrams comparing the compositional variation in (A) NiO and (B) CaO, between the core (black square ■) and the rim (open square □) of the olivine crystals, and the olivines in the matrix (represented by ×).

7.1.1 Olivine/Liquid Equilibrium Conditions $\left(K_{DFe/Mg}^{ol/liq}\right)$

The incorporation of an element *i* on a mineral/solid is defined by the partition coefficient of the element ($D_i^{s/liq}$), which is dependent on the ratio between the concentration of the element i on the mineral/solid (C_i^s), and its concentration on the liquid (C_i^{liq}) (*in* Shaw, 2006):

(Eq. 7.1) $$D_i^{s/liq} = \frac{C_i^s}{C_i^{liq}}$$

If $D_i^{s/liq}$>1, than the element is compatible and will enter the mineral structure while if $D_i^{s/liq}$<1, then the element is incompatible with the mineral and will remain preferentially in the liquid. For the pair olivine–liquid where there is a complete solid solution between forsterite and fayalite and a strong dependency on melt composition, it is possible to constrain the physical conditions in which olivine crystallization occurs. Several experimental studies have focus on the relationship between the partition coefficients ($D_i^{s/liq}$), melt composition, pressure (P) and temperature (T).

Although (Eq. 7.1) is useful for calculating the partition coefficients in olivines as predicted by Beattie *et al.* (1993), Roeder & Emsile (1970) defined the exchange partition coefficient $K_{DFe/Mg}^{ol/liq}$ [6] as a good indicator for the behavior of Fe and Mg. As previously mentioned, the composition of the olivines is strongly dependent on the composition of the liquid what can be understood by the strong dependency of the FeO/MgO ratio on the pair olivine/liquid. In this perspective, the exchange partition coefficient, $K_{DFe/Mg}^{ol/liq}$, that is independent from temperature, will allow to identify situations where the olivines crystallized on an equilibrium situation (Roeder & Emsile, 1970). The value defined by those authors for olivine-liquid equilibrium in the mantle is 0.3, signaling an overall increase in the FeO/MgO of the liquid as olivine fractionates.

The $K_{DFe/Mg}^{ol/liq}$ was determined for the most forsteritic olivine cores of each lava analyzed in São Jorge, using the concentration or the molar fraction of Fe and Mg in the olivine and in the liquid according with the next equation:

[6] Nomenclature as in Beatti *et al.* (1993)

(Eq. 7.2) $$K_{DFe/Mg}^{ol/liq} = \left[\frac{\chi^{ol}}{\chi^{liq}}\right] FeO^* \left[\frac{\chi^{liq}}{\chi^{ol}}\right] MgO$$

The results obtained for the $K_{DFe/Mg}^{ol/liq}$ are presented in Table 7.2, and are within the 0.21-0.40 interval with an average value of 0.29, which is very close to the olivine/liquid equilibrium defined by Roeder & Emsile (1970). Also, if we consider Ford *et al.* (1983) experimental work, which proposed the interval between 0.25 and 0.38 for $K_{DFe/Mg}^{ol/liq}$, the olivines presented in Table 7.2 fall within this interval.

Table 7.2 – In this table are presented the compositions of the most forsteritic olivine cores and their respective $K_{DFe/Mg}^{ol/liq}$ calculated according with (Eq. 7.2) from Roeder & Emsile (1970). The $D_{Ni}^{ol/liq}$ was determined for the olivines considered to be in equilibrium with the liquid using (Eq. 7.1).

	Fo in olivine	**Mg# rock**	$K_{DFe/Mg}^{ol/liq}$	$D_{Ni}^{ol/liq}$
SJ7	73%	42%	0.27	27.9
SJ8	81%	50%	0.23	
SJ9	82%	51%	0.22	
SJ20	80%	57%	0.34	7.5
SJ29	84%	59%	0.27	13.8
SJ32	81%	53%	0.27	31.3
SJ49	84%	54%	0.21	
SJ52	81%	56%	0.30	19.2
SJ55	75%	46%	0.27	67.6
SJ70	86%	72%	0.40	
SJ77	85%	59%	0.26	8.2
SJ83	82%	61%	0.34	6.5
SJ91	78%	55%	0.34	14.3
SJ107	77%	48%	0.28	6.0
D17	83%	60%	0.32	11.6

In Fig. 7.2, the equilibrium lines of Ford *et al.* (1983) are represented and the olivines are plotted in terms of the Mg# of the rock and the percentage of forsterite of the olivines. Overall, the diagram suggests that most olivines crystallized in equilibrium with the liquid although, some of them are not in equilibrium with their host magma and plot above or below the interval lines. Generally, it is very hard to give a right answer regarding olivines provenience but some hypotheses can be brought up to give an explanation.

The $K_{DFe/Mg}^{ol/liq}$ <0.25 implies that the olivines were in equilibrium with a liquid more enriched in MgO than the one forming the lava. One hypothesis is that the olivines crystallized from a different liquid or that they were a part of a cumulate, which was later brought to the surface by the host lava. This could be the case of the olivine, which also presents kinkbands, pointing to an early and deeper crystallization of olivine followed by deformation during her ascent to shallower levels (e.g. olivine SJ49 of Table 7.2).

Other olivines, which show low $K_{DFe/Mg}^{ol/liq}$, belong to lavas from São João lava sequence (e.g. SJ8 and SJ9). As previous observed these lavas have considerable amounts of plagioclase, possible the first mineral to form, and its crystallization produces an increase of Mg and Fe in the liquid (Roeder & Emsile, 1970). In addition, the presence of Fe-Ti rich oxides would retrieve some of the Fe from the liquid, and so Mg# increases and the olivines become more forsteritic.

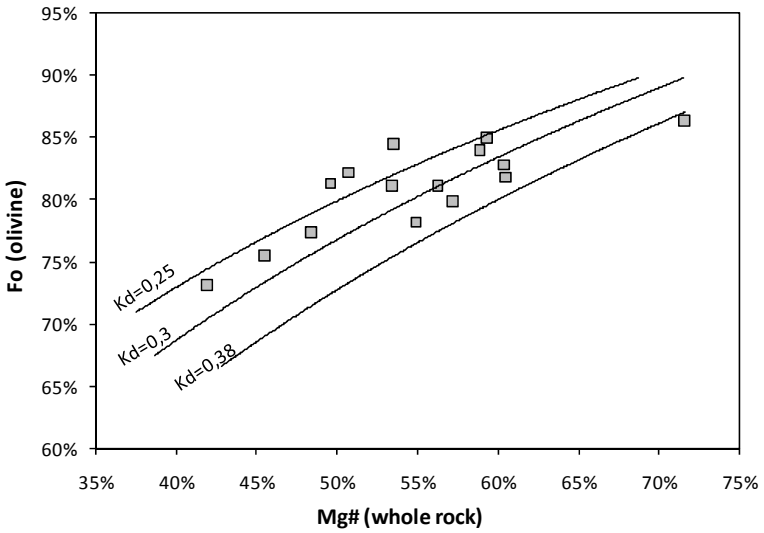

Fig. 7.2 – In this diagram is presented partition coefficients for the olivines in terms of their Fo (%) content and of Mg# found on the lava.

The olivines cores with $K_{DFe/Mg}^{ol/liq}$ higher than 0.38 suggest that the liquid, in equilibrium with the olivines, was relatively enriched in FeO. One explanation for this could be that the olivines crystallize from a Fe-rich magma and are xenocrysts incorporated the present lava. Another explanation is that olivines are slightly more iron rich at high pressures than they would be at low pressures (Ford *et al.*, 1983; Ulmer, 1989). None of the previous hypothesis is able to explain the olivine in lava SJ70 because are Mg-rich. So, possibly, the olivine in the lava is a xenocryst incorporated in the host magma.

7.1.2 Ni Partition Coefficients $\left(D_{Ni}^{ol\ /\ liq}\right)$

The partition coefficients for Ni presented in Table 7.2, were calculated on the olivines believed to be in equilibrium with the magmatic liquid using (Eq. 7.1). The values obtained present a wide range, with sample SJ55 displaying extremely high partition coefficients. The reason for the high $D_{Ni}^{ol/liq}$ in most cases would be the high concentration of Ni on the olivine relatively to the overall Ni concentration on the lava, nonetheless the $D_{Ni}^{ol\ /\ liq} = 67.6$, in the lava SJ55, does not seem reasonable.

In the next lines the $D_{Ni}^{ol\ /\ liq}$ will be calculated based on its relation with Mg partitioning coefficient ($D_{Mg}^{ol/liq}$). As demonstrated by Beattie *et al.* (1991), the behavior of trace elements as Ni, ($D_{Ni}^{ol\ /\ liq}$) is linearly dependent from Mg partitioning coefficient values ($D_{Mg}^{ol\ /\ liq}$), explaining the Ni increase along with forsterite increase. Initially, Beattie *et al.* (1991) method determines the $D_{Mg}^{\alpha\ /\ liq}$ by combining the composition of the liquid (molar fraction of the elements (χ_{iO}^{liq}), with two empirical constants, ($A_i^{ol/liq}$ and $B_i^{ol\ /\ liq}$) determined by the regression of experimental data, and with the molar proportion of the position M on the olivine (ψ^{ol}) as presented in the next equation:

(Eq. 7.3) [7] $$D_{Mg}^{ol\ /\ liq} = \frac{\psi^{ol} - B_{Fe}^{ol\ /\ liq}\chi_{FeO}^{liq}}{A_{Fe}^{ol\ /\ liq}\chi_{FeO}^{liq} + \chi_{MgO}^{liq}}$$

From (Eq. 7.3), which is relatively easy to calculate, $D_{Mg}^{ol/liq}$ is dependent on the degree of evolution of the magmas and, as the liquids are becomes more evolved the partition coefficients increase as predicted also by Hirschmann & Ghiorso (1994). Following Beatti *et al.* (1991) method, it is possible to calculate $D_{Ni}^{ol/liq}$ in the pair olivine/liquid from the values obtained previously for

[7] The general equation is: $D_{Mg}^{ol\ /\ liq} = \frac{\psi^{ol} - \sum_{i=1}^{n} B_i^{ol\ /\ liq}\chi_{iO}^{liq}}{\sum_{i=1}^{n} A_i^{ol\ /\ liq}\chi_{iO}^{liq}}$

$D_{Mg}^{ol/liq}$. From thermodynamic analyses, it was found that there is a linear relationship between $D_{Mg}^{\alpha/liq}$ and the partition coefficients of other elements as Ni, allowing regression into equation:

(Eq. 7.4) $$D_i^{ol/liq} = A_i^{ol/liq} D_{Mg}^{ol/liq} + B_i^{ol/liq}$$

Using the previous equation (Eq. 7.4) the partition coefficients were also determined for Fe and Mn as well the $K_{DFe/Mg}^{ol/liq}$ for the liquids. The results are presented in Table 7.3, and represent the equilibrium conditions for olivine saturation according with liquid composition. As can be seen by the $K_{DFe/Mg}^{ol/liq}$ values 0.304±0.002, olivines are very close to the equilibrium defined by Roeder & Emsile (1970), which is 0.3.

Table 7.3 – Expected partition coefficients for Mg, Ni, Fe and Mn for the pair olivine/liquid, determined using Beatti *et al.* (1991) method. The Fe-Mg exchange partition coefficient is the ratio between $D_{Fe}^{ol/liq}$ and $D_{Mg}^{ol/liq}$.

	$D_{Mg}^{ol/liq}$	$D_{Ni}^{ol/liq}$	$D_{Mn}^{ol/liq}$	$D_{Fe}^{ol/liq}$	$K_{DFe/Mg}^{ol/liq}$
SJ7	11.08	33.41	2.82	3.34	0.3014
SJ20	4.52	11.45	1.12	1.38	0.3050
SJ29	4.41	11.07	1.09	1.34	0.3051
SJ32	4.95	12.91	1.23	1.51	0.3045
SJ49	5.49	14.69	1.37	1.67	0.3039
SJ52	4.80	12.41	1.20	1.46	0.3046
SJ55	5.51	14.76	1.38	1.67	0.3039
SJ70	3.05	6.54	0.74	0.94	0.3079
SJ77	3.94	9.51	0.97	1.20	0.3059
SJ82	4.25	10.57	1.05	1.30	0.3053
SJ91	5.55	14.90	1.39	1.69	0.3039
SJ107	6.76	18.97	1.70	2.05	0.3030
D17	4.32	10.81	1.07	1.32	0.3052

7.1.3 Olivine/Liquid Equilibrium Temperature

During Roeder & Emsile (1970) work several experiments that involved variable conditions of temperature, oxygen fugacity and liquid composition, attempted to establish the equilibrium condition between olivine and basaltic liquids. One of the results showed that the exchange

partition coefficient $K_{DFe/Mg}^{ol/liq}$ is independent from temperature so it cannot be used as a geothermometer (Roeder & Emsile, 1970; Ulmer, 1989; Beatti *et al.*, 1991). However, it was found that the logarithm of magnesium partition coefficient ($\log D_{Mg}^{ol/liq}$) correlates positively with temperature.

Using the previous calculated $D_{Mg}^{ol/liq}$ from Beatti *et al.* (1991), which represent the equilibrium conditions for olivine crystallization, the temperature of saturation of olivine, i.e. the temperature when the first olivine began to crystallize is calculate using Roeder & Emsile (1970) equation:

(Eq. 7.5)[8] $$\log D_{Mg}^{ol/liq} = \frac{3740}{T} - 1.87$$

The calculated temperatures are presented in Table 7.4 with an average value of 1185±72; however, two lavas (SJ7 and SJ70) exhibit extreme temperature, 1010 and 1316 ºC respectively.

Table 7.4 – Temperature of equilibrium for the pair olivine/liquid determined using (Eq. 7.5). The results are presented accordingly with the stratigraphic position or lava group.

		T (ºC)
Fajã de São João sequence	SJ7	1010
Topo Volcanic Complex	SJ49	1160
	SJ52	1193
	SJ55	1160
	SJ70	1316
Rosais Volcanic Complex	SJ82	1224
	SJ91	1158
	SJ29	1215
Manadas Volcanic Complex	SJ20	1208
	SJ32	1185
	SJ77	1244
	SJ107	1112
Pillow lava	D17	1219

[8] Where T is in Kelvin and was corrected to ºC.

As previously presented in Table 7.2, on lava SJ7 the pair olivine/liquid seems to be in equilibrium ($K_{DFe/Mg}^{ol/liq}$ = 0.27) although it has a relative low Mg# (42%) and Fo (73%). When calculating the $D_{Mg}^{ol/liq}$ using Beatti *et al.* (1991) method the low Mg# produces higher partition coefficients for Mg. In this sense the calculated temperatures that are dependent on $D_{Mg}^{ol/liq}$ are lower than average.

The temperature calculated for olivines on lava SJ70 is, approximately, 130 ºC higher than the average value. Considering that, this lava has one of the most primitive compositions found in São Jorge, it would be expected to have fractionated at higher temperatures.

7.1.4 Olivine Characterization on São Jorge Lavas

In Fig. 7.3 is represented a histogram with the forsterite (Fo) composition of the olivines found on each lava group of São Jorge Island: Topo, Rosais and Manadas volcanic complexes, Fajã de São João lava sequence and on the submarine pillow lavas. The majority of the olivines show a wide variation of the forsterite molecule concentration that ranges between Fo_{87} and Fo_{60}, with exception of few crystals that can reach values as low as Fo_{29}.

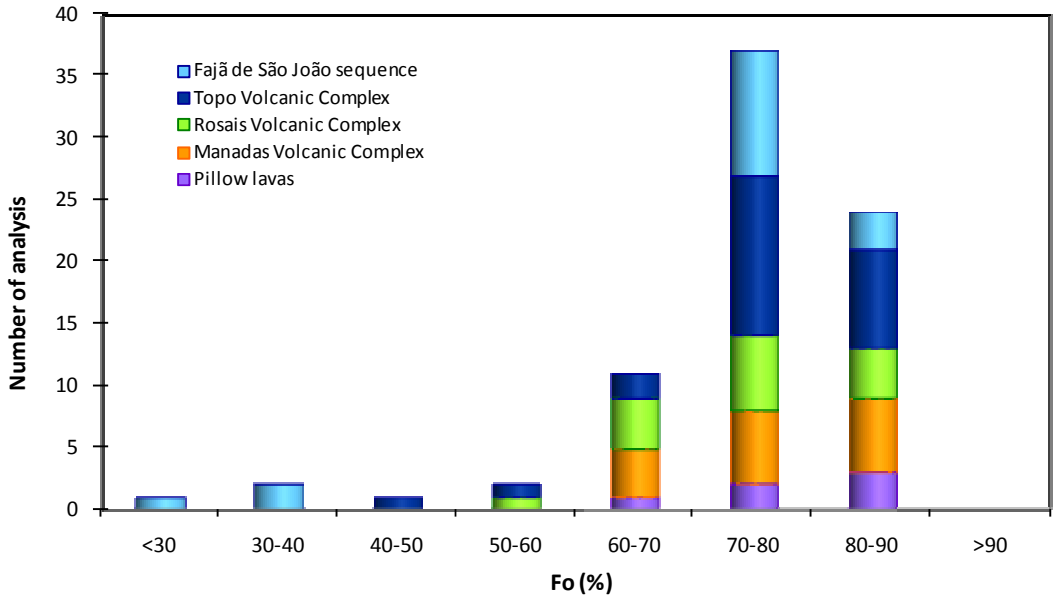

Fig. 7.3 – Histogram with the forsteritic composition of each lava group in São Jorge Island.

Fajã de São João lava sequence displays in Fig. 7.3 a clear bimodal distribution. The Fo rich group presents an increase in frequency from Fo_{90} towards Fo_{70}, while the olivines with low Fo, obtained on the most evolved lavas have a forsteritic molecule below Fo_{40}.

The forsterite content in the olivines from Topo Volcanic Complex ranges between Fo_{40} and Fo_{90}. Although there is a strong predominance of the high magnesium olivines (Fo_{70} to Fo_{90}), the measurements performed on the matrix and on crystal rims were considerable less magnesian (Fo<60%). The olivines from Rosais Volcanic Complex seem to be characterize by a Fo content ranging between the 60 and 90%, although few analysis reveal less magnesian olivines.

The forsteritic content of Manadas Volcanic Complex is distributed only between Fo_{60} and Fo_{90}, however, the overall pattern for these olivines in Fig. 7.3 shows that they have a strong magnesian component. In a similar way, the olivines in the pillow lavas have a simple distribution with high forsteritic cores (Fo_{80-90}) and more evolved rims that show a simple crystal fractionation path.

7.2 Feldspars

The observation under the microscope showed that feldspars are very abundant in São Jorge lavas, in particular in Fajã de São João lava sequence, and are present in the matrix as well in the phenocryst phase.

Most feldspars form a solid solution in a ternary system, where the end-members are ortose ($KAlSi_3O_8$), albite ($NaAlSi_3O_8$) and anortite ($CaAl_2Si_2O_8$). The feldspars in the composition range of ortose-albite are referred to as alkaline feldspars and in the range of albite-anortite as plagioclases (Deer *et al.*, 1992).

The plagioclases series is divided into six compositional intervals depending on the percentage of the anortite molecule (An): anortite (An_{100-90}), bytwonite (An_{90-70}), labradorite (An_{70-50}), andesine (An_{50-30}), oligoclase (An_{30-10}) and albite (An_{10-0}).

In Fig. 7.4 it is showed that most feldspars in São Jorge lavas are within the anortite-albite range with exception of three crystals that fall within the ortose-albite solid solution with Or_{39-17} and Ab_{54-68}. Plagioclase population in São Jorge, which is important and sometimes dominant in several lavas, has a composition range between An_{81-7} although 86% of the plagioclases have a composition between bytwonite and labradorite (An_{81-55}).

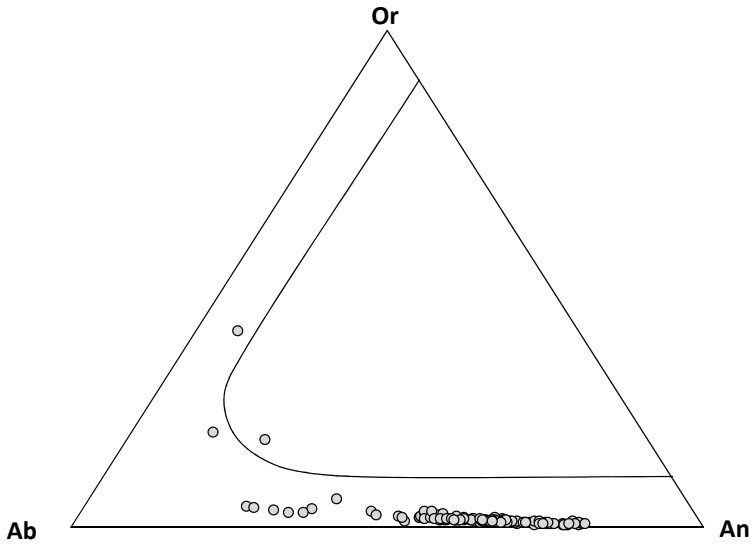

Fig. 7.4 – Composition of the feldspars in terms of their anortite-albite-ortose molecules.

The composition of the feldspars in terms of the anortite molecule is intimately related with the degree of evolution of the lava (Fig. 7.5). The most undersaturated basanite/tefrites and basalts have plagioclases with the highest anortite concentration (bytwonite and labradorite) while, the hawaiites and mugearites have low Ca concentrations and are in the oligoclase and albite range (see APPENDIX II.B).

The feldspars analyzed in Fajã de São João lava sequence contrast with the remaining lava groups because they present a continuous compositional trend along the anortite-albite solid solution (Fig. 7.6). In these lavas, the plagioclases cores are characterized by the highest anortite content (An_{80-70}), while the rims and matrix are enriched in sodium and potassium, i.e. in albite and ortose molecules. One explanation for finding very high Ca concentration in the cores of Fajã de São João olivines may result from the fact that pyroxene is scarce or absent, thus during fractional crystallization processes the Ca available is integrated in the plagioclase.

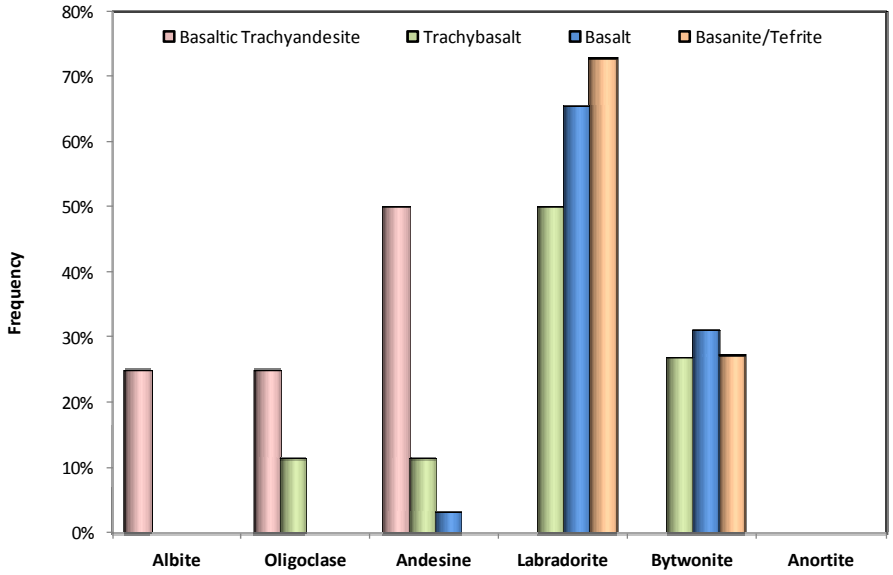

Fig. 7.5 – Distribution of the feldspar composition in terms of the anortite molecule in the lithologies of São Jorge.

The plagioclases found in Topo and Rosais volcanic complexes and in the pillow lavas fall on the bytwonite-labradorite range while the plagioclases analyzed in Manadas present a more wide compositional range (Fig. 7.6). It was observed that in this last lava group, the plagioclases cores with An_{80} present a decrease in Ca and increase in Na towards the rim that reaches a compositions in the oligoclase field.

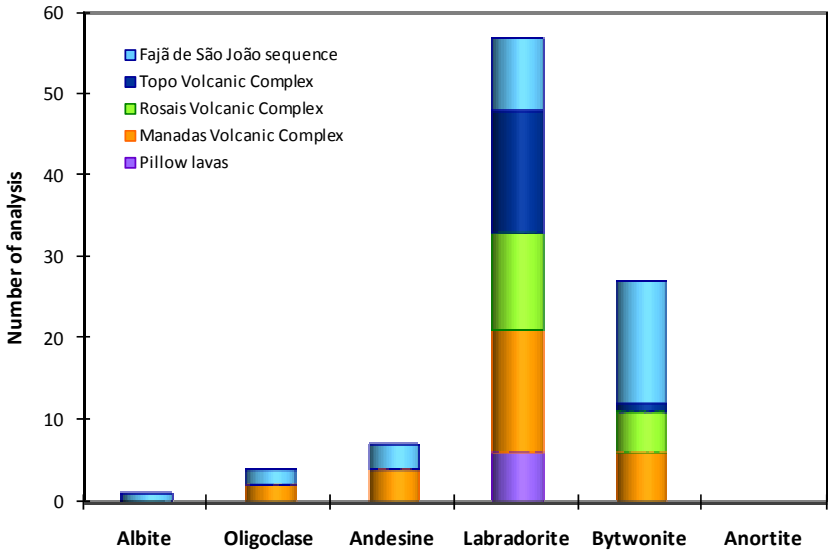

Fig. 7.6 – Distribution of plagioclase composition, in terms of the percentage of the anortite molecule, on the lava groups in São Jorge.

As crystal fractionation progresses and the temperature of crystallization decreases, plagioclases become relatively enriched in sodium. Such compositional zoning, from calcic cores to more sodic rims, is common in plagioclases because they are sensitive to liquid composition. However, small changes in the liquid often produce compositional zoning, with crystal showing alternating "layers" with respect to the An content. In addition, in some cases it is found that the plagioclases present reverse zoning with the rims having higher percentage of anortite molecule (Deer *et al.*, 1992).

In São Jorge lavas, several plagioclases presented oscillatory zoning as can be depicted from Fig. 7.7, where anortite content displays a visible core-rim variation. This variation is not only present in a single crystal but can also be extended to the small microphenocrysts incorporating the groundmass.

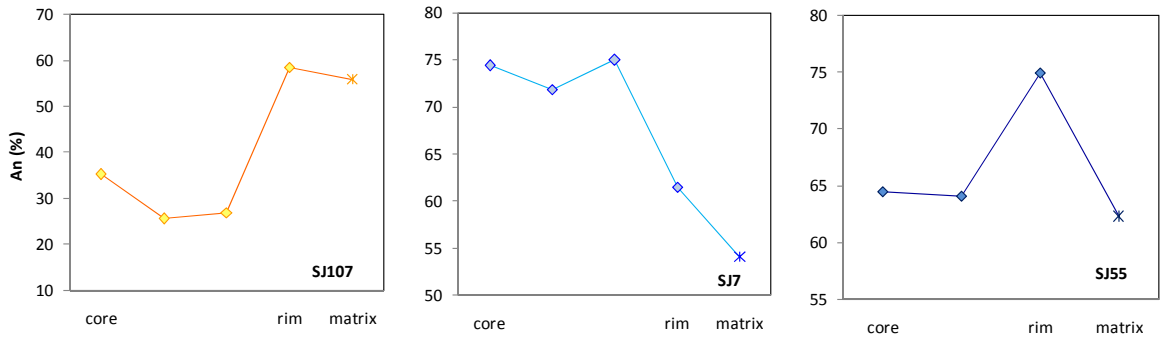

Fig. 7.7 – Compositional zoning found in some of the analyzed plagioclases on Manadas (SJ107), Fajã de São João (SJ7) and Topo (SJ55) lavas.

7.3 Pyroxene

The petrographic analysis of lavas showed that pyroxene is an important mineral phase in São Jorge lavas, which is present in the phenocryst phase as well in the matrix. Most of the pyroxenes exhibit characteristics, under the microscope, that point to a general augitic composition and, frequently, to core-rim chemical variations. The chemical composition of the pyroxenes is explored here in order to better characterize this mineral phase in São Jorge Island and to differentiate the minerals in each lava group of this island.

7.3.1 General Characterization of the Pyroxenes

Pyroxenes are ferromagnesian chain silicates very abundant in most of alkaline igneous rock of oceanic islands. Their general structural formula ($M2M1T_2O_6$) allows for a wide compositional variability, which depends on the substitutions of several cations in the two octahedral positions (M1 and M2) and in the tetrahedral position (T) (Morimoto *et al.*, 1988). According with the substitutions on the M and T positions, the pyroxenes can be divided into four groups, where the extreme compositions can be considered as end-members. These groups are the quadrilateral pyroxenes (QUAD), where Ca, Mg and Fe are the most important elements, the calcium-sodium pyroxenes (Ca-Na), the sodium pyroxenes (Na) and, a fourth group, that includes the remaining pyroxenes (Morimoto *et al.*, 1988).

The diagram that classifies the pyroxenes in the four mentioned groups is represented in Fig. 7.8. As can be observed in the diagram, the analyzed crystals plot of the field of the quadrilateral pyroxenes (QUAD), with the $(Q+J)$[9] index ranging between 1.5 and 2.

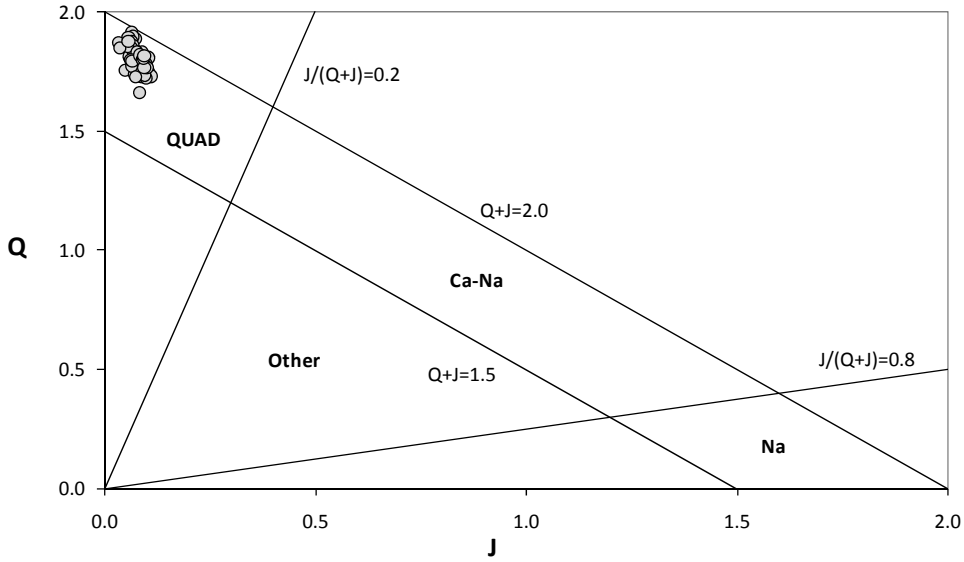

Fig. 7.8 – Projection of all analyses of São Jorge pyroxenes in the discriminatory diagram from Morimoto *et al.* (1988).

[9] The indexes are: Q = Ca +Mg + Fe^{2+} (a.f.u.) and J = 2Na (a.f.u.)

A more detailed characterization of the quadrilateral pyroxenes, Ca-Fe-Mg, can be achieved by using a ternary diagram that discriminates between compositions with different proportions of those three elements. The pure extreme compositions are the Mg-rich component ($Mg_2Si_2O_6$) named enstatite (En), the Fe-rich component ($Fe_2Si_2O_6$) called ferrosilite (Fs), and the Ca-rich, which is called wollastonite (Wo). The latter however, is only considered as a quadrilateral pyroxene until a maximum of 50% of Ca, therefore the considered extreme compositions for these pyroxenes are $CaMgSi_2O_6$ (Diopside) and $CaFeSi_2O_6$ (Hedenbergite).

The classification of São Jorge pyroxenes in the ternary diagram is presented in Fig. 7.9. All analyzed crystals plot below the Diopside-Hedenbergite line and fall on the fields defined for pyroxenes with Diopside and Augite composition. Nonetheless, some crystal present compositions are close to the Hedenbergite-Augite compositional line.

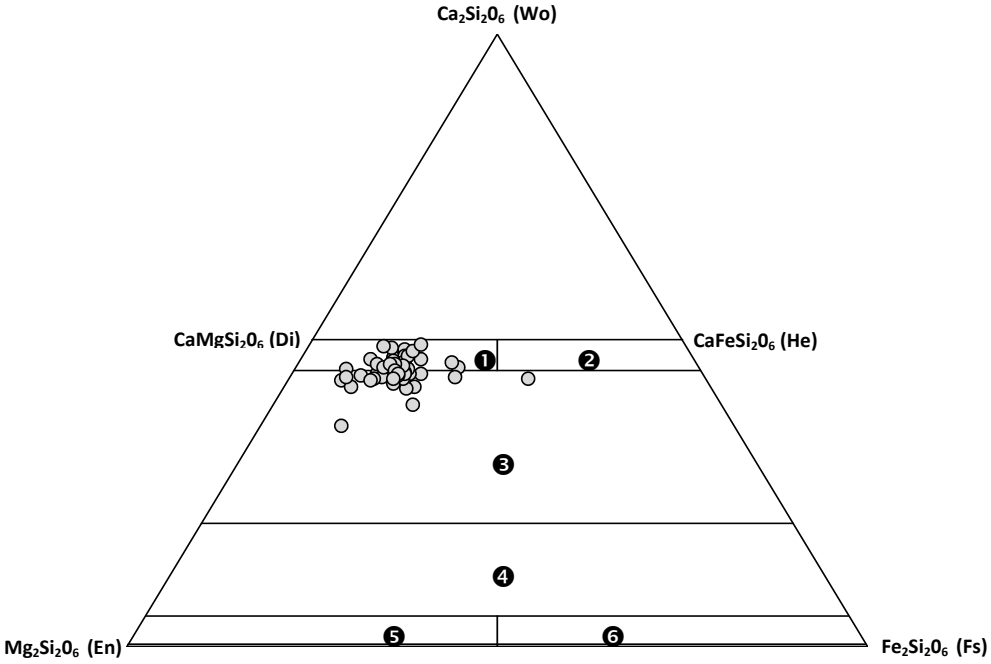

Fig. 7.9 – Projection of the analyzed pyroxenes in the ternary diagram, which specifies the composition of the quadrilateral pyroxenes. The vertices of the diagram are defined by the pure compositions of En-Fs-Wo ($Mg_2Si_2O_6$ – $Fe_2Si_2O_6$ – $Ca_2Si_2O_6$ respectively) and the compositional fields are: ❶ Diopside; ❷ Hedenbergite; ❸ Augite; ❹ Piegonite; ❺ Enstatite and ❻ Ferrosilite. For the nomenclature of the Ca-Mg-Fe pyroxenes normalization must be made to Ca + Mg + ΣFe = 100, where $\Sigma Fe = Fe^{2+} + Fe^{3+} + Mn$ (Morimoto *et al.*, 1988).

The compositional variability of the pyroxenes (see APPENDIX II.C), although relatively small in this case, results frequently from a deficit of Si^{4+} in the tetrahedral position, which is compensated by the entrance of Al^{3+}. In the analyzed pyroxenes the entrance of Al^{3+} into the tetrahedral

position is confirmed by the good correlation ($r^2 = 1$) between Si and Al (Al^{iv}) displayed in Fig. 7.10, where the concentration of both cations overlap the line Si +Al^{iv} = 2. The Si ↔ Al^{iv} substitutions in the tetrahedral position (T) produces changes in the chemical balance of the pyroxenes that need to be re-equilibrated by the entrance into the octahedral positions (M) of other cations as Al^{vi}, Ti, Fe^{3+} and Cr, to the position M1, and/or by the substitution of Na by Ca in the position M2.

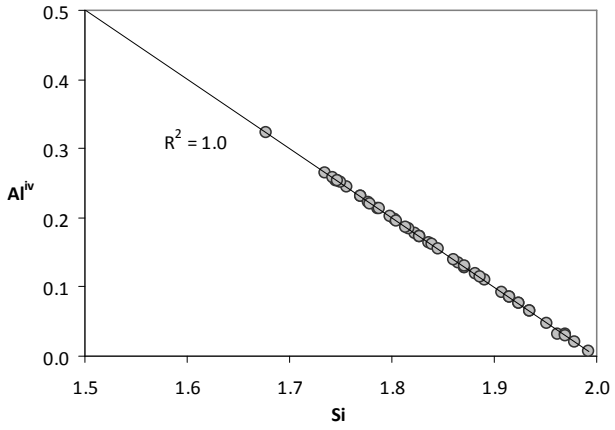

Fig. 7.10 – Diagram showing the good correlation between Si and Al^{iv} and the entrance of the last in to the tetrahedral position of the pyroxenes of São Jorge. The overlapping of the samples on the Si+ Al^{vi} = 2 line emphasize the occupation of the T position by these two cations.

The good correlation between Ti and Al^{iv} as showed in Fig. 7.11 suggests that Ti has an important role in balancing the ionic charges in the position M1. In fact, the entrance of Ti into the pyroxene produces and excess of charge, which ionic re-balances is frequently interpreted by the chemical equation $Ti^{4+} + 2Al^{3+}{}_{iv} = (Mg + Fe)^{2+} + 2Si^{4+}$ (Tracy & Robinson, 1977).

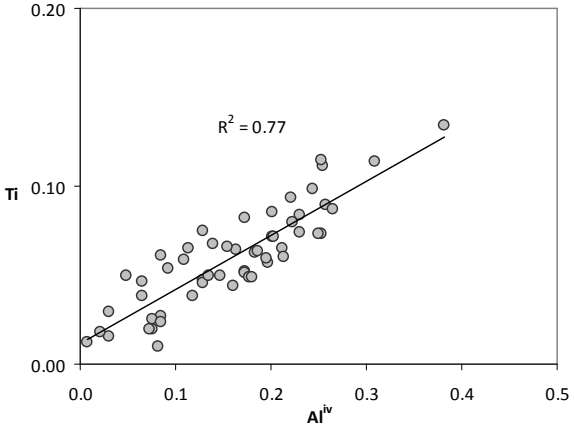

Fig. 7.11 – Projection of the composition of the pyroxenes analyzed on São Jorge lavas according with the Al^{iv} vs. Ti (a.f.u.). Overall, the pyroxenes present a good correlation indicating the entrance of Ti to the M1 position.

Accordingly, with the previous chemical equation the sum of the cations, Ti, Fe^{2+} and Mg would have to be equal to one in order to fill the M1 position. However, this is not the case because the sum of the three cations exceeds that value established by the equation $Ti+Fe^{2+}+Mg = 1$ and plot on the right of the line (Fig. 7.12). In addition, the Al^{iv}/Ti ratio on the pyroxenes should be equal to 2 but the average value calculated for this ratio is 2.7. Therefore, the substitutions on the octahedral position (M1) of the pyroxenes should require other cations to balance the ionic charges.

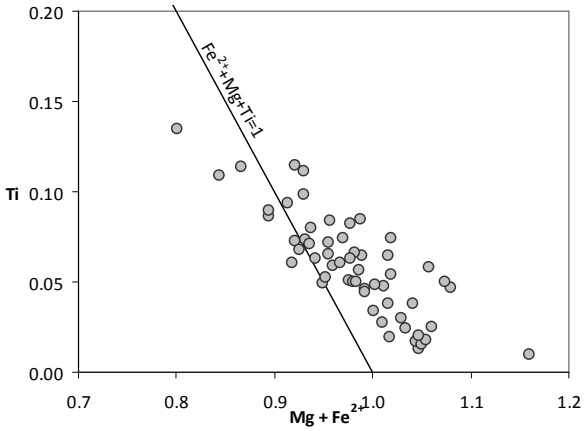

Fig. 7.12 – Diagram showing the relation between Ti and $Mg+Fe^{2+}$ on the pyroxenes. Most of the analyzed crystals plot on the right of the $Ti+Fe^{2+}+Mg = 1$ line showing an excess of $Mg+Fe^{2+}$.

The position M1 on the pyroxenes is also occupied by Fe^{3+} and Cr that, frequently, help to balance Al^{iv}. In the analyzed pyroxenes, the concentrations in Fe^{3+} and Cr are relatively low and in many cases the pyroxenes don't have any of these cations as can be observed in Fig. 7.13. This suggests that when these cations are present in the M1 position, they can balance the ionic charges but it should not be enough.

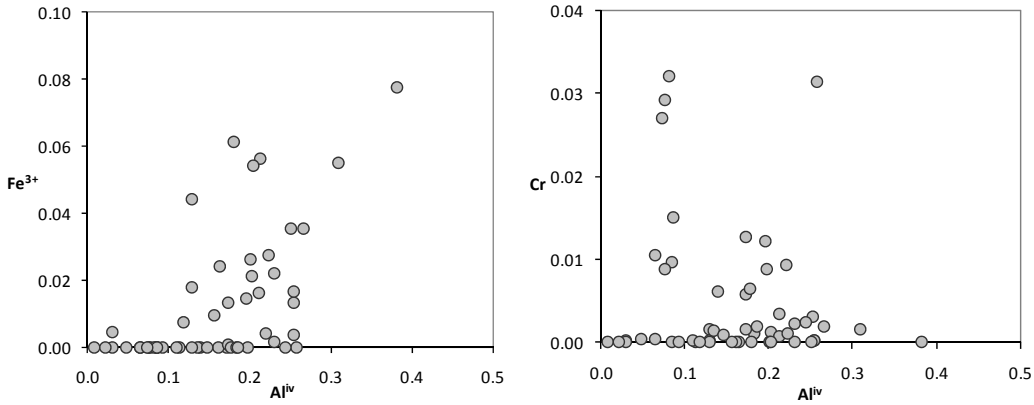

Fig. 7.13 – Diagram showing the lack of correlation between Al^{iv} and Fe^{3+} and Cr. It is of notice that the two cations present very low compositions or are absent of these pyroxenes.

The other cation available is Na that has, in the present analysis, a concentration ranging between 0.25 and 0.76%. Sodium occupies the octahedral position (M2) and could help to compensate the entrance of Al into the tetrahedral position. When this cation is considered as in the diagram of Fig. 7.14, it is obtained a good correlation for all the pyroxenes. This correlation points to Na as the cation balancing the chemical formula of the pyroxenes when the M1 position is occupied by Al^{vi}+Ti+Fe^{3+}+Cr.

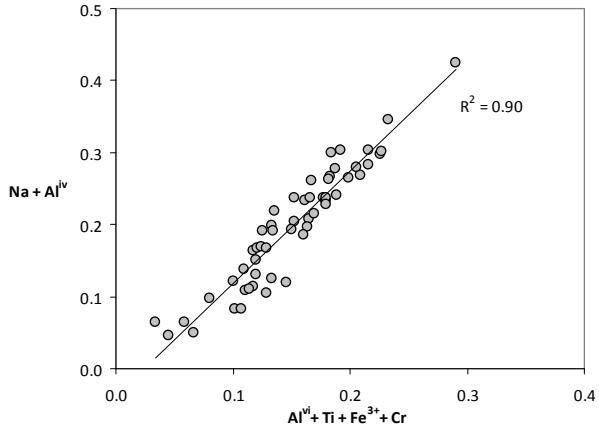

Fig. 7.14 – Diagram showing the relation of the cations Al^{vi}+Ti+Fe^{3+}+Cr, which occupy the position M1 in the structure of the pyroxenes and the sum of Na+ Al^{iv}.

7.3.2 Pyroxene Characterization on São Jorge Lavas

The composition of the pyroxenes of São Jorge Island is detailed here, in order to characterize the composition of this mineral in the lava groups, i.e. Fajã de São João lava sequence, Topo, Rosais and Manadas volcanic complexes, with exception of the pillow lavas, which don't have pyroxene. In Fig. 7.15, the pyroxenes of each lavas group are presented in the ternary diagram accordingly with their Wo-En-Fs content.

The most distinctive compositions are observed on the pyroxenes from Fajã de São João lava sequence (Fig. 7.15a) that develop a trend with increasing amount of the ferrosilite molecule. The average higher FeO concentrations found on the core of these pyroxenes (FeO = 13.11%), when compared with the other lava groups, shows that São João has twice the amount of FeO (Table 7.5). The high FeO concentrations and the increase in the Fs molecule produces the composition to trend toward the hedenbergite field, which is associated with lower temperature of crystallization of pyroxene (Deer *et al.*, 1992).

The pyroxenes of the volcanic complexes, Topo, Rosais and Manadas present similar characteristics, which are similar with compositions plotting in the diopside-augite fields. Nonetheless, the pyroxenes from Topo Volcanic Complex (Fig. 7.15b) display a wider compositional variability (Wo=46±2, En=41±5 and Fs=13±4) when compared to Rosais (Fig. 7.15c), which composition is less dispersed (Wo=45±1, En=43±2 and Fs=12±2). The pyroxenes on Manadas Volcanic Complex (Fig. 7.15d) are similar to the ones from Topo and Rosais but present a trend that continuously crosses the diopside field and enters the augite compositional field.

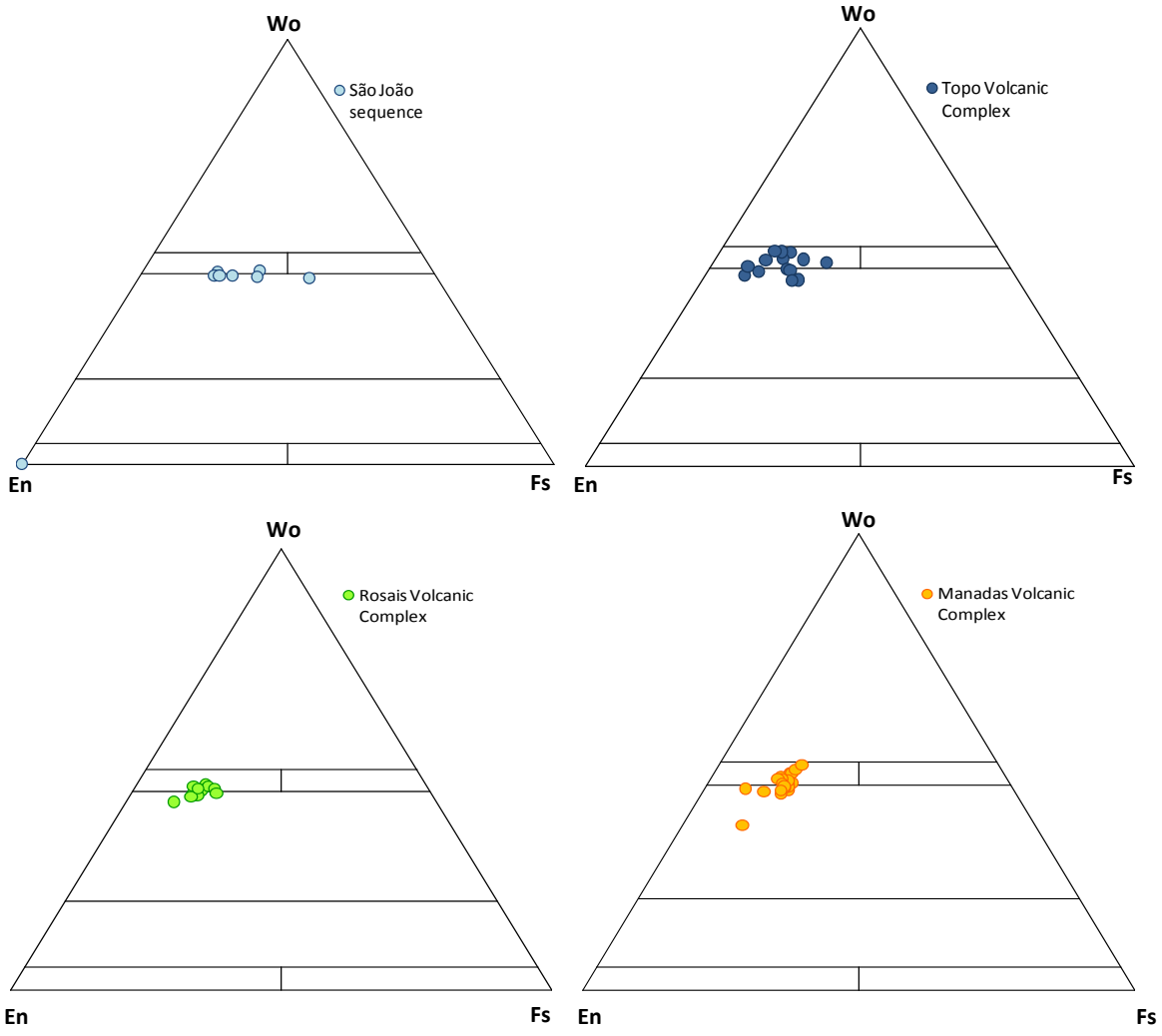

Fig. 7.15 – Projection of the analyzed pyroxenes in the triangular diagram En-Wo-Fs. The compositions fields are the same as in Fig. 7.9. In diagram are represented the pyroxenes from Fajã de São João lava sequence, from Topo Volcanic Complex, from Rosais and Manadas volcanic complex.

The composition of pyroxene cores in terms of oxides is presented in Table 7.5. The comparison between the three volcanic complexes does show important dissimilarities, even so, Topo has the highest Mg#, Cr_2O_3, and CaO content, Manadas has the lowest Mg# but the highest Fe_2O_3, MnO and TiO_2 and Rosais presents the highest K_2O contents. The most important differences are observed when the three complexes are compared with the pyroxenes from Fajã de São João. These pyroxenes are characterized by higher SiO_2 and MnO concentrations and much lower TiO_2, Al_2O_3, Cr_2O_3 and MgO (Mg#) suggesting that these crystals could have fractionated from a more evolved magmatic liquid (Table 7.5).

Table 7.5 – Average oxide composition obtained from the cores of the pyroxenes of each lava group. The pyroxenes analyzed on Fajã de São João lava sequence present a distinct composition from the rest of the island. Mg# = Mg^{2+} * (Mg^{2+} + Fe^{2+}).

Concentration (%)	SiO_2	TiO_2	Al_2O_3	Cr_2O_3	FeO	Fe_2O_3	MnO	MgO	CaO	Na_2O	K_2O	Mg#
Fajã de São João seq.	51.6	0.66	1.19	0.002	13.11	0.16	0.55	10.96	20.72	0.46	0.012	59%
Topo Volcanic Complex	50.0	1.85	4.89	0.395	5.79	0.10	0.10	14.36	21.01	0.52	0.007	81%
Rosais Volcanic Complex	49.0	1.82	6.52	0.220	6.35	0.10	0.14	14.18	20.06	0.53	0.018	80%
Manadas Volcanic Complex	48.8	1.93	6.04	0.170	6.92	0.58	0.15	13.74	19.83	0.61	0.009	78%

According with Wass (1979), the entrance of Al to the octahedral position (Al^{vi}) is usually related with the pressure conditions in which the pyroxene fractionate, where the higher pressures produce an increase in the Al^{vi}/Al^{iv} ratio. The limit between the high and low pressures (P) is defined by the Al^{vi}/Al^{iv} ratio (=0.25) and as can be observed in Fig. 7.16, most of the pyroxenes analyzed point to fractionation at high pressure.

In general, the fractionation at high pressures is more evident for the core of the crystals (Fig. 7.16), where most of the analysis plot above the Al^{vi}/Al^{iv} = 0.25 line, while the rim of the pyroxenes and the small microphenocrysts of the matrix present (Fig. 7.16) slightly lower Al^{vi}/Al^{iv} ratios. These differences indicate a pressure reduction toward the latter stages of fractionation; however, this pressure reduction is small and suggests that the pyroxenes fractionated earlier than any residence time at shallow levels before erupting.

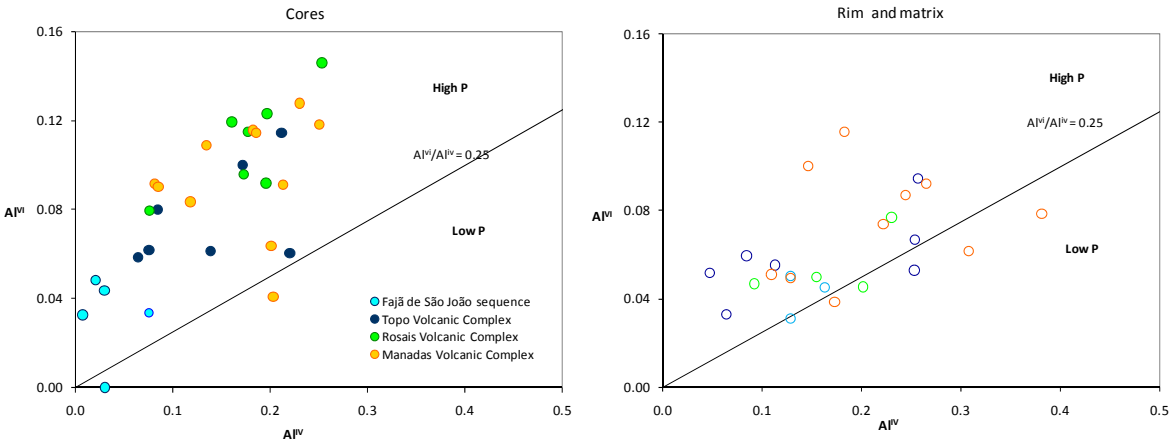

Fig. 7.16 – Diagrams with the Al^{vi} vs. Al^{iv} concentrations of the core, rims and matrix of the four lava groups. The line defined by Wass (1979) is plotted in both diagrams and separates the high and low pressures (P) fields (Al^{vi}/Al^{iv}=0.25). The majority of the pyroxenes analyzed plot above the line on the high P field.

Despite this, in some crystals the conditions in which fractionation occurs, seems to be more complex as observed in several crystals profiles (Fig. 7.17). The Al^{vi}/Al^{iv} ratios increase of from the core towards an intermediate point in the crystal (core-rim) and then its decrease towards the rim, points to a polibaric fractionation of these minerals.

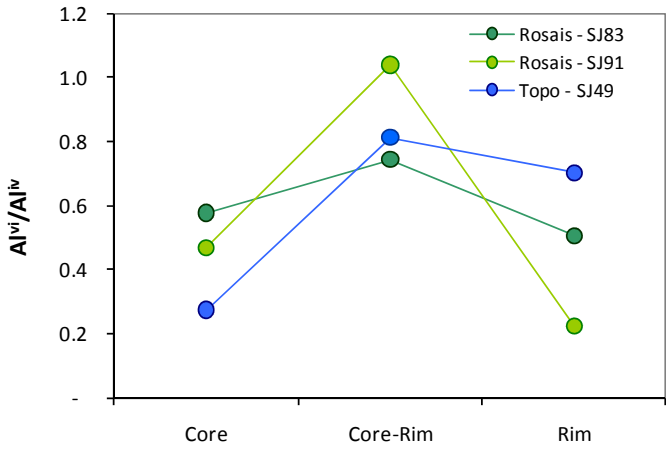

Fig. 7.17 – Diagram showing the core-rim variation in Al^{vi}/Al^{iv} of three different pyroxenes. The three crystals in the intermediate zone between the core and the rim have higher Al^{vi}/Al^{iv} suggesting an increase in pressure during the fractionation of the crystal.

7.3.3 Pyroxene/Liquid Equilibrium Pressure and Temperature

During crystallization processes, pressure and temperature conditions can be estimated using the pyroxenes as geothermobarometers. The method developed by Putirka *et al.* (1996, 2003) considers the pyroxenes and the magmatic liquids that are in equilibrium and follow the condition $K_{DFe/Mg}^{cpx/liq} = 0.27^{(+0.03)}_{(-0.05)}$ to enter the calculations[10]. The equations used for the geothermobarometers were obtained from Putirka *et al.* (2003) and are:

$$\frac{10^4}{T(K)} = 4.6 - 4.37\times10^{-1}\ln\left[\frac{\left[Jd^{cpx}Ca^{liq}Fm^{liq}\right]}{\left[DiHd^{cpx}Na^{liq}Al^{liq}\right]}\right] - 6.54\times10^{-1}\ln\left[Mg^{liq}\right]$$

(Eq. 7.6)

$$-3.26\times10^{-1}\ln\left[Na^{liq}\right] - 6.32\times10^{-3}\left[P(Kbar)\right] - 0.92\ln\left[Si^{liq}\right] + 2.74\times10^{-1}\ln\left[Jd^{cpx}\right]$$

and

$$P(Kbar) = -88.3 + 2.82\times10^{-3}T(K)\ln\left[\frac{\left[Jd^{cpx}Ca^{liq}Fm^{liq}\right]}{\left[Na^{liq}Al^{liq}\left(Si^{liq}\right)^2\right]}\right] + 2.19\times10^{-2}T(K)$$

(Eq. 7.7)

$$-25.1\ln\left[Ca^{liq}Si^{liq}\right] + 7.03\left[Mg^{liq}\right] + 12.4\ln\left[Ca^{liq}\right]$$

From the pyroxenes analyzed, only eight analysis on the phenocryst cores are within the interval 0.22> $K_{DFe/Mg}^{cpx/liq}$ >0.30 and therefore are considered to be in equilibrium with the host magma. The results obtained from the latest model of Putirka *et al.* (2003), which considers hydrated and SiO_2-rich magmatic liquids, are presented in Table 7.6.

[10] Pressure, Temperature and $K_{DFe/Mg}^{cpx/liq}$ where calculated using the excel spreadsheet http://www.csufresno.edu/geology/Faculty&Staff/Putirka/Keith_Putirka.html#download

Table 7.6 – In this table is presented the estimated temperature and pressure of crystallization for the pair pyroxene-liquid believed to be in equilibrium ($0.22 > K_{DFe/Mg}^{cpx/liq} > 0.30$). The temperatures obtained for the pyroxenes cores can be compared with the temperature results for the olivines in the same lavas.

		T (°C) Putirka *et al.* (2003)	P (kbar) Putirka et al. (2003)	Depth (km)	T_{oliv} (°C)
SJ8	0,28	1117	4,5	15,3	
SJ18	0,25	1002	5,4	18,4	
SJ49	0,27	1183	9,6	32,7	1160
SJ55	0,25	1183	10,6	36,1	1160
SJ83	0,29	1189	9,9	33,7	1124
SJ91-core	0,27	1193	10	34,0	1158
SJ91-middle	0,24	1184	9,1	31,0	1158
SJ91-rim	0,26	1182	9,3	31,6	1158

The pressure and temperature conditions estimated show clearly that pyroxenes and the magmatic liquids of lavas SJ8 and SJ18, both from Fajã de São João lava sequence, are considerable lower and occurred at relatively shallow depth. In fact, the estimated 15.3 and 18.4 km are just below the mantle-crust limit, predicted to be at approximately 14 km depth beneath the Azores Plateau (Escartín *et al.*, 2001). As previously mentioned, the core-rim composition of the pyroxenes in terms of Al^{vi}/Al^{iv} ratios points to a polibaric fractionation of this mineral, suggesting that this mineral formed at the base of the crust, continued to fractionate as the magma ascended to shallower crustal levels.

The fractionation at lower temperatures of Fajã de São João pyroxenes, when compared with the other pyroxene, emphasizes the chemical results obtained, where the pyroxenes from Fajã de São João presented higher Fs content, which is associated with lower temperature of crystallization.

The other results, from Topo (SJ49 and SJ55) and Rosais (SJ83 and SJ91) reveal that the pyroxenes and the magmatic liquids were in equilibrium at higher pressures and temperatures. However, both parameters are within small intervals (P = 9.1 - 10.6 Kbar and T = 1182-1193 °C) suggesting that during the construction of the volcanic complexes pressure and temperature conditions were maintained. It is also important to notice, that the estimated olivine temperatures for these magmas are slightly lower that to the clinopyroxene-liquid pair.

In lava SJ91, it was found three pyroxene-liquid equilibriums with small variations on pressure and temperature conditions. These small variations point to fractionations of the pyroxenes as they ascend for almost 3 km, emphasizing again the polibaric fractionation of this mineral as already suggested by the chemical composition.

7.4 Oxides

The lavas from São Jorge Island are also characterized by the presence of opaque minerals, which revealed to be Fe-Ti rich oxides. The presence of opaque minerals in these lavas as a well-developed mineral phase is not as frequent as their presence in the matrix or as inclusions in olivine, pyroxene and plagioclase phenocrysts. In addition, the Fe-Ti oxides were observed on two phaneritic nodules, in lavas from Manadas Volcanic Complex, and in one of the cases is associated with amphibole phenocrysts forming a reaction corona.

The chemical analyses of the opaque minerals unveils that two different types of oxides can coexist in the lavas. The most abundant belong to the spinel group (*s.l.*) and are titanomagnetites, cromites and magnetite (only one analysis), and the remaining are ilmenites. These mineral species can be distinguished by the concentration in some elements and, in this specific case, the Fe-Ti oxides of São Jorge are characterized by the concentrations presented in Table 7.7 and in APPENDIX II.D1 and APPENDIX II.D2.

Table 7.7 – In this table is presented the compositional range of the most important elements forming the four mineral species analyzed for the present study. The predominance of the titanomagnetites over the other oxide mineral is reveal by the 22 analyses obtained.

		Titanomagnetite	Cromite	Magnetite	Ilmenite
	nº analysis	22	4	1	7
Concentraion (%)	**TiO_2**	26-16	8-2	1.6	51-36
	Al_2O_3	10-1	20-13	1.7	<1
	FeO	52-35	26-15	27	41-20
	Fe_2O_3	32-16	16-8	65	36-5
	Cr_2O_3	< 5	45-19	0.5	< 0.2

The most distinctive features from Table 7.7 are the high FeO and TiO_2 contents of the titanomagnetites, when compared with the other spinels, and the high Al_2O_3 and Cr_2O_3 of the cromites. The ilmenites are also enriched in FeO and TiO_2 but have almost absent Al_2O_3 and Cr_2O_3 when compared with the spinels.

The general formula of the spinels is AB_2O_4 where the A position is occupied by cations with tetrahedral coordination and the B position by cations with octahedral coordination (Deer *et al.*, 1992). The predominance of cations in the A and B positions allows dividing the oxides into three major series, the spinel (Al^{3+}), magnetite (Fe^{3+}) and the cromite series (Cr^{4+}). The substitution of cations in each series can occur between pure end-members generating a variety of solid solutions as can be seen in terms of the system FeO-Fe_2O_3-TiO_2, which show the major solid solutions of the series Magnetite-Ulvöspinel and Hematite-Ilmenite (Fig. 7.18). For Magnetite-Ulvöspinel solid solution considerable amounts of Ti^{4+} substitute the Fe^{3+} of the magnetite until the end-member (Fe_2TiO_4) is reached, while for cromite ($FeCr_2O_4$) the B position is occupied essentially by Cr^{4+}. (Deer *et al.*, 1992)

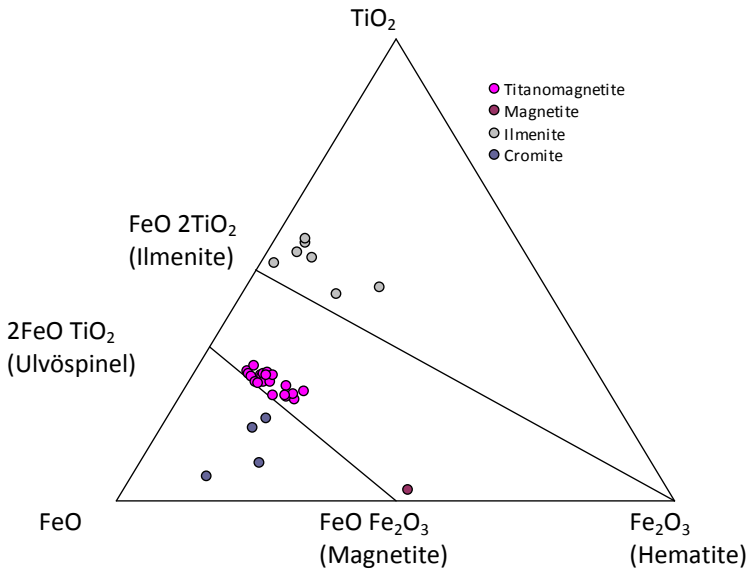

Fig. 7.18 – Triangular diagram showing the system FeO-Fe_2O_3-TiO_2 and the solid solutions series Magnetite-Ulvöspinel and Hematite-Ilmenite (adapted from Deer *et al.*, 1992). The compositional variability of the oxide minerals analyzed in São Jorge is dominated by the titanomagnetites as presented in the diagram.

In Fig. 7.18, the oxides minerals analyzed in São Jorge lavas plot along the mentioned solid-solutions with the cromites trending towards relative enriched FeO compositions. The relation between a certain type of oxide and their abundance in a particular lava group, it could not be

established. One of the reasons should be the lack of more analytical data that would allow a statistical approach. In addition, the predominance of the titanomagnetites, its frequent coexistence with other oxide minerals and their presence in any textural environment does not permit a characterization of the oxides inside each lava group.

The diagram of Fig. 7.19 illustrates the relation of the Al^{3+}, Fe^{3+} and Cr^{3+} cations, which define the spinels series. The analyzed oxides evidence the enrichment in Cr of the cromites relative to the other minerals and the dispersion of the titanomagnetites along the Al-Fe^{3+} axis.

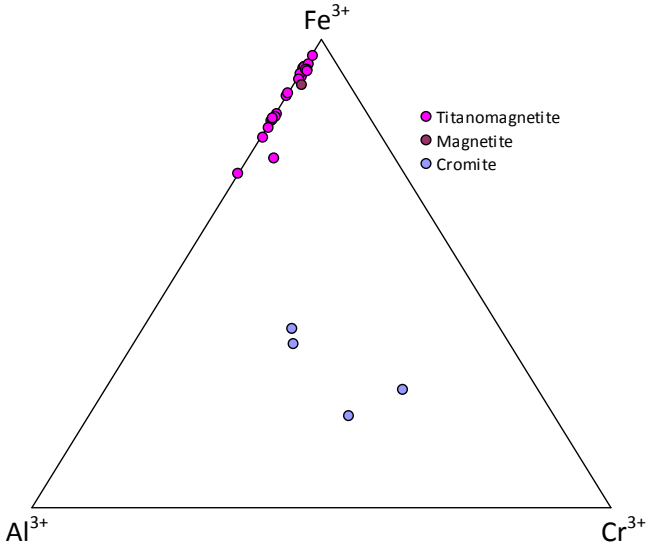

Fig. 7.19 – Ternary diagram showing the relationship between Al^{3+}, Fe^{3+} and Cr^{3+} (a.f.u.) of the spinels of São Jorge.

7.4.1 Oxygen Fugacity and Temperature Conditions for the Pair Ilmenite-Spinel

In four lavas it was found that spinel and ilmenite coexist. These two minerals are commonly used to characterize the oxidation state of the magmas or oxygen fugacity (fO_2). The oxygen fugacity modeling program named QUILF, from Andersen *et al.* (1993), was used to determine the temperature and fO_2 based on the composition of both minerals. The results are presented in Table 7.8 and in Fig. 7.20 . Two of the basalts, SJ29 from Rosais Volcanic Complexes and SJ32 from Manadas Volcanic Complex, have relative low fO_2. The first plots below and above the NNO

buffer curve, while the second is located between the NNO and FMQ buffer[11]. The lowest fO_2 was determined on a tefritic lava from Topo Volcanic Complex. Considering the age of the volcanic complexes the diagram of Fig. 7.20 show a progressive decrease in fO_2. The result of the analysis of the oxides in lava SJ91 was obtained on a single large phenocrysts, which petrographically suggests a solid solution transformation at low temperature, thus justifying the high oxidizing conditions and low temperature determined.

Table 7.8 – Temperature and fO_2 values determined for the Spinel-Ilmenite pair using QUILF program from Andersen *et al.* (1993)

	SJ29	SJ32	SJ55	SJ91
T°C	924	1023	830	634
log fO_2	-12.29	-9.76	-15.49	-14.13

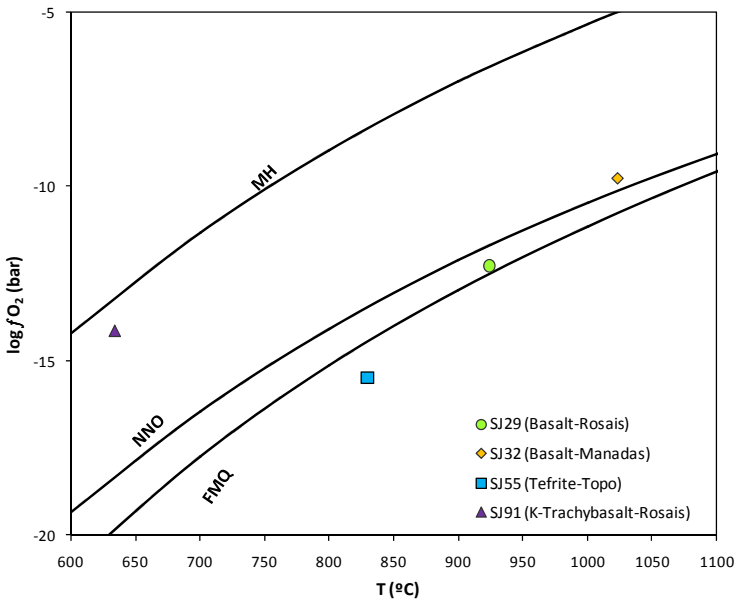

Fig. 7.20 – Log fO_2 versus temperature (ºC) for São Jorge lavas. The oxygen buffer was obtained from Eugster & Wones (1962). MN is the Magnetite-Hematite buffer, NNO is the Nickel-Nickel Oxide buffer and the FMQ is the Fayalite-Magnetite-Quartz buffer.

[11] The NNO buffer was determined by $\log \int O_2 = 8.94 - \frac{24709}{T}$ while for the FMQ buffer it was used the equation $\log \int O_2 = 10.30 - \frac{27300}{T}$

The temperatures obtained for ilmenite-spinel equilibrium are considerable lower than the temperatures obtained for the pair olivine-liquid and pyroxene-liquid in the same lavas. This can be justified by the fact that the Fe-Ti oxides analyzed correspond to small matrix crystals that should have fractionate in latter crystallization stages at lower temperatures.

7.5 Amphibole

The petrographic observation of the lavas from Manadas Volcanic Complex identified the presence of amphiboles with optic characteristics of kaersutite. In two of the lavas, amphibole was on the phenocryst phase and was surrounded by a corona of titanomagnetite, while on the third case amphibole was found on a phaneritic nodule associated with pyroxene.

The analysis performed in minerals, of one hawaiitic lava and on the nodule, presented characteristics of tschermakitic amphiboles, which belong to the hornblende family (see APPENDIXII.E). The tschemarkite-ferrotschemarkite amphiboles have a general formula (Ca_2[Mg, Fe]$_4Al_2[Si_6Al_2O_{22}](OH)_2$) in which the continuous substitution of AlAl↔Si(Fe, Mg) takes place between the two end-members. As can be seen in Fig. 7.21, the amphiboles analyzed have Mg# ranging between 64 and 70% and Si cations around 6 (a.f.u.). However, these amphiboles have a high TiO_2 content, which is in average 5.6±0.2 and is typical of the kaersutites.

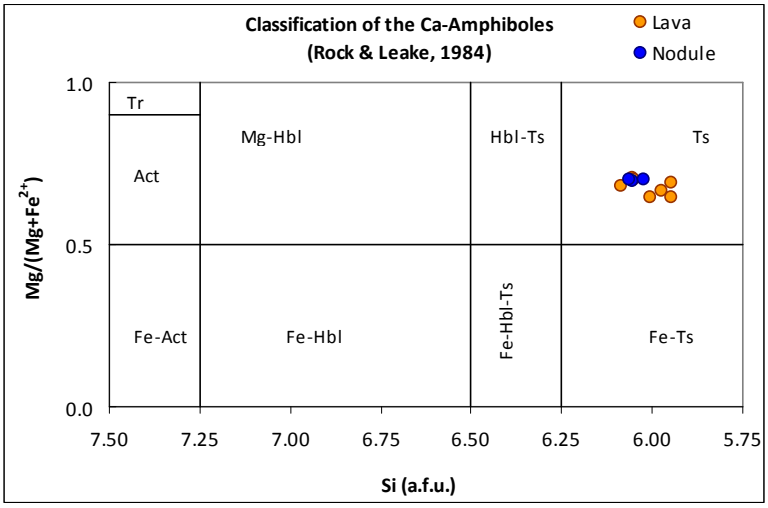

Fig. 7.21 – Diagram with the classification fields of the Ca-amphiboles defined by Rock & Leake (1984). The amphiboles analyzed in Manadas lava and nodule present similar compositions

Another important characteristic of these amphiboles is that they do not present any compositional zoning between the core and rim of the crystals, and in this sense contrasting with the pyroxenes where important chemical variations where observed.

Chapter 8: Geochemical Characterization of São Jorge Volcanism

8.1 Introduction

In this chapter is presented new major and trace element data of São Jorge Island. This data was obtained on lavas from the three main volcanic complexes, Topo, Rosais and Manadas, on lavas from Fajã de São João sequence and on the submarine pillow lavas, recovered on São Jorge southeast flank during EMEPC\Açores\G3\2007 cruise.

A general analysis of the geochemical data will allow characterizing the rocks outcropping in São Jorge and the magmatic process involved in their origin. At the same time, a more detail examination of the geochemical data will allow a finer characterization of each lava group, individualizing chemical and/or temporal variations in magmatic process. The geochemical data used in this chapter are documented in APPENDIX I.

A special focus is given to the geochemical characterization and to the petrogenetic processes involved in the generation of the lavas from Fajã de São João. This lava sequence, until recently, was considered a part of Topo Volcanic Complex but the geochronological data from Hildebrand *et al*. (2008) and from this study shows that is much older. In addition, the lavas from Fajã de São João show distinct characteristics that were detected during fieldwork, from petrography and from mineral chemistry. Therefore, when considered necessary, the characterization of this lava sequence will be treated separately.

8.2 The Evaluation of the Geochemical Data

Despite the exclusion of several samples from whole rock analysis due to alteration, as mentioned in chapter 4, a major concern was to exclude samples that reveal signs of alteration on the geochemical analysis, thus masking the composition of the lavas.

From geochemical data, it is also possible to verify the occurrence of alteration process, mainly in the chemical elements that are more sensitive to weathering processes, as for instance K_2O. In this sense, is expected a decrease in K_2O/P_2O_5 ratios in weathered lavas, because alteration removes K_2O from the lavas. As well, "loss on ignition" (LoI) values is expected to increase with alteration due to the incorporation of water into the rocks.

The diagram in Fig. 8.1, does not displays a negative correlation trend between K_2O/P_2O_5 and LoI, confirming the freshness of São Jorge lavas. Nonetheless, two lavas from Fajã de São João lava sequence plot outside the range of the remaining lavas. These are lava SJ19, which is a plagioclase-bearing basalt, and lava SJ18, which is the most evolved lava in São Jorge with high K_2O content.

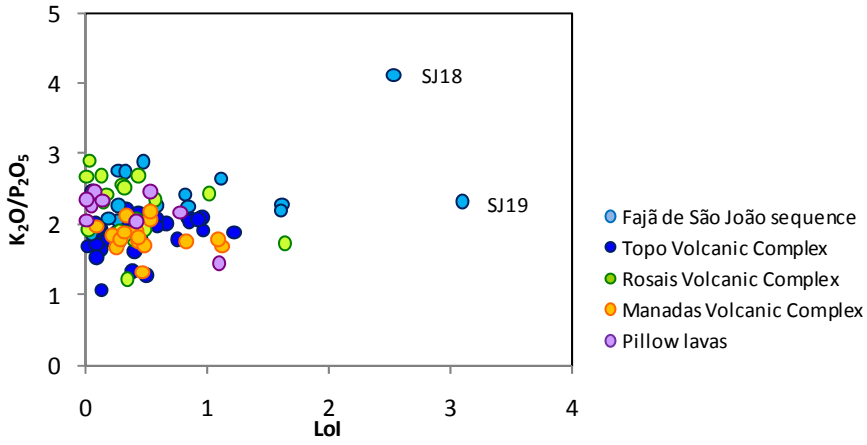

Fig. 8.1 – LoI vs. K_2O/P_2O_5 diagram for São Jorge lavas. During alteration processes, it is expected that lavas loose K_2O and gain LoI. The observed correlation between K_2O/P_2O_5 and LoI points to the freshness of São Jorge lavas.

Mineral accumulation during crystal fractionation process is another factor that affects the geochemical composition of lavas and their interpretation. Most of São Jorge lavas exhibit porphyric textures with olivine, pyroxene and plagioclase phenocrysts, however, some lavas from Fajã de São João lava sequence present highly porphyric textures with massive plagioclase, suggesting accumulation of this mineral (see chapter III). Eu and Sr are two trace elements

compatible with plagioclase, thus the geochemical analyses of these plagioclase cumulates should have a positive Eu anomaly, expressed as Eu/Eu* ($Eu/Eu^{*} = Eu_n / \sqrt{Sm_n \times Gd_n}$), and should correlate positively with Sr/Nd ratio.

From the diagram in Fig. 8.2, only the lavas from Fajã de São João lava sequence exhibit a positive trend with four samples presenting high Sr/Nd ratios and Eu/Eu* values, evidencing plagioclase accumulation. These lavas, with plagioclase accumulation, present geochemical characteristics that are distinct to the common lavas, bearing interesting interpretations. Thus, the characterization of these lavas and of Fajã de São João lava sequence will be given a special attention.

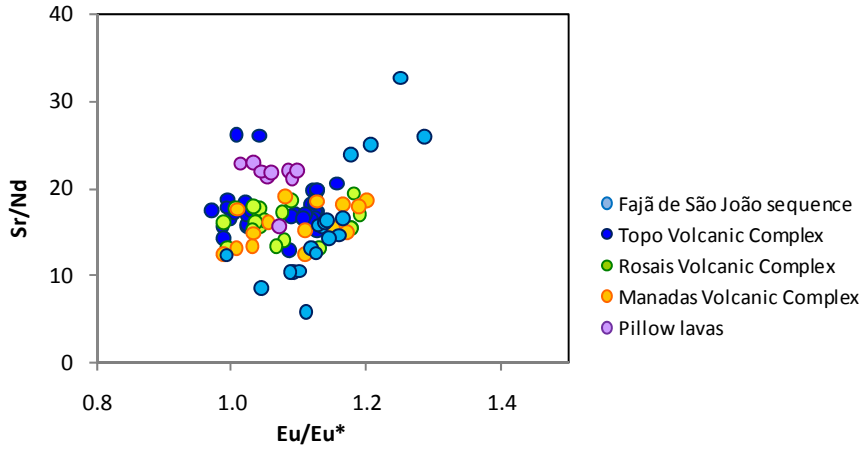

Fig. 8.2 – Eu/Eu* vs. Sr/Nd diagram for all lavas from São Jorge. The lavas from Fajã de São João exhibit a positive correlation for those element ratios and the high are the Eu/Eu* vs. Sr/Nd ratios corresponds to the lavas with higher plagioclase content, evidencing coherency with the petrographic observations.

8.3 Major Element Geochemical Characterization of São Jorge Lavas

The classification diagram from IUGS[12] (TAS), displayed in Fig. 8.3, reveals that São Jorge lavas are sub-saturated, with SiO_2 content ranging between 43.7 and 54.0%, and are alkaline, plotting

[12] International Union of Geological Sciences

above the alkaline line defined by MacDonald (1968 *in* Rollinson, 1993), with alkalis content (Na_2O + K_2O) in the interval 2.67 to 7.24%.

The lavas from São Jorge mainland present compositions that vary between the basanite/tefrite and the basaltic trachyandesite, even though there is a predominance of basaltic lithotypes. The lavas recovered in São Jorge southeast submarine flank plot in the basaltic field, exhibiting very homogenous chemical composition, accompanying the narrow variability found in São Jorge. The lavas from Fajã de São João sequence although alkaline have, in some cases, less alkalis content for a given SiO_2 content when compared with lavas from the other volcanic complexes. Several lavas from this group plot on the basaltic trachyandesites field showing more evolved compositions that the remaining lavas of the island.

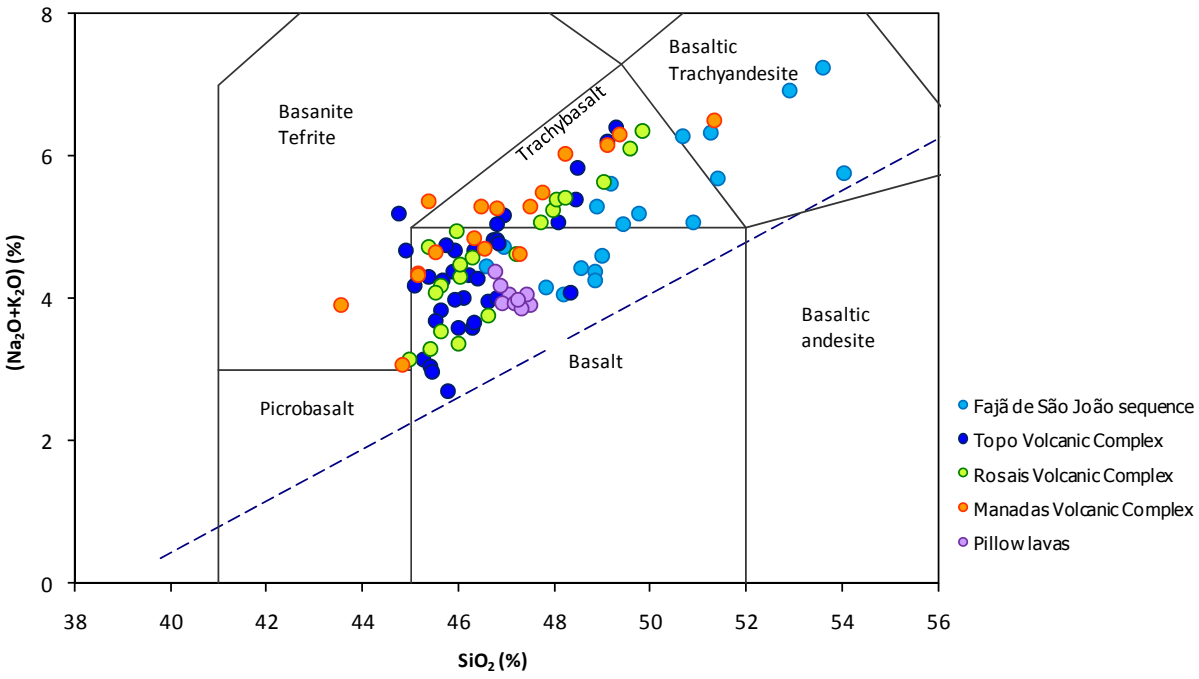

Fig. 8.3 – São Jorge lavas from mainland and from the offshore are plotted in the classificative TAS diagram. The lavas plot above the alkaline line (dash blue) defined by MacDonald (1968) evidencing their alkaline affinity. Rock classification is present in the diagram but it is necessary to consider criterions of sub-classification for each field: Tefrite has MgO lower than 8% while the basanites present MgO higher than 8%. The trachybasalts are divided into Hawaiites when Na_2O-2>K_2O or into K-trachybasalts if Na_2O-2<K_2O. Using the same criteria, basaltic trachyandesites can be divided into mugearites with low K_2O or shoshonites with higher K_2O.

In the Azores archipelago context, as previously mentioned in chapter, the lavas outcropping in the islands are essentially basaltic but it is common to find more evolved compositions, as for

instance, trachyandesites in Pico Island (França, 2000), trachytes and ryolites in Terceira and trachytes in São Miguel (e.g. Schmincke & Weibel, 1972). The mentioned islands have one or more central volcanoes contrasting with São Jorge, which has formed mainly by fissural volcanism. The narrow lithological variability found in São Jorge could be related with this, since it reflects the regional volcano-tectonic conditions triggering magmatic activity and the time required of residence of the magmas before erupting.

Major element concentrations as K_2O and SiO_2, in most lavas with SiO_2<48% from Rosais and Manadas volcanic complexes are enriched in K_2O when compared with lavas from Topo Volcanic Complex and the pillow lavas, which contain K_2O lower than 1%. Fajã de São João volcanic sequence displays a different composition with high potassium concentrations for the most evolved rocks (Fig. 8.4A), but when compared with Rosais and Manadas, is depleted in K_2O for a given SiO_2 content.

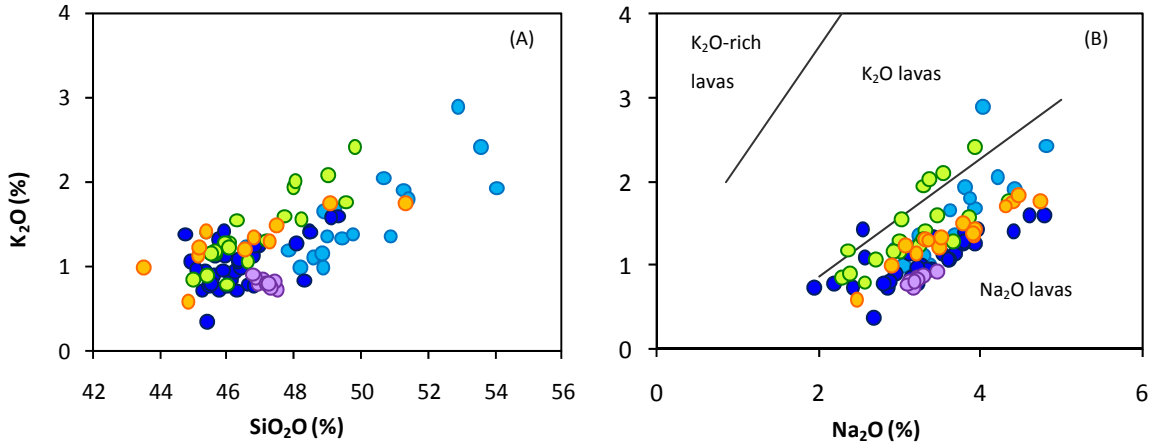

Fig. 8.4– (A) SiO_2 vs. K_2O diagram evidencing the increase in K_2O concentrations with the degree of evolution for São Jorge lavas. Rosais lavas are relatively enriched in potassium for a given SiO_2 concentration. (B) Diagram comparing Na_2O and K_2O concentrations in São Jorge revealing the sodic character of the majority of the lavas. Symbols as in Fig. 8.3.

The sodic nature of São Jorge volcanism is displayed in the Na_2O vs. K_2O diagram (Fig. 8.4(B)) with most of the samples plotting in the Na_2O field. However, some samples have somewhat K-enriched compositions, as found in five lavas from Rosais complex, one lava from Fajã de São João and another one from Topo.

All lavas from São Jorge are represented in the Yoder & Tilley (1962) normative diagram presented in Fig. 8.5 (*from* Best & Christiansen, 2001). Almost all normative compositions[13] plot in the alkaline basalt field however a small tendency for saturation is given by few samples from Rosais and Manadas that plot on the edge of olivine tholeiite field.

The lavas from Fajã de São João lava sequence are clearly distinguished from the rest of lavas, plotting mainly in the alkaline and olivine tholeiite fields, but two of the samples plot on the quartz tholeiite field exhibiting a strong tendency towards normative quartz.

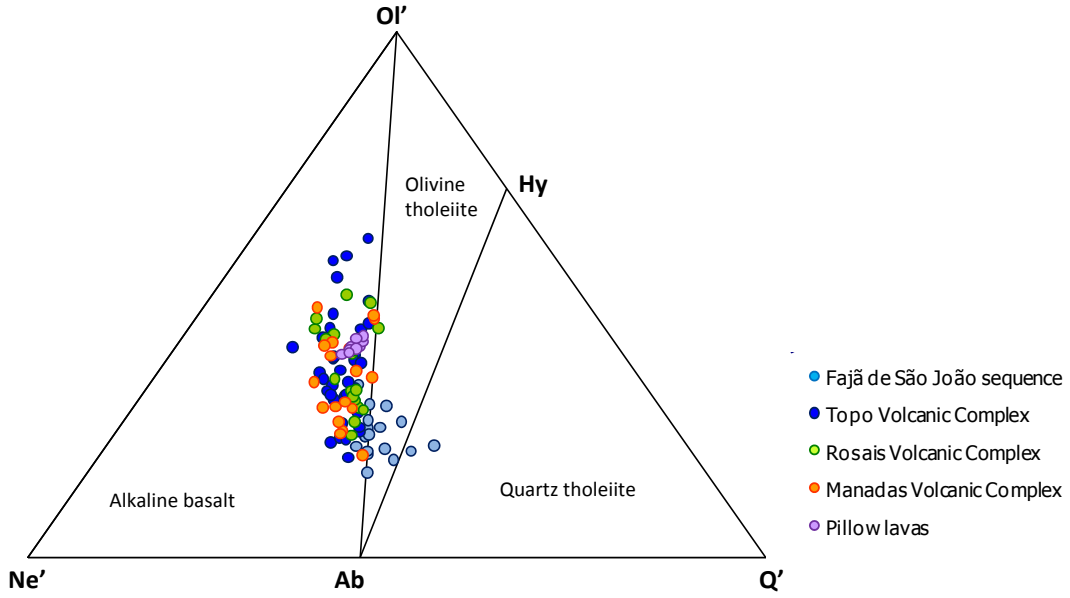

Fig. 8.5 – Normative composition for São Jorge lavas plotted in the base of Yoder & Tilley (1962) tetrahedron diagram (*in* Best & Christiansen, 2001). Most of São Jorge lavas plot in the alkaline basalt area with only two lavas located at the edge of the olivine tholeiite field. The lavas from Fajã de São João sequence exhibit a different behavior and plot also in the olivine tholeiite and quartz tholeiite fields The apices of the triangles are adjusted to the normative minerals: Ol' = Ol+[0.714–(Fe/(Fe+Mg))*0.067]*Hy; Ne' = Ne+0.542*Ab; Q' = Q+0.4*Ab+0.25*Hy.

[13] The normative composition of a rock is the hypothetical mineral assemblage determined from the chemical composition of that rock. The norm calculation assumes that the magma is anhydrous and for certain minerals uses only compositional end-members of solid solutions. For norm calculations is very important the oxidation state of Fe because will have a strong effect on the result. Some Fe oxidation states have been recommended, e.g. Cox *et al.*, (1979) suggested oxidation state where $Fe_2O_3/FeO=0.15$, but here it was use iron ratios as proposed by Middlemost (1989) with standard values for different fields as in TAS diagram. Yoder & Tilley (1962), using normative minerals defined a classification tetrahedron for basaltic rocks (*in* Best & Christiansen, 2001). The normative minerals mentioned in this text are, nepheline (Ne), diopside (Di), olivine (Ol), hyperstene (Hy) and quartz (Q).

Olivine tholeiites are not common in Atlantic islands and in the Azores as demonstrated by Schmincke (1973) and White (1979), with exception of Terceira Island. In fact, Madureira (2006) has recently described olivine tholeiites in Terceira lavas, as resulting from a transitional behavior, which was also confirmed by trace element ratios such as Y/Nb. Nevertheless, this is not the case in these lavas since Y/Nb ratios are consistently lower than 1, what reinforces the alkaline nature of São Jorge volcanism.

In variation diagrams, it is common to use SiO_2 to characterize the variability of a rock suit in terms of major elements. However, because of the narrow range in SiO_2 in São Jorge (Fig. 8.3) MgO is used here as the reference oxide (Fig. 8.6).

In a general view, the variation diagrams for SiO_2, Na_2O and mainly Al_2O_3, display overlapping trends for each complex following a single fractionation path suggesting a co-magmatic origin. However, this idea seems to be contradicted by the variation diagrams for K_2O, CaO and P_2O_5, where lavas for each volcanic complex exhibit distinct trends. As a matter of fact, if we consider all lavas with MgO = 6.0 ± 0.2%, the variation of P_2O_5 and K_2O concentrations between the lava groups suggest that lavas derived from magmatic liquids with different initial composition i.e. have a non-cogenetic origin.

Small distinctions can be observed between the trends delineated by Topo, Rosais and Manadas volcanic complexes. Topo Volcanic Complex characterized by having the widest MgO range, with the highest MgO concentrations in São Jorge (MgO=13.61%), the lower P_2O_5 and higher CaO concentrations for a given MgO, when compared to Rosais and Manadas volcanic complexes, and the highest FeO and TiO_2 concentrations on several lavas with MgO ≈ 6%.

The lavas from Rosais Volcanic Complex have globally higher K_2O concentrations, which are responsible by the presence of K-rich lithologies as the K-trachybasalts, while lavas from Manadas Volcanic Complex present an intermediate composition between Topo and Rosais. The submarine pillow lavas, recovered in São Jorge southeast flank, overprint the composition of Topo Volcanic Complex, but show slight differences as higher SiO_2 and lower TiO_2, CaO and P_2O_5.

The most distinct compositions observed in Fig. 8.6 correspond to the lavas from Fajã de São João sequence, which has the lower MgO concentrations. Most of the lavas follow the same trend as the other lava groups, but several samples present for MgO contents lower than 5%, anomalous

compositions, as the concentrations in Al_2O_3, CaO and K_2O. These characteristic put to evidence the different geochemical behavior of the lavas from Fajã de São João lava sequence.

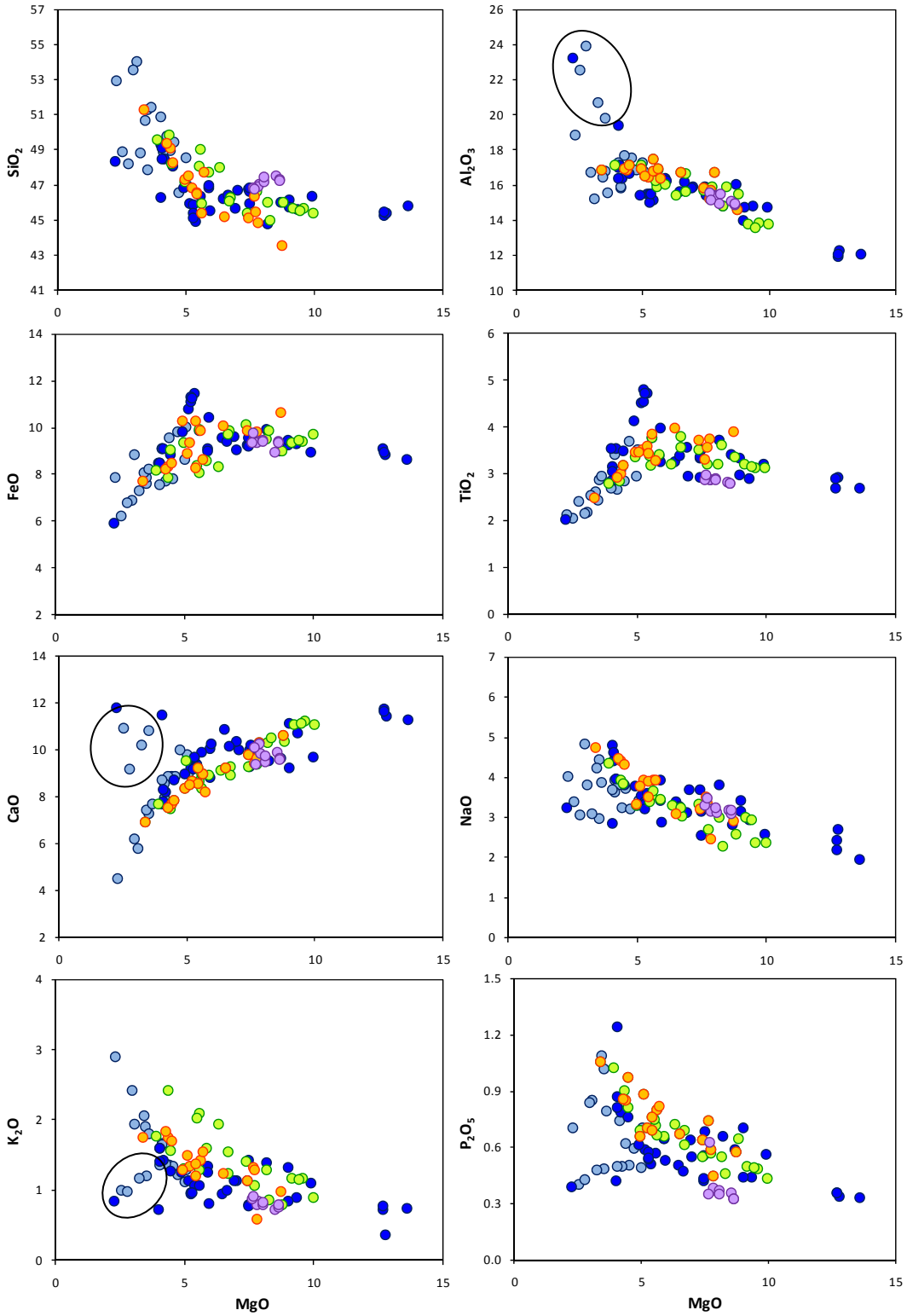

Fig. 8.6 – Major element composition from all lavas in São Jorge Island is presented in these Harker diagrams where MgO is used as the reference oxide. All oxides units are in percentage (%) and symbols are the same as in Fig. 8.5.

As can be depict from Fig. 8.6, MgO can be considered as an index of differentiation of the lavas, thus evidencing that differentiation processes as fractional crystallization, are in the origin of MgO spectrum.

8.4 Lithological Variability

The compositional fields from TAS diagram, such as the trachybasalts and basaltic trachyandesites, can be subdivided into sub-fields according with the relative concentration in Na_2O and K_2O. The sodic lithologies for the trachybasalts and basaltic trachyandesites are named hawaiites and mugearites, respectively, yet if the concentration in K_20 is such that $Na_2O\text{-}2<K_20$, then the lavas are named K-trachybasalts and K-basaltic trachyandesites. Other lithologies as the basanites and tefrites are distinguished by the MgO concentration, if MgO> 8% then the lava is a basanite and for lower MgO content the lava is a tefrite.

The lithologic diversity of the three main volcanic complexes, Topo, Rosais and Manadas, of Fajã de São João sequence and of the submarine pillow lavas is displayed in Fig. 8.7. Since each volcanic complex developed at different time intervals, the diagrams give an overview of how the lavas evolved during the early volcanic stages until the present.

Fajã de São João sequence, the oldest lava sequence in São Jorge, is located in the southeast coast of the island and has 42% of basaltic rocks. Several of these basalts, described in the petrography (chapter 6) and presented by Ribeiro *et al*. (2007), are extremely enriched in plagioclase and are classified as plagioclase-bearing basalts. The remaining lithologies, frequently with high K_2O concentration in the more evolved lavas, are trachybasalts (21% hawaiites and 5% K-trachybasalts) and basaltic trachyandesites (21% of mugearites and 11% of K-basaltic trachyandesites).

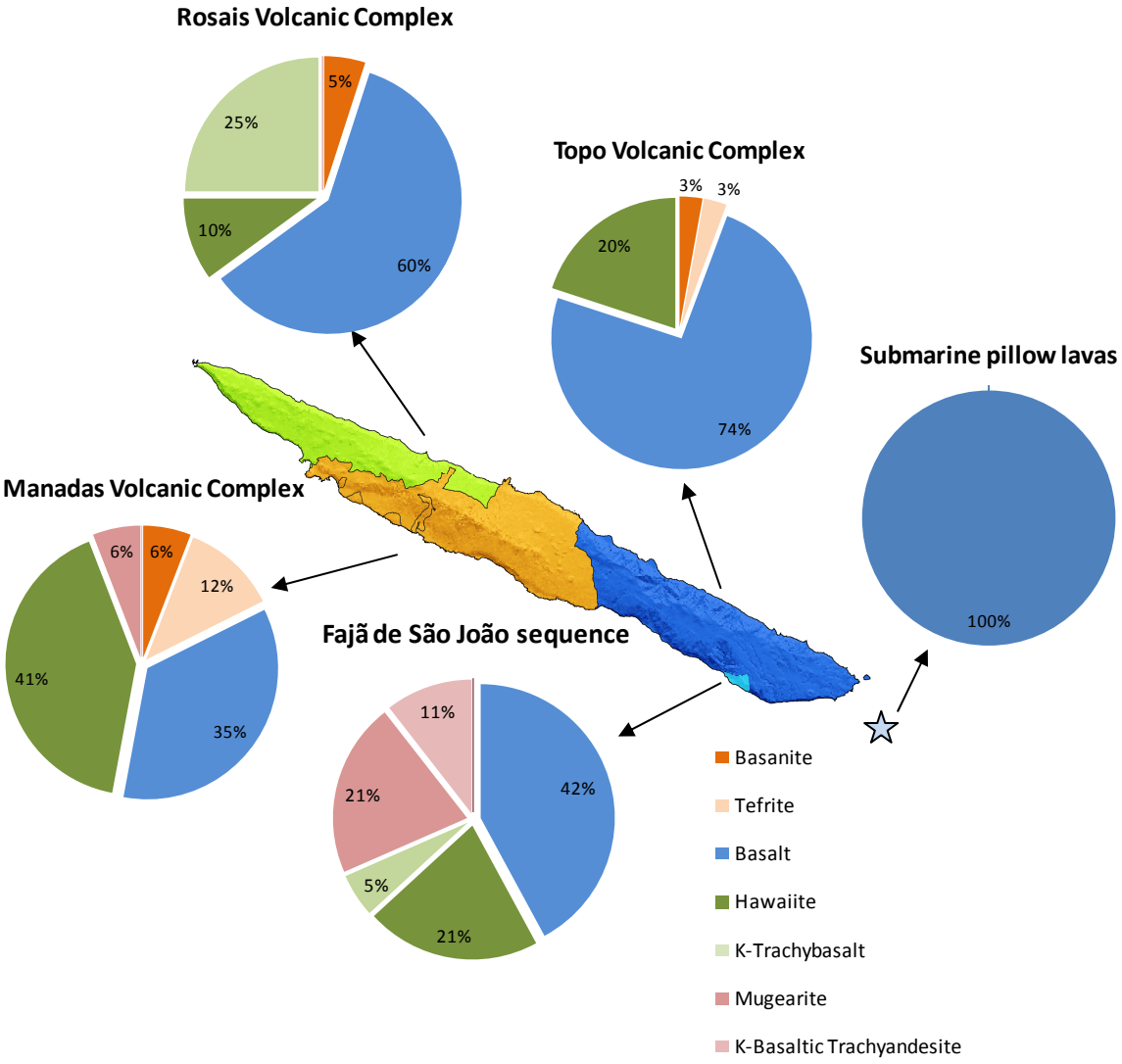

Fig. 8.7 – Lithological variability of São Jorge lavas for each volcanic complex/lava sequence. The classification is in accordance with TAS diagram presented in Fig. 8.3. It is of notice the predominance of basaltic lavas followed by the trachybasalts.

Topo Volcanic Complex is mainly formed by basalts (74%) followed by hawaiites (20%). The most under-saturated lavas, basanites and tefrites correspond only to 6% of the group. Towards the west in Rosais Volcanic Complex, there is a reduction in basalts (60%) relatively to Topo and an increase of the trachybasalts (35%). The particularity of this complex is that only 10 % of the trachybasalts are hawaiites, while the rest of the lavas have high K_2O concentrations, as expressed by the 25% of K-trachybasalts.

In the youngest volcanic complex, Manadas, K-rich lavas are absent contrasting with Rosais and Fajã de São João sequence. An important feature in Manadas Volcanic Complex is the decrease in basalts (35%) with the increase of more sub-saturated rocks as the basanites/tefrites (12%) and the presence of more evolved lavas represented by hawaiites (41%) and mugearites (6%).

The lithological variability of submarine lavas contrasts with the subaerial lavas in São Jorge because they present exclusively basaltic composition.

8.5 Geochemical Characterization of São Jorge using Trace Elements

Several chemical elements that are present in a geochemical analysis have concentrations lower than 0.01% (or less than 1000 ppm) and are classified as trace elements. The diversity of trace elements is greater than major elements and their behavior serve as powerful petrogenetic indicators during magmatic processes.

One of the key issues is the sensitivity of trace elements during magmatic processes, which can be divided into compatible and incompatible trace elements depending on the concentration ratio or partition coefficient of an element between the crystalline phase and the melt. The partition coefficient ($D_i^{s/liq}$) of the element *"i"* is measured by the ratio between the concentration of the element i on the mineral/solid (C_i^s), and its concentration on the liquid (C_i^{liq}):

(Eq. 8.1) $$D_i^{s/liq} = \frac{C_i^s}{C_i^{liq}}$$

If $D_i^{s/liq}$>1, than the element is compatible and will enter the mineral structure while if $D_i^{s/liq}$ <1, then the element is incompatible with the mineral and will remain preferentially in the liquid. Partition coefficients can also be calculated for a rock using the previous equation, but this requires the knowledge of the $D_i^{s/liq}$ for each mineral in the rock and the weight of each mineral in the overall paragenesis so that:

(Eq. 8.2) $$D = X_1 D_1^{s/liq} + X_2 D_2^{s/liq} + ... + X_n D_n^{s/liq}$$

A comparison between major and trace is presented in the diagram of Fig. 8.8, where the compositional variability of the lavas is showed in terms of Mg#[14] and Ni, the latter is a compatible trace element. The lavas present a large compositional range, between the less differentiated lavas, from Topo Volcanic Complex having Ni = 316 ppm and Mg# = 0.74, and the most differentiated lavas from Fajã de São João with Ni = 2 ppm and Mg# = 0.34. The trend defined by the lavas in Fig. 8.8, can be interpreted as the degree of evolution of the lavas and evidences that the progressive decrease in Mg# and Ni should be related to differentiation processes, in which fractional crystallization had an important role.

During fractional crystallization process, important changes in trace element concentrations can occur since the fractionation of a mineral phase changes the partition coefficients, e.g., liquids become enriched in the most incompatible elements. In order to avoid this, the characterization of the lavas in terms of trace elements should cover lavas with primary compositions, i.e. magmatic liquids in equilibrium with the mantle source, or at least, with primitive compositions. The expected composition in terms of MgO, Mg# and Ni for primary magmas requires MgO contents higher than 10%, Mg# higher than 0.69 (Frey *et al.*, 1978) and Ni > 250ppm (Wilson, 1989). In addition, lavas should not show evidences of mineral accumulation such as olivine, thus Ni/MgO ratio must be lower than 30.

In São Jorge only three lavas from Topo Volcanic Complex are representative of primary liquids with MgO=12.7-13.6%, Mg#=0.72-0.74, Ni=302-316ppm and Ni/MgO=22.3-24.3. Nonetheless, for a better characterization of all lava groups in terms of incompatible trace elements, the less differentiated lavas from Rosais and Manadas volcanic complexes and from the submarine pillow lavas where selected. These lavas present compositions with MgO=7.6-12.7%, Mg#=0.59-0.71, Ni=115-214ppm and Ni/MgO=13.5-20.6, and are considered the most primitive of each lava group. The samples from Fajã de São João sequence, due to their particular characteristics and their low Ni concentrations (1-52 ppm), are not included in this characterization.

[14] $$Mg\# = \frac{Mg^{2+}}{Mg^{2+} + Fe^{2+}}$$

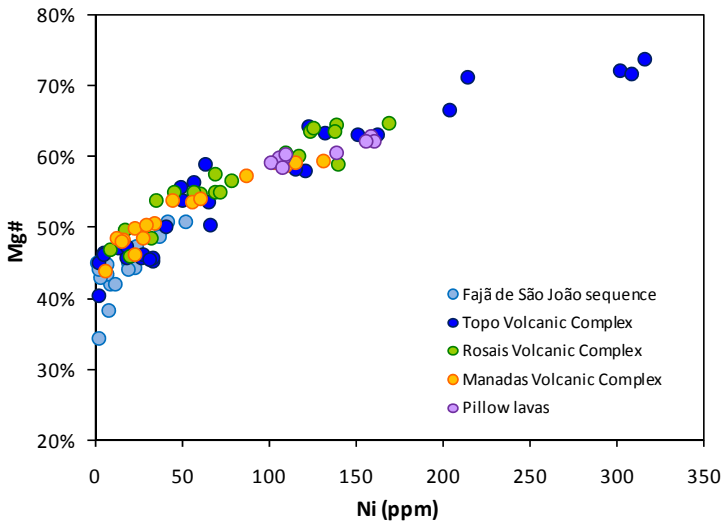

Fig. 8.8 – Ni vs. Mg# diagram for São Jorge lavas. These lavas display a continuous trend from primary compositions to very low concentrations in Ni and Mg#, due to magmatic liquids affected by petrogenetic process as fractional crystallization.

The spiderdiagram of Fig. 8.9 shows the patterns in incompatible trace elements of the most primitive lavas in São Jorge normalized to McDonough & Sun (1995) primitive mantle. The enrichment in incompatible trace elements relative to the primitive mantle is present in all lavas as observed in ocean islands basalts, and in particular in the Azores (e.g. Flower *et al*., 1976; White *et al*., 1979; França, 2000; Madureira, 2006).

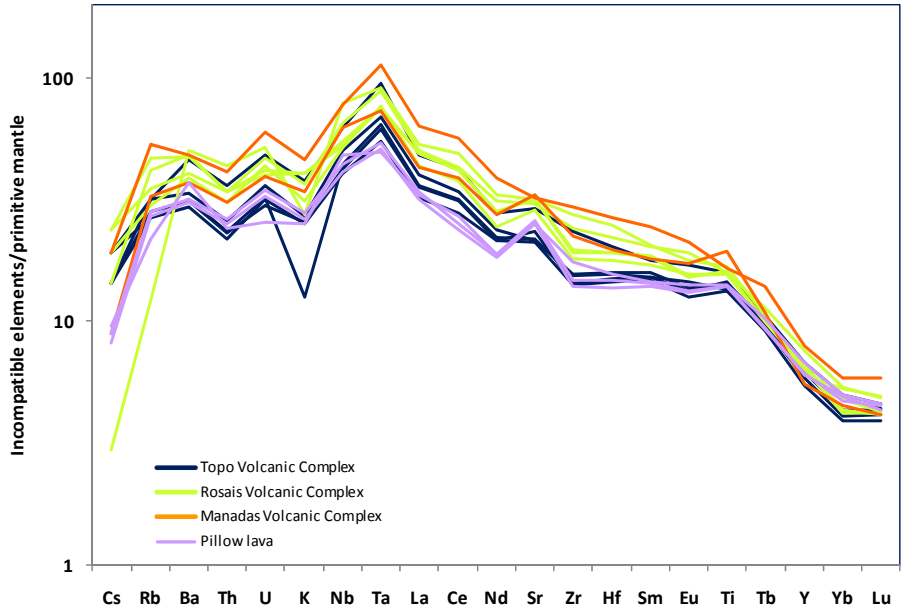

Fig. 8.9 – Incompatible trace element spiderdiagram showing the patterns for São Jorge most primitive lavas of each volcanic complex and the submarine pillow lavas, normalized to primitive mantle accordingly with McDonough & Sun (1995). Elements are ordered with decreasing degree of incompatibility.

In general, lavas present similar trends with enrichment in Nb and Ta relative to LILE and LREE, a small enrichment in Ba, U and Sr and a small negative anomaly in K (Fig. 8.9). Even so, Topo Volcanic Complex and the pillow lavas, both geographically located on the east side of São Jorge, display trends which evidence slightly more depleted concentrations in the most incompatible elements, than the lavas from Rosais and Manadas volcanic complexes. The depletion on Topo Volcanic Complex should result from the primary nature of the lavas; however, the submarine pillow lavas have comparable Mg# and Ni contents to Rosais and Manadas lavas. Thus, the incompatible trace element compositions of the submarine pillow lavas could reflect less enrich magmatic liquids, which can result from heterogeneities in the mantle source or from different condition of magma generation, as the degree of partial melting or shallower depth of mel0ting.

The enrichment in incompatible trace elements it is also extended to the rare earth elements group (REE) (Fig. 8.10), when compared with the concentration of these elements in chondrites (McDonough & Sun, 1995). As in other ocean island basalts it is found a strong enrichment in LREE relatively to MREE [(La/Sm)n =2.47] and to HREE [(La/Yb)n =9.1]. From Fig. 8.10 it is also possible to observe an increase in the fractionation in REE from the lava groups located on the east side of São Jorge to the ones located on the west side. This east-west increase is demonstrated by the growth of the average (La/Sm)n ratio, from 2.36 to 2.58, and of the average (La/Yb)n ratio, from 7.9 to 10.4.

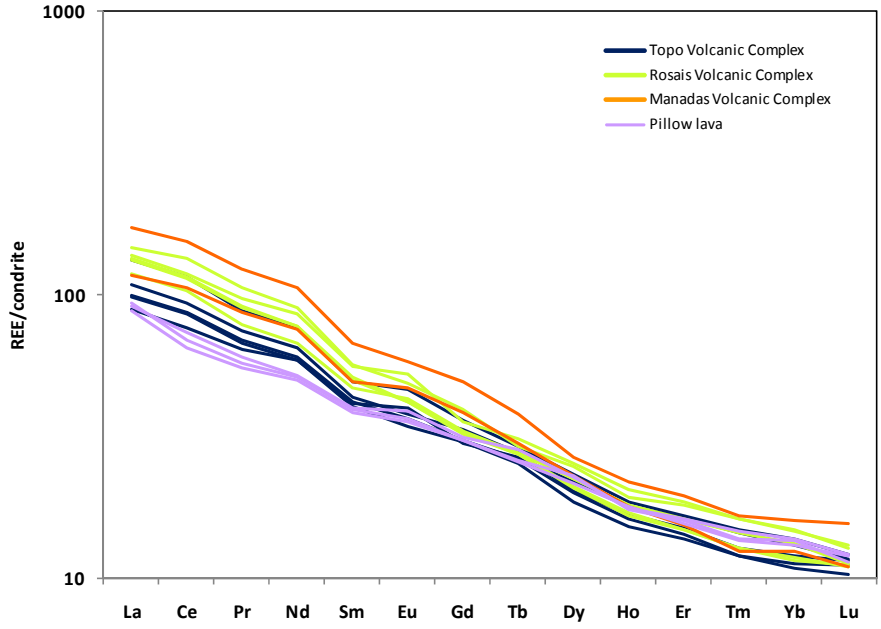

Fig. 8.10 – REE patterns for São Jorge most primitive lavas, normalized to chondrites accordingly with McDonough & Sun (1995).

If mantle heterogeneities or mantle melting conditions affected incompatible element concentrations, then these should also be reflected in incompatible trace elements ratios. Fig. 8.11 displays the ratios between incompatible trace elements with different geochemical behaviors as Ba and K, two LILE, La from the REE group, and Nb a HFSE. The lavas show relative constant Ba/Nb ratios (6.0 - 7.7) when compared with K/Nb ratios (104-236), but two lavas from Rosais show higher Ba/Nb and K/Nb ratios (9.0 and 275 respectively), evidencing that some of Rosais most primitive lavas are relative enriched in LILE (Fig. 8.11). This relative enrichment in LILE was found also in Rb as demonstrated by Rb/Nb ratios of 0.75 in those two lavas, when compared with the rest of the primitive lavas, with Rb/Nb ratios ranging between 0.14 and 0.63.

The relative enrichment in HSFE relative to LREE is presented in Fig. 8.11, where the Nb/Zr concentrations, which ranges within a narrow range (0.16 - 0.20) for all lava groups in São Jorge evidence differences in Nb/La ratios. The lavas from Rosais Volcanic Complex have the highest and lowest Nb/La ratios with an average of 0.81±0.10, while the most of the lavas from Topo and Manadas volcanic complexes and the submarine pillow lavas present relative constant ratios with an average of 0.77±0.05. The two higher Nb/La ratios in this diagram belong to the same samples in Rosais with higher Ba/Nb and K/Nb.

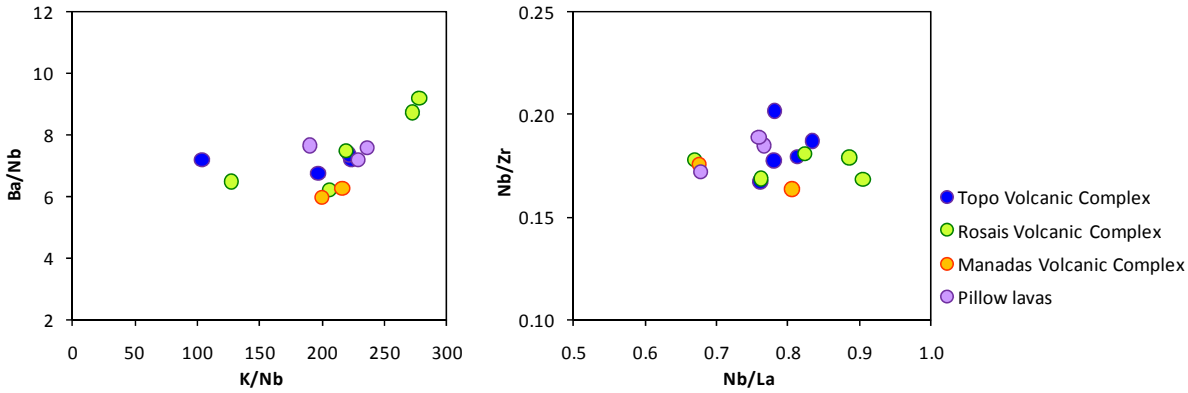

Fig. 8.11 – Trace element ratios (A) K/Nb vs. Ba/Nb and (B) Nb/La vs. Nb/Zr, showing the relation between LILE, HSFE and LREE in São Jorge most primitive lavas of each lava group considered in this study.

The lava from Rosais Volcanic Complex with low K/Nb ratio (Fig. 8.11) also shows low Cs and Rb and a slight more depletion in K than the remaining primitive lavas (Fig. 8.9). Comparing these fluid-mobile elements with Th, which has similar incompatible behavior but is immobile, the lava from Rosais has unusual high Th/Cs, Th/Rb and Th/K ratios, thus it can be considered that alteration processes affected the elements. The same reasoning does not work with the lava from

Topo Volcanic Complex that has low K/Nb ratio, because this lava is not depleted in any other mobile element, suggesting that the strong depletion in K is related with source composition (Fig. 8.9).

8.6 Fajã de São João Lava Sequence: an Exceptional Case on São Jorge Island

Fajã de São João lava sequence is a 400m stack up of lavas cut by dykes, outcropping in the southeast coast of São Jorge, which forms the cliff behind the Fajã de São João. This lava sequence was considered as a part of Topo Volcanic Complex that has a maximum age of 743 ka, as presented in this study. However, the geochronological data from Hildenbrand *et al.* (2008) constrained temporally Fajã de São João lava sequence between 1.32 and 1.21 Ma. The differences between Fajã de São João sequence and the rest of the island extends to the mineralogical and geochemical characteristics that strongly suggest a distinct volcanic phase from Topo Volcanic Complex. In a petrographic and mineralogic perspective, Fajã de São João lavas are considerably enriched in plagioclase and in some of the samples, this mineral corresponds at least to 20% of the volume of the lava. In addition, the geochemical analysis of these plagioclase-rich lavas delivered a basaltic composition (see Fig. 8.3) and in this sense, the lavas were named plagioclase-bearing basalts (Ribeiro *et al.*, 2007). The geochemical composition of these lavas presents other important characteristics that in conjunction with the remaining lavas of this sequence are analyzed in this chapter.

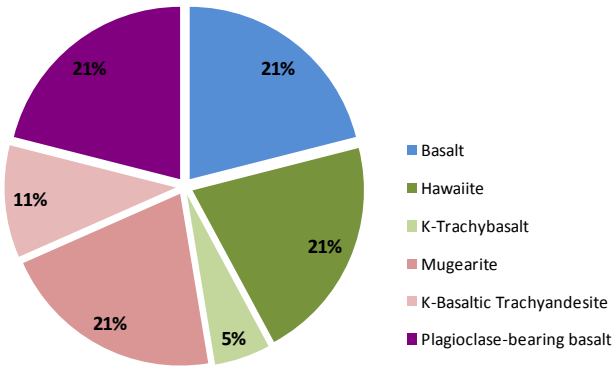

Fig. 8.12 – This diagram presents the lithological variability of Fajã de São João lavas. The classification of the lavas was obtained previously from TAS diagram; however, the presence of important amounts of large plagioclases crystal in the basalts subdivided this group into 21% of basalts and 21% of plagioclase-bearing basalts.

The TAS diagram presented in Fig. 8.3 sorted the lavas recovered along Fajã de São João sequence as 42% of basalts, 21% of trachybasalts (hawaiites), 5% of K-trachybasalts, 21% of basaltic trachyandesites (mugearites) and 11% of K-rich basalt trachyandesite. However, the presence of large amounts of large plagioclase phenocryst (>1cm) in several of these basalts divides this group into basalt (21%) and into plagioclase-bearing basalts (21%) as presented in Fig. 8.12.

In Fig. 8.12 the presence of K-rich lithologies evidences the potassium nature of several lavas as in Rosais Volcanic Complex; nonetheless, the higher percentage of Na-rich lavas compared to the ones enriched in K_2O evidences the predominance of the sodic alkaline lithotypes.

In order to better characterize the lavas from Fajã de São João sequence, incompatible elements normalized to primitive mantle (McDonough & Sun, 1995), are displayed in Fig. 8.13. The basalts, trachybasalts and basaltic trachyandesites present a progressive increase in incompatible trace elements that is coherent with the progressive increase of these elements in the magmatic liquid as fractional crystallization processes produce more evolved magmas.

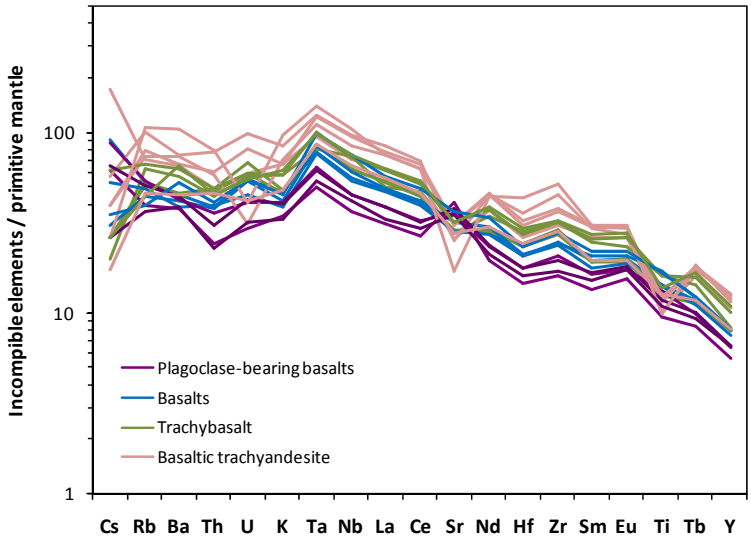

Fig. 8.13 – Spiderdiagram of incompatible elements normalized to primitive mantle (McDonough & Sun, 1995) for Fajã de São João lava sequence. Notice the Sr and Eu positive anomaly for the plagioclase-bearing basalts and Sr, Ti negative anomaly for basaltic trachyandesitic lavas.

However, it would be expected that the plagioclase-bearing basalts would present a similar pattern as the other basalts, but instead, they show lower concentrations in incompatible trace elements. Nonetheless, in all lava, the elements between K and Ce and Nd and Sm exhibit sub-parallel patterns with increasing concentrations as they become more evolved, as expected for a

co-magmatic series. The exceptions are the incompatible trace elements such as Sr and Ti and Eu that disrupt the patterns in Fig. 8.13. Sr exhibits a positive anomaly for the plagioclase-bearing basalts but a negative anomaly for the trachybasalts, which becomes more marked toward the basaltic trachyandesites. Ti, on the other hand, which is a moderately incompatible element, has a negative anomaly for the trachybasalts and basaltic trachyandesites, while Eu presents a positive anomaly that is more emphasized for the plagioclase-bearing basalts.

The REE patterns of Fig. 8.14 show that these elements have a similar behavior than the incompatible trace elements (Fig. 8.13). Again, the plagioclase-bearing basalts are the most depleted in REE while the remaining lavas become progressively enriched.

The Eu positive anomaly is better observed in Fig. 8.14, where all the REE patterns are displayed. In reduced magmas Eu exists mostly as Eu^{2+}, rather than in the trivalent state (Eu^{3+}) as other REE, and is a compatible element in plagioclase, as is Sr. So, accumulation of this mineral phase will give rise to a positive Eu anomaly (Best & Christiansen, 2001). This anomaly may be quantified by comparing the measured Eu concentration with an expected concentration obtained by interpolating between the normalized values of Sm and Gd ($Eu/Eu^{*} = Eu_n / \sqrt{Sm_n \times Gd_n}$). Thus the ratio Eu/Eu* is a measure of the anomaly and a value greater than 1 indicates a positive anomaly whilst a value lower than 1 is a negative anomaly (Rollinson, 1993).

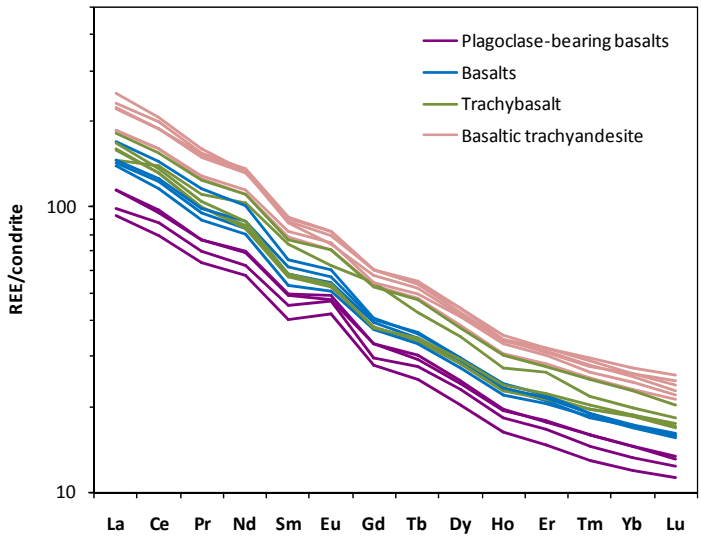

Fig. 8.14 – REE patterns for São João lavas, normalized for chondrites (McDonough & Sun, 1995).

All lavas from Fajã de São João have Eu/Eu* ratios higher than 1 evidencing the incorporation of this element in plagioclase, nonetheless average Eu/Eu* values of 1.11 were obtained for the

basalts, trachybasalts and basaltic trachyandesites of this sequence, while the plagioclase-bearing basalts presented an average ratio of 1.23.

Chapter 9: Petrogenese of São Jorge Magmas

9.1 Introduction

The geochemical characterization of São Jorge presented previously, showed that the composition in major and trace elements changes considerably when MgO, Mg# and Ni are used as an indicator of the degree of differentiation of the lavas. Likewise, incompatible trace element ratios and REE ratios on the less differentiated lavas from each volcanic group on São Jorge showed differences that suggest the existence of mantle source heterogeneities and/or variable melting conditions, as the degree of partial melting, pressure and temperature of melting, during the generation of magmatic liquids.

The role of these petrogenetic processes in São Jorge can be evaluated, in first hand, based on the geochemical behavior of two trace elements as Th and Y. In Fig. 9.1, the concentration in both elements presents two different trends, one for Fajã de São João lavas and Topo Volcanic Complex and a second, sub-horizontal, for lavas from Rosais Volcanic Complex. The lavas from Manadas Volcanic Complex in Fig. 9.1 appear divided between both trends although most of them seem to plot closer to Topo lavas.

During partial melting in the presence of garnet, Y is retained on the source and behaves as a compatible element while, Th behaves as an incompatible element. However, during magma differentiation process as fractional crystallization, both elements are incompatible in the mineral phases fractionating in São Jorge lavas. Therefore, the magmatic liquid after being extracted from the mantle source will show progressive enrichment in Th and Y as lava become more evolved, forming a linear and steep trend, as of instance on lavas from Fajã de São João and Topo Volcanic Complex (Fig. 9.1).

In opposition to this reasoning, the trend defined by lavas from Rosais Volcanic Complex is sub-horizontal, suggesting that Y is more compatible even for the most differentiated lavas. Since this

is highly improbable during the fractionation of olivine, pyroxene and plagioclase, because Y is incompatible with these minerals, it could be possible that the lavas where produced by different batch of magmas generated from different episodes of partial melting. In this case, the concentrations in Y instead of reflecting fractional crystallization processes reflect the concentration of this element in lavas produced by different parent liquids and/or by different melting events with different conditions, as the degree of partial melting depth and or temperature (Fig. 9.1).

As demonstrated, both partial melting and fractional crystallization processes are important for understanding the composition and the generation of lavas from São Jorge Island and is detailed in this chapter.

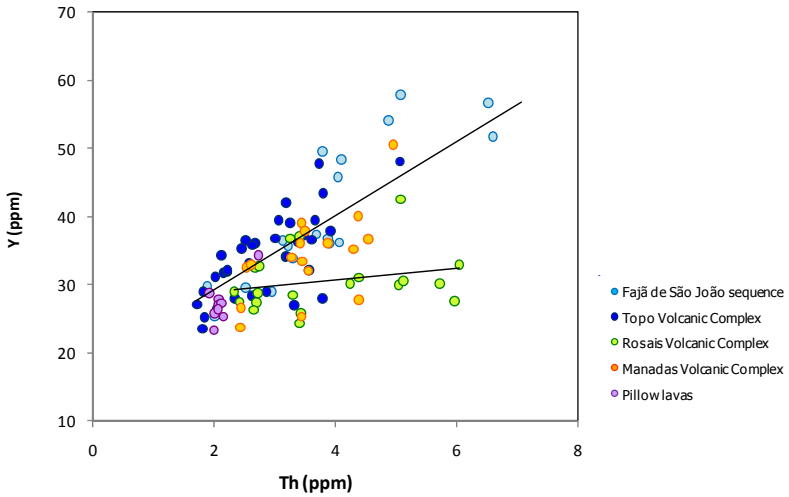

Fig. 9.1 – Diagram comparing Th and Y concentration of the lavas from each lava group in São Jorge. The regression lines in the diagram are from Topo Volcanic Complex and Rosais Volcanic Complex, and their distinct slopes are interpreted as the results of different magmatic processes producing different magma batches.

9.2 Characterization of Fractional Crystallization Processes

In major element variation diagrams (Fig. 8.6), MgO is used as an evolution index and it is possible to observe that the behavior of the major elements with the progressive decrease MgO forms curvilinear trends, which put to evidence the importance of magmatic differentiation processes (Best & Christiansen, 2001). The compositional variability observed for these elements should be related with the fractionation of the mineral paragenesis present in the lavas. Therefore, as

olivine, pyroxene, plagioclase and Fe-Ti rich oxides begin to fractionate from magmatic liquids, major element compositions should reflect the effects of fractional crystallization. Usually, the stronger inflexions on the curvilinear trend, results from the fractionation of a mineral that extracts from the liquid a specific element and the inflection normally happens at the same point in a rock series (Rollinson, 1993). Specifically in São Jorge, the stronger inflections observed occur at an MgO content of approximately 6%. These inflections are more evident for CaO and K_2O when the fractionation of plagioclase becomes predominant and overcomes the crystallization of olivine and pyroxene. Also, from this inflection onward (MgO=6%), FeO and TiO_2 concentrations suddenly decrease pointing to the fractionation of Fe-Ti rich oxides (i.e. titanomagnetite, the most abundant Fe-Ti oxide).

The influence of a mineral phase(s) fractionating during differentiation processes can be evaluated using Pearce diagrams (Fig. 9.2). Pearce shows that using the concentrations ratios of each oxide (or recast as cations) to one, which is know, or assumed to be constant, avoids the closed array drawback and creates a straight line that reflects the mineral phases evolved in the process. For the mineral phases present in São Jorge lavas the relationship between MgO, FeO, SiO_2 and K_2O, all recalculated as cations, shows that all three mineral phases, olivine+clinopyroxene+plagioclase are needed to explain fractional crystallization process for São Jorge lavas. The good correlations obtained for Rosais and Manadas volcanic complexes and the submarine pillow lavas evidences that the mineral proportions are similar in all three lava groups. However, lavas from Topo Volcanic Complex do not show such good correlation, probably because in some of the lavas plagioclase or olivine was the dominant mineral phase to fractionate.

The projection of the lavas from Fajã de São João sequence in the Pearce diagram shows a distinct trend, with a gentle slope, evidencing that plagioclase is the predominant mineral phase during fractional crystallization processes. These results are coherent with the mineralogical and geochemical characterization presented in the previous chapters that point out the influence of this mineral on the lavas. Because once again this sequence presents contrasting characteristics with the remaining lavas of the island, the analysis and interpretation of differentiation processes of these lavas will be presented separately.

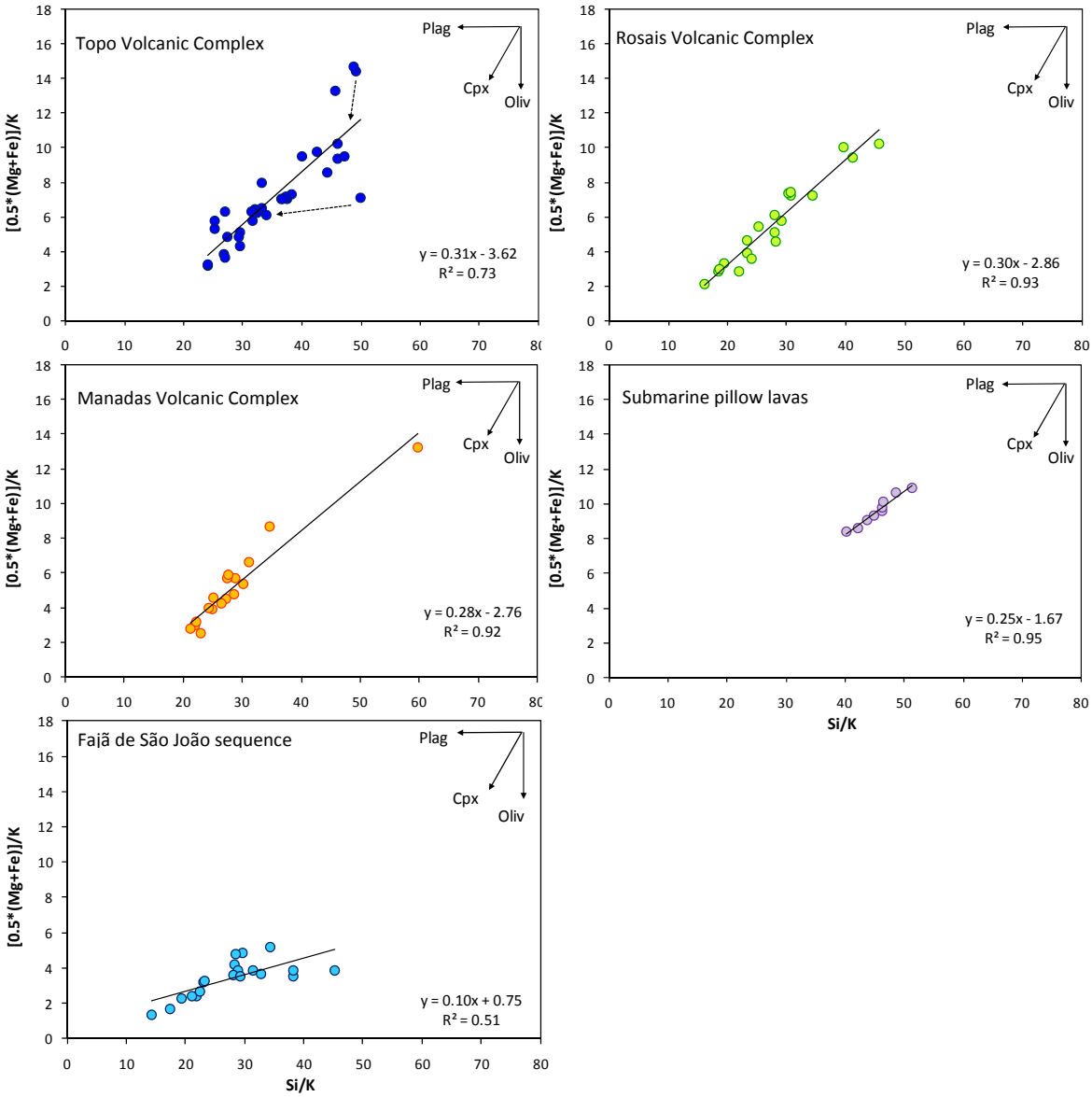

Fig. 9.2 – Projection of the lavas from all lava groups in São Jorge (Topo, Rosais and Manadas volcanic complexes, São João lava sequence and the submarine pillow lavas) in a Pearce diagram Si/K vs. [0.5*(Mg+Fe)]/K. The good correlation between the lavas from São Jorge submarine flank and from Rosais and Manadas volcanic complexes evidences the all three mineral phase (olivine+pyroxene+plagioclase) influence fractional crystallization processes. In Topo Volcanic Complex the dispersion of the lavas in Pearce diagram affected the correlation between the lavas and reveals that for several samples, either olivine or plagioclase played an important role during fractional crystallization.

Trace elements are more sensitive to fractional crystallization processes than major elements. This result from the fact that specific trace elements are incorporated into the mineral phase fractionating from the magmatic liquid, and so, the element behaves compatibly. On the other hand, if the concentration of the trace element increases in the evolving magma the trace element behaves incompatibly. Thus, the extent of crystallization of a magma system is an

important control of trace element concentration on the residual melt and the solids. The relationship between these parameters is described by the Rayleigh law:

(Eq. 9.1) $$C_i^{liq} = C_i^{liq^0} \times F^{(D-1)}$$

where C_i^{liq} is the concentration of an element in the liquid; $C_i^{liq^0}$ is the concentration of an element in the initial liquid; F is the proportion of liquid remaining and Dis the partition coefficient.

If the element is very incompatible, in a way that $D \approx 0$, then the previous equation (Eq. 9.1) can be rewritten:

(Eq. 9.2) $$F = \frac{C_i^{liq^0}}{C_i^{liq}}$$

Modeling trace elements during fractional crystallization processes may evolve the comparison between two highly incompatible elements, which would produce a linear trend, or between elements with opposite compatibilities that generate strongly curved trends.

The first situation can be observed for two elements that usually behave very incompatibly in basaltic magmas and in the mineral paragenesis observed in São Jorge, as Th and Nb. The variation between these two elements displayed by lavas from Topo Volcanic Complex, which has the widest Mg# and Ni content (Fig. 8.8), shows that both elements correlate through a straight-line as expected for two highly incompatible trace elements (Fig. 9.3). In addition, the correlation line does not pass through the origin as expected if the two elements had a similar incompatible behavior, instead the correlation line crosses the Nb axis at 3.19, thus indicating that Th is more incompatible than Nb for Topo lavas.

Since Th is highly incompatible in these lavas ($D \approx 0$), (Eq. 9.2) was used in order to estimate the amount of fractional crystallization that occurred between the most primitive lavas and the more evolved ones in Topo Volcanic Complex. Overall, (Eq. 9.2) predicts that 51% of fractional crystallization is necessary to originate the most evolved compositions in this lava group.

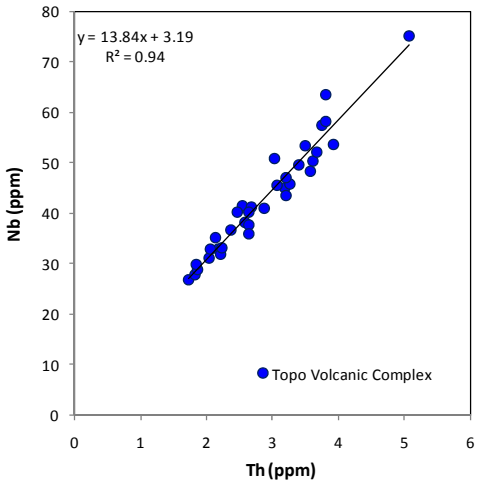

Fig. 9.3 – Diagram showing the good correlation between Th and Nb concentrations of Topo Volcanic Complex, which evidences the incompatible nature of the elements in these lavas. The correlation trend for the elements crosses the Nb axis showing that Th is more incompatible than Nb.

The modeling of two trace elements with different compatibilities in basaltic magmas, as Ni and Zr, delivers different information than the previous. Ni is an element that is very compatible with olivine ($D_{Ni}^{ol/liq} = 5.9\text{-}29$) and to a lesser extent with pyroxene ($D_{Ni}^{cpx/liq} = 1.4\text{-}14$), indicating that in basaltic magmas fractionating both minerals, Ni concentrations would decrease rapidly (data from Rollinson, 1993). In opposition, Zr is incompatible with olivine and pyroxene and its concentration increases during fractional crystallization. Therefore, if the initial composition of a magmatic liquid is known, i.e. the primary composition after the magma being segregated from the source, it is possible to predict the fractional crystallization path that this liquid follows.

This reasoning was applied to the lavas from Topo Volcanic Complex since they have primary compositions, which here will be assumed as the initial liquid composition. Estimates on the partition coefficients of Ni and Zr can be made on Topo lavas using (Eq. 9.1) in conjunction with the 51% of fractional crystallization between the most primitive and differentiated samples of the sequence. The values calculated, attribute to Ni a compatible behavior with $D_{Ni} = 8.03$, which is in the range expected for this element, and attribute to Zr a strong incompatible behavior with $D_{Zr} = 0.0006$. The application of the estimated partition coefficients and the assumed initial liquid composition (Ni = 308 ppm and Zr = 163 ppm), to (Eq. 9.1) permits to calculate the expected fractional crystallization path for incrementing degrees of fractional crystallization (F). The resulting fractionation path is presented in Fig. 9.4 where the Ni and Zr compositions of Topo, Rosais and Manadas volcanic complexes and of the submarine pillow lavas are projected.

All lava groups exhibit and important decrease in Ni evidencing the importance of olivine fractionation. In particular, several lavas from Topo Volcanic Complex and the pillow lavas follow the predicted fractionation path suggesting that olivine and pyroxene fractionated from the same magmatic liquid. However, for Ni concentrations lower than 150 ppm there is dispersion from the predicted trend of some of the lavas from Topo, Rosais and Manadas volcanic complexes. This suggests either that the magmas were generated by a different mantle source or that different melting events were in the origin of the lavas.

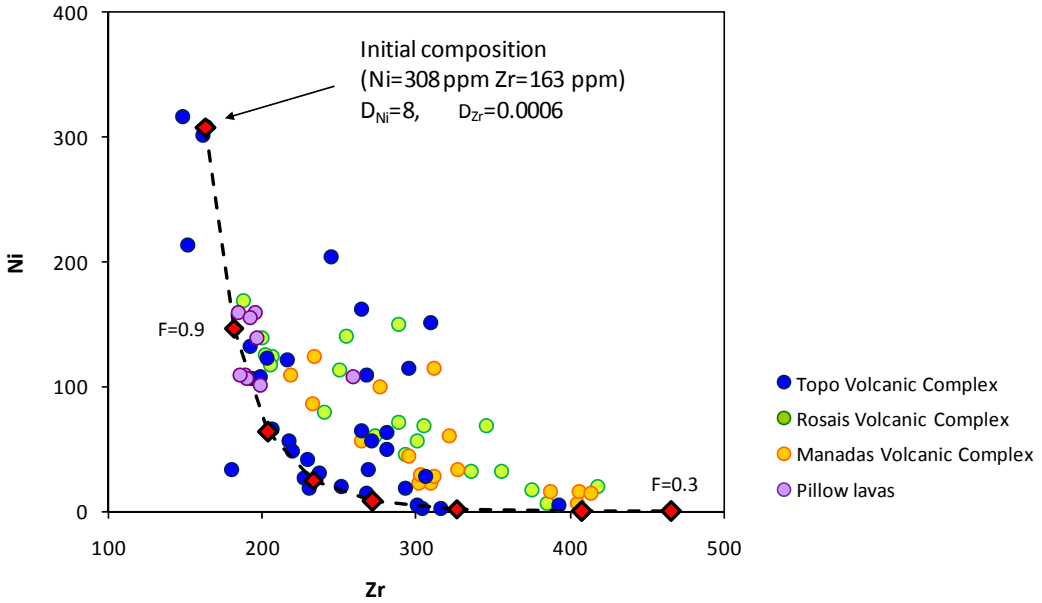

Fig. 9.4 – Diagram showing the composition in Ni and Zr of the lavas from Topo, Rosais and Manadas volcanic complexes and the submarine pillow lavas. The fractional crystallization trend exhibit in this diagram was calculated using equation (Eq. 9.1) for the lavas from Topo Volcanic Complex assuming an initial liquid composition of Ni = 308 ppm and Zr = 163 ppm. The partition coefficients used ($D_{Ni}=8.03$ $D_{Zr}=0.0006$) were calculated based on the incompatible behavior of Th in these lavas. F values, represented as red diamonds, correspond to increments of 0.1 between the initial composition and F=0.3.

It has been showed, from major elements that the crystallization of pyroxene and plagioclase are important during fractional crystallization processes in São Jorge lavas. Therefore, the previous modeling was applied to elements that are compatible with both minerals. This is the case of Sc, which is compatible with pyroxene ($D_{Sc}^{px}=1.7-3.2$), and of Sr, which is compatible with plagioclase ($D_{Sr}^{plag}=1.83$), according with the data in Rollinson (1993). Therefore, Sc and Sr partition coefficients were calculated for São Jorge lavas using the same method as Ni and Zr.

The estimated partition coefficient of 2.14 for Sc in lavas fractionating in Topo Volcanic Complex evidences the compatible behavior of this element and the effective fractionation of pyroxene. In opposition, the partition coefficient for Sr is 0.17, suggesting that plagioclase does not play an important role in the differentiation of magmas.

The predicted fractionation trend for Sc (Fig. 9.5A) is overlapped by the lavas of the three volcanic complexes, confirming that pyroxenes fractionation influences the composition of these lavas. The exceptions are the pillow lavas that do not follow the fractional crystallization trend predicted for Sc and Zr and so reduce the importance of pyroxene fractionation.

The Sr and Ni compositions (Fig. 9.5B) for the three volcanic complexes do not seem to follow the fractional crystallization path for plagioclase, in particular for Sr concentrations lower than 700 ppm. Conversely, the submarine pillow lavas seem to follow the crystallization path for plagioclase suggesting that this mineral is important during differentiation processes.

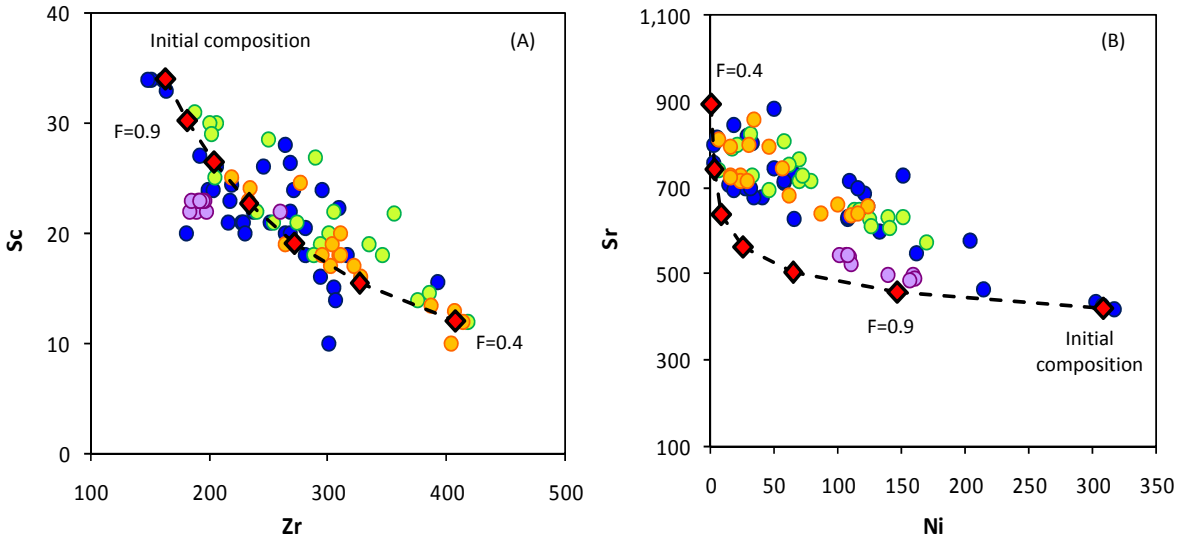

Fig. 9.5 – (A) Sc vs. Zr and (B) Sr vs. Ni variation diagrams showing the composition of the lavas from Topo, Rosais and Manadas volcanic complexes and the submarine pillow lavas. The fractional crystallization trend exhibit in this diagram was calculated using equation (Eq. 9.1) for the lavas from Topo Volcanic Complex assuming an initial liquid composition of Ni = 308 ppm and Zr = 163 ppm. The partition coefficients used are $D_{Ni} = 8.03$, $D_{Zr} = 0.0006$, $D_{sr} = 0.17$ and $D_{Sc} = 2.14$, and were calculated based on the incompatible behavior of Th in these lavas. F values were calculated in increments of 0.1. Symbols as in Fig. 9.4.

Overall, in São Jorge fractional crystallization processes are able to explain the mineralogy observed in the lavas. The geochemical composition in major and trace elements seems to be able to explain mineral phases fractionating from the magmatic liquids, which become progressively more differentiated. The no-comagmatic nature found between different lavas groups, or even inside a group, point to the existence of magmas either derived from different source or by separated melting events. Nonetheless, olivine and pyroxene seem to be the mineral phases that dominate fractional crystallization processes in Topo, Rosais and Manadas volcanic complexes contrasting with the submarine pillow lavas, where olivine and plagioclase are the dominant mineral phases.

9.3 The Effects of Fractional Crystallization and Plagioclase Accumulation in Fajã de São João Lava Sequence

The geochemical data analyzed in the previous sections shows that the fractional crystallization process are in the origin of the compositional diversity observed in Fajã de São João lava sequence. A more details approach to these processes can be done using major and trace element composition in order to identify and quantify the mineralogy observed in these lavas.

The major elements, Al_2O_3 and CaO are usually elements sensitive to the fractionation of plagioclase, which incorporates preferentially CaO in their structure, of pyroxene, which prefers Al_2O_3, and of olivine since this mineral maintains unchanged Al_2O_3/CaO ratios. In Fig. 9.6 the relationship between these two elements, expressed as the logarithm of Al/Ca ratio in conjunction with Zr, is used to distinguish between the fractionation of plagioclase, olivine and pyroxene, in Fajã de São João lavas. The plagioclase–bearing basalts present a negative trend that coincides with the trend expected for plagioclase. The basalts and trachybasalts present a discrete positive trend evidencing a more important role of olivine and pyroxene in the fractionation of the lavas, while the basaltic trachyandesites show increasing pyroxene fractionation.

The relation between Ni and Mg# contents, as in Fig. 8.8, shows that least evolved basalt in Fajã de São João sequence (SJ9) has Mg# = 51% and Ni = 52ppm, while the most differentiated basaltic trachyandesite (SJ18) has Mg# = 34% and Ni = 2ppm. From these two lavas, used as compositional

end-members of the sequence, it was estimated that 62% of fractional crystallization is necessary to produce the changes between lavas SJ9 and SJ18. So, based in the value of F, the partition coefficients for Zr (D_{Zr} = 0.19) and Ni (D_{Ni} = 4.4) were calculate, as well the predicted fractional crystallization path, as presented in Fig. 9.7 (Ribeiro *et al.*, 2007).

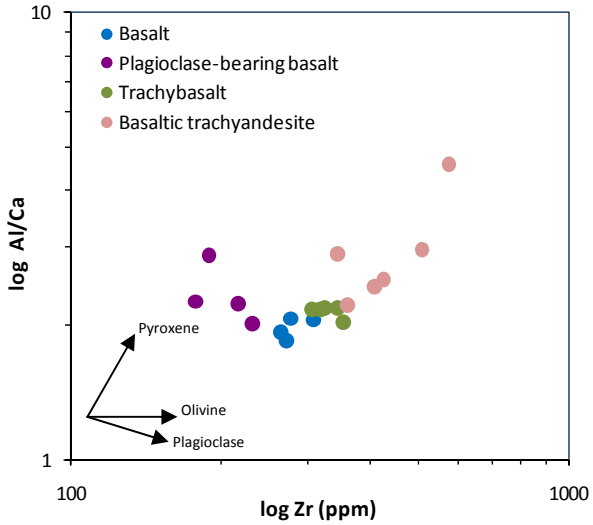

Fig. 9.6 – In this diagram is depicts the correlation between the logarithm of Al/Ca cationic proportions and the logarithm of Zr for Fajã de São João lavas. The variations in log Al/Ca as lavas become more differentiated allows to distinguish the role plagioclase, pyroxene and olivine fractionation.

The plagioclase-bearing basalts display a positive correlation in the diagram of Fig. 9.7 contradicting the fractional crystallization pattern followed by the other lavas. The positive correlation observed between Ni and Zr predicts that these elements behave incompatibly in these lavas. In fact, Ni and Zr are incompatible with plagioclase, so the accumulation of this mineral should be responsible by the anomalous correlation. This happens because the accumulation of a mineral phase increases considerably the composition of certain elements masking the concentration of others. In this specific case, plagioclase accumulation in these basalts has produced a strong enrichment in elements compatible with plagioclase as CaO and Al_2O_3, and Sr (Fig. 8.6, Fig. 8.13 and Fig. 9.6).

In this sense, is important to determine the amount of plagioclase accumulation in the basalts and then correct the Zr and Ni compositions. For this, it was assumed that only plagioclase accumulation was responsible by shifted compositions. The formula “Corrected concentration = Concentration in lava x 100 /(100 - plg. inc.%)” was applied in order to remove the excess of

plagioclase and shift Zr and Ni concentration towards the fractional crystallization trend in Fig. 9.7.

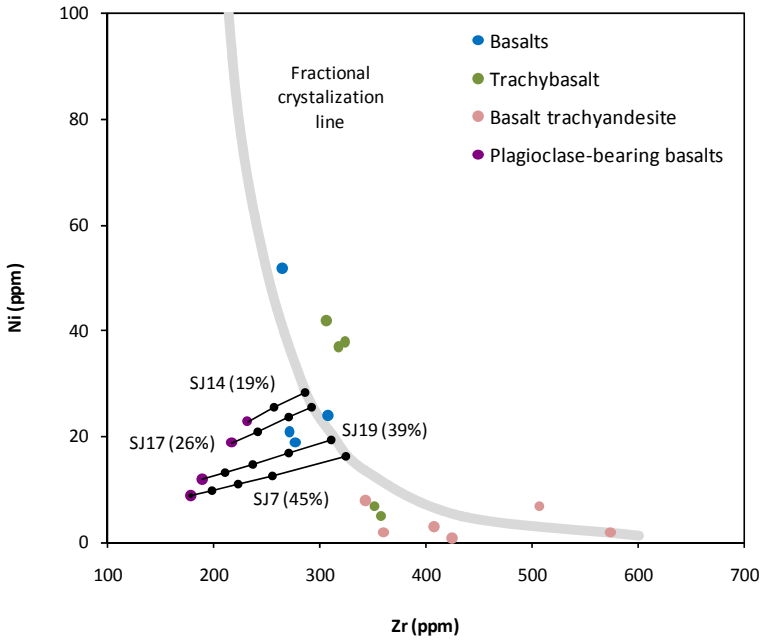

Fig. 9.7 – Lavas from Fajã de São João sequence are projected according with their Ni and Zr content. The predicted fractional crystallization line was calculated considering an initial magma composition, with Ni = 308 ppm and Zr = 163 ppm, and the partitions coefficients D_{Zr} = 0.19 and D_{Ni} = 4.4. The composition of the plagioclase-bearing basalts is corrected by retrieving the volume of plagioclase that masks Ni and Zr concentrations, this correction is represented by the black dotted lines.

The calculations for lava SJ7 are presented in Table 9.1, and plotted in Fig. 9.7. The corrected concentration for Ni and Zr intercepts the crystal fractionation path, used as a reference composition, when 45% of the volume of the plagioclase is retrieved from the lava.

Table 9.1 – Table with the correction concentrations estimated for lava SJ7 using the formula "Corrected concentration = Concentration in lava x 100 /(100 - plg. inc.%)". Plagioclase accumulation percentage used in the calculation ranges between 5 and 48%.

SJ7		
Correcting plagioclase accumulation	**Ni (ppm)**	**Zr (ppm)**
Initial	9.0	178
10%	10.0	198
20%	11.3	223
30%	12.9	254
40%	15.0	297
45%	16.4.3	324

Using the same procedure, Ni and Zr compositions were corrected for lavas SJ14, SJ17 and SJ19, for which it was necessary to retrieve 19, 26 and 39% respectively, of accumulated plagioclase, as presented in Fig. 9.7.

One of the most distinctive elements in Fig. 8.13 is Sr, considered to be incompatible in basaltic magmas fractionating olivine and pyroxene but compatible with plagioclase ($D_{Sr}^{plag} = 1.83$; Rollinson, 1993). Therefore, it is expected to observe enrichment in Sr in the plagioclase-bearing basalts, which should be corrected using the estimated volume of plagioclase accumulated. In Fig. 9.8, is presented the corrected composition in Sr and Zr for those lavas demonstrating that without the accumulation of plagioclase, the liquids have Sr content similar to the renaming lavas of Fajã de São João sequence.

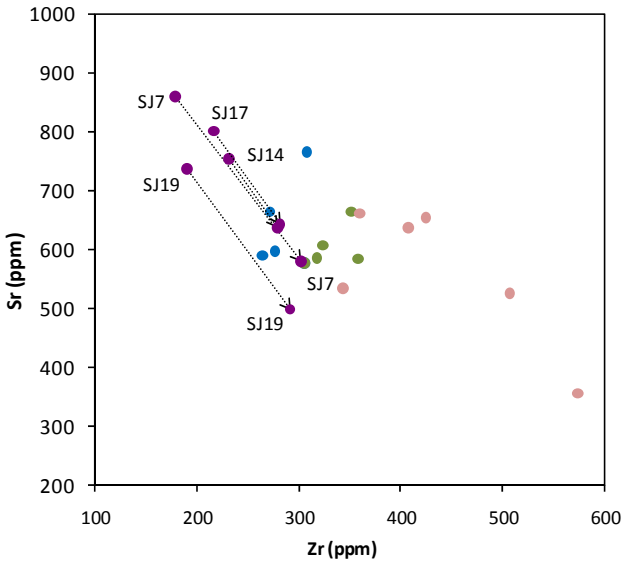

Fig. 9.8 – Sr vs. Zr concentration of the lavas from Fajã de São João lava sequence. The composition of the plagioclase-bearing basalts is corrected for the lava by retrieving the volume of plagioclase, which is 45%, 19%, 26% and 39% for lavas SJ7, SJ14, SJ17 and SJ19 respectively. Legend as in previous figures.

9.4 Temporal-Changes of Magmatic Process in São Jorge

As presented previously, fractional crystallization is the main processes responsible for the differentiation of the lavas in São Jorge and, consequently, for the fractionation of the mineral assemblage observed in most lava sequences with exception of Fajã de São João, where accumulation of plagioclases has an important role.

In order to compare the occurrence of these processes in Fajã de São João with the rest of the island, the lavas from Fajã de São João and Fajã dos Cubres sequences are compared according with their stratigraphic position on the lava pile, with their age and with their MgO content (Fig. 9.9). This comparison is able to give an overview of the chemical variation occurred during the period in which the lava piles formed and of the changes in the magmatic process between the edification of both lava sequences, i.e. between the first and second volcanic phases.

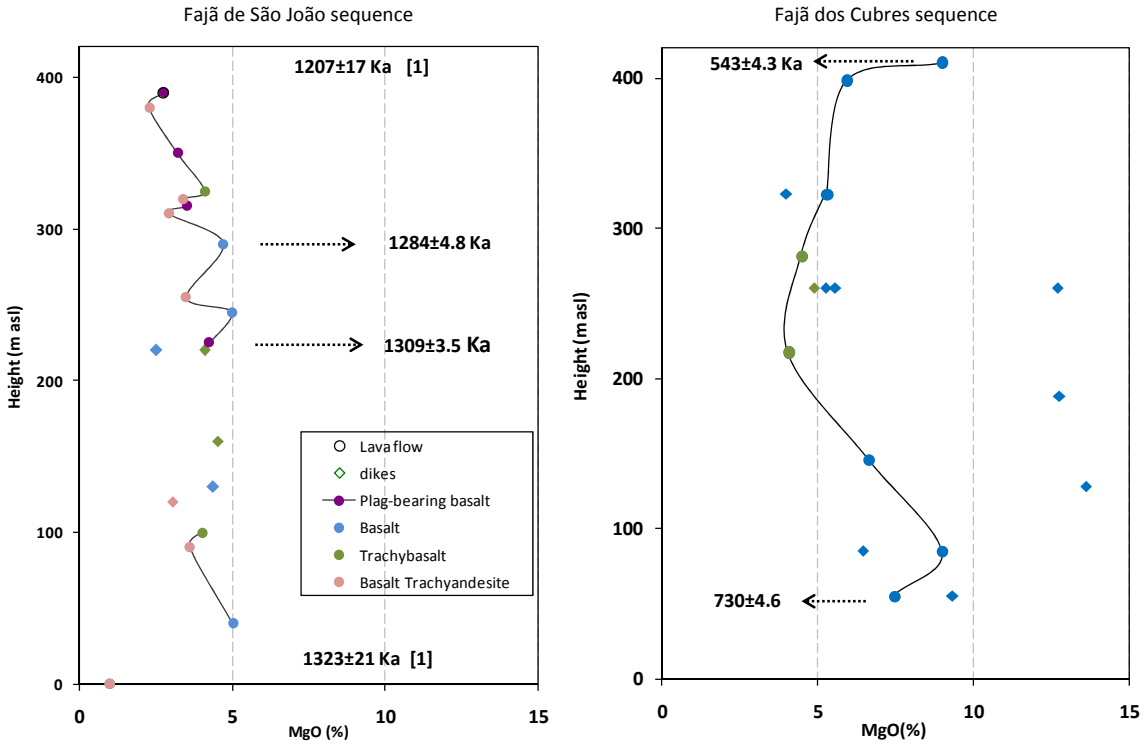

Fig. 9.9 – Stratigraphy of Fajã de São João and Fajã dos Cubres lava sequences showing temporal chemical variations based on MgO concentrations. Inter-sequence differences and intra-sequence characteristics put to evidence important temporal changes on the processes originating the lavas. Geochronological data presented in this study and by [1] Hildebrand *et al*. (2009).

The two lava sequences exhibit important chemical differences based on their MgO content, which is much higher on Fajã dos Cubres, and on its variation along the stratigraphic succession.

The lava sequence at Fajã de São João, which has an alkaline signature but with the presence of normative hypersthene, displays a strong oscillatory behavior formed by the periodic eruption of lavas with alternating compositions. These oscillations require the occurrence of fractional crystallization processes but also the periodic supply of less fractionated magmatic liquids. The existence of a well-developed magma chamber/plumbing system feeding the volcanic system of Fajã de São João is able to explain this oscillatory behavior. In addition, the development of large

plagioclase phenocrysts and their accumulation suggested by the extrusion of the plagioclase-bearing basalts is easily explained by gravitational segregation process in a magma chamber. The relative fast growth rates of 3.4 m/ka, estimated for Fajã de São João, in conjunction with the previous observations suggests a relative shallow level and dynamic magma chamber with fast and periodic replenishment by new magma alternating with the eruptions of lavas or intrusions.
Compared to Fajã de São João, the lava sequence of Fajã dos Cubres is characterized by a stronger alkaline signature and by the presence of lavas with primitive composition (i.e. MgO>12.5%). Instead of a compositional oscillatory behavior, this lava sequence presents a large cycle from base to top, with the most evolved lavas outcropping at the middle of the pile. The presence of primitive compositions suggest that the magmatic liquids, after being extracted from the source, ascend quickly to the surface while the hawaiites require some time of residence before being erupted. Also, as previously mentioned, lavas from Fajã dos Cubres form a cogenetic rock series what suggest that the magma was hosted on a reservoir, or in the conduits, and with time lavas become more differentiated and the hawaiites are formed. The increase in MgO content on the lavas outcropping on a stratigraphic level above the hawaiites could possible indicates the re-injection of a new magma batch.

Overall, when compared with Fajã de São João, the lower growth rates of Fajã dos Cubres (1.9 m/ka) in conjunction the presence of one large compositional cycle suggest a different magmatic regime during this stage of the second volcanic phase, possibly with a decrease in magma production.

9.5 Characterization of São Jorge Mantle Source and of Melting Conditions

The large geochemical variability found on the Azores Islands and in the submarine lavas of the Plateau, based on incompatible trace elements compositions, led to the conclusion that mantle heterogeneities at inter-island scale (≈100 km) or even at intra-island scale (≈40 km) exist in the Azores Plateau (e.g. White *et al*., 1979; Turner *et al.*, 1997; Widom *et al.*, 1997; Beier *et al.*, 2006 and Elliot *et al*., 2007).

These geochemical heterogeneities can result from different melting conditions and mantle source compositions usually associated with (1) the long-term evolution and evolution of the plateau, which started at approximately 20 Ma ago (Gente *et al.,* 2003), (2) the Azores mantle plume located beneath Terceira Island (Moreira *et al*., 1999) and by (3) the proximity of the Mid-Atlantic Ridge. The local tectonic setting as Terceira Axis, interpreted as an ultra-slow spreading center, could also have affected the geochemical composition of the lavas as presented by Beier (2008).

The characterization of São Jorge in terms of incompatible trace elements (Fig. 8.9) evidences that the mantle source beneath the island is enriched in incompatible trace elements relative to the primitive mantle. The slight differences in the patterns of incompatible trace elements and in highly incompatible trace element ratios (Fig. 8.11), of the most primitive lavas, suggest the presence of small mantle heterogeneities, in particular in some of the lavas from Rosais Volcanic Complex. In addition, REE patterns and LREE/HREE ratios (Fig. 8.10) point that out those melting processes occurred in the presence of residual garnet in the mantle source, evidencing deep mantle melting. The depth of melting and the degree of partial melting seems to change in an east-west direction based on the variation between LREE/HREE ratios. The information obtained from the characteristics of the most primitive lavas will be detailed in order to better characterize the processes associated with magma production beneath São Jorge.

9.5.1 Geochemical heterogeneities in São Jorge mantle source

In order to compare incompatible trace elements composition between the primitive lavas from each complex, incompatible trace elements were normalized to the average primary composition of two lavas from Topo Volcanic Complex. The spiderdiagrams of Fig. 9.10 puts to evidence the variations in incompatible trace elements between each volcanic complex relative to the primary compositions. These variations do not occur only between lava groups but also in geographically closed-space lavas of lavas from the same volcanic complex, where enrichment can be 1.5 to 2 times greater than primary compositions

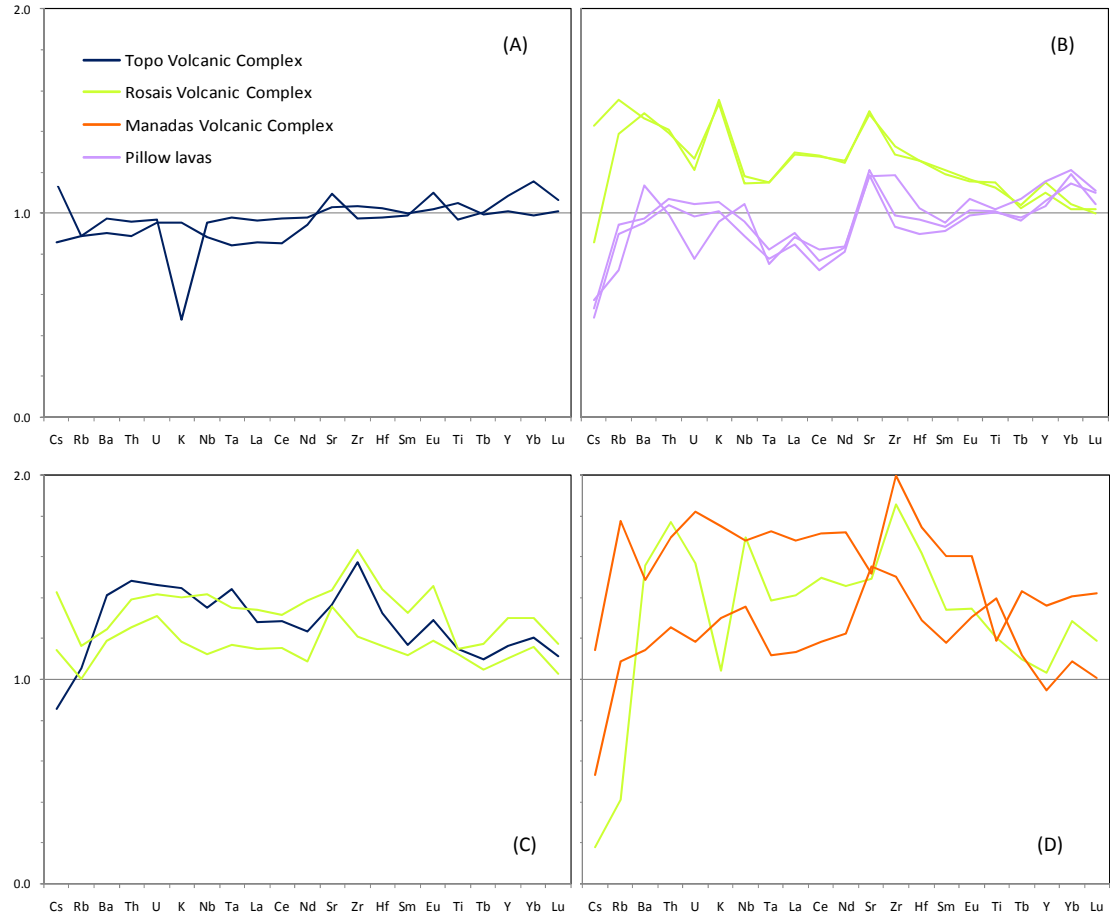

Fig. 9.10 – Spiderdiagrams showing incompatible trace elements compositions of the most primitive lavas normalized to the average composition of two lava from Topo Volcanic Complex with primary compositions (Ni = 308-316 ppm and Mg# = 0.72-0.74). The lavas are presented according with the enrichment patters in order to become more visible and make a clear distinction between the patterns.

In detail, the lavas from Topo Volcanic Complex present horizontal trends evidencing similar composition to the normalizing lavas, with the exception of a strong depletion in K in one of the lavas in Fig. 9.10(A). The submarine pillow lavas in Fig. 9.10(B) are similar to the lavas from Topo although they present small depletions in Rb, Ta, La Ce and the enrichments in Sr, Y, Yb and Lu relative to primary magmas. The depletion in LREE (La and Ce) and the enrichment in HREE (Yb and Lu) and Y, could be related with higher degrees of partial melting or to shallower melting processes. In opposition, the lavas from Rosais Volcanic Complex in Fig. 9.10(B) are enriched up to 1.5 times in most of the incompatible trace elements with stronger peaks in LILE (Rb, Ba, and K) and Sr. However, from Zr through Lu, concentrations decrease and become more similar the primary compositions of Topo. These two lavas from Rosais Volcanic Complex also have similar patterns evidencing that they were originated from the same mantle source. In Fig. 9.10(C), the

lavas from Topo and Rosais volcanic complexes are in general relative enriched with respect to the primary liquids, with small positive peaks in Sr, Zr and Eu, and slight higher Y, Yb and Lu contents. In Fig. 9.10(D), the lavas from Rosais and Manadas volcanic complexes show very different incompatible trace elements patterns with variable degrees of enrichment relative to the primary compositions.

The different patterns developed by the most primitive lavas in São Jorge reveal that melting processes sampled mantle compositions with different degrees of fertility and suggest that the mantle source beneath the island is not chemically homogeneous. It could be suggested that different degrees of partial melting produced the observed variations in the patterns; however, it would be expected to have higher degrees of enrichment for lower degrees of melting in highly incompatible elements, as Ba, K and Nb, instead of the crosscutting patterns displayed. Nonetheless, it has to be taken into consideration that the maximum enrichment in incompatible trace elements represented in Fig. 9.10 is only 2 times the concentrations of primary compositions, thus the chemical heterogeneity observed suggest that melting processes sampled mantle compositions with slight different degrees of fertility.

9.5.2 The influence of amphibole in the composition of São Jorge magmas

As previously observed the negative K anomaly observed in Fig. 8.9, is common to all lavas in São Jorge, and it is frequently found in other islands as for instance Pico and Terceira in the Azores Archipelago (França, 2000; Madureira, 2006; respectively) or Madeira Island (Mata, 1996).

The depletion in K, in the most primitive samples, could be attributed to the intrinsic nature of the mantle source, where a mineral phase could retain this element during small degrees of partial melting. Usually the minerals that could produce this effect, during partial melting, would be a K-rich amphibole or phlogopite. In this case, it is also expected to have melts depleted in Rb and Sr in presence of amphibole, or strong depletions in Ba in the presence of phlogopite, because this mineral retains this element.

To distinguish between these minerals phases, amphibole and phlogopite, is necessary to look at the partition coefficients and the behavior of São Jorge lavas relative to K and Rb. If amphibole is the mineral phase present in the mantle source during partial melting, then Rb would behave incompatibly with $D_{Rb}^{amp/liq} = 0.023$, while if it is phlogopite, then Rb would be a compatible element with $D_{Rb}^{phl/liq} = 1.7$ (*in* Halliday *et al*., 1995). At the same time, K partition coefficients for phlogopite are very similar to Rb so that $D_{K/Rb}^{phl/liq} = 0.9$, but in the presence of amphibole K behaves much more compatibly than Rb and $D_{K/Rb}^{amp/liq} = 9.6$ (*in* Halliday *et al*., 1995). Therefore, partial melting will produce melts with relative high K_2O/Rb ratios in the presence of phlogopite (K_2O/Rb=0.132, Greenough, 1988) and melts with lower K_2O/Rb ratios in the presence of amphibole (K_2O/Rb=0.012, Greenough, 1988).

The values obtained for K_2O/Rb ratios in São Jorge are in average 0.05±0.02 as presented in Fig. 9.11, suggesting the presence of amphibole in the mantle source. The presence of this mineral has been described in other ocean islands in the Atlantic (Halliday *et al.,* 1995) as in Madeira Island Mata, 1996 and Ribeiro, 2001) and, in particular, in the Azores, e.g. Corvo Island (França *et al.,* 2006).

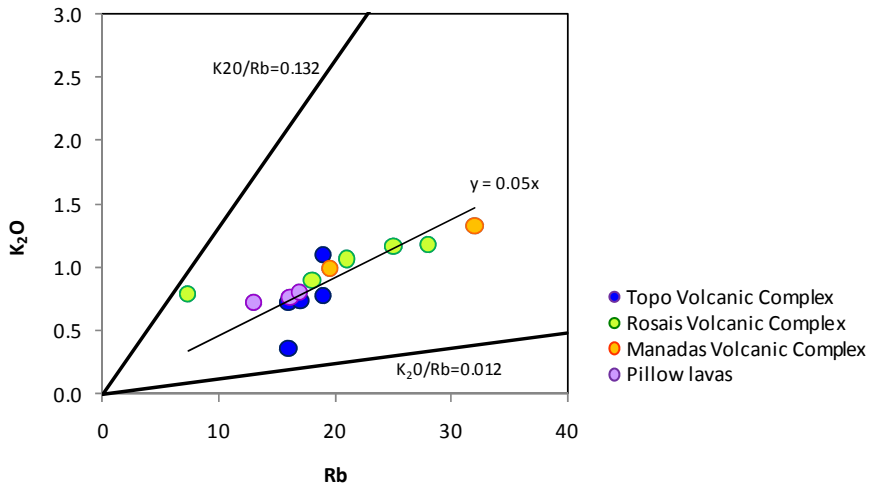

Fig. 9.11 – This diagram shows the Rb and K_2O concentrations and low K_2O/Rb ratios for the most primitive lavas. The regression obtained for the lavas, points to the presence of residual amphibole in the mantle source as the mineral phase retaining K during partial melting processes.

9.5.3 The presence of garnet in São Jorge mantle source

Enriched concentrations in incompatible trace elements and, in particular, in light rare earth elements (LREE) are typical of oceanic islands in which small degrees of partial melting affects an enriched mantle source. In the diagram of Fig. 8.10, it is showed a strong fractionation between LREE and HREE, which the principal mineral phases of the mantle, as olivine, orthopyroxene and clinopyroxene, are not able to produce. Those trends require the presence of another mineral phase in the mantle capable to fractionate efficiently the REE, and produce the pattern observed. Usually, the mineral phase present in the mantle source that has very different partition coefficients between the LREE and the HREE is garnet.

For small degrees of partial melting, concentration in La is considerably high because this element is strongly incompatible with garnet $D_{La}^{grt/liq} = 0.0007$, while concentration in Yb is low because this element is retained in the garnet structure and has $D_{Yb}^{grt/liq} = 6.4$ (Halliday *et al*., 1995). As a result, the melts produced in the presence of garnet will fractionate La and Yb and the La/Yb ratios will be higher for small degrees of partial melting or for a mantle source with a higher proportion of garnet (e.g. deeper mantle source). Since La is strongly incompatible with garnet, magmatic liquids produced by small degrees of partial melting will be enriched in this element and as the degree of partial melting increases, the concentration in La is diluted. In this sense, La could be used as a measure of the degree of partial melting.

The (La/Yb)n ratios obtained for the most primitive lavas of São Jorge (Fig. 9.12) show that the REE of lavas from Topo, Rosais and Manadas volcanic complexes were more efficiently fractionated with an average ratio of 9.6, than the submarine pillow lavas with an average (La/Yb)n ratio of 6.8.

In the diagram of Fig. 9.12, it is showed a positive correlation between (La)n and (La/Yb)n for most of the lavas in São Jorge, which points out that the more fractionated liquids originating Rosais and Manadas lavas should have been generated by lower degrees of partial melting. In opposition, the submarine pillow lavas from the east side of São Jorge, and the lavas from Topo Volcanic Complex have less fractionation between LREE and HREE evidencing higher degrees of partial melting. Considering the volcanostratigraphic evolution of the islands, the REE indicate that the younger lavas were generated by smaller degrees of partial melting.

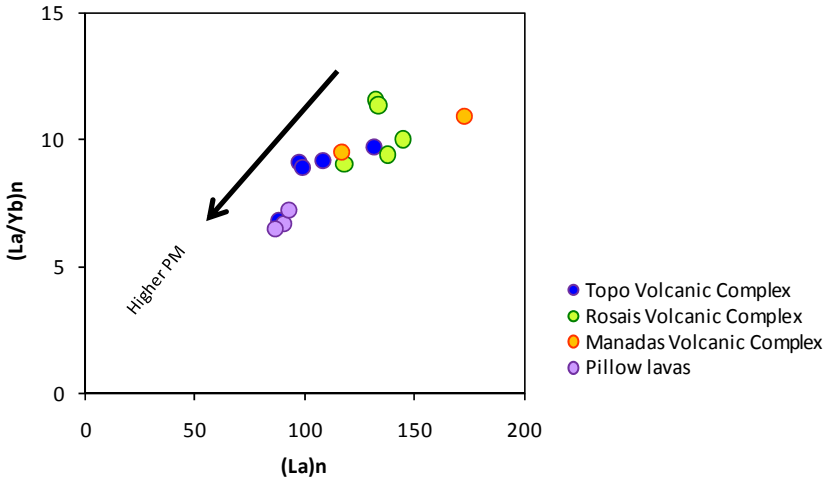

Fig. 9.12 – (La)n vs. (La/Yb)n diagram for the most primitive samples in São Jorge, showing a positive correlation, which indicates that for higher (La)n i.e. lower degrees of partial melting (PM) there is higher fractionation between LREE and HREE. Values are normalized to chondrites (McDonough & Sun, 1995).

Nonetheless, two lavas from Rosais Volcanic Complex have slight higher (La/Yb)n ratios for a given (La)n, suggesting that for the same degree of partial melting the source was able to fractionate more efficiently LREE from HREE. If this is the case, then the mantle source in the in the origin of this two samples could be enriched in garnet and/or could be located at greater depth.

9.5.4 Possible role for a mafic lithology in São Jorge mantle source

The characterization of the mantle source in São Jorge supports the idea that melting of an enriched and slight heterogeneous mantle source occurred in the garnet stability field. In a general perspective, it can be assumed that the garnet-bearing mantle source in the Azores is a peridotite, however it has been invoke, in some cases, that the presence of mafic lithologies produces enriched compositions in oceanic island (Sigmarsson *et al*, 1995). In fact, several works (Hirschmann & Stolper, 1996; Stracke *et al.*, 1999; Elkins *et al.*, 2008) argue for the presence of enriched lithologies as garnet pyroxenite or eclogite within the mantle source of ocean islands.

Experimental studies done by Bennett *et al.* (2003) showed that a garnet-bearing mantle source produces small changes in partition coefficients between Zr and Hf, allowing to distinguish between two garnet-bearing mantle lithologies. In garnets with higher pyrope content, such as those found in garnet peridotites, Zr is more incompatible than Hf ($D_{Zr} < D_{Hf}$), while the reverse

occurs in grossular rich garnets more common on eclogites of recycled crustal origin ($D_{Zr} > D_{Hf}$). In Fig. 9.13, both elements plot along the same regression line, however, the line shows that D_{Zr} is slightly lower than D_{Hf}. As a result, it is possibly that these two elements reflect the presence of a pyropic garnet as found in garnet peridotites instead of, grossular garnet usually found in eclogitic sources (Bennett *et al.,* 2003). Also, the melting of an eclogitic/pyroxenitic lithology beneath São Jorge should be reflect on other incompatible trace elements, as REE since these lithologies have different partition coefficients for the LREE and HREE (Tuff & Gibson, 2007). In fact, Fig. 8.10 does not show significant differences in REE making improbable the presence of these mafic lithologies beneath São Jorge Island (Ribeiro *et al.*, 2007a).

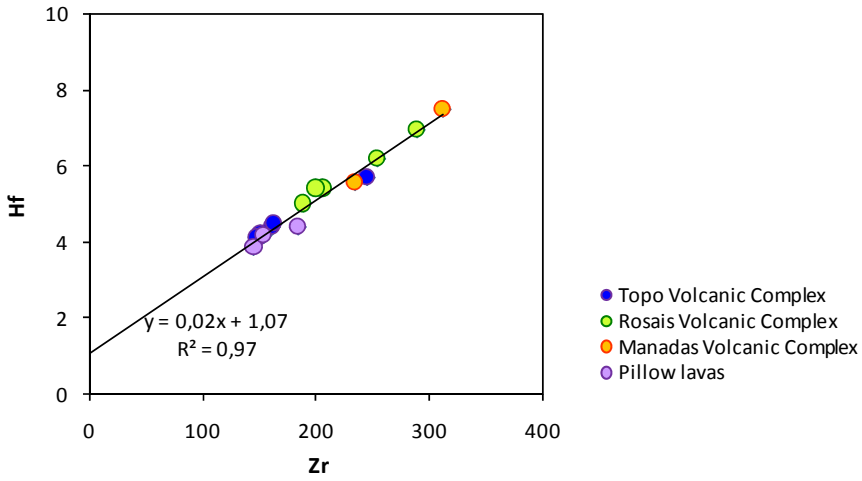

Fig. 9.13 – Diagram exhibiting the concentrations of Zr and Hf of São Jorge lavas. Both elements are well correlated (r^2=0.97) and the correlation line indicated that Hf is slightly more compatible than Zr.

This interpretation for São Jorge is consistent Bourdon *et al*. (2005) study that considers unlikely the presence of mafic lithologies in the Azores based on U-series disequilibria data. Moreover, Elkins *et al*. (2008) suggest that the melting a peridotite with enriched signatures produces liquids that, when mixed with melts of normal peridotite, could account for the enrichments observed in ocean islands including the Azores.

9.6 Estimative of the Degree of Partial Melting

As earlier mentioned, trace elements are very sensitive to petrogenetic processes and are good tools to characterize these processes. The variation in trace elements during partial melting processes can be quantified using the equation for batch melting also called equilibrium partial melting. This equation describes the formation of a partial melting in which the melt is continuously reacting and re-equilibrating with the solid residue at the site of melting until mechanical conditions allow it to escape as a single batch (Rollinson, 1993):

(Eq. 9.3) $$C_i^{liq} = \frac{C_i^0}{D + F(1 - D)}$$

where C_i^{liq} is the concentration of element i in the melt, C_i^0 is the concentration of element "I" in the source, D is the partition coefficient and F the degree of partial melting.

If "i" is a strongly incompatible element with $D \approx 0$, than the previous equation can be re-written as:

(Eq. 9.4) $$C_i^{liq} = \frac{C_i^0}{F}$$

meaning that the concentration of the element in the liquid is dependent only on the degree of partial melting.

The (Eq. 9.3) was transformed by Minster & Allègre (1978) which shows the relationship between two trace elements "i" and "j":

(Eq. 9.5) $$\frac{C_i^{liq}}{C_j^{liq}} = \frac{D_j - D_i \times \frac{1 - D_j}{1 - D_i}}{C_j^0} \times C_i^{liq} + \frac{C_i^0}{C_j^0} \times \frac{1 - D_j}{1 - D_i}$$

This equation (Eq. 9.5), can be compared to the equation of a straight line defined by two element on a diagram (C_j^{liq} / C_i^{liq}), where A_j is the slope and B_j is the point where the line crosses the Y-axis:

(Eq. 9.6) $$A_j = \frac{D_j - D_i \times \frac{1-D_j}{1-D_i}}{C_j^0}$$

(Eq. 9.7) $$B_j = \frac{C_i^0}{C_j^0} \times \frac{1-D_j}{1-D_i}$$

Again, both equations (Eq. 9.6) and (Eq. 9.7) can be simplified if $D_j >> D_i$ and $D_i \approx 0$, into:

(Eq. 9.8) $$A_j = \frac{D_j}{C_j^0}$$

(Eq. 9.9) $$B_j = \frac{C_i^0}{C_j^0} \times \left(1 - D_j\right)$$

These two simplified equations allow to calculate the partition coefficients of the elements without any assumption on the residual mantle paragenesis; however, some assumptions have to be made as the initial concentration of an element in the mantle source.

Usually the chosen element to calculate the degree of partial melting is Yb, because it is very compatible with residual garnet, its concentration does not vary considerable in the mantle and it is reasonable to assume that its concentration in the mantle source is 2 to 4 times the concentration in the chondrites (Clague &Frey, 1982).

So, assuming that the concentration in Yb in the mantle source is 3 times the concentration in the chondrites (0.483=3 x 0.161; McDonough & Sun, 1995) and re-calculating the concentrations of Yb and La in the initial liquid (reverse crystallization of olivine; Danyushevsky, 2000), it is possible to calculate D_{Yb}. In the diagram of Fig. 9.14, the regression of the most primitive lavas has a slope of 0.422 that used in (Eq. 9.8) calculates a partition coefficient for Yb of $D_{Yb} = 0.204$.

Using the partition coefficient calculated for Yb, the concentration of this element in the liquid before any fractional crystallization and the predicted concentration on the mantle source, in (Eq. 9.3) it is possible to calculate the degree of partial melting (%F) to the most primitive lavas in São Jorge.

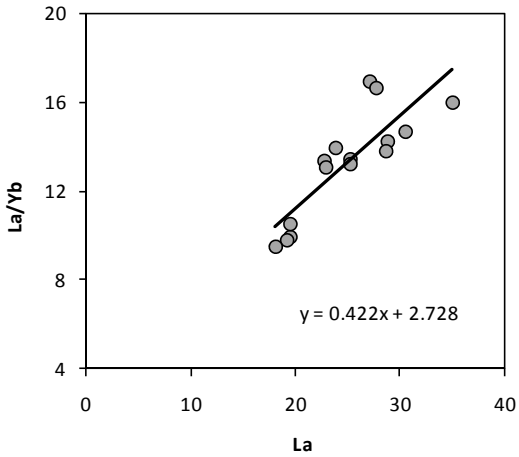

Fig. 9.14 – Concentrations in La and La/Yb of the magmatic liquids in São Jorge after the correction of fractional crystallization of olivine (Danyushevsky, 2000).

According with the results in Table 9.2, the magmas in São Jorge were generated between 2% and 12% of partial melting of the mantle source, which can be considered a large range in the degree of partial melting. Nonetheless, the average degree of partial melting is 7%, and is within the interval proposed by White *et al*. (1979) as the degree for partial melting in the Azores (6 to 13%), an within the most recent estimates made by Bourdon *et al*. (2005) for the region (5 to 6%).

Table 9.2 – This table presents the degree of partial melting from which the magmatic liquids produced the lavas in São Jorge. The lavas shaded in grey are located on the lava sequences that outcrop along the shorelines and correspond to older volcanic events in the volcanic complex. The remaining lavas are related with the most recent events of Topo and Rosais volcanic complexes, from Manadas Volcanic Complex and from the submarine southeast flank of São Jorge.

	Sample	F
Topo Vol. Comp.	SJ50	5%
	SJ63	10%
	SJ65	9%
	SJ70	7%
	SJ103	4%
Rosais Vol. Comp.	SJ89	12%
	SJ92	11%
	SJ29	3%
	SJ99	6%
	SJ101	4%
Manadas Vol. Comp.	SJ77	10%
	SJ79	2%
Pillow lavas	D01-011	5%
	D01-018	6%
	D01-019	7%

The comparison of the calculated degrees of partial melting with the concentrations in La, used previously as an indicator of this process, shows that the lavas with higher La content are in fact the ones that went through smaller degrees of partial melting (Fig. 9.15). However, two different situations are observed in Fig. 9.15. The first is that for the same degree of melting the pillow lavas are depleted in La evidencing a less enrich mantle source, possibly shallower, while the lavas from Rosais Volcanic Complex with the highest degree of partial melting are enriched in La, suggesting that the mantle source, beneath Rosais, must be enriched in incompatible trace elements.

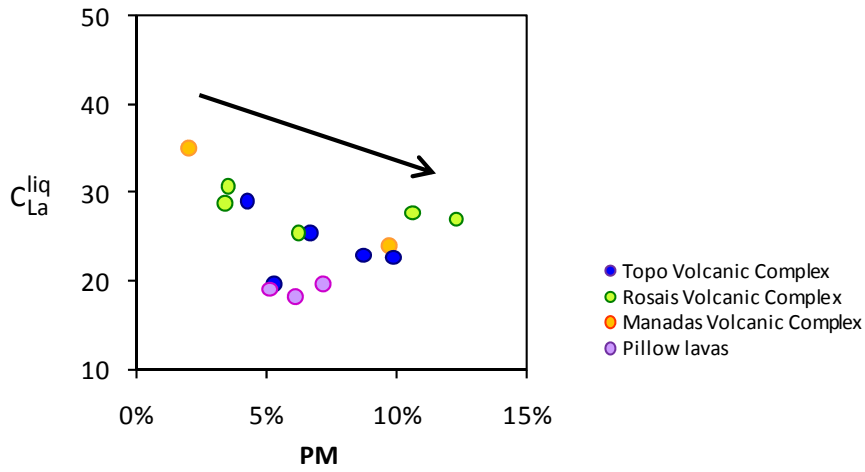

Fig. 9.15 – Comparison between the predicted La concentration in primitive liquids and the degree of partial melting (PM).

Considering the volcanostratigraphy of the island and the stratigraphic position of the lavas, two distinct groups are recognized. The first encompasses the oldest lavas from Topo Volcanic Complex, SJ50, SJ63, SJ65 and SJ70, and lavas from Rosais Volcanic Complex, SJ89 and SJ92, collected along the main volcanic lava sequences, which outcrop on the shorelines (shaded lavas in Table 9.2). A second group of lavas includes the lavas from Manadas Volcanic Complex, the submarine pillow lavas, the lava SJ103 from Topo and the other lavas from Rosais (SJ29, SJ99, SJ101) representing either the most volcanic events on the island or the most recent volcanic eruptions of each complex.

In the first group, the average degree of partial melting is approximately 9%, while for the second group (with the exception of lava SJ77) the average degree of partial melting is 5%. The differences obtained for lavas with different volcanostratigraphic positions, suggest that the older

lavas from Topo and Rosais volcanic complexes, which edified the main structure of the island, were generated by higher degrees of partial melting, what might be associated with a higher melting production during the early phases of volcanism.

The decrease in the degree of partial melting during the later stages of volcanism in oceanic islands has been described in other islands in the Atlantic as Madeira Island (Mata, 1996) and the Canary Islands (Geldmacher *et al.*, 2005).

9.7 Conditions of Melting: Pressure and Temperature

The mineral characterization of the mantle source based on trace element concentrations presented earlier, suggests that the magmatic liquids generating São Jorge lavas were extracted from an enriched mantle source in the presence of garnet. The stability field of garnet in the mantle mineralogy requires pressures higher than 25 kbar (≈75 km), so according with trace element data, the lavas should have been extracted at higher pressures.

Pressure and temperature conditions in which melting of the mantle occurred can be estimated based on major element data using Albarède (1992) or Haase (1996) methods.

Albarède (1992) establish a method to estimate pressure (P) and temperature (T) of magma extraction using major elements, considered to be insensitive to mantle process that create heterogeneities e.g. SiO_2, MgO, FeO and CaO. This method is based in experimental data and uses SiO_2 and MgO concentrations, which are compatible elements and are independent of source composition and of the degree of partial melting:

(Eq. 9.10) $$T(ºC) = 2000 \times \frac{MgO}{SiO_2 + MgO} + 969$$

(Eq. 9.11) $$LnP(kbar) = 0.0025 \times T(ºC) - 0.12 \times SiO_2 + 5.027$$

The method was applied to the most primitive lavas (Ni: 214-316 ppm; Mg#: 71-74%), but their compositions was corrected for olivine fractionation (Fo_{90}). The results are presented in Table 9.3 and show that lavas from Rosais Volcanic Complex were extracted from a deeper source (≈75 km) and at higher temperatures (≈1432 °C) than the lavas from Topo Volcanic Complex (≈68 km and ≈1412 °C). The lavas from Manadas Volcanic Complex show distinct values, i.e. lava SJ79 has conditions similar to the lavas from other complexes, but lava SJ77, which is a basanite, indicates that the lava was extracted at much higher temperatures and much deeper in the mantle. The submarine pillow lavas, on the other hand, were extracted at similar temperatures but at shallower depth (≈63 km).

Based on similar concepts as Albarède (1992), Haase (1996) considered that SiO_2 content is unaffected by mantle heterogeneities or by melting processes. Thus, SiO_2 content on the magmas indicates the average pressure generation because it reflects the melting maximum at relatively shallow depth in the melting column. Experimental data on several depleted mantle peridotites gave similar variations of SiO_2 content with pressure, and the regression through the experimental data gives the equation:

(Eq. 9.12) $$P(GPa) = 23.217 - 0.4381 \times SiO_2$$

In this case, the estimated pressures are independent on the concentration in MgO of the magmatic liquids. In addition, (Eq. 9.12) allows to estimate the pressure condition during partial melting and do not go against Albarède (1992) equations, which estimate the conditions during magma extraction. The pressures estimated using Haase (1996) equation are presented in Table 9.3.

The estimates based on (Eq. 9.12) produce considerable higher pressures, which predict deeper melting conditions for São Jorge magmas in the garnet stability field. When pressure is compared to LREE/HREE ratios (Fig. 9.16) shows a good correlation evidencing that garnet becomes more important during partial melting processes as pressure increases. It is also relevant in Fig. 9.16, that melting depth increases from Topo Volcanic Complex, forming the east side of São Jorge, towards Rosais Volcanic Complex, building up the west side of the island (Ribeiro *et al*., 2008). This progression also denotes a temporal evolution of the conditions of melting.

Table 9.3 - Estimated pressure and temperature for lavas from Topo, Rosais and Manadas volcanic complexes and the submarine pillow lavas. The first three columns with the results present the values calculated according with Albarède (1992) method, while the fourth and fifth columns correspond to pressure and depth of melting of the magmatic liquids calculated according with Haase (1996). The results obtained in GPa from (Eq. 9.12) were converted to kbar in this table.

		Albarède (1992)			Haase (1996)	
		Temperature (°C)	Pressure (kbar)	Depth (km)	Pressure (kbar)	Depth (km)
Topo Vol. Comp.	SJ50	1407	21	69	30	100
	SJ63	1427	21	69	28	93
	SJ65	1408	21	68	30	98
	SJ70	1406	20	67	29	97
	SJ103	1411	20	65	28	92
Rosais Vol. Comp.	SJ89	1417	22	73	31	103
	SJ92	1427	23	74	31	103
	SJ29	1454	23	77	30	98
	SJ99	1441	24	79	32	105
	SJ101	1422	22	72	30	100
Manadas Vol. Comp.	SJ77	1477	33	108	40	133
	SJ79	1429	22	73	30	99
Pillow lavas	D01-011	1411	18	60	25	81
	D01-018	1430	20	65	26	85
	D01-019	1428	20	65	26	85

The sample from Manadas Volcanic Complex that displays very high pressures of melting (40 kbar) is a basanite (SJ77). Basanites have lower SiO_2 than the basalts and so, both Albarède (1992) and Haase (1996) equations will estimate high pressures. In addition, experimental work suggests that basanite is not in equilibrium with mantle mineral phases (olivine, orthopyroxene and garnet) if melting occurs under volatile-free conditions (Green, 1973). However, during low degrees of partial melting (<6%) basanite could be generated by melting of wet mantle peridotite under pressures of 20 to 30 kbar (Green, 1973) or in the presence of a high-volatile content (high CO_2/H_2O; Eggler, 1978). What this experimental work suggest is that basanite should have been generated under pressures comparable to the other lavas in São Jorge and implies that the mantle source beneath São Jorge is somewhat enriched in H_2O and volatiles (Bonatti, 1990).

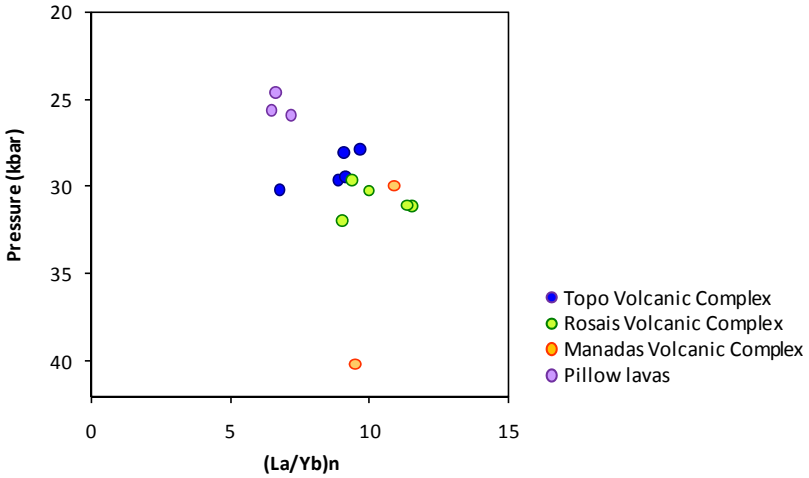

Fig. 9.16 – Estimated pressure and temperature extraction conditions for São Jorge lavas using Albarède (1992) method. In order to avoid changes in major element compositions, the concentrations used in (Eq. 9.12) were corrected for olivine fractionation.

Another important aspect of the melting condition beneath São Jorge is temperature. Haase (1996) showed for most oceanic islands lying above a lithosphere younger than 100 Ma, as the Azores does, that the average pressure of melting lies beneath the thermal boundary layer defined by the 1300°C isotherm. The temperature estimated from Albarède (1992) method is considerable higher (≈100 to 180°C) than the 1300°C predicted for the boundary. The excess of temperature observed, has been also predict by Bourdon *et al*. (2005) for the Azores Plateau, and in particularly, beneath its neighbor Terceira island, where it is located the Azores plume (Moreira *et al*., 1999).

Chapter 10: Isotope Characteristic of São Jorge Lavas: an insight into their Mantle Source

In this chapter are presented new isotopic data from 18 samples from São Jorge Island. Sr, Nd, Hf and Pb isotopes were obtained (1) on one lava flow from Fajã de São João lava sequence, (2) on 6 lavas from Topo Volcanic Complex, (3) on 5 pillow lavas from the southeast submarine flank, (4) on 4 lavas from Rosais Volcanic Complex and (5) 3 lavas from Manadas Volcanic Complex.

In Fajã de São João lava sequence, formed during the first volcanic phase in São Jorge, it was only obtained one isotopic analysis, because at the time, this lava sequence was thought to be a part of Topo Volcanic Complex. As for the pillow lavas collected on the southeast flank of São Jorge, during EMEPC\Açores\G3\2007 cruise, could be considered a part of Topo Volcanic Complex, due to the proximity and some of the geochemical similarities observed.

10.1 Isotopes

New Sr, Nd, Hf and Pb isotope data obtained on São Jorge lavas are presented here. The $^{87}Sr/^{86}Sr$ isotope ratios measured on the lavas broaden between 0.70306 and 0.70402, while $^{143}Nd/^{144}Nd$ varies between 0.51282 and 0.51292 and $^{176}Hf/^{177}Hf$ ranges within 0.28291 and 0.28311. For these three isotopic systems, Topo Volcanic Complex and the submarine pillow lavas, with one exception, form a cluster presenting similar isotopic signatures with the highest $^{143}Nd/^{144}Nd$ and $^{176}Hf/^{177}Hf$ ratios and with intermediate $^{87}Sr/^{86}Sr$ (Fig. 10.1). In contrast, the lavas from Manadas and Rosais volcanic complexes are more spread in the isotopic fields and exhibit slightly lower

$^{143}Nd/^{144}Nd$ and $^{176}Hf/^{177}Hf$, but in terms of $^{87}Sr/^{86}Sr$ the lavas from Rosais Volcanic Complex have higher and lower values when compared with Topo. The isotopic analysis on the lava from Fajã de São João sequence presents intermediate values for the Nd and Hf isotopic ratios (Fig. 10.1) but similar $^{87}Sr/^{86}Sr$ to the lavas from Topo Volcanic Complex.

Lead isotopic ratios in the majority of São Jorge lavas (Fig. 10.1) exhibits a wide variation for $^{206}Pb/^{204}Pb$ ranging from 18.93 to 20.36, while $^{207}Pb/^{204}Pb$ and $^{208}Pb/^{204}Pb$ ratios displays a more limited range with values between 15.61 and 15.65 for $^{207}Pb/^{204}Pb$, and between 39.09 and 39.43 for $^{208}Pb/^{204}Pb$. The lava from Fajã de São João, the oldest lava sequence in the island, has intermediate $^{206}Pb/^{204}Pb$ of 19.35 but lower $^{207}Pb/^{204}Pb$ and $^{208}Pb/^{204}Pb$ ratios of 15.55 and 38.76 respectively.

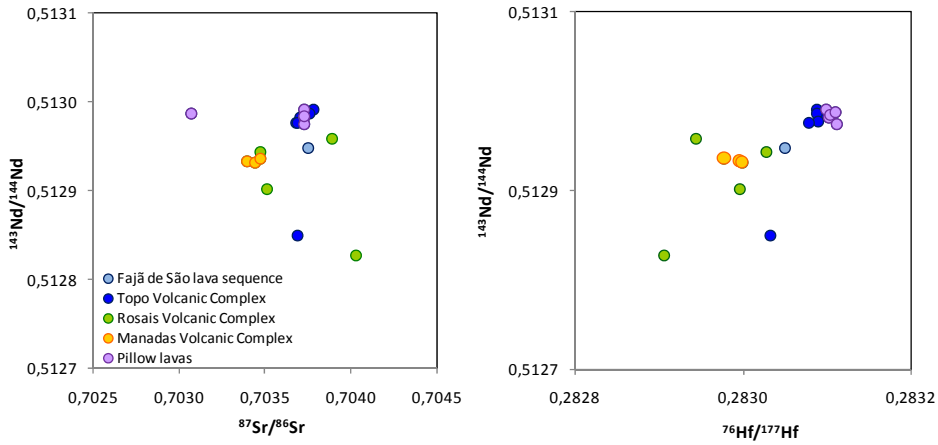

Fig. 10.1 – Sr, Nd, Hf and Pb isotopic ratios obtained on the five lava groups considered in this study for São Jorge Island. The lavas from Topo Volcanic Complex and the submarine pillow lavas have similar Sr, Nd and Hf isotopic compositions, with higher Hf and Nd isotope ratios and intermediate Sr than the lavas from Rosais and Manadas volcanic complexes. The lava from Fajã de São João has intermediate values between both groups

From the $^{206}Pb/^{204}Pb$ vs. $^{208}Pb/^{204}Pb$ diagram (Fig. 10.2) it is possible to observe that lavas split into two distinct arrays. In fact, samples collected east of the Ribeira Seca Fault, on Topo Volcanic Complex and on the submarine flank, are well correlated (r^2 = 0.93) and define a trend that extends from $^{206}Pb/^{204}Pb$ = 19.87 to $^{206}Pb/^{204}Pb$ = 20.36 (y=0.682x+25.525), with its most radiogenic and stratigraphically most recent lava located at the summit of Fajã dos Cubres

sequence. Conversely, the lavas recovered on Manadas and Rosais volcanic complexes, also well correlated (R^2 =0.88), form a less steep array crossing the NHRL[15], (y=0.212x+35.076), that extends from $^{206}Pb/^{204}Pb$ = 19.93 to one of the most unradiogenic isotope ratios ($^{206}Pb/^{204}Pb$ = 18.93) found on the Azores.

In a $^{206}Pb/^{204}Pb$ vs. $^{87}Sr/^{86}Sr$ diagram (Fig. 10.3) it is also possible to make a clear distinction between the lavas from the east side and the lavas from Rosais and Manadas volcanic complexes. The first form a horizontal trend with constant $^{87}Sr/^{86}Sr$, while the second, curiously, display a negative correlation where the most $^{87}Sr/^{86}Sr$ enriched lavas have the less radiogenic lead. Also, combining lead isotopes as in $(^{208}Pb/^{206}Pb)^*$ with Hf isotopes, the lavas from Topo Volcanic Complex and the submarine flank form a cluster with lower $(^{208}Pb/^{206}Pb)^*$ and higher $^{176}Hf/^{177}Hf$, while the most recent lavas from Rosais and Manadas volcanic complexes correlate negatively. Remarkably, the lava from Fajã de São João fit the trend developed by the western lavas on Fig. 10.3.

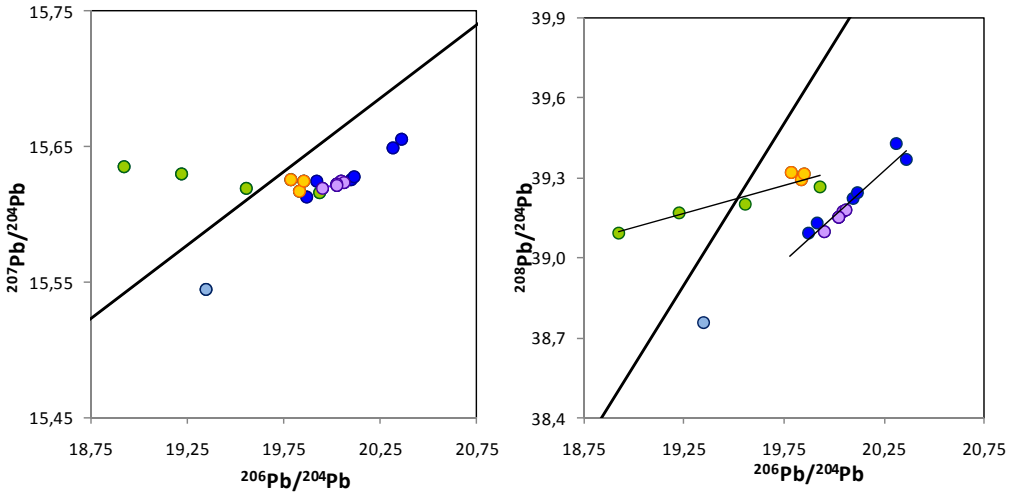

Fig. 10.2 – Lead isotopic ratios obtained on the five lava groups of São Jorge Island. On the $^{206}Pb/^{204}Pb$ vs.$^{208}Pb/^{204}Pb$ diagram the lavas for two distinct arrays. The lavas from Topo Volcanic Complex and from the submarine pillow lavas, both located east of Ribeira Seca Fault, form a steeper trend (y=0.682x+25.525) than the lavas from Rosais and Manadas volcanic complexes that plot along a shallower trend (y=0.212x+35.076) and cross the North Hemisphere Reference Line (NHRL), see APPENDIX III. The same two trends are present on the $^{206}Pb/^{204}Pb$ vs.$^{207}Pb/^{204}Pb$ diagram although the distinction between the two sets is more discrete. The $^{207}Pb/^{204}Pb$ isotopic ratios of the lavas from Rosais increase slightly as the $^{206}Pb/^{204}Pb$ ratio decreases. The lava from Fajã de São João lava sequence is located on the extension of the lavas from the east side but has considerable lower $^{207}Pb/^{204}Pb$ and $^{208}Pb/^{204}Pb$ ratios. Legend as in Fig. 10.1.

[15] NHRL – North Hemisphere Reference Line

Overall, the combination of the four isotopic systems, and in particularly of lead isotopes, separates São Jorge lavas into two groups with different signatures. One of the groups corresponds to the lavas from Topo Volcanic Complex and the submarine pillow lavas, and the second encompasses the lavas from Manadas and Rosais volcanic complexes. The change in the isotopic signature between Topo and Rosais could be related with the temporal evolution of the island, although it seems unlikely because Manadas, the most recent volcanic complex, has intermediate isotopic composition between Topo signature and the extreme compositions of Rosais. Instead, if these isotopic ratios mimic the isotopic signature of the mantle source located below each sample, then lavas from Topo and the submarine flank, both located on the east side of Ribeira Seca Fault, sample a mantle with similar isotopic signature, which becomes different towards the west side of the of the island beneath Manadas and Rosais volcanic complexes. Thus, these two different arrays could be denominated as the eastern and western isotopic signatures.

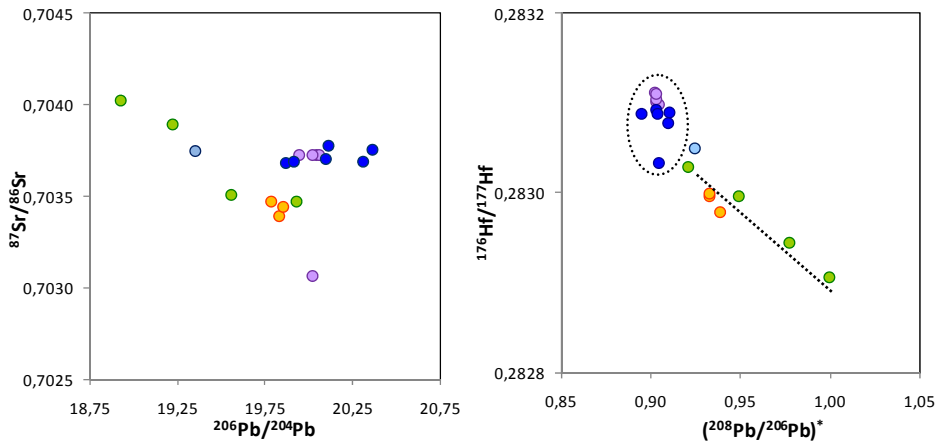

Fig. 10.3 – Diagrams showing the combination of lead isotopes with $^{87}Sr/^{86}Sr$ and $^{176}Hf/^{177}Hf$. On both diagrams the western lavas developed a negative array while the eastern lavas present variable $^{206}Pb/^{204}Pb$ for a given $^{87}Sr/^{86}Sr$ composition and a homogeneous composition on the $(^{208}Pb/^{206}Pb)^*$ vs. $^{176}Hf/^{177}Hf$ diagram. Legend as in Fig. 10.1.

In many situations, as in the $^{206}Pb/^{204}Pb$ vs. $^{207}Pb/^{204}Pb$ isotopic space, samples forming linear arrays represent isochrones, which slope is proportional to the age. If this were the case for the eastern lavas then it would correspond to an age of approximately 1.2 Ga but, as it will be seen further ahead, this linear array also corresponds to a binary mixing. On the other hand, the western lavas from Rosais and Manadas volcanic complexes developed a sub-horizontal linear array crossing the NHRL and thus delivering a zero age. In this case, the trend defined by Rosais

and Manadas is better explained by the mixing between two mantle end-members with extreme isotopic compositions. One of these end-members has very unradiogenic $^{206}Pb/^{204}Pb$ while the other, has higher $^{206}Pb/^{204}Pb$ ratios that are similar to the isotopic signature of Topo Volcanic Complex.

The recent work of Millet *et al.* (2009) also based on Sr, Nd and Pb isotopic data brought a new insight into São Jorge isotopic signature. In terms of lead, Millet *et al.* (2009) isotope ratios are similar to the ones presented in this work and make the distinction between the lavas form the east and west side of the island. Nonetheless, two of Millet *et al.* (2009) lavas from Topo have more radiogenic lead than the ones presented in this study. In addition, his lavas from Rosais lavas are not sufficiently unradiogenic to plot on the left of the NHRL and the lava from Fajã de São João sequence has higher $^{207}Pb/^{204}Pb$ and $^{208}Pb/^{204}Pb$ isotope ratios but the same $^{206}Pb/^{204}Pb$. In terms of Sr and Nd isotopes, Millet *et al.* (2009) presents very similar values to the data in this study, with Topo Volcanic Complex having slight higher Nd and Sr ratios that the lavas from Rosais and Manadas volcanic complexes.

10.2 The Isotopic Signature of São Jorge in the Azores Context

The Azores Archipelago is characterized by an uncommonly large isotopic diversity interpreted as the reflex of small-scale mantle heterogeneities (40 - 100 km), where for example São Miguel, Terceira and Graciosa islands define three distinct isotopic arrays. Isotopic diversity is also detected at even smaller scales on a single island as in São Miguel, where the Sete Cidades Complex is comparatively less radiogenic than Nordeste complex (e.g. Turner *et al.*, 1997; Widom *et al.*, 1997 and Beier *et al.*, 2006).

On the Sr-Nd diagram (Fig. 10.4) São Jorge lavas are clearly overlapping the composition of the other islands of the central group and the less enriched lavas from São Miguel. Nonetheless, small differences can be noted in São Jorge for the westerns lavas (Rosais and Manadas) that seem more similar to several lavas from Graciosa, Pico and São Miguel, while the eastern lavas (Topo and the submarine pillow lavas) exhibit comparable $^{143}Nd/^{144}Nd$ with Terceira but with slight higher $^{87}Sr/^{86}Sr$ ratios.

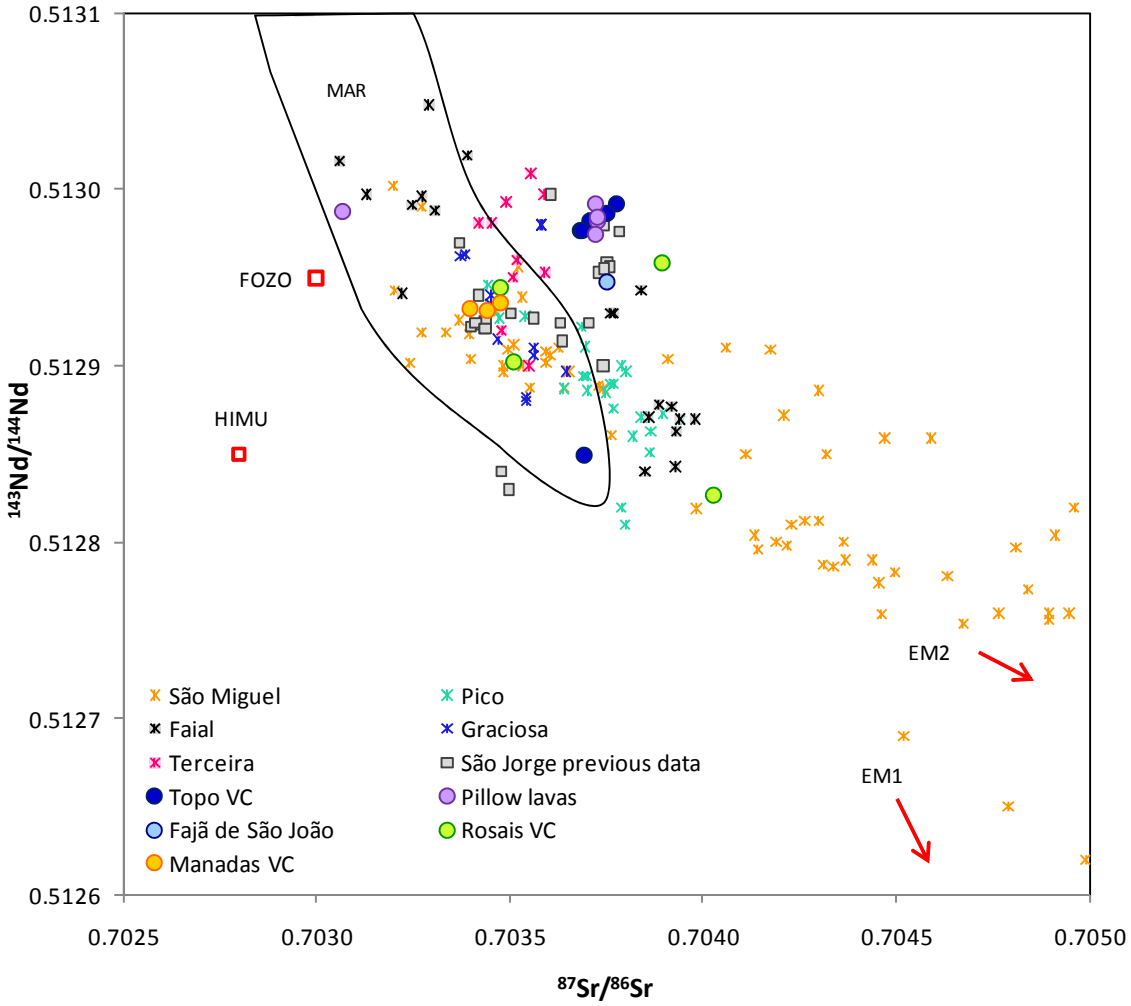

Fig. 10.4 – Diagram showing the Sr and Nd isotope data of the lavas of São Jorge presented in this study and the isotopic composition of the lavas from the Azores Islands, São Miguel, Terceira, Graciosa, Pico and Faial, combined with previously data from São Jorge and the records from the MAR at the Azores latitude. Mantle end members DMM, HIMU, EM1 and EM2 from Faure & Mensing (2005), and FOZO from Stracke *et al.* (2005). Azores data from Beier (2006); Beier *et al.* (2007, 2008; Davies *et al.* (1989); Dupré *et al.* (1982); Elliot *et al.* (2007); França (2000); França *et al.* (2006); Halliday *et al.* (1992); Hawkesworth *et al.* (1979); Jochum *et al.* (1997); Machado *et al.* (2008); Millet *et al.* (2009); Moreira *et al.* (1999); Oversby (1971); Pfandër *et al.* (2007); Snyder *et al.* (2004); Sun (1980); Turner *et al.* (1997); White *et al.* (1979); Widom *et al.* (1997). MAR isotope data from PetDB database.

On the Pb-Pb bi-dimensional plots is where the Azores islands reveal more clearly their differences (Fig. 10.5 and Fig. 10.6). São Miguel plots above the NHRL ranging between the MAR signature and very radiogenic $^{207}Pb/^{204}Pb$ and $^{208}Pb/^{204}Pb$, while Terceira extends from the MAR towards more radiogenic $^{206}Pb/^{204}Pb$ and Graciosa has variable $^{206}Pb/^{204}Pb$ for a given $^{207}Pb/^{204}Pb$. Each isotopic array has been attributed to mixing between mantle components: one “enrich”

mantle component with a specific composition that characterized each island and a depleted component related to the close presence of the MAR. In fact, the isotopic array of the islands along Terceira Rift and the basalts erupted on the MAR converge to a single composition with $^{87}Sr/^{86}Sr = 0.7035$, $^{143}Nd/^{144}Nd = 0.5129$ and $^{206}Pb/^{204}Pb = 19.5$, as outlined by (Beier *et al.*, 2008).

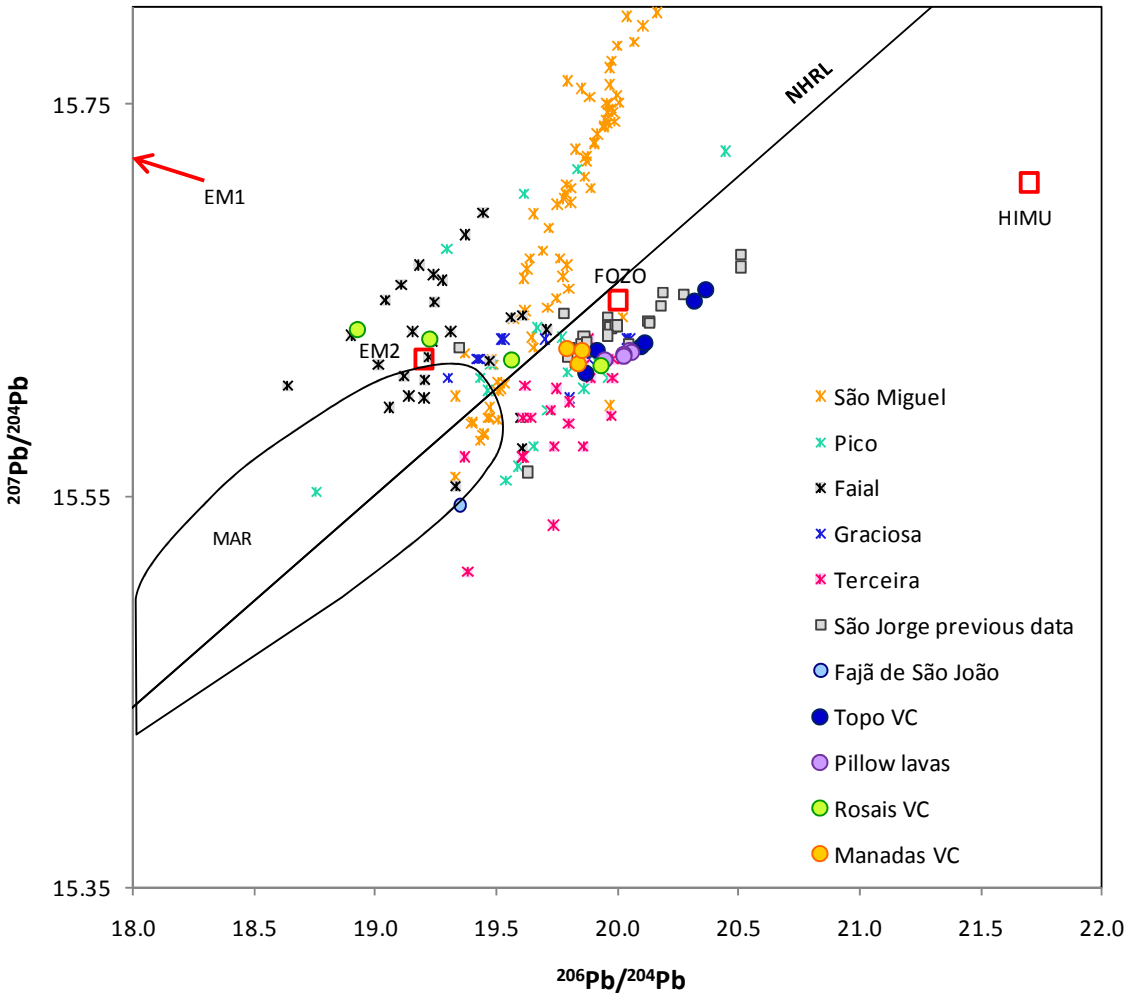

Fig. 10.5 – Comparison between $^{206}Pb/^{204}Pb$ vs. $^{207}Pb/^{204}Pb$ isotope ratios of the Azores region encompassing São Miguel, Terceira, Graciosa, Pico, Faial and previous data on São Jorge and the data presented in this study. MAR isotope field from data on the lavas of the ridge at the Azores latitude. Data source as in Fig. 10.4.

In lead isotopic space, the lavas from the eastern side of São Jorge clearly overlap Terceira array, although some samples are more radiogenic while, the western lavas overlap Graciosa array and trend towards the unradiogenic Faial signature. Both São Jorge arrays merge to a common composition with average $^{206}Pb/^{204}Pb = 20.0$ and $^{207}Pb/^{204}Pb = 15.6$ similar to the intersection point between Terceira and Graciosa arrays as reported by Beier *et al.* (2008). The convergence of the

isotopic composition of Terceira, Graciosa and São Jorge, in terms of lead isotopes, suggests that the central island group, with the exception of Faial, has a common isotopic signature. In addition, this convergence point falls inside the field of the FOZO mantle component redefined recently by Stracke *et al.* (2005).

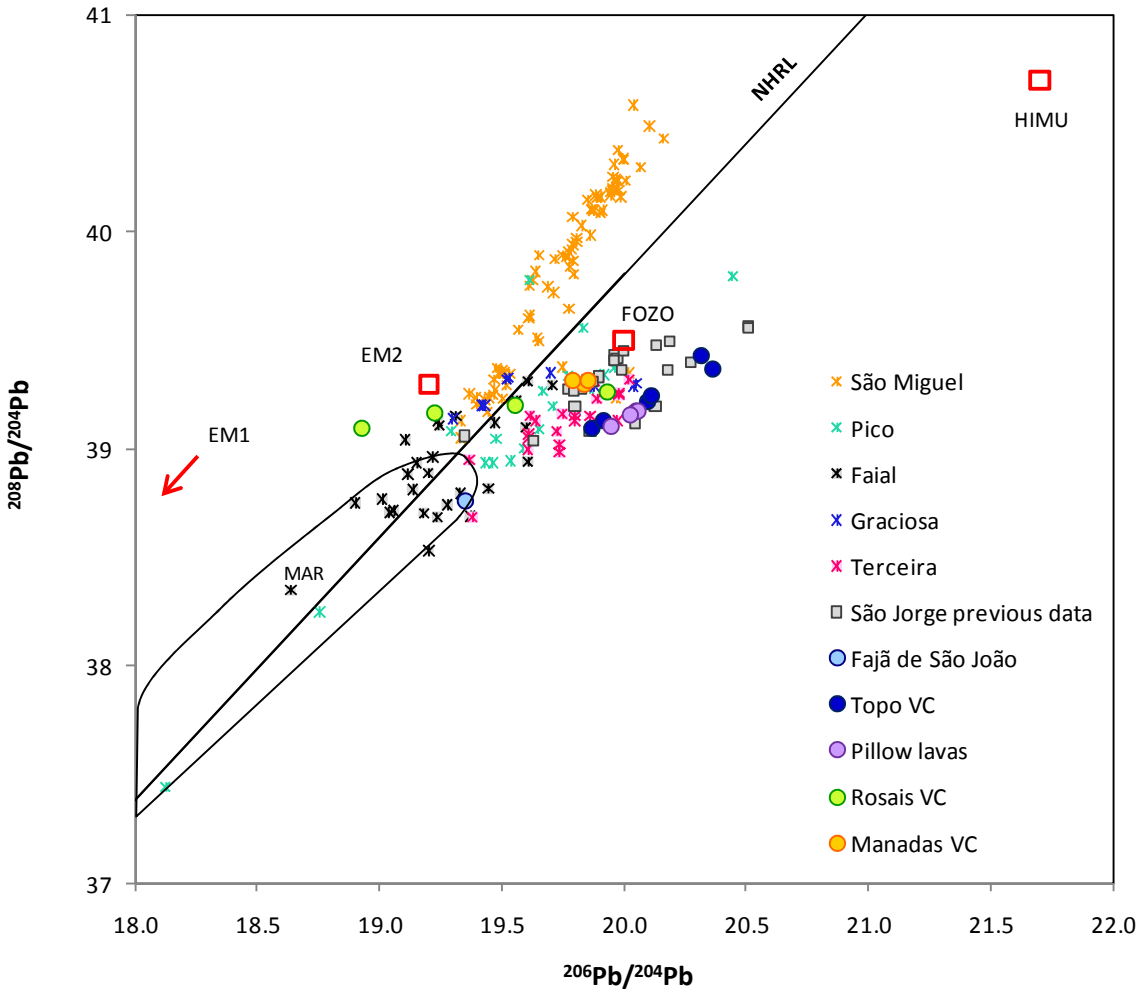

Fig. 10.6 – Comparison between $^{206}Pb/^{204}Pb$ vs. $^{208}Pb/^{204}Pb$ isotope ratios of the Azores region encompassing São Miguel, Terceira, Graciosa, Pico, Faial and previous data on São Jorge and the data presented in this study. MAR isotope field from data on the lavas of the ridge at the Azores latitude. Data source as in Fig. 10.4.

Until now, Hf isotopic data on the Azores was limited to São Miguel and Pico islands (Elliot *et al.*, 2007). São Miguel displays on εNd–εHf space (Fig. 10.7) a remarkably linear array with a stepper trend than the mantle array. In comparison, the eastern lavas from São Jorge show higher $^{206}Pb/^{204}Pb$ isotopic ratios relative to São Miguel and plot in the intersection of São Miguel array and the mantle array, while several of the western lavas fall below São Miguel array.

Curiously, the western lavas of São Jorge (Rosais and Manadas) plot below São Miguel array showing lower εHf for a given εNd.

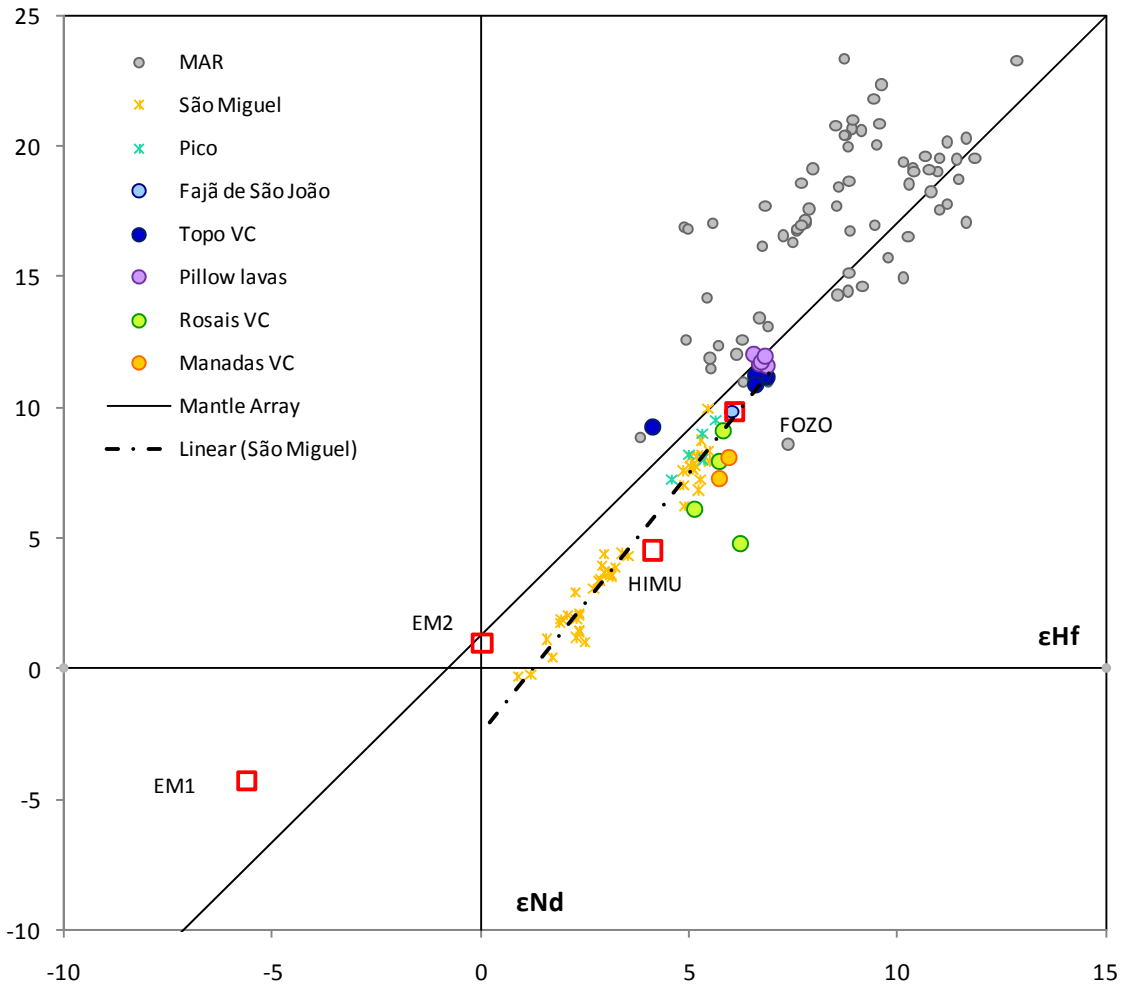

Fig. 10.7 – Diagram showing the εNd vs. εHf isotope data of the lavas of São Jorge presented in this study and the isotopic composition of the lavas from São Miguel and Pico islands, combined with data from the records from the MAR at the Azores latitude. The lavas from São Miguel Island form a stepper array than the mantle Array. Mantle end members DMM, HIMU, EM1 and EM2 from Faure & Mensing (2005) and FOZO from Stracke *et al*. (2005). Mantle Array from São Miguel and Pico data from Elliot *et al*. (2007). MAR data from PetDB.

10.3 Lead Isotopes and κ_{Pb} in São Jorge

The U-Th-Pb system is a special case in the "isotope world" because U decays to two different stable Pb isotopes while Th decays to a third Pb isotope. Because all three elements have

different geochemical behaviors, lead isotopes are a powerful interpreter of past and present petrogenetic processes.

The rate to which both U decay (^{238}U and ^{235}U) to lead is very different and is faster for the ^{235}U-^{207}Pb system with a halflife of $0.7038*10^{9}$ years than the ^{238}U-^{206}Pb system which has halflife of $4.468*10^{9}$years (see APPENDIX III for equations). Therefore, if a reservoir as the early earth with a certain U/Pb ratio ($\mu=^{238}U/^{204}Pb$) is in a close system, i.e. without any gain or loss of U and Pb, then the reservoir will evolve isotopically presenting a curved path, which evidences an early growth of $^{207}Pb/^{204}Pb$ ratio and the latter growth of $^{206}Pb/^{204}Pb$ ratio (Fig. 10.8).

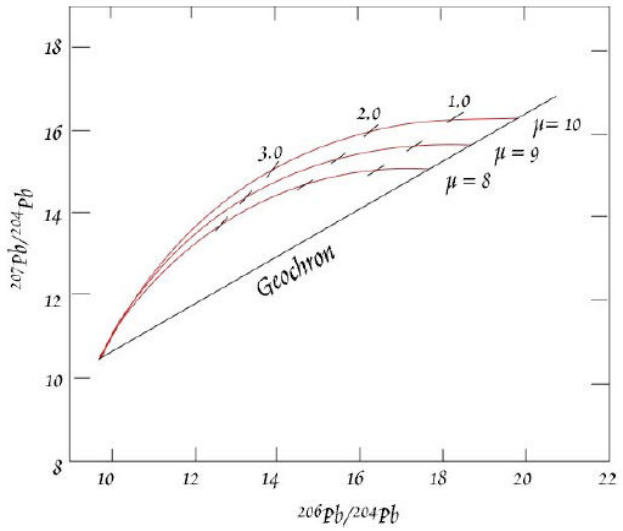

Fig. 10.8 – Diagram showing the evolution of Pb isotope ratios through time. The curve lines represent the evolutionary paths for systems having μ values of 8, 9 and 10. The hash marks on the evolution curves mark Pb isotope compositions 1.0, 2.0, and 3.0 Ga ago and define straight lines. For the present, lead isotopes converge to the straight line called Geochron. Adapted from White online Geochemistry book[16]

For different reservoirs with different initial μ (e.g. μ=8, 9 or 10; Fig. 10.8), isotopic decay will developed distinct curve paths through time, but for specific time value in each curve, samples plot along a straight line called isochron. From all possible isochrones, the one that represents the present, i.e. time = 0, is called the Geochron.

[16] http://www.imwa.info/geochemistry/

However, lead isotopes are involved in the "lead paradox" that results in the fact that mantle reservoirs, which originate MORB and OIB, plot on the right of the Geochron, contradicting the expected geochemical behavior of Th-U-Pb for large-scale mantle-crust evolution and differentiation during earth history. Regardless of the discussion surrounding this major issue, the fact that OIB and in particular the Azores lavas plot on the right of the Geochron, indicates that the mantle source generating these lavas, at a certain point in the past, was characterized by an increase in U/Pb ratios.

The dependence of $^{207}Pb/^{204}Pb$ and $^{206}Pb/^{204}Pb$ isotope ratios from early U/Pb ratios indicate that these must have increase sometime earlier in the past in order to produce those values. In particular, the HIMU mantle component (high μ) defined by Zindler & Hart (1986), which is frequently identified in MORB and in some ocean island basalts has been attributed to the fractionation between U and Pb during subduction processes and recycling of altered oceanic crust, produces very high $^{206}Pb/^{204}Pb$ ratios.

The μ values where determined for São Jorge Island using the equations on Appendix III. The average $^{206}Pb/^{204}Pb$ isotope ratio of the whole island is 19.86 delivering a μ_{206} of 10.3, while the average $^{207}Pb/^{204}Pb$ in São Jorge of 15.62 yields a μ_{207} of 8.4.

The decay of Th to ^{208}Pb has a halflife of $14.010*10^9$ years, which is greater than the decay of ^{238}U to ^{206}Pb, and can be measure according with equations in Appendix III. The decay of both Th and ^{238}U can be combined by using the equations established for the two daughters lead isotopes, ^{206}Pb and ^{208}Pb, in:

(Eq. 10.1) $$\kappa_{Pb} = \left(\frac{^{208}Pb}{^{206}Pb} \right)^{*} \times \frac{\left(e^{\lambda_{238} t} - 1 \right)}{\left(e^{\lambda_{232} t} - 1 \right)}$$

The equation (Eq. 10.1) based on the present measurements of radiogenic lead, indicates the time-integrated evolution of Th/U ratio since the beginning of the earth at $4.55*10^9$y; hence, an ideal reservoir evolving in a close system should have the same Th/U ratio (i.e. a fix $^{232}Th/^{238}U$), as the time integrated Th/U ratios derived from κ_{Pb}. However, Galer & O'Nions (1985), which considered that the primitive mantle has κ_{Pb}=3.9, compared Th/U elemental ratios with κ_{Pb} values on MORB and obtained for the first ratio an average value of approximately 2.5 and for the

second an average of 3.7. The large difference between the values has strong implications on the dynamics of the upper mantle considered the source of MORB. The low Th/U elemental ratios of the source indicate that they could not have a residence time superior to 600 Ma (White, online Geochemistry book) because after that period the isotopic decay of both elements would affect κ_{Pb} values.

Nonetheless, the different Th/U ratios on the primitive mantle and MORB should result from the fractionation between both elements during the processes attributed to the evolution of the upper mantle and its interaction with the lower mantle. The fractionation between Th and U can be depict from different geochemical behaviors like in magmatic processes, due to distinct partition coefficients, or in the presence of fluids, where Th is an immobile element while U is considered mobile. Thus, it is likely that during these processes Th/U ratios changed.

In São Jorge, κ_{Pb} values where calculated for the lavas and the results are presented in Fig. 10.9. In all cases the time integrated Th/U ratios are greater than the present Th/U ratios measured from trace element concentrations so, the samples plot on the left of the line for an "ideal reservoir" where κ_{Pb} =Th/U is expected. This implies that the mantle source needed to have some time in the past higher Th/U ratios due to U depletion (or Th enrichment) in order to produce the present κ_{Pb} values. At the island scale, the κ_{Pb} values change considerably from an average value of 3.67 on the lavas from the east side of São Jorge, towards increasing values on the lavas from Rosais Volcanic Complex at a maximum of 4.06. This makes a clear distinction between the lavas of both arrays and suggests that some king of small-scale ancient mantle heterogeneity should be responsible for these differences on a single island. It is of notice that κ_{Pb} value for the lava from Fajã de São João is similar to the lavas from Rosais and Manadas, i.e. the west side of São Jorge.

The idea that the lavas forming the eastern array developed an isochron with 1.2 Ga in the $^{207}Pb/^{204}Pb$ vs. $^{206}Pb/^{204}Pb$ diagram (Fig. 10.5) contradicts the results of Fig. 10.9. The fact that these lavas have lower Th/U ratios than expected from κ_{Pb} suggests that the mantle source went through considerable changes, i.e. Th/U fractionation, and that is not in radioactive equilibrium. Thus, the regression defined by the eastern lavas in the $^{207}Pb/^{204}Pb$ vs. $^{206}Pb/^{204}Pb$ diagram, that resemble an isochron could probably be the result of a mixing between different components.

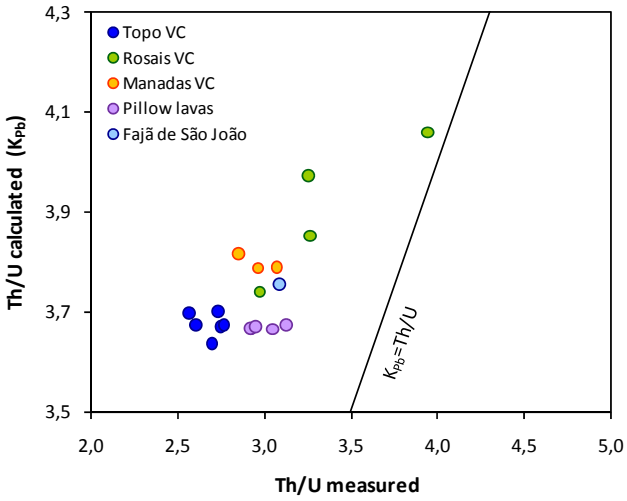

Fig. 10.9 – Comparison between the Th/U elemental ratios on São Jorge lavas and the κ_{Pb} values calculated using (Eq. 10.1).

10.4 The Particular εNd and εHf Isotopic Composition of São Jorge

The Lu and Hf isotopic system is, in many ways, similar to Sm-Nd, due to their geochemical behavior, although the decay of ^{176}Lu to ^{176}Hf has a shorter halflife of 35.7*10^{9}years when compared to the decay of ^{147}Sm to ^{143}Nd with a halflife of 1.06*10^{11} years (see Appendix III for equations).

Geochemically, these elements are relatively immobile so it is not expected to have strong parent/daughter fractionation during weathering or in the presence of a fluid phase. During magmatic processes, Hf and Nd are more incompatible than Lu and Sm entering preferentially, into the melt phase, in particularly in the presence of garnet because it inhibits Lu from entering the melt, thereby increasing Lu/Hf of the residual solids and producing important constrains in terms of isotopic signatures. Due to this, at the earth scale, the mantle has average higher Lu/Hf and Sm/Nd ratios than the crust, making higher, present-day, ^{176}Hf/^{177}Hf and ^{143}Nd/^{144}Nd isotopic composition on the mantle. Nonetheless, in both cases elements are refractory so it is possible to assume that the bulk earth has Lu/Hf and Sm/Nd close to chondrites.

The ε notation, which gives the measure of Hf and Nd isotopes relative to bulk earth (or CHUR[17]), is determined by equations:

(Eq. 10.2) $$\varepsilon_{Hf}^{sample} = \left[\frac{\left({}^{176}Hf/{}^{177}Hf \right)_{sample}}{\left({}^{176}Hf/{}^{177}Hf \right)_{CHUR}} - 1 \right] * 10^4$$

and

(Eq. 10.3) $$\varepsilon_{Nd}^{sample} = \left[\frac{\left({}^{143}Nd/{}^{144}Nd \right)_{sample}}{\left({}^{143}Nd/{}^{144}Nd \right)_{CHUR}} - 1 \right] * 10^4$$

with $\left({}^{176}Hf/{}^{177}Hf \right)_{CHUR,present} = 0.282772$ and $\left({}^{143}Nd/{}^{144}Nd \right)_{CHUR,present} = 0.512638$ (both from DePaolo & Wassenburg, 1976, *in* Faure and Mensing, 2005)

Samples with high εHf and εNd have higher $^{176}Hf/^{177}Hf$ and $^{143}Nd/^{144}Nd$ ratios than the corresponding values of CHUR for Hf and Nd. Consequently, mantle-derived volcanic rocks have positive ε, while crustal rocks have negative ε for both elements. However, the similarity of the geochemical properties of Lu-Hf and Sm-Nd causes isotope ratios of samples to be positively correlated, along a regression line called Hf-Nd mantle array. This regression line is defined by equation:

(Eq. 10.4) εNd=-3.6148+0.5737εHf

The position of sediments can be displaced from this mantle array because some mineral in sedimentary deposits as zircon are extremely enriched in Hf. Therefore, some old sediments will have lower εHf for a given εNd and will plot below the mantle array, and will evolve through a different isotopic path.

The εHf and εNd in São Jorge exhibit positive values as expected for ocean island basalts but two different clusters are observed. One for the lavas from Topo and the submarine flank, the eastern

[17] CHUR: Chondritic Uniform Resevoir.

lavas, showing isotopic compositions closer to the MAR while the lavas from Rosais have lower εHf and εNd and trend to values lower than the mantle array and the even São Miguel array.

10.5 Characterization of the Mantle Source Components on São Jorge

The combination of the lead isotopes with the other three isotopic systems, Sr, Nd and Hf allows characterizing the nature of São Jorge mantle source. According with the previous description, the lavas on São Jorge form different mixing arrays with variable $^{206}Pb/^{204}Pb$ and $^{208}Pb/^{204}Pb$ ratios, what, in conjunction with their geographical location relative to Ribeira Seca Fault, divides the lavas into the western and eastern lavas groups. Both arrays have end-members with extreme compositions, but in the other end the arrays converge to common $^{206}Pb/^{204}Pb$, $^{207}Pb/^{204}Pb$, $^{176}Hf/^{177}Hf$ and $^{143}Nd/^{144}Nd$ isotopic composition.

Overall, the differences observed on the isotopic compositions of each group suggest that each side of São Jorge Island samples different mantle signals. Mantle heterogeneities have been described on the Azores, even at island scale as in São Miguel Island, where is commonly described exotic components influencing the isotopic signature of the lavas. Usually, the differences observed on the isotopic composition are accompanied by clear differences on the geochemistry of trace elements. What is puzzling in São Jorge is that only the isotopic signatures make a clear distinction between the eastern and western lavas. One explanation for this might be that the fertilization of the mantle source was relatively discreet and that magma generation beneath the island homogenized trace elements signatures leaving isotopes as evidence of this fertilization.

The origin of the mantle heterogeneity beneath São Jorge could have more than one explanation. Melting processes beneath São Jorge occurred through different degrees of partial melting, at separated geographic locations and at different depths as presented earlier. Therefore, it could be possible that these melting events sampled small different sources.

Lead isotopes of the western lavas overlap the signature of the MAR suggesting a stronger influence of a depleted component in this side of São Jorge, which is also closer to the MAR.

However, Nd and Hf isotopes combined contradict this hypothesis since these ratios on the western lavas trend away from the MAR signature, thus a different component should have originated this signature. In addition, the continuous isotopic trend defined by the lavas from Rosais which coincides with the westward position of the samples (progressively lower $^{206}Pb/^{204}Pb$, $^{143}Nd/^{144}Nd$ and $^{176}Hf/^{177}Hf$). Therefore, the lack of randomness in isotopes signatures suggests a stronger westward influence of this mantle component.

Conversely, the isotopic signature of São Jorge can be considered at a regional scale, or at least at the scale of the Central Island Group. The islands of Terceira and Faial seem to share similarities with the eastern and western arrays, respectively. Therefore, it could be possible that the mantle source beneath São Jorge sampled two different and larger mantle heterogeneities localized beneath Terceira and Faial.

Considering this, the characterization of the isotopic signature of São Jorge lavas is analyzed here in terms of the distinct components that influence their isotope ratios as well the possible origin for these components.

10.5.1 The Common Mantle Component

The proximity of the Azores to the Mid-Atlantic Ridge (MAR) and the anomalous geochemical composition found on the MAR lavas at the Azores latitude has been attributed to a plume ridge interaction (e.g. Schilling, 1975; White *et al.*, 1975; White *et al.*, 1976). As well, the most depleted isotopic compositions observed in the Azorean islands have been ascribed to the existence a depleted mantle component (Turner *et al.*, 1997; Beier *et al*., 2008; Millet *et al*., 2009). In fact, at the Azores scale, it is consensual that each island has a less radiogenic component, to which Sr and Nd isotope ratios overlap and lead isotope arrays converges, that is common to the isotopic compositions of the MAR basalts in the Azores region. Although the exact nature of the interaction of the MAR processes and the Azores Plateau are not constrained and are debatable, the close presence of the MAR and the development of the Azores Plateau, over the last 20 Ma (Gente *et al*., 2003), could be assumed as a strong component influencing the isotopic compositions of the lithosphere beneath the islands.

For lead isotopes, this less radiogenic component seems to be common to the lava from Fajã de São João lava sequence, to the less radiogenic lavas of the eastern array and to the lavas from the western array. In addition, the high Nd-Hf isotopic signature, in particular for the eastern array, and the relatively low Sr composition of São Jorge points to an affinity with this depleted mantle component.

10.5.2 The Eastern Mantle Component

The lavas from Topo Volcanic Complex and from the submarine flank, which form the eastern isotopic array, define a trend that extends from less radiogenic compositions (the common mantle component) towards a HIMU-like composition (Zindler & Hart, 1986) with high $^{206}Pb/^{204}Pb$ and $^{208}Pb/^{204}Pb$, along a short array sub-parallel to the NHRL. These lavas present also a Pb and Nd isotopic composition that overlaps its neighbor Terceira Island but several samples reach to higher $^{206}Pb/^{204}Pb$ ratios as also showed by Millet *et al.* (2009). The resemblance of this trend with Terceira and also to a HIMU-like source bring important implications for all the isotopic systems used here to characterize São Jorge, thus it requires a detailed analysis.

Several works based on $^{187}Os/^{188}Os$ (Widom & Shirey, 1996), $^{3}He/^{4}He$ (Moreira *et al.*, 1999) and combined $^{3}He/^{4}He$ and $^{20}Ne/^{22}Ne$ (Madureira *et al.*, 2005) suggested that the Azores mantle plume has its stronger signal on Terceira mantle source. However, the tendency for a relatively high radiogenic Pb of Terceira lavas points to the existence of a shallower recycled crustal component (HIMU-like) superimposed on the "primitive" component. Although there is only one Os isotopic measurement and none noble gas data on São Jorge, the geographic proximity and the isotopic overlapping between Terceira and the eastern array could reasonably indicate that the mantle source beneath the east side of São Jorge is similar to Terceira although with a stronger influence of the recycled component (higher $^{206}Pb/^{204}Pb$).

The HIMU mantle component is associated with the recycling of ancient altered oceanic crust capable to produce extreme enrichments of ^{206}Pb and ^{208}Pb but considerable low $^{87}Sr/^{86}Sr$ values (Zindler & Hart, 1986) since Rb, the parent element, is removed during subduction. In the eastern array despite the fact that a signal for recycled subducted oceanic crust capable of producing high $^{206}Pb/^{204}Pb$ ratios is present, lead isotopes are not coupled with the observed Sr-Nd-Hf isotopic signatures, which do not present HIMU-like signatures. On an Nd-Hf bi-dimensional space (Fig.

10.7) it is clear that the eastern lavas (with average εNd= 6.5 and εHf=11.3) sample a more depleted component, similar to the MAR. In addition, the $^{87}Sr/^{86}Sr$ ratios are considerably higher than expected for an HIMU component.

If the FOZO mantle component as defined by Stracke *et al.* (2005) is considered, than is possible to obtain a better fit. FOZO is characterized by having less radiogenic Pb and significantly more radiogenic Sr, producing signatures that lie on the extension between the MORB and HIMU arrays. Mantle processes as normal mantle melting, continuous recycling and aging are attributed as the main causes for the FOZO array (Stracke *et al.*, 2005).

Overall, the lavas forming the eastern array seem to have sampled a mantle source with a strong affinity to the FOZO mantle component concerning lead isotopes. The proximity to its neighbor Terceira Island might support also the influence of lower mantle material entrained on São Jorge that would have to be confirmed by Os and noble gas data. The less radiogenic lavas on this array combined with the decoupling of lead with the other isotopic data (Sr-Nd-Hf) suggests that a more depleted mantle source, possible related with the near MAR, is also reflected on the eastern side of the São Jorge.

10.5.3 The Western Mantle Component

The most recent lavas erupted on São Jorge are from the Rosais and Manadas volcanic complexes and build-up the western side of the island. These lavas define an isotopic array on the $^{206}Pb/^{204}Pb$ and $^{208}Pb/^{204}Pb$ space with a shallow slope and a slightly enrichment in $^{208}Pb/^{204}Pb$ relative to the eastern lavas. This array shows the binary mixing between two different end-members, where the most radiogenic end-member converges towards the eastern lavas, while the unusual low $^{206}Pb/^{204}Pb$ end-member overlaps the isotopic signature of Faial Island.

The western array is comparable, in some extent, to the shallow trend defined by Graciosa Island (Beier *et al*., 2008). Graciosa lies on the convergence of the MAR field and all the three Terceira Axis trends, being suggested as common mantle end-member for the Azores and MORB compositions in the Azores region (Beier *et al.*, 2008). In this sense, São Jorge western lavas, which are geographically closer to Graciosa, could also sample this common mantle component.

Nonetheless, the less radiogenic lavas expand towards the Faial isotopic signature and are harder to explain. Considering this, several hypotheses are explored below.

The presence of delaminated subcontinental lithosphere has been discuss as an enrich component fertilizing the composition of lavas in the Azores and other OIB. On a first approach, the $^{206}Pb/^{204}Pb$ combined with $^{207}Pb/^{204}Pb$ and $^{208}Pb/^{204}Pb$ isotope ratios of the western lavas, plotting above the NHRL (i.e. positive Δ8/4 and Δ7/4), could argue for the presence of delaminated subcontinental lithosphere beneath São Jorge (Millet *et al*., 2009), in a similar way as proposed to São Miguel (Widom *et al.,* 1997). Compared to São Miguel, São Jorge has much lower $^{207}Pb/^{204}Pb$ isotopic ratios and less incompatible trace element enrichment, which argue against this hypothesis. In fact, the $^{207}Pb/^{204}Pb$ ratios are relatively constant thought-out São Jorge eastern and western side, requiring an early history of relative constant U/Pb ratio previously to the U depletion that originated the high κ_{Pb} values. In addition, Hf isotopes do not seem to corroborate the presence of a subcontinental lithosphere signature, since Hf isotope should be highly radiogenic (Salters & Zindler, 1995; Gonzaga *et al*., 2010) and would necessary produce much higher εHf than the observed in São Jorge.

The presence of a widespread recycled component, HIMU-like (Zindler & Hart, 1986) or FOZO (Stracke *et al*., 2005), is widely accepted for several Azorean islands as a component of their mantle source (Widom & Shirey, 1996; Moreira *et al*., 1999; Beier *et al*., 2008; Millet *et al*., 2009). However, the presence of this component in the eastern lavas seems more likely than in the western lavas. Yet, a recycled oceanic crust with sediments has not be considered and it could be an acceptable hypothesis since the western lavas trend towards low $^{206}Pb/^{204}Pb$ as the enriched mantle components (EM) as defined by Zindler & Hart (1996). The EM's are believed to result from the addition of sediments (terrigenous or pelagic) to the subducted slab, which are recycled in the mantle producing isotopic signatures with lower $^{206}Pb/^{204}Pb$ ratios than HIMU basalts.

The presence of recycled sediments in the mantle source of the westerns lavas could explain the lead isotopes, since a recycled crustal component is invoked for the region. In addition, it could also explain the Hf and Nd signature of São Jorge lavas, since in other oceanic islands it has been proposed a mixture of recycled oceanic crust and sediments with depleted peridotitic mantle (Chauvel *et al*., 2008).

10.5.4 Recycled Sediments in São Jorge Mantle Source from Nd-Hf Isotopes

On the Azores Archipelago, only on São Miguel and Pico islands, the Hf isotopes, in conjunction with other isotopic systems as Nd, have been used to document the geochemical variability observed along the islands and to trace the process involved in the origin of their mantle source (Elliot *et al.*, 2007; Beier *et al.*, 2008).

On a first approach, the combination of Hf and Nd isotopes allows a general characterization of São Jorge confirming the division of the lavas into two different groups. The eastern lavas, with higher εNd and εHf are clustered between the mantle array and São Miguel and plot closer to MORB composition; while the western lavas, with lower εHf for a given εNd, overlap and/or plot below São Miguel array (Fig. 10.7).

The Lu-Hf isotopic system can bring new constrains to the origin OIB mantle source because, in opposition to U, Th and Pb, these elements are relatively unfractionated during magmatic process and during the recycling of oceanic crust on subduction zones (Faure & Mensing, 2005). In fact, the isotopic composition of oceanic islands for the combined Nd-Hf isotopic systems exhibits a linear relationship that is thought to result from the mixing between the depleted mantle source and the recycled oceanic crust. However, according with Chauvel *et al.* (2008) both sources are not enough to reproduce the mantle array and a sedimentary component during recycling is required, since sediments fractionate Lu/Hf and Sm/Nd more efficiently than magmatic processes.

Considering the efficiency of sedimentary process in fractionating Lu/Hf and Sm/Nd leading to a larger isotopic diversity with time, their mix with oceanic crust during recycling, (Vervoort & Blichert-Toft, 1999; Chauvel *et al.*, 2008), seems a good option to verify if a sedimentary recycled component is able to reproduce the present day isotope ratios observed in São Jorge.

Usually, two different kinds of sediments, pelagic and terrigenous, are considered to mix with oceanic crust during subduction processes, which display different isotopic and geochemical compositions in terms of Hf and Nd (Vervoort & Blichert-Toft, 1999; Chauvel *et al.*, 2008). Three different sediments are considered in order to check the evolution of the sources. These sediments are (1) pelagic sediment, (2) GLOSS (global subducting sediment) and (3) terrigenous sediment. Since the Hf and Nd concentration on the sediments are essential for reproducing the model, primitive mantle (McDonough & Sun, 1995), which has Hf/Nd ratio of 0.226, is used as a reference for identifying the sediments with high or low ratios Hf/Nd ratios. GLOSS, represents an

average composition for subducted sediments as defined by Plank & Langmuir (1998) and has an Hf/Nd ratio of 0.15. The other two other sediments, terrigenous and pelagic, were chosen from Vervoort & Blichert-Toft (1999) with higher and lower Hf/Nd ratios. The terrigenous sediments have Hf/Nd=0.319 and the pelagic sediment has Hf/Nd of 0.114 (for other data on the sediments see legend of Fig. 10.10 and Appendix IV.A).

To model the isotopic composition of recycled oceanic crust it was considered an average MORB composition with present-day εHf of 17.5 and εNd of 10. This MORB was mixed with sediments during subduction process in several proportions (0%, 2%, 4%, 6%, 10%, 20% and 100%) at the time of subduction, assumed to have occurred at 1 Ga ago, and then remained isolated in the mantle until recently (see legend of Fig. 10.10 for details).

Commonly pelagic sediments present high Lu/Hf and low Hf/Nd ratios and display isotopic compositions that plot mainly above the mantle array in the εHf-εNd space. Through isotopic decay, as in old recycled pelagic sediments, the low Hf/Nd sediments are only able to produce isotopic compositions displaced to the left of the mantle array (Chauvel *et al.*, 2008), as represented by the convex line in Fig. 10.10. Considering this, neither modern-day or ancient pelagic sediments, even older than 1Ga, are able to reproduce the observations on São Jorge as described above and exemplified by the modeled shale (Fig. 10.10).

The composition of the average subducted sediments, GLOSS (Plank and Langmuir, 1998) was also modeled in order to obtain an intermediate scenario, however the convex curve with the mixture between GLOSS and MORB produces higher εHf relative to the mantle array and don't match in any case São Jorge lavas.

The presence of terrigenous sediments in São Jorge mantle source should be evaluated as it was on other Azorean islands (Widom *et al.*, 1997, Beier *et al.*, 2007 Elliot *et al.*, 2007). These sediments tend to have lower Lu/Hf and higher Hf/Nd ratios, mainly because of zircons that are a repository of Hf (Patchett *et al.*, 1984), and because through isotopic decay they can develop signatures that lie below the mantle array i.e. lower εHf for a given εNd. Despite the fact that only a restrict number of sediments have these marked characteristics, their recycling with oceanic crust can produce lower εHf and a mixing curve subparallel to the mantle array. The mixture of MORB with 10% of terrigenous sediments, represented by a turbidities with Hf/Nd=0.319, is able to produce an isotope composition similar to São Jorge eastern lavas. Thus, this hypothesis should

not be excluded since previously it was mentioned a recycled component mantle source of the eastern side of São Jorge. However, these results are not satisfactory for the western lavas because these sediments are not able to produce the lower εHf as required.

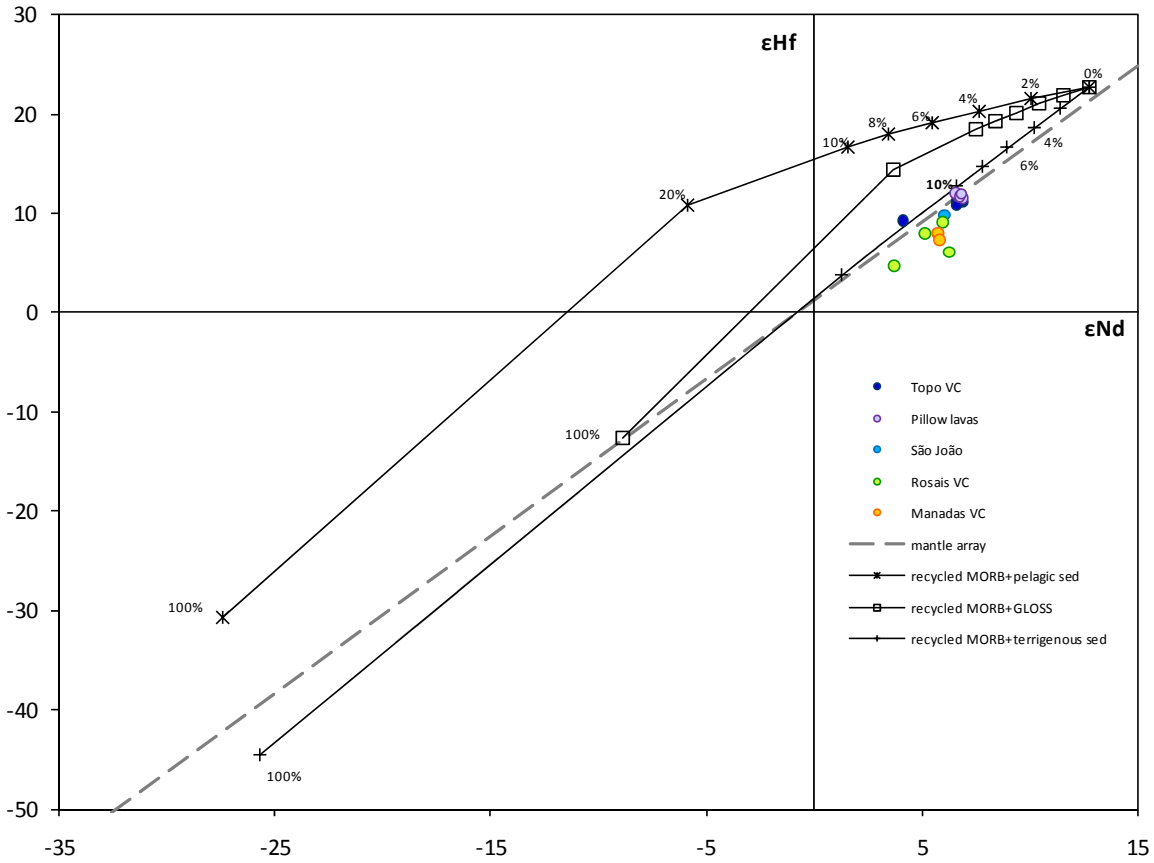

Fig. 10.10 – Model of recycled MORB and sediments at 1Ga ago. The subduction of 10% of terrigenous sediments and MORB is able to reproduce in terms of Nd-Hf isotope systems the signature found in the eastern lavas of São Jorge but fails to reproduce the composition of the western lavas. Modeling parameters: Present-day: MORB has εHf=17.5 and εNd=10; GLOSS has εHf=-17.3 and εNd=-8.9 plotting above the mantle array; pelagic sediment (shale) has εHf=-34.6 and εNd=-27.5 and terrigenous sediment (turbidite) has εHf=-46 and εNd=-25.7. All isotopic present-day compositions where recalculated for 1 Ga ago and then MORB and sediments where subducted according with Stracke *et al*. (2003) (see Appendix IV.B for compositions). Convex curves represent the mixture of MORB with several proportions of sediments (0%, 2%, 4%, 6%, 10%, 20% and 100%) having present-day isotopic compositions.

10.5.5 An Ancient (>2Ga) Mantle Source sampled by São Jorge western lavas

The unique isotopic signature in the most enriched lavas of São Miguel Island, lead to several models proposing the presence of ancient mantle components beneath the island. Some of the hypothesis suggested the presence of underplated enriched ancient (≈3 Ga) modest-degree melt

(≈2%) from a garnet peridotite source (Elliot *et al.*, 2007) or even a recycled seamount with 3Ga (Beier *et al*., 2007).

In Faial and Pico islands, according with the unique $^{187}Os/^{188}Os$ subchondritic ratios, Schaefer *et al*. (2002) argues that an ancient mantle source, which is formed by a harzburgitic lithosphere from an Archaean oceanic plate subducted into the deep mantle, has been sampled by those lavas.

Because the most common mantle components that result from recycled oceanic crust, with or without sediments, are not able to explain some of the isotopic signatures of the Azores, the hypothesis of an old source, that was able to rest in the mantle for a long time, seems able to reproduce those signatures.

Despite no Os isotope data has been published on São Jorge yet, the similarities observed between the western lavas of São Jorge and Faial in terms of Sr, Nd and principally Pb signatures, lead us to explore the presence of an old source. In addition, if an ancient (>2Ga) component is entrained in the Azores mantle, it could be widespread on the region showing a stronger signal away from the center of the plume believed to be beneath Terceira island (Moreira *et al*., 1999; Madureira *et al*., 2005).

The combined geochemical behavior of Hf and Nd during magmatic and recycling processes and their present day composition, in trace elements and isotopic signature, precludes that they can trace ancient mantle source signatures, even in altered rocks (Pearce *et al.*, 1999). Therefore, the peculiar εNd and εHf signature of São Jorge, where it is observed a decrease in εHf for a given εNd, could have resulted from ancient magmatic event.

This reasoning is applied here, to São Jorge lavas, in order to see if is possible to match the lavas from the western side of the island with the mixing of a depleted mantle component (e.g. the common mantle component of the Azores) with an ancient melt in a similar way as Elliot *et al.* (2007). This model is just a simplistic way to try to obtain the Hf and Nd isotopic compositions of the western lavas, since recycled sediments are not able to produce the adequate paths. In addition, the production and evolution of the ancient melt presented here, which fertilized the mantle source of São Jorge, is modeled in few and simple steps and thus it should be considerable carefully.

As mentioned, the lavas from São Miguel Island display a linear array in the εHf and εNd space, which plots below the mantle array with a stepper trend (Fig. 10.7). São Miguel source was ingeniously interpreted by Elliot and co-workers (2007) as being an ancient (≈ 3Ga) moderate-degree melt (≈ 2%) from garnet peridotite entrained in the mantle oceanic lithosphere. This interpretation based on the relatively well-constrained partition coefficients of Sm, Nd, Lu and Hf (Blundy *et al.*, 1998; Salters & Longhi, 1999 and McDade *et al.*, 2003) during melting in the presence of garnet. D_{Lu} is considerable higher than D_{Hf} in the presence of garnet and the result after melting is a liquid with low Lu/Hf ratio, thus producing unradiogenic Hf isotope compositions (negative εHf). In addition, Sm and Nd can be considerable fractionated on a garnet peridotite for moderate-degrees of melting and produce over time appropriate isotopic signatures (negative εNd), (Elliot *et al.*, 2007).

Larger melting degrees forming the MORB can also account for Hf-Nd isotopic composition bellow the mantle array, since Lu and Hf are fractionated and Sm/Nd ratios only have small changes for such larger degrees of melting. As a result, MORB plots below the mantle array and it is possible to have variable εHf for a given εNd (Chauvel & Blichert-Toft, 2001). In addition, because MORB is produced from a depleted mantle source has positive εHf and εNd values.

To create the initial depleted source at 4.2 Ga, the primitive mantle (McDonough & Sun, 1995) went through a melting event producing a depleted residue, which remained in the mantle until a melting event produced an enrich liquid. During the melting event it was considered that the liquids formed by 1, 3 and 5 % of partial melting in the garnet stability field and then was isolated for evolve isotopically until present time (for melting parameters se Appendix IV.B). For the purpose of this study, and in order to test more than one hypothesis, the melting event was modeled for two different times. The first hypothesis considerers an older liquid with 3Ga, and the second hypothesis was modeled in order to considerer a liquid with 2Ga (Fig. 10.11). Both liquids, the 3Ga and the 2Ga, mix with the common mantle component beneath São Jorge in several proportions, i.e. 1%, 2%, 5%, 10% 20% and 50% of the magmatic liquid entrained the lithosphere beneath São Jorge.

The result of this model is presented in Fig. 10.12. Contrary to the observed for the sediments, the ancient melt mix with the common mantle component seems to be able to produce the same isotopic signature observed in the lavas from São Jorge Island, since 5 to 10% of this ancient melt fertilizes the depleted source. As previously mentioned, the common mantle component

observed on the isotopic signature of São Jorge and of the Azores, which is related with the close presence of the MAR, corresponds to this depleted mantle source.

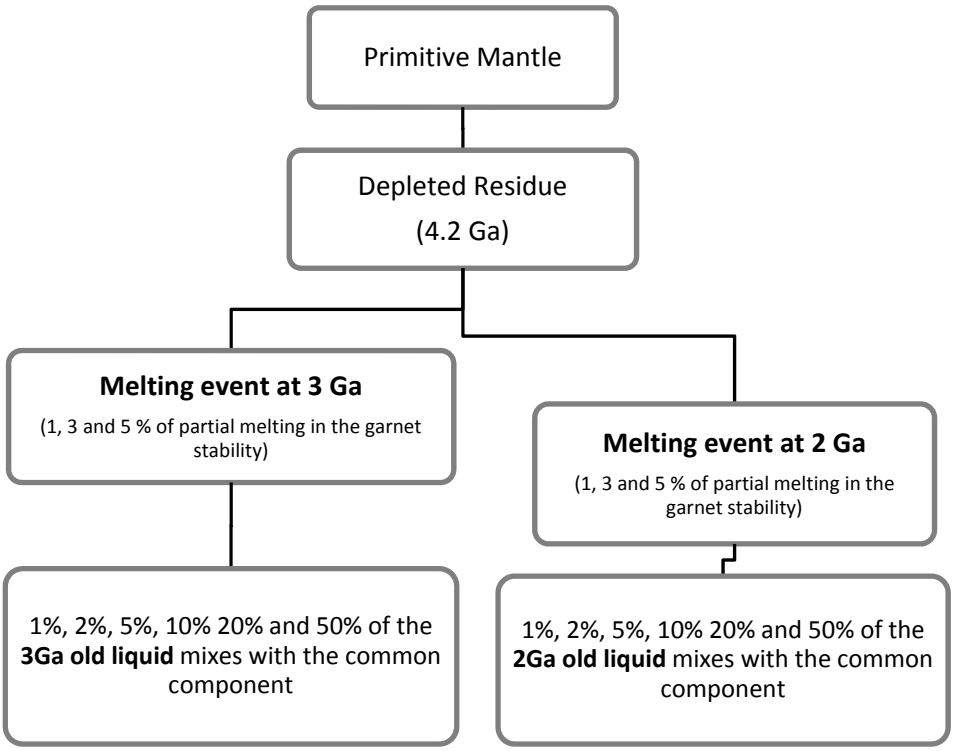

Fig. 10.11 – Diagram showing the evolution of the ancient source until it mixes with the common mantle component.

The magmatic liquids generated at 2 and 3 Ga ago have an isotopic signature that is able to produce low εHf for a given εNd, when mixed with the common component. Therefore, it can be proposed that a magmatic liquid generated in that period provides a good fit for the western lavas. As for the degree of partial melting, if it is low (≈1%) the behavior of Hf and Nd produces a similar pattern to the mantle array, but, for higher degrees of partial melting, (e.g. 3 to 5%), both elements show an adequate behavior.

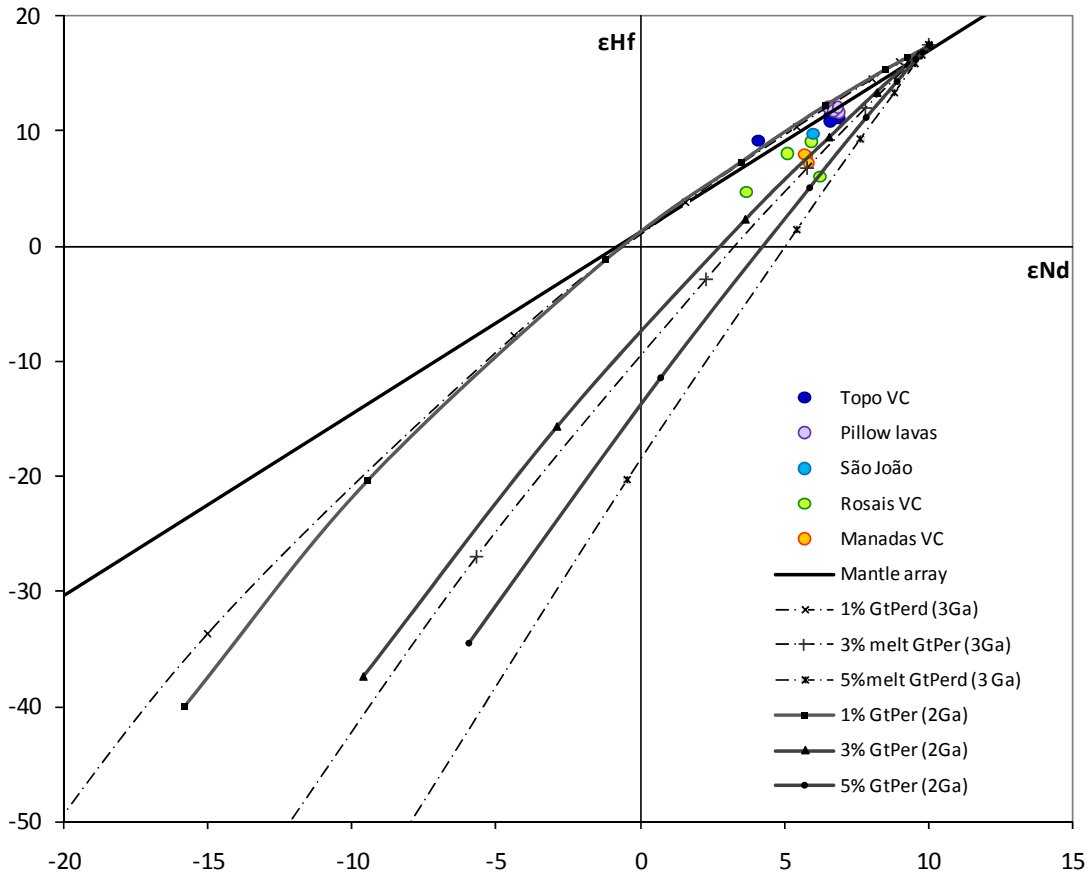

Fig. 10.12 – εHf vs. εNd space showing the model curves that mix a depleted component with an ancient enriched melt in order to reproduce the isotopic composition of the lavas forming the west side of São Jorge. This model follows several of the main constrains of Elliot *et al*. (2007) modeling described in (Appendix IV.B). Dash line shows the 3Ga old melt produced by 1 and 3% of melting, while the full line shows the curve for the 2Ga old melt produced by 1, 3 and 5% melting, both mixing with a depleted mantle in different proportions (1%, 2%, 5%, 10% 20% and 50%). Both melts are able to produce the isotopic composition of the lavas on the western side.

According with the diagram of Fig. 10.12, the influence of the ancient source becomes stronger to the west side of the island, as εHf decreases, suggesting that towards Faial island the influence of this magmatic liquids could be stronger. In addition, the lavas do not follow a single mixing line, what could be explained by the fact that fertilization of the mantle was not uniform in the mantle located beneath this area. The lavas from the east side are also represented in Fig. 10.12, exhibiting a good correlation with the modeled curves, nonetheless, these lavas were previously interpreted as being influence from a different mantle component, the eastern component, which is similar to Terceira Island.

10.5.6 The Ancient Lead Signature in São Jorge

The modeling of Hf and Nd showed in Fig. 10.12, suggests that São Jorge isotopic signature, and in particularly the western lavas, samples a mantle source entrained by a liquid formed by a moderate-degree partial melting event that could have occurred between 2 and 3Ga. This magmatic event with melting degrees between 2 and 5% on the garnet stability field was able to produced Lu/Hf and Sm/Nd fractionation that allowed the liquid to evolve isotopically to low εHf and εNd. The mixture between this ancient source and the depleted upper mantle was able to produce the present day compositions.

The lead isotopic ratios on São Jorge lavas, and in particularly on the western side, should also reflect this ancient magmatic event; however, U, Th and Pb isotopic systems are complex and more sensitive to magmatic and non-magmatic process and harder to model.

Initially, it is necessary to consider the Th, U and Pb geochemical behavior during melting. The present Th/U ratios measured on São Jorge do not allow to discriminate between the eastern and western lavas, suggesting that their ratios result from the recent magmatic conditions beneath the island. However, the κ_{Pb} suggests a mantle source with a time-integrated history with high Th/U ratios in the western side of the island (Fig. 10.9).

Studies on elements partition coefficients during melting of garnet peridotites points to higher compatibilities of U relatively to Th (Elkins *et al.*, 2008), with $D_U/D_{Th}=2$ (Stracke *et al.*, 1999), thus for low degrees of partial melting it is possible to produce liquids with high Th/U ratios relatively to their residues (Shaw, 2006). Pb behavior is harder to predict because of the few studies on the partition coefficients, however it is believed that Pb is more compatible than Th and U and that sometimes Pb behaves as siderophile element. Thus, from partial melting it is possible to fractionate Pb from U and Th and have the right parent/daughter elemental ratios. If a magmatic liquid with this characteristics remains isolated from 2 to 3Ga, than its composition would remain unchanged, it is possible evolve isotopically until the present.

For modeling the isotopic composition we used two models, the first starting as a single stage model with BE composition at 4.55 Ga and second using the two-stage model of Stacey & Kramers (1975). These models evolution is interrupted at 3Ga or 2Ga by the magmatic event with an increase of the Th/U ratio and U/Pb ratio where a new stage begins until present day. This modeling is certainly an oversimplification since the source is considered undisturbed before

modeling and the ancient melting event is restricted to one single event, however it is a simple and best-fitting approximation of the isotopic evolution.

The two stage model (Fig. 10.13) starts at 4.55Ga with a source with μ=8 and κ_{Pb}=3.9, the chondritic value, then at 2Ga (Fig. 10.13A) or at 3Ga (Fig. 10.13B) due to the melting event both μ and κ_{Pb} increase. We assumed that κ_{Pb} increases to 4.06 because this is the values calculated on the lavas, however μ was not constrained and several possibilities were used to model the evolution of the system. In Fig. 10.13 the results for μ=10, 11, 12 and 13 expressed in terms of $^{206}Pb/^{204}Pb$, $^{207}Pb/^{204}Pb$ and $^{208}Pb/^{204}Pb$.

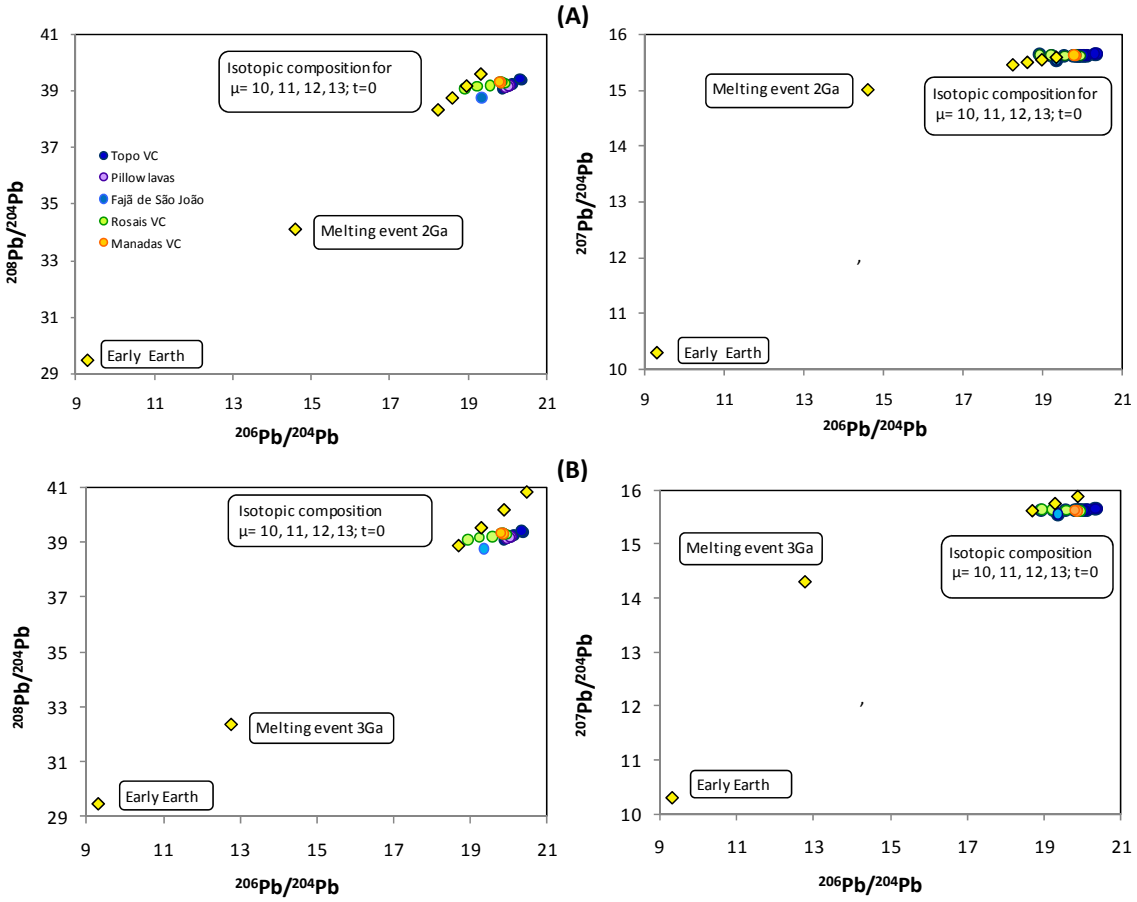

Fig. 10.13 – Single stage model for the melting event at (A) 2 Ga and the melting event at (B) 3 Ga (see Appendix IV.C). The melting event produced an increase of the Th/U and U/Pb ratios, which is represented by an increase of μ values. For the melting event at 2Ga μ=12 seems to be the best fit for the western lavas while for the 3Ga old melt the best fit is for μ ranging between 10 and 11.

For the Stacey & Kramers model (Fig. 10.14), the second stage starts at 3.7 G and is interrupted at 2Ga (Fig. 10.14A) and at 3Ga (Fig. 10.14B). At this point the κ_{Pb} of the system increases from 3.78

to 4.06 (estimated using Stacey and Kramers, 1975), but again several isotopic composition are estimated for variable $^{238}U/^{204}Pb$ (μ=10, 11 and 12.0).

After modeling the isotopic composition of the ancient melt, its composition should mix with a depleted component in the same proportion as in the Nd-Hf model. However, because the results for lead isotopes overlap the compositional field of the lavas erupted along the MAR, the mixing between the ancient component and the widespread depleted component located beneath the Azores would not change significantly lead isotopic signature.

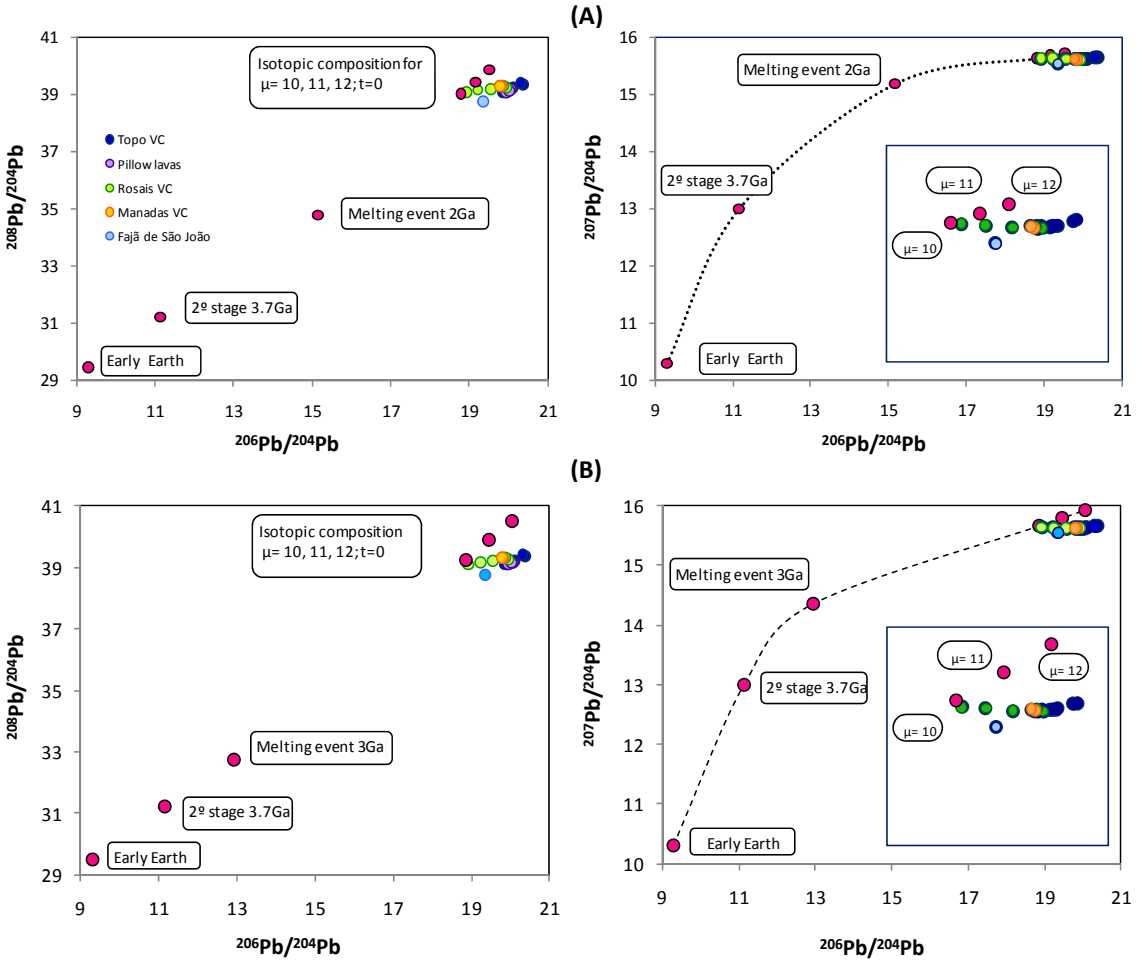

Fig. 10.14 – Stacey & Kramers model for the melting event at (A) 2 Ga and the melting event at (B) 3 Ga (see Appendix IV.C). The melting event produced an increase of the Th/U and U/Pb ratios, which is represented by an increase of μ values. For the melting event at 2Ga a μ value between 10 and 11 seems to be the best fit for the western lavas while for the 3Ga old melt the best fit is for μ= 10.

The result of modeling lead isotopes (both models and both ages) shows that is possible to obtain $^{207}Pb/^{204}Pb$ ratios in the range of the values observed on São Jorge. In addition, $^{206}Pb/^{204}Pb$ ratios

modeled using μ raging between 10 and 13 are able to account for the low isotopic ratios observed on the western lavas. These μ values are much lower than the values predicted for São Miguel enriched mantle source (Elliot *et al.*, 2007) meaning that the fractionation between Th, U and Pb was not as efficient as in São Miguel.

Considering the average μ_{206} of 10.3_{206} as presented earlier, the 3Ga melting event seems to have the best fit with the western lavas with μ ranging between 10 and 11. However for the Stacey & Kramers model the 2Ga old melt with μ=10 has the best isotopic composition.

Despite the discrepancy between both methods of modeling lead isotopes, it seems that an ancient melt is able to reproduce the lead isotope compositions observed on the lavas of the west side of São Jorge. In addition, it seem possible to couple lead isotopes Hf and Nd isotopes if this ancient melt has between 2 and 3Ga.

Chapter 11: Summary: the Evolution of São Jorge Island

In this chapter is presented a compilation of the data on São Jorge introduced and discussed previously, which comprises geomorphologic, stratigraphic, tectonic, seismic, volcanological, geochronological, petrographic, geochemical and isotopic information from previous works and the new data acquired during this study. Because the information presented in the earlier chapters as well as its origin was discussed in detail, in the next paragraphs will not be made any reference to previous works. The combination of the diverse information will provide, hopefully, a better knowledge on the general evolution and on the petrogenetic processes that originated São Jorge Island. Additionally, it was found that the basalts of São Jorge, sample an isotopic heterogeneous mantle source, which brings important information on the characteristic of the mantle on the Azores Region and, in particularly, on the Central Island Group of the Archipelago.

The Azores Region is a complex tectonic and magmatic/volcanic region that combines the triple junction between three major plates (American, Eurasian and Nubian Plates), with major large-scale tectonic structures, as the Mid-Atlantic Ridge (MAR), with an excess of magmatism/volcanism. The result is the Azores Plateau, a relative shallow region defined roughly by the 2000m bathymetric line, that has been active and evolving for the last 20 Ma. In this intricate and controversial region, magmatic and volcanic activity was able to reach the surface and formed the Azores Archipelago, as well all submarine volcanic reliefs.

Major tectonic structures, as the Terceira Axis or the East Azores Fracture Zone, play an important role on the past and present evolution of the Plateau and are responsible for its tectono-magmatic internal structure. In the area of the Central Island Group, where São Jorge occupies a central position, the internal structure of the Azores Plateau is dominated by the 120°N and 150°N directions, along which the main tectonic and volcanic structures developed. In addition, volcanic activity seems to be strongly conditioned by the tectonics, since volcanism is

concentrated along the main faults or on the intersections of faults, developing submarine volcanic structures, which can emerge and form islands. In the case of São Jorge, the island is the superficial expression of a larger edifice classified as a linear volcanic ridge, formed by fissural volcanic activity along the 120°N direction.

The island tectonic setting mimics the tectonic pattern of the Azores Plateau, thus, beside the predominance of the 120°N direction, along which most of the volcanic structures are aligned, the more subtle 150°N tectonic direction is present and important faults as the Ribeira Seca Fault follows this direction. This fault, which divides the island into the east and west side, is believed to have a left strike-slip and dip-slip components that produced the northward displacement of the east side of São Jorge in the order of 3 to 3.5 km.

The geomorphology and stratigraphy of São Jorge, as other islands of the Central and Eastern island groups, shows evidences for a westward migration of volcanic activity during their development. Absolute geochronology supports these evidences and constrains temporally the volcanic events that contributed to the edification of the island. One of the most important constrain in São Jorge is related with the beginning of the subaerial volcanism, which is much older than initially thought, and the second is related with the development of the island during two distinct volcanic phases.

The first volcanic phase, which corresponds to the subaerial volcanic activity that edified a proto-island, was active between 1320 ka and 1210 ka ago. After this period, volcanism apparently stooped for approximately 450 ka, restarting at least at 757 ka ago, with the beginning of the second volcanic phase, which is still active.

Concomitant with the first and second volcanic phases other geologic processes as sea erosion, flank instability and tectonic activity, were active and shaped the landscape. The peculiar geomorphologic characteristics of São Jorge, as the sub-vertical shorelines where the volcanic sequences are exposed, the formation of the fajãs, the high altitude of most of the landmass of the island (300 to 600m height) and the smooth topography on summit areas, are an example of the interaction of constructive and destructive geologic processes.

The lava sequence located on the southeast shoreline of the island; named Fajã de São João is the only known record of the first volcanic phase. The lava sequence with 400m height was formed, mainly, by effusive volcanic activity that accumulated relative thick lava flows frequently cut by

dikes, which can reach metric width. Towards the top, the lava flows of Fajã de São João sequence are more often interbedded with baked soils suggesting larger intervals between eruptions. The volcanism in this sequence is mainly basaltic s.l. and alkaline but has slight lower alkaline content when compared with the rest of the island. The degree of evolution of the lavas is narrow and the magmatic liquids were only able to produced basalts, trachybasalts and basaltic trachyandesites, sometimes enriched in potassium, where plagioclase is the dominant mineral phase during fractional crystallization processes. In some of the lavas, i.e. the plagioclase-bearing basalts, the abundance of plagioclase can correspond to almost 45% of the volume of the lava suggesting other magmatic processes. The characteristic of these lavas suggests that fractional crystallization, gravitational segregation and accumulation processes occurred in a shallow magma chamber. In addition, the oscillatory compositional character of the lava sequence, the average fast growth rate of the sequence (3.4 m/ka), when compared with the rest of the island, also points to the existence of an active magma chamber feeding the volcanic activity at the surface. Estimates on the conditions of pressure and temperature of the lavas based on olivine and pyroxene crystals, in equilibrium with the magmatic liquids, suggests that these crystals fractionated at 1000-1100 ºC and at an approximately depth of 17 km (≈5kbar). This means that these crystals fractionated at relative shallow depth, close to the mantle-crust limit, predicted to be located at approximately 14 km depth beneath the Azores Plateau. However, the magma chamber feeding Fajã de São João sequence would be expected to be considerable shallower.

During the second volcanic phase, which is still active, the three main volcanic complexes that constitute the island, Topo, Rosais and Manadas, were formed. Volcanic activity should have been mainly effusive but large pyroclastic deposits are observed in several locations or interbedded with lava flows that evidence episodes of explosive activity.

The volcanic phase that edified Topo Volcanic Complex occurred between 757 and 543 ka ago, even though, volcanism continued active for some time after on summit areas as in Piquinho da Urze. The submarine southeast flank of the island, which should correspond to the submarine prolongation of Topo Complex Volcanic, was also characterized in this study with pillow lavas collected at 1200 m depth during EMEPC\Açores\G3\2007 cruise. The pillow lavas are not temporally constrained, but the lack of alteration due to the interaction with seawater allows assuming that they are relative young.

After the onset of Topo Volcanic Complex, volcanism migrates westward and begins to edified Rosais Volcanic Complex, what should have started at approximately 368 ka ago and continued active at least until 117 ka ago. A particularity of Rosais is that volcanism could have occurred in several places simultaneously, during the early stages and over a period of 150 ka, instead of a progressive westward migration of volcanic activity from the center of São Jorge towards Ponta dos Rosais.

The beginning of the volcanic activity in Manadas Volcanic Complex marks the migration of volcanic activity towards the center of the island, although is not temporally constrained. Presently, in São Jorge this is the most seismically and volcanically active area as demonstrated by the historical earthquakes and eruptions. The recent volcanic deposits and historical eruptions show evidences of explosive volcanism with pyroclastic materials and pyroclastic flows and of highly explosive hydromagmatic eruptions. The possibility of a new eruption in São Jorge with this characteristic affecting the south side of the island, which is, presently, the area that encompasses the most populated parishes, should be taken into consideration by the local authorities responsible by for volcanic and seismic risk.

The lavas erupted during the second volcanic phase are mainly basaltic s.l. and alkaline having a relative narrow lithological spectrum i.e. basalts, trachybasalts and basaltic trachyandesites. The lack of lithological diversity might be related with the volcano-tectonic conditions that triggered magmatic activity, which did not allowed magmatic liquids to evolve to lithotypes that are more acid. However, according with the dataset presented here from Topo (including the submarine pillow lavas), Rosais and Manadas volcanic complexes it seems that volcanism chemically evolves from predominately basaltic on Topo, to slight more evolved and K-rich compositions on Rosais and finally, to more subsaturated lavas on Manadas.

The lavas from the second volcanic phase present evidences of having a non-comagmatic origin, demonstrating that the magmatic liquids, from which the lavas were generated, had to be produced from different magma batches. This is more evident in Rosais Volcanic Complex where lavas from the same volcanic sequence formed from different batches of melt. In addition, the possibility of coeval volcanism in Rosais is supported by the production of these magma batches.

The mineral assemblage observed in the lavas is composed mainly by olivine, pyroxene, plagioclase and titanomagnetite, which is the most abundant Fe-Ti rich oxide. The pillow lavas

share the same mineralogy with exception of pyroxene that is scarce or absent. Nonetheless, fractional crystallization processes were responsible by the fractionation of this mineral paragenesis, in which olivine and pyroxene phenocrysts should have been the first to form. In fact, the average temperature and pressure estimated for the beginning of the fractionation of both minerals is ≈ 1190°C at 10kbar and under low fO_2 conditions (log fO_2 of -15.5). These results contrast with the first volcanic phase, evidencing that fractional crystallization processes occurred at deeper levels.

The generation of the magmas occurred in the mantle in the presence of garnet and amphibole, as showed by the fractionation between the light and heavy rare earth elements and by the depletion in potassium, respectively. As expected for an oceanic island, São Jorge magmas were generated by small degrees of partial melting with an average degree of melting of 7%, which is able to produce enriched lavas in incompatible trace elements. Notwithstanding, higher degrees of partial melting (5-12%) are associated with the oldest lavas from Topo and Rosais volcanic complexes, while the magmatic liquids generated by lower degrees of partial melting (2-7%) are associated with the younger lavas from Topo and Rosais volcanic complexes, located on summit areas, with the lavas from Manadas Volcanic Complex and with the submarine pillow lavas. These differences on the degree of partial melting could be associated with a higher melting production during the early phases of volcanism in each complex.

The pressure conditions, in which the magmatic liquids were generated during the second volcanic phase, seem to increase towards the west side of São Jorge. Pressure estimates showed that the pillow lavas were generated at the lowest pressure conditions of 26kbar, which is close to the transition zone between garnet and spinel stability fields. The lavas from Topo Volcanic Complex were generated at pressures between 28 and 30kbars, while melting beneath Rosais and Manadas volcanic complexes occurred at pressures between 30 and 32 kbars. Conversely, the temperatures at which the magmas were extracted from the source, range between 1406 and 1454°C, and apparently are independent of any temporal or geographic constraint. Nonetheless, temperatures are considerably high but and are in the range of the Azorean islands, where excess of temperature has been proposed.

The most primitive lavas from the second volcanic phase are enriched in incompatible trace elements, which reflects the enrich nature of the mantle beneath the São Jorge. Nonetheless, this enrichment shows only subtle differences between the lavas from each volcanic complex and

from the submarine flank of the island, revealing that the mantle has slight different degrees of fertilization. The submarine pillow lavas are slight depleted when compared with the lavas from Topo Volcanic Complex, but the lavas from Rosais and Manadas volcanic complexes are enriched in the most incompatible trace elements and in addition show different degrees of enrichment.

The subtle chemical differences mentioned, contrast with the isotopic signature of the lavas. The isotopic compositions in terms of Sr, Nd, Pb and Hf, points out that the lavas from Topo Volcanic Complex and from the submarine flank, sample a mantle source with similar isotopic signature, while the lavas from Rosais and Manadas volcanic complexes sample a mantle source that becomes progressively more distinct towards the west end of the island. In this sense, the lavas from the second volcanic phase can be divided into the east and west side, with the Ribeira Seca Fault materializing this division. The isotopic composition of the first volcanic phase is characterized by intermediate signature between the eastern and western lava groups, but also by lower $^{207}Pb/^{204}Pb$ and $^{208}Pb/^{204}Pb$ isotopic ratios.

The isotopic signature of São Jorge can be compared with the reaming islands of the Azores Archipelago, which present very different compositions between islands and, in some cases, different compositions on the same island, revealing important small-scale mantle heterogeneities though out the Archipelago. In the case of São Jorge, the lavas from the eastern side of the island overlap the isotopic signature of Terceira Island, while the western side trends towards the isotopic composition of Faial Island. This fact reinforces the presence of small-scale mantle heterogeneities in the Azores region and that São Jorge, during its evolution, was able to sample two isotopically distinct mantle sources.

The analysis of the two isotopic signatures beneath São Jorge reveal that more than one mantle component is necessary to produce the isotopic ratios observed. One of this components should derive from a relative deplete and less radiogenic mantle source that is probably related to the close presence of the Mid-Atlantic Ridge and the evolution of the Azores Plateau. In fact, these less radiogenic compositions seem to be common to all the Azores Islands and consequently was called the common component. The second component, named the eastern component, is observed in the most radiogenic lavas of Topo Volcanic Complex and the submarine pillow lavas. Its geographical proximity and isotopic similarity with Terceira Island does not exclude the influence of the Azores mantle plume, but also evidences the signals of a recycled component with FOZO signature.

The third component observed in São Jorge Island is the western component, which is similar to Faial Island, and has an isotopic signature that was harder to identify because the isotopic systems seem to present contradictory signals. However, if an ancient mantle source formed by small to moderate degrees of melting at 2 to 3 Ga ago was able to evolve isotopically and then entrained the mantle beneath the Azores, than it is possible to produce the peculiar isotopic signature observed in the west side of São Jorge.

APPENDIX

APPENDIX I: Rock Analysis: Analytical Methods and Results

The analytical methods used to obtain geochemical and isotopic data, on the onshore and offshore samples from São Jorge Island, are described below, as well the analytical methods for obtaining $^{40}Ar/^{39}Ar$ ages. The final table of this appendix is a list of the location of the samples presented in this project.

APPENDIX I.A Major and Trace Elements (ICP and ICP-MS)

The selected samples went through whole rock analyses, including major elements, trace elements and rare earth elements (REE), performed at the Activation Laboratories Ltd following the WRA+4B2+4B1 procedure.

Briefly, each sample is mixed with a lithium metaborate and lithium tetraborate solution and then fused. The molten melt was immediately poured into a solution of 5% of nitric acid containing an internal standard and mixed continuously until complete dissolution.

For these samples major elements were measured by Inductively Coupled Plasma (ICP: Thermo Jarrell-Ash ENVIRO II ICP or a Spectro Cirros ICP), and trace elements (including REE) were measured by Inductively Coupled Plasma-Mass Spectrometry (ICP-MS9 using a Perkin Elmer SCIEX ELAN 6000 or 6100 ICP-MS.

Detection limits for major elements are 0.01% for all oxides with exception of MnO and TiO_2 with detection limits as low as 0.001%. For trace elements the detection limits are considerable low (generally less than 5 ppm) allowing good results for geochemical interpretation. The exception was Ni with a 20 ppm detection limit. To reduce Ni detection limit to 1 ppm an additional analysis

was performed with dilution of the sample in four acid solutions and analyses in a Perkin Elmer Optima 3000 ICP.

The standards materials used were: GXR1, WGM-1, NIST 694, DNC-1, BIR-1, MICA-FE, GXR-2, SDC-1, SCO-1, GXR-6, FK-N, LKSD-3, MAG-1, NIST 1633b, SY-3, W-2a, OREAS 13P, NIST 696, GBW 07239, CTA-AC-1 GXR-4, JSD-3. Precision of the analyses was better than 2% for major oxides and better than 5% for trace elements including REE.

APPENDIX I.B Trace Elements (HR-ICP-MS) and Isotopic Analyses

Trace elements analysis using the HR-ICP-MS and isotopic analyses of Sr, Nd, Pb and Hf, were carried out on several rock samples. Sample preparation and mass spectrometric analyses of trace element and isotopic compositions were carried out in Class 1000 clean labs at the Pacific Centre for Isotopic and Geochemical Research (PCIGR). All reagents used were sub-boiled, all dilutions were made using more than 18.2 MΩ cm of de-ionized water, and all labware was acid-washed prior to use.

APPENDIX I.B.1 Trace elements

Even though some samples had been previously analyzed by ICP-MS, new trace elements analyses using HR-ICP-MS were perform of some of the samples and on three sample reference materials (BHVO-2, Koolau and Kilauea 93) using an ELEMENT2 high-resolution (HR)-ICP-MS (Thermo Finnigan, Germany), housed at the PCIGR. The obtained results were preferentially used in the geochemical interpretation of trace element data collected on these samples.

Comprehensive sample preparation and analytical procedures for trace element analysis of mafic rocks at the PCIGR are described in Pretorius *et al.* (2006). Unleached whole-rock sample powders were digested in a mixture of concentrated HF and HNO3 in sealed Teflon® vessels on a hot-plate and subsequently diluted (with 1% HNO3 and 10 ppb In) to 1000 and 3000 times for the REE and high field strength element (HFSE) analyses, respectively. The REE were measured in high

resolution, whereas U, Pb and Th were measured in low resolution. The majority of the HFSE were measured in medium resolution, except for Sr, Zr and Ba, which were measured in high resolution to avoid overloading the detector. Indium (In) was used as internal standard in all blank, standard and sample solutions. All the analyses were quantified using external calibration curves and normalized to the internal standard and blank subtracted. Data reproducibility was demonstrated by the analysis of complete procedural duplicates of some samples.

APPENDIX I.B.2 Radiogenic isotope analyses (TIMS and MC-ICP-MS)

Radiogenic isotopes, Sr, Nd, Hf and Pb were analyzed on fresh basaltic lavas and sample selection was done accordingly with their location and their petrographic and geochemical characteristics (major and trace element composition obtained either by ICP-MS or HR-ICP-MS).

Prior to isotopic analysis, all sample powders were acid-leached to remove secondary alteration phases, following the sequential leaching procedure of Weis *et al.* (2006). Leached sample powders were digested in a mixture of concentrated HF and HNO_3 in sealed Teflon® vessels and processed on several chromatographic ion exchange columns for Pb, Sr, Nd and Hf purification. A thorough review of the sample dissolution, isotopic purification and analytical procedures used can be found in Weis *et al.* (2006 and 2007).

Sr and part of the Nd isotopic ratios were measured on a Thermo Finnigan Triton thermal ionization mass spectrometer (TIMS) in static mode with relay matrix rotation on a single Ta and double Re-Ta filament, respectively. Sr and Nd isotopic compositions were corrected for mass fractionation using $^{86}Sr/^{86}Sr=0.1194$ and $^{146}Nd/^{144}Nd=0.7219$ respectively. The data was normalized using the average of the corresponding reference material (SRM 987 for Sr and LaJolla for Nd) in the barrel, relative to the values of $^{87}Sr/^{86}Sr=0.710248$ and $^{143}Nd/^{144}Nd=0.511858$ (Weis *et al.*, 2006). The average values of the SRM 987 Sr standard and the LaJolla Nd standard analyzed during the course of this study are reported in Supplement Table 1.

The remaining of the Nd isotopic compositions, as well as the Pb and Hf isotope ratios of all samples, were determined on a Nu Plasma MC-ICP-MS (Nu Instruments Ltd, UK), under dry plasma conditions using a membrane desolvator (Nu DSN100) for sample introduction, All isotope

measurements were collected in static multi-collection mode, following the procedures detailed in Weis *et al.* (2006 and 2007).

During the Nd isotopic analyses by MC-ICP-MS, masses 147 (Sm) and 140 (Ce) were simultaneously monitored to allow for interference corrections on masses 144, 148 and 150 (Sm) and 142 (Ce). The ^{144}Sm, ^{148}Sm, ^{150}Sm and ^{142}Ce corrections were made assuming natural isotopic abundances (^{144}Sm = 0.030734, ^{147}Sm = 0.149934, ^{148}Sm = 0.112406, ^{150}Sm = 0.073796, ^{140}Ce = 0.88449, ^{142}Ce = 0.11114; Rosman & Taylor, 1998) adjusted for instrumental mass discrimination using an exponential law as monitored by the ^{146}Nd/^{144}Nd ratio. Nd isotope ratios were normalized internally to ^{146}Nd/^{144}Nd=0.7219 (as for the Triton TIMS measurements) and then to the daily average value of the Rennes Nd reference material analyses, relative to the value of^{143}Nd/^{144}Nd=0.511973 (Chauvel & Blichert-Toft, 2001). The average value for the Rennes Nd standard determined during the period of analyses is reported in Supplement Table 1.

Pb isotope measurements were internally corrected for potential ^{204}Hg isobaric interference on the ^{204}Pb ion beam assuming natural abundances (^{202}Hg/^{204}Hg = 4.35) adjusted for instrumental mass fractionation, and for mass fractionation using ^{205}Tl/^{203}Tl=2.3885 (Weis *et al.* 2006). Pb isotopic compositions were further corrected by off-line normalization to the triple-spike values (^{206}Pb/^{204}Pb = 16.9405, ^{207}Pb/^{204}Pb = 15.4963, and ^{208}Pb/^{204}Pb = 36.7219) of the NBS 981 Pb standard (Galer & Abouchami, 1998), using the ln-ln method as described in Albarède *et al.* (2004). During the period of sample analyses the NBS 981 Pb standard yielded mean values of ^{206}Pb/^{204}Pb = 16.9432 ± 0.0022, ^{207}Pb/^{204}Pb = 15.4999 ± 0.0023, and ^{208}Pb/^{204}Pb = 36.7224 ± 0.0067 (n=22) (Supplement Table 1), which are within 2SD of the triple spike values (Galer & Abouchami, 1998).

Hf isotopic compositions were corrected for potential ^{176}Lu, ^{176}Yb and ^{174}Yb interferences, and instrumental mass fractionation was corrected for using ^{179}Hf/^{177}Hf=0.7325. Results were then normalized to the daily average of the JMC 475 Hf standard relative to the ^{176}Hf/^{177}Hf value of 0.282160 of Vervoort & Blichert-Toft (1999). The JMC 475 Hf standard analyzed over the period of analyses gave an average value of ^{176}Hf/^{177}Hf= 0.282140 ± 0.000012 (n=25) as reported in Supplement Table 1.

To ensure the quality of the analyses, USGS reference materials (G-2 and BHVO-2) and other rock standards (Kilauea 93 and Koolau) were also processed and analyzed during the course of this

study. All the isotopic compositions obtained for these reference materials are in agreement with their respective published values (Weis *et al.*, 2006 and 2007). Isotopic data reproducibility was demonstrated by the analysis of complete procedural duplicates of some samples

Supplement Table 1 – Results obtained for the normalization material during analyses of the first and second batch of samples.

	1º batch		
In-run standards	isotope ratio		2 SD
SRM 987 standard (n=6)	$^{87}Sr/^{86}Sr$	0.710237	0.000013
La Jolla Standard (n=7)	$^{143}Nd/^{144}Nd$	0.511850	0.000008
JMC 475 Standard (n=25)	$^{176}Hf/^{177}Hf$	0.282140	0.000012
NBS 981 Standard (n=22)	$^{208}Pb/^{204}Pb$	36.7224	0.0067
	$^{207}Pb/^{204}Pb$	15.4999	0.0023
	$^{206}Pb/^{204}Pb$	16.9432	0.0022
	2º batch		
NBS 987 (n=11)	$^{87}Sr/^{86}Sr$	0.710245	0.000020
Rennes Standard (n=13)	$^{143}Nd/^{144}Nd$	0.511964	0.000037
	$^{145}Nd/^{144}Nd$	0.348389	0.000018
JMC 475 Standard (n=16)	$^{176}Hf/^{177}Hf$	0.282167	0.000014
NBS 981 Standard (n=14)	$^{208}Pb/^{204}Pb$	36.7212	0.0039
	$^{207}Pb/^{204}Pb$	15.4998	0.0021
	$^{206}Pb/^{204}Pb$	16.9436	0.0022

	Fajã de São João Sequence								
Location									
Sample	**SJ1**	**SJ2**	**SJ3**	**SJ5**	**SJ7**	**SJ8**	**SJ9**	**SJ10**	**SJ12**
Lithotype	B. Trachyand.	Basalt	Trachybasalt	Trachybasalt	Basalt	Trachybasalt	Basalt	B. Trachyand.	Basalt
SiO_2	53.39	48.29	48.66	49.05	48.38	49.62	48.5	51.39	45.87
Al_2O_3	15.02	16.49	17.27	15.82	22.31	17.65	17.25	16.88	16.63
$Fe_2O_3^T$	12.8	12.38	10.87	12.84	8.1	10.85	11.29	11.14	12.7
MnO	0.18	0.15	0.15	0.18	0.11	0.16	0.16	0.19	0.17
MgO	3.03	4.33	4.46	4.11	2.51	4.24	4.98	3.51	4.65
CaO	5.7	8.75	8.72	7.93	10.83	8.84	9.8	7.31	9.86
Na_2O	3.77	3.2	3.65	3.93	3.35	3.8	3.3	4.44	3.17
K_2O	1.91	1.34	1.32	1.67	0.99	1.38	1.11	1.91	1.21
TiO_2	2.15	3.03	2.80	3.43	2.03	2.66	2.96	2.44	3.65
P_2O_5	0.84	0.61	0.5	0.74	0.4	0.5	0.49	1.02	0.59
LOI	1.61	1.60	1.11	0.57	0.05	0.27	0.27	0.04	0.25
Total	100.40	100.17	99.51	100.27	99.05	99.97	100.11	100.28	98.75
Mg#	*0.38*	*0.45*	*0.51*	*0.45*	*0.42*	*0.50*	*0.51*	*0.45*	*0.46*
Sc	12	19	19	20.70	11	18	21	13	22
Be	2	2	2		1	2	2	3	2
V	104	235	214	230	134	192	240	128	299
Cr	20	30	80	0.80	20	90	100	20	20
Co	18.0	26.0	29.0	24.6	17.0	27.0	31.0	19.0	33.0
Ni	8	19	42	5.08	9	38	52	1	21
Cu	30.0	30.0	30.0	17.84	20.0	30.0	30.0	10.0	30.0
Zn	130	170	120	118.7	80	110	100	130	120
Ga	24.0	23.0	24.0	23.80	24.0	24.0	23.0	29.0	24.0
Ge	1.8	1.4	1.3		1.0	1.4	1.2	1.4	1.4
As	460	185	30		61	18	26	21	35
Rb	45.0	33.0	32.0	39.4	25.0	33.0	31.0	50.0	28.0
Sr	534	598	577	584	860	607	590	655	664
Y	48.3	35.7	36.1	37.3	25.3	36.2	33.8	57.8	36.5
Zr	342	276	305	357	178	323	264	424	271
Nb	50.4	39.9	43.7	52.5	25.6	44.7	38.4	66.8	43.1
Sn	3.0	23.0	3.0	2.7	2.0	3.0	3.0	3.0	2.0
Sb	0.8	0.4	0.2		0.5	0.2	0.2	0.2	0.9
Cs	4.0	2.1	0.6	0.456	1.4	0.6	1.2	0.9	0.7
Ba	456	311	308	396	262	320	269	468	288
La	44.3	33.8	37.8	34.71	22.1	37.4	33.0	54.9	34.6
Ce	98.0	74.9	80.4	85.31	48.6	80.3	71.1	122.0	76.7
Pr	11.6	8.9	9.3	10.33	5.9	9.2	8.4	14.3	9.2
Nd	50.9	38.3	39.4	47.12	26.3	38.5	36.6	62.0	40.7
Sm	11.60	8.63	8.47	10.92	5.98	8.38	7.88	13.60	9.10
Eu	3.97	3.06	3.03	3.53	2.37	2.95	2.85	4.61	3.19
Gd	10.60	7.84	7.49	10.75	5.57	7.58	7.38	12.00	7.98
Tb	1.72	1.25	1.22	1.53	0.90	1.22	1.20	1.93	1.31
Dy	9.45	7.06	6.96	8.67	4.97	6.92	6.70	10.80	7.28
Ho	1.67	1.27	1.24	1.49	0.89	1.24	1.19	1.93	1.27
Er	4.53	3.34	3.45	4.20	2.33	3.40	3.27	5.13	3.43
Tm	0.62	0.45	0.48	0.54	0.32	0.48	0.45	0.71	0.47
Yb	3.71	2.73	3.00	3.17	1.91	2.95	2.70	4.19	2.75
Lu	0.52	0.38	0.42	0.45	0.28	0.41	0.38	0.60	0.39
Hf	8.0	6.3	7.2	8.62	4.5	7.4	6.3	10.0	6.5
Ta	3.88	3.18	3.48	3.29	2.01	3.50	3.11	4.94	3.41
W	2.90	3.40	0.80		5.80	2.70	0.80	1.50	2.50
Tl	0.17	0.13	0.05		0.07	0.07	0.05	0.05	0.05
Pb	5.0	5.0	5.0	1.79	5.0	5.0	5.0	5.0	5.0
Th	4.10	3.23	3.91	3.69	2.01	4.07	3.30	5.09	3.14
U	1.24	1.15	1.23	1.19	0.61	1.41	0.94	1.68	1.12
Li				7.66					
Cd				0.39					
$^{87}Sr/^{86}Sr$				0.703752					
$^{143}Nd/^{144}Nd$				0.512948					
$^{176}Hf/^{177}Hf$				0.283050					
$^{208}Pb/^{204}Pb$				38.7590					
$^{207}Pb/^{204}Pb$				15.5450					
$^{206}Pb/^{204}Pb$				19.3498					

	Fajã de São João Sequence								
Location									
Sample	SJ13	SJ14	SJ15	SJ16	SJ17	SJ18	SJ19	SJ41	SJ43
Lithotype	B. Trachyand.	Basalt	B. Trachyand.	Trachybasalt	Basalt	B. Trachyand.	Basalt	Basalt	B. Trachyand.
SiO_2	53.59	47.18	50.11	49.02	48.59	51.22	46.36	46.8	50.95
Al_2O_3	16.72	19.57	16.31	15.94	20.61	18.24	23.03	16.73	15.44
$Fe_2O_3^T$	10.1	10.19	11.69	12.84	9.52	11.11	8.58	13.09	11.93
MnO	0.18	0.13	0.19	0.19	0.13	0.19	0.12	0.19	0.18
MgO	2.96	3.47	3.38	4.13	3.22	2.23	2.66	5.02	3.59
CaO	6.21	10.65	7.34	8.61	10.14	4.37	8.82	8.93	7.64
Na_2O	4.82	2.92	4.17	3.64	3.08	3.9	2.94	3.42	3.84
K_2O	2.42	1.18	2.03	1.66	1.16	2.8	0.95	1.29	1.78
TiO_2	2.15	2.83	2.60	3.41	2.52	2.08	2.32	3.52	2.93
P_2O_5	0.84	0.48	1.08	0.8	0.48	0.68	0.41	0.7	0.79
LOI	0.47	0.05	0.24	0.18	0.81	2.53	3.09	0.13	0.58
Total	100.45	98.65	99.14	100.42	100.26	99.35	99.27	99.81	99.65
Mg#	*0.43*	*0.44*	*0.43*	*0.45*	*0.44*	*0.34*	*0.42*	*0.47*	*0.44*
Sc	13	17	13	20	14	12	13	18	17
Be	2	2	2	3	2	2	2	2	2
V	124	223	152	243	185	68	158	244	173
Cr	20	20	30	20	20	20	20	30	20
Co	17.0	24.0	19.0	26.0	22.0	13.0	20.0	34.0	20.0
Ni	7	23	3	7	19	2	12	24	2
Cu	10.0	20.0	20.0	30.0	20.0	20.0	20.0	20.0	10.0
Zn	130	100	140	120	90	150	90	120	130
Ga	29.0	24.0	27.0	26.0	24.0	32.0	26.0	25.0	26.0
Ge	1.5	1.3	1.5	1.4	1.2	1.7	1.2	1.4	1.5
As	45	45	27	66	22	20	15	16	18
Rb	64.0	34.0	46.0	42.0	32.0	67.0	23.0	25.0	28.0
Sr	525	754	637	664	801	356	738	765	662
Y	56.6	29.0	54.1	45.8	29.6	51.7	29.7	36.9	49.5
Zr	506	231	407	351	216	573	189	307	359
Nb	69.1	32.0	60.1	51.0	31.8	74.1	29.8	53.0	52.9
Sn	4.0	3.0	4.0	3.0	3.0	5.0	2.0	2.0	3.0
Sb	0.3	0.2	0.2	0.2	0.2	0.2	0.2	0.2	0.7
Cs	1.3	2.0	0.9	1.4	1.5	0.6	0.6	0.8	0.6
Ba	522	294	515	437	308	727	266	365	454
La	59.1	27.1	53.1	43.1	27.2	52.4	23.3	40.2	44.3
Ce	127.0	59.6	115.0	94.9	58.3	115.0	54.1	88.4	98.4
Pr	14.8	7.1	14.2	11.5	7.1	13.9	6.5	10.8	12.0
Nd	61.0	31.6	61.2	50.5	32.0	59.9	28.5	46.0	52.6
Sm	13.00	7.25	13.20	11.30	7.33	13.50	6.67	9.68	12.10
Eu	4.19	2.67	4.49	3.98	2.75	4.64	2.64	3.39	4.22
Gd	11.50	6.60	12.00	10.40	6.59	12.00	5.87	8.12	10.80
Tb	1.88	1.05	1.93	1.70	1.09	1.99	1.00	1.30	1.79
Dy	10.30	5.90	10.50	9.28	6.02	10.80	5.65	7.23	10.10
Ho	1.87	1.05	1.85	1.65	1.07	1.87	0.99	1.31	1.81
Er	5.12	2.84	4.99	4.41	2.82	4.94	2.66	3.51	4.82
Tm	0.73	0.39	0.69	0.61	0.39	0.68	0.36	0.47	0.65
Yb	4.38	2.34	4.10	3.65	2.34	4.18	2.13	2.78	3.91
Lu	0.63	0.32	0.56	0.50	0.33	0.59	0.30	0.40	0.54
Hf	10.9	5.4	9.3	8.3	5.4	13.4	4.9	7.1	9.0
Ta	5.10	2.62	4.53	4.12	2.52	5.66	2.19	4.02	4.05
W	3.90	8.30	3.50	4.10	9.40	1.50	2.60	4.20	1.70
Tl	0.08	0.12	0.05	0.08	0.09	0.05	0.05	0.06	0.05
Pb	5.0	5.0	5.0	5.0	5.0	5.0	5.0	7.0	5.0
Th	6.53	2.96	4.89	4.05	2.53	6.61	1.89	3.42	3.80
U	2.05	0.86	0.65	1.25	0.89	0.85	0.66	1.15	1.15
Li									
Cd									
$^{87}Sr/^{86}Sr$									
$^{143}Nd/^{144}Nd$									
$^{176}Hf/^{177}Hf$									
$^{208}Pb/^{204}Pb$									
$^{207}Pb/^{204}Pb$									
$^{206}Pb/^{204}Pb$									

	F.São João
Location	
Sample	SJ44
Lithotype	Trachybasalt
SiO_2	51.2
Al_2O_3	17.36
$Fe_2O_3^T$	10.75
MnO	0.16
MgO	4.05
CaO	8.77
Na_2O	3.72
K_2O	1.37
TiO_2	2.72
P_2O_5	0.5
LOI	0.18
Total	100.78
Mg#	*0.49*
Sc	18
Be	2
V	207
Cr	70
Co	27.0
Ni	37
Cu	20.0
Zn	110
Ga	25.0
Ge	1.4
As	11
Rb	29.0
Sr	585
Y	36.8
Zr	317
Nb	46.4
Sn	3.0
Sb	0.3
Cs	0.4
Ba	312
La	39.5
Ce	83.4
Pr	9.7
Nd	40.7
Sm	8.59
Eu	3.01
Gd	7.48
Tb	1.25
Dy	7.20
Ho	1.29
Er	3.53
Tm	0.50
Yb	3.00
Lu	0.43
Hf	7.4
Ta	3.53
W	1.70
Tl	0.05
Pb	5.0
Th	3.88
U	0.87
Li	
Cd	
$^{87}Sr/^{86}Sr$	
$^{143}Nd/^{144}Nd$	
$^{176}Hf/^{177}Hf$	
$^{208}Pb/^{204}Pb$	
$^{207}Pb/^{204}Pb$	
$^{206}Pb/^{204}Pb$	

	Topo Volcanic Complex					
Location	Caldeira-Cubres Volcanic Sequence					
Sample	SJ45	SJ46	SJ47	SJ48	SJ49	SJ50
Lithotype	Basalt	Trachybasalt	Basalt	Basalt	Basalt	Basalt
SiO_2	47.91	47.46	45.83	46.24	46.18	45.16
Al_2O_3	23.02	16.08	15.63	15.72	16.19	11.93
$Fe_2O_3^T$	7.71	12.57	11.63	11.98	11.77	11.93
MnO	0.10	0.18	0.17	0.17	0.17	0.17
MgO	2.23	4.09	6.86	7.34	5.81	12.66
CaO	11.7	8.04	9.8	9.16	9.92	11.71
Na_2O	3.22	3.89	3.62	3.64	3.38	2.42
K_2O	0.83	1.39	1.11	1.13	1.32	0.72
TiO_2	2.01	3.47	2.90	2.88	3.22	2.69
P_2O_5	0.39	0.77	0.54	0.55	0.64	0.36
LOI	0.08	0.96	1.21	0.33	0.95	0.12
Total	99.20	98.90	99.30	99.15	99.55	99.88
Mg#	*0.40*	*0.45*	*0.58*	*0.59*	*0.54*	*0.71*
Sc	18	15	21	20	20	34
Be		2	2		2	2
V	236	238	247	263	250	298
Cr	1	20	160	104	100	560
Co	26.2	28.0	42.0	35.0	36.0	59.0
Ni	2	2	121	64	65	214
Cu	8.0	20.0	40.0	22.8	30.0	50.0
Zn	119	140	110	99	110	100
Ga	23.4	28.0	23.0	21.1	23.0	18.0
Ge		1.5	1.4		1.3	1.5
As		7	19		20	14
Rb	36.6	36.0	27.0	30.0	33.0	16.0
Sr	798	759	687	730	731	462
Y	43.3	47.7	33.2	27.0	34.1	27.1
Zr	316	304	216	281	264	151
Nb	63.4	57.5	38.1	49.7	45.1	26.8
Sn	2.6	3.0	2.0	1.8	2.0	2.0
Sb		0.2	0.2		0.2	0.3
Cs	0.4	0.6	0.6	0.3	0.9	0.4
Ba	388	382	291	334	343	193
La	41.7	44.1	30.7	31.8	35.7	20.9
Ce	92.0	96.4	66.0	78.0	78.4	46.7
Pr	11.1	11.6	8.1	9.4	9.4	5.9
Nd	49.1	50.2	34.8	39.7	40.1	26.6
Sm	10.56	11.20	7.68	8.34	8.75	6.12
Eu	3.47	3.95	2.72	2.73	2.99	2.23
Gd	9.59	10.20	7.13	7.96	7.59	5.95
Tb	1.42	1.63	1.17	1.11	1.24	0.96
Dy	7.87	8.94	6.38	6.41	6.80	5.38
Ho	1.40	1.59	1.14	1.12	1.20	0.97
Er	3.70	4.33	3.10	2.89	3.27	2.60
Tm	0.50	0.59	0.43	0.39	0.44	0.36
Yb	2.93	3.51	2.57	2.52	2.70	2.10
Lu	0.40	0.48	0.35	0.33	0.37	0.30
Hf	8.1	7.4	5.4	6.4	6.3	4.2
Ta	4.17	4.15	2.70	3.16	3.46	2.04
W		3.90	1.20		1.70	1.30
Tl		0.05	0.07		0.05	0.05
Pb	2.2	5.0	5.0	1.8	5.0	5.0
Th	3.80	3.74	2.58	3.33	3.18	1.72
U	1.39	1.47	1.02	1.28	1.31	0.64
Li	7.24			5.86		
Cd	0.35			0.29		
$^{87}Sr/^{86}Sr$	0.703706			0.703779		
$^{143}Nd/^{144}Nd$	0.512982			0.512991		
$^{176}Hf/^{177}Hf$	0.283092			0.283088		
$^{208}Pb/^{204}Pb$	39.2212			39.2455		
$^{207}Pb/^{204}Pb$	15.6257			15.6279		
$^{206}Pb/^{204}Pb$	20.0985			20.1159		

	Topo Volcanic Complex								
Location	Caldeira-Cubres Volcanic Sequence								
Sample	SJ51	SJ52	SJ53	SJ54	SJ55	SJ56	SJ58	SJ59	SJ60
Lithotype	Basalt	basalt	Basalt	Basanite	Tefrite	Trachybasalt	Trachybasalt	Basalt	Basalt
SiO_2	45.76	44.96	46.5	44.57	44.93	46.97	48.98	46.43	45.37
Al_2O_3	15.47	15.59	15.82	14.72	15.16	16.23	16.92	15.55	14.72
$Fe_2O_3^T$	14.11	12.39	12.12	12.95	15.05	12.73	11.61	11.98	12.11
MnO	0.18	0.18	0.16	0.19	0.18	0.18	0.20	0.16	0.17
MgO	5.13	6.81	7.44	8.14	5.39	5.88	4	7.4	9.28
CaO	9.21	10.19	9.97	9.49	9.41	8.83	7.62	9.95	10.65
Na_2O	3.52	3.08	3.15	3.79	3.61	3.93	4.77	3.2	2.93
K_2O	1.13	1.12	0.79	1.38	1.06	1.25	1.59	0.77	0.89
TiO_2	4.49	3.53	3.34	3.70	4.73	3.38	2.83	3.33	2.88
P_2O_5	0.59	0.63	0.42	0.66	0.51	0.65	0.81	0.43	0.44
LOI	0.39	0.85	0.06	0.45	0.42	0.01	0.11	0.08	0.27
Total	99.98	99.32	99.77	100.04	100.45	100.04	99.45	99.28	99.70
Mg#	*0.46*	*0.56*	*0.59*	*0.60*	*0.46*	*0.54*	*0.46*	*0.59*	*0.64*
Sc	21	24	23	22	21	18	10	24	24
Be	2	2	2	2	2	2	3	2	2
V	369	302	266	314	384	246	149	272	251
Cr	20	90	180	120	20	60	20	190	230
Co	41.0	41.0	43.0	47.0	44.0	38.0	23.0	43.0	49.0
Ni	20	57	107	109	27	50	5	108	123
Cu	30.0	30.0	40.0	40.0	30.0	30.0	20.0	50.0	30.0
Zn	140	110	100	130	150	130	120	100	100
Ga	27.0	24.0	22.0	24.0	26.0	25.0	23.0	22.0	20.0
Ge	1.4	1.4	1.3	1.4	1.5	1.4	1.3	1.3	1.3
As	29	17	9	9	13	11	12	9	5
Rb	29.0	29.0	18.0	32.0	24.0	30.0	34.0	34.0	20.0
Sr	701	712	627	715	700	744	810	630	657
Y	39.5	36.3	31.1	36.8	36.5	36.6	37.8	31.7	28.4
Zr	251	271	193	268	227	281	300	199	203
Nb	45.4	49.6	31.0	50.8	41.5	50.3	53.5	32.9	35.8
Sn	2.0	2.0	2.0	5.0	2.0	2.0	2.0	2.0	2.0
Sb	0.3	0.2	0.2	0.3	0.2	0.2	0.2	0.2	0.2
Cs	0.6	0.5	0.5	0.4	0.5	0.6	0.5	0.5	0.3
Ba	305	294	230	361	265	340	406	235	249
La	34.4	38.5	23.5	37.3	30.5	41.2	45.0	24.5	30.5
Ce	75.3	84.0	52.9	81.7	67.5	88.8	96.4	55.7	65.2
Pr	9.3	10.0	6.7	9.8	8.3	10.5	11.3	7.0	7.6
Nd	40.5	43.0	30.5	41.8	36.6	45.3	48.1	31.8	33.0
Sm	9.32	9.04	7.21	8.92	8.57	9.67	9.92	7.36	6.92
Eu	3.34	3.18	2.67	3.06	3.09	3.37	3.37	2.65	2.46
Gd	8.81	8.23	6.86	8.13	8.17	8.71	8.98	6.98	6.39
Tb	1.41	1.29	1.11	1.29	1.33	1.37	1.39	1.13	1.04
Dy	7.76	7.11	6.18	7.10	7.28	7.33	7.53	6.39	5.66
Ho	1.36	1.26	1.07	1.26	1.28	1.31	1.35	1.15	1.00
Er	3.67	3.45	2.89	3.42	3.46	3.62	3.74	3.04	2.73
Tm	0.50	0.47	0.40	0.47	0.46	0.48	0.52	0.41	0.37
Yb	2.93	2.83	2.41	2.75	2.70	2.89	3.10	2.46	2.19
Lu	0.40	0.39	0.32	0.39	0.38	0.40	0.43	0.33	0.30
Hf	6.5	6.5	4.8	6.5	6.0	6.8	7.0	5.1	5.1
Ta	3.42	3.66	2.31	3.80	3.14	3.81	4.12	2.48	2.60
W	0.80	1.10	1.30	0.80	1.20	1.40	1.10	1.00	1.10
Tl	0.05	0.05	0.05	0.05	0.05	0.06	0.05	0.05	0.05
Pb	5.0	5.0	5.0	9.0	5.0	5.0	5.0	5.0	5.0
Th	3.07	3.40	2.03	3.02	2.53	3.61	3.93	2.16	2.63
U	1.41	1.33	0.78	1.12	0.96	1.28	1.01	0.85	0.95
Li									
Cd									
$^{87}Sr/^{86}Sr$									
$^{143}Nd/^{144}Nd$									
$^{176}Hf/^{177}Hf$									
$^{208}Pb/^{204}Pb$									
$^{207}Pb/^{204}Pb$									
$^{206}Pb/^{204}Pb$									

	Topo Volcanic Complex								
Location	Caldeira-Cubres Volcanic Sequence								
Sample	SJ61	SJ62	SJ63	SJ64	SJ65	SJ66	SJ67	SJ68	SJ69
Lithotype	Basalt	Basalt	Basalt	Basalt	Basalt	Trachybasalt	Trachybasalt	Basalt	Basalt
SiO_2	45.72	45.9	45.48	45.76	45.21	48.3	46.29	45.67	45.93
Al_2O_3	13.88	15.51	12.02	15.94	12.24	17.07	15.28	15.86	15.51
$Fe_2O_3^T$	12.05	12.46	11.28	12.14	11.51	11.91	13.7	12.74	14.56
MnO	0.17	0.18	0.16	0.17	0.16	0.19	0.19	0.18	0.19
MgO	8.91	6.42	13.52	6.54	12.71	4.04	4.84	5.49	5.26
CaO	11.05	10.8	11.21	10.02	11.41	8.28	8.88	9.75	9.18
Na_2O	3.12	3.36	1.94	3.23	2.68	4.4	3.75	3.55	3.41
K_2O	0.84	0.94	0.73	0.98	0.36	1.4	1.24	1.05	0.96
TiO_2	2.94	3.23	2.67	3.34	2.92	3.15	4.10	3.73	4.55
P_2O_5	0.44	0.5	0.33	0.47	0.34	0.87	0.61	0.56	0.54
LOI	0.08	0.25	0.49	0.92	0.10	0.38	0.03	0.57	0.30
Total	99.21	99.55	99.84	99.51	99.64	99.99	98.90	99.15	100.38
Mg#	*0.63*	*0.55*	*0.74*	*0.56*	*0.72*	*0.46*	*0.47*	*0.50*	*0.46*
Sc	27	23	34	24	34	14	20	21	20
Be	2	2	1		2	2	2	2	2
V	279	289	281	289	298	171	318	309	351
Cr	360	80	730	61	650	40	20	40	20
Co	49.0	40.0	58.0	40.3	55.0	29.0	34.0	39.0	40.0
Ni	132	57	316	49	302	28	14	41	18
Cu	40.0	30.0	50.0	18.9	60.0	20.0	20.0	40.0	30.0
Zn	100	100	80	90	80	120	140	120	130
Ga	21.0	20.0	17.0	19.4	17.0	24.0	26.0	24.0	25.0
Ge	1.4	1.4	1.2		1.3	1.3	1.4	1.3	1.3
As	18	33	8		5	12	21	10	10
Rb	18.0	20.0	17.0	21.9	16.0	31.0	33.0	27.0	26.0
Sr	597	714	418	882	433	821	708	676	696
Y	31.8	32.1	23.5	28.0	25.2	39.4	39.1	36.1	35.8
Zr	192	217	148	219	161	306	268	229	230
Nb	31.9	33.0	27.7	36.7	28.9	52.0	45.7	41.2	40.1
Sn	2.0	2.0	1.0	1.7	1.0	2.0	2.0	1.0	2.0
Sb	0.3	0.2	0.2		0.2	0.3	0.2	0.2	0.2
Cs	0.5	0.5	0.3	0.2	0.3	0.5	0.7	0.7	1.2
Ba	215	245	206	264	208	386	327	317	287
La	26.2	30.8	23.1	26.1	23.5	48.3	38.8	33.6	32.9
Ce	59.2	70.2	52.2	60.3	53.2	105.0	86.5	74.9	74.3
Pr	7.4	8.7	6.3	7.8	6.4	12.3	10.5	9.1	9.1
Nd	32.6	38.0	26.6	33.7	27.5	52.3	44.7	39.8	39.9
Sm	7.43	8.56	5.96	7.63	6.17	10.70	9.97	8.78	8.78
Eu	2.66	2.78	1.93	2.47	2.06	3.39	3.25	2.93	3.03
Gd	7.02	8.47	5.96	7.29	6.09	9.52	9.41	8.70	9.15
Tb	1.13	1.28	0.91	0.97	0.95	1.44	1.47	1.34	1.39
Dy	6.23	6.27	4.56	5.85	4.93	7.48	7.53	6.77	6.98
Ho	1.10	1.12	0.83	1.04	0.88	1.32	1.32	1.20	1.24
Er	3.01	2.95	2.20	2.82	2.28	3.48	3.53	3.20	3.21
Tm	0.41	0.39	0.29	0.36	0.30	0.47	0.46	0.42	0.42
Yb	2.41	2.39	1.73	2.19	1.80	2.83	2.73	2.62	2.54
Lu	0.34	0.37	0.26	0.30	0.28	0.44	0.43	0.41	0.39
Hf	5.1	5.7	4.1	5.5	4.4	7.3	6.7	5.9	6.2
Ta	2.37	2.68	2.27	2.50	2.37	4.11	3.63	3.17	3.31
W	2.20	1.00	0.90		0.60	0.90	3.80	1.20	1.30
Tl	0.05	0.05	0.05		0.05	0.05	0.06	0.05	0.06
Pb	5.0	5.0	5.0	1.7	5.0	5.0	5.0	5.0	5.0
Th	2.21	2.23	1.82	2.35	1.85	3.67	3.26	2.68	2.64
U	0.84	0.92	0.61	0.87	0.65	1.02	1.16	0.99	0.93
Li				5.73					
Cd				0.22					
$^{87}Sr/^{86}Sr$				0.703755					
$^{143}Nd/^{144}Nd$				0.512986					
$^{176}Hf/^{177}Hf$				0.283088					
$^{208}Pb/^{204}Pb$				39.3693					
$^{207}Pb/^{204}Pb$				15.6549					
$^{206}Pb/^{204}Pb$				20.3616					

	Topo Volcanic Complex								
Location	Caldeira-Cubres Volcanic Sequence							Vimes	Topo Village
Sample	SJ70	SJ71	SJ72	SJ73	SJ74	SJ75	SJ76	SJ95	SJ102
Lithotype	Basalt	Trachybasalt	Basalt	Basalt	Basalt	Basalt	Basalt	Trachybasalt	Basalt
SiO_2	45.42	47.47	44.82	45.97	44.47	44.75	45.48	49	45.43
Al_2O_3	12.04	16.45	14.83	19.26	15.31	15.98	14.64	16.36	15.27
$Fe_2O_3^T$	11.73	12.35	14.68	11.03	14.59	13.45	12.3	11.92	12.43
MnO	0.17	0.19	0.19	0.14	0.18	0.17	0.18	0.21	0.19
MgO	12.69	4.41	5.2	3.98	5.22	5.82	8.94	4.04	7.4
CaO	11.65	8.63	9.51	11.4	9.54	10.09	9.16	7.76	10.1
Na_2O	2.2	3.75	3.3	2.84	3.18	2.84	3.39	4.6	2.52
K_2O	0.78	1.26	0.94	0.72	0.95	0.79	1.32	1.59	1.41
TiO_2	2.89	3.46	4.74	3.52	4.65	3.91	3.32	3.06	3.49
P_2O_5	0.36	0.75	0.57	0.42	0.54	0.52	0.7	1.24	0.68
LOI	0.01	0.12	0.43	0.14	0.31	1.01	0.16	0.43	1.08
Total	99.93	98.84	99.21	99.42	98.95	99.33	99.59	100.20	100.00
Mg#	*0.72*	*0.47*	*0.45*	*0.46*	*0.46*	*0.50*	*0.63*	*0.46*	*0.58*
Sc	33	16	26	20	22	26	22	16	24
Be	2	2		2	2	2			3
V	296	226	316	289	346	301	249	159	302
Cr	700	30	21	60	30	150	167	3	210
Co	59.0	27.0	41.5	34.0	45.0	43.0	43.6	21.1	42.0
Ni	308	18	34	33	31	66	151	5	115
Cu	90.0	20.0	25.5	30.0	30.0	30.0	20.7	8.8	40.0
Zn	90	130	117	110	140	120	99	122	120
Ga	18.0	24.0	22.7	24.0	25.0	24.0	19.8	22.7	24.0
Ge	1.3	1.4		1.2	1.4	1.4			1.5
As	15	13		5	5	8			6
Rb	19.0	27.0	17.7	16.0	20.0	18.0	28.4	33.5	31.0
Sr	425	845	679	802	699	626	728	814	698
Y	26.4	42.0	34.2	28.9	35.3	34.3	28.0	48.1	37.2
Zr	163	293	268	180	237	206	309	392	295
Nb	32.9	46.9	43.4	29.8	40.3	35.2	58.2	75.1	53.4
Sn	2.0	2.0	1.6	2.0	2.0	2.0	2.1	2.6	2.0
Sb	0.2	0.2		0.2	0.2	0.2			0.2
Cs	0.4	0.6	0.1	0.4	0.3	0.3	0.3	0.3	0.4
Ba	222	361	276	217	271	256	335	453	365
La	25.7	42.5	28.5	24.8	32.3	28.6	34.5	51.9	38.8
Ce	57.3	96.2	69.8	56.4	73.3	65.8	82.6	116.7	85.5
Pr	6.9	11.7	9.1	7.1	9.1	8.1	10.1	15.0	9.7
Nd	29.7	51.0	38.7	30.8	39.2	36.4	40.8	64.5	40.8
Sm	6.43	11.10	9.44	7.09	8.86	8.44	8.69	14.17	8.60
Eu	2.12	3.67	2.93	2.51	3.00	2.86	2.68	4.32	3.05
Gd	6.64	11.30	8.98	7.61	9.38	8.92	7.80	12.49	8.18
Tb	1.00	1.64	1.25	1.13	1.38	1.35	1.06	1.73	1.24
Dy	4.97	8.30	7.04	5.58	6.85	6.62	6.12	9.65	6.80
Ho	0.91	1.47	1.27	1.00	1.22	1.19	1.12	1.73	1.23
Er	2.39	3.83	3.49	2.55	3.24	3.16	2.98	4.64	3.25
Tm	0.31	0.49	0.45	0.34	0.42	0.41	0.40	0.65	0.45
Yb	1.91	3.06	2.68	2.07	2.54	2.47	2.37	3.79	2.68
Lu	0.29	0.47	0.35	0.32	0.38	0.37	0.32	0.50	0.39
Hf	4.5	7.3	7.1	4.7	6.1	5.3	7.8	9.8	6.9
Ta	2.57	3.86	3.04	2.35	3.28	2.76	4.34	4.79	4.46
W	0.80	1.50		0.70	0.70	2.20			1.50
Tl	0.05	0.05		0.05	0.05	0.05			0.05
Pb	5.0	5.0	1.5	5.0	5.0	5.0	2.3	2.8	5.0
Th	2.05	3.20	3.20	1.83	2.46	2.13	3.80	5.07	3.49
U	0.73	1.00	1.17	0.64	0.97	0.86	1.37	1.97	0.89
Li			5.55				6.15	3.90	
Cd			0.24				0.26	0.35	
$^{87}Sr/^{86}Sr$			0.703684				0.703691	0.703690	
$^{143}Nd/^{144}Nd$			0.512977				0.512849	0.512976	
$^{176}Hf/^{177}Hf$			0.283090				0.283033	0.283078	
$^{208}Pb/^{204}Pb$			39.0939				39.4269	39.1308	
$^{207}Pb/^{204}Pb$			15.6123				15.6492	15.6246	
$^{206}Pb/^{204}Pb$			19.8704				20.3137	19.9194	

	Topo Volcanic Complex	
Location	Topo Village	
Sample	SJ103	SJ109
Lithotype	Basalt	Basalt
SiO_2	46.11	45.18
Al_2O_3	14.65	15.77
$Fe_2O_3^T$	11.65	11.61
MnO	0.16	0.17
MgO	9.86	8.51
CaO	9.67	9.49
Na_2O	2.56	2.76
K_2O	1.09	0.77
TiO_2	3.19	3.37
P_2O_5	0.56	0.58
LOI	0.28	0.83
Total	99.78	99.03
Mg#	*0.66*	*0.63*
Sc	26	28
Be	2	2
V	267	308
Cr	310	370
Co	44.0	44.0
Ni	204	162
Cu	30.0	50.0
Zn	90	100
Ga	20.0	22.0
Ge	1.4	1.4
As	11	5
Rb	19.0	8.0
Sr	576	546
Y	29.0	32.1
Zr	245	264
Nb	41.0	48.4
Sn	2.0	15.0
Sb	1.1	0.2
Cs	0.3	0.3
Ba	302	390
La	31.2	42.1
Ce	70.5	88.7
Pr	8.1	10.2
Nd	34.7	42.0
Sm	7.24	8.30
Eu	2.61	2.92
Gd	7.14	8.10
Tb	1.05	1.16
Dy	5.69	6.33
Ho	1.01	1.11
Er	2.65	2.92
Tm	0.37	0.40
Yb	2.19	2.52
Lu	0.31	0.34
Hf	5.7	6.4
Ta	3.49	4.02
W	1.10	2.20
Tl	0.05	0.05
Pb	5.0	11.0
Th	2.87	3.57
U	0.98	1.19
Li		
Cd		
$^{87}Sr/^{86}Sr$		
$^{143}Nd/^{144}Nd$		
$^{176}Hf/^{177}Hf$		
$^{208}Pb/^{204}Pb$		
$^{207}Pb/^{204}Pb$		
$^{206}Pb/^{204}Pb$		

	Rosais Volcanic Complex				
Location	João Dias Sequence				
Sample	SJ82	SJ84	SJ85	SJ86	SJ87
Lithotype	Trachybasalt	Basalt	Basalt	Trachybasalt	Trachybasalt
SiO_2	47.62	45.95	45.38	49.15	47.91
Al_2O_3	15.44	14.76	15.68	16.68	15.42
$Fe_2O_3^T$	11.09	12.42	13.26	10.97	11.75
MnO	0.15	0.18	0.18	0.17	0.17
MgO	5.39	8.14	7.39	4.29	6.31
CaO	8.14	10.28	9.3	7.41	9.12
Na_2O	3.44	3	3.32	3.88	3.29
K_2O	2.03	1.29	1.41	2.38	1.94
TiO_2	3.10	3.22	3.51	2.82	3.20
P_2O_5	0.7	0.55	0.55	0.89	0.72
LOI	1.63	0.39	0.31	0.27	0.42
Total	98.73	100.17	100.29	98.92	100.24
Mg#	*0.55*	*0.61*	*0.57*	*0.50*	*0.57*
Sc	18.00	28.51	22.00	14.00	22.00
Be	3.00		2.00	3.00	2.00
V	259	279	309	215	281
Cr	110.00	242.47	110.00	20.00	120.00
Co	32.0	45.6	43.0	26.0	35.0
Ni	69.00	113.04	79.00	17.00	69.00
Cu	30.00	32.32	30.00	20.00	30.00
Zn	110.0	90.2	110.0	120.0	100.0
Ga	24.00	19.27	22.00	26.00	23.00
Ge	1.3		1.4	1.3	1.3
As	5.00		5.00	5.00	17.00
Rb	48.0	25.1	29.0	55.0	43.0
Sr	717	648	717	791	765
Y	30.1	24.3	28.5	32.9	30.0
Zr	345	250	240	375	305
Nb	56.3	48.8	44.1	64.2	52.6
Sn	2.0	1.7	2.0	2.0	2.0
Sb	0.2		0.3	0.2	0.2
Cs	0.400	0.183	0.300	0.400	0.500
Ba	526	335	378	601	540
La	55.00	30.81	37.80	62.10	51.10
Ce	116.00	75.82	83.20	132.00	109.00
Pr	12.90	9.34	9.93	14.80	12.30
Nd	50.80	37.55	41.70	58.80	49.10
Sm	9.25	7.60	8.27	10.50	9.41
Eu	2.85	2.55	2.58	3.18	2.77
Gd	7.02	6.85	6.92	7.86	6.98
Tb	1.09	0.94	1.06	1.19	1.07
Dy	5.55	5.36	5.39	6.01	5.56
Ho	0.99	0.94	0.97	1.07	0.98
Er	2.54	2.50	2.50	2.78	2.47
Tm	0.33	0.36	0.33	0.38	0.32
Yb	2.12	2.03	1.98	2.39	2.00
Lu	0.33	0.29	0.32	0.37	0.32
Hf	7.90	6.89	6.30	8.90	7.40
Ta	4.53	3.40	3.63	5.22	4.17
W	0.70		1.00	1.20	1.00
Tl	0.05		0.05	0.05	0.05
Pb	5.00	2.29	5.00	5.00	5.00
Th	5.73	3.42	3.30	6.05	5.05
U	1.60	1.05	1.04	1.39	1.39
Li		5.45			
Cd		0.24			
$^{87}Sr/^{86}Sr$		0.703893			
$^{143}Nd/^{144}Nd$		0.512959			
$^{176}Hf/^{177}Hf$		0.282944			
$^{208}Pb/^{204}Pb$		39.1682			
$^{207}Pb/^{204}Pb$		15.6300			
$^{206}Pb/^{204}Pb$		19.2236			

	Rosais Volcanic Complex								
Location	João Dias Sequence						Rosais		
Sample	SJ88	SJ89	SJ90	SJ91	SJ92	SJ93	SJ28	SJ29	SJ30
Lithotype	Trachybasalt	Basalt	Basalt	Trachybasalt	Basalt	Basalt	Basalt	Basalt	Trachybasalt
SiO_2	48.08	45.56	45.9	47.12	45.01	45.12	45.34	46.05	48.03
Al_2O_3	16.24	13.75	15.48	15.87	13.64	13.45	16.66	15.72	17.1
$Fe_2O_3^T$	11.87	12.24	12.81	11.98	12.18	12.27	12.84	12.48	12.7
MnO	0.17	0.17	0.17	0.17	0.17	0.17	0.18	0.16	0.20
MgO	5.49	9.14	6.65	5.79	9.44	9.34	5.51	7.63	4.44
CaO	8.66	11.08	9.23	8.8	11.1	11.05	8.86	9.27	7.75
Na_2O	3.38	3.01	3	3.42	2.33	2.9	3.61	2.67	3.84
K_2O	2.02	1.16	1.54	1.58	1.16	1.15	1.27	1.05	1.56
TiO_2	3.38	3.20	3.78	3.37	3.10	3.13	3.74	3.16	3.18
P_2O_5	0.75	0.5	0.61	0.65	0.48	0.49	0.66	0.56	0.81
LOI	0.34	0.43	0.46	0.21	0.41	0.08	0.32	0.47	0.06
Total	100.39	100.24	99.63	98.96	99.02	99.15	98.98	99.22	99.67
Mg#	*0.54*	*0.64*	*0.55*	*0.55*	*0.64*	*0.64*	*0.50*	*0.59*	*0.47*
Sc	21.87	30.00	21.00	20.00	30.00	29.00	19.00	21.00	14.58
Be		2.00	2.00	3.00	2.00	2.00	2.00	2.00	
V	270	317	341	283	305	307	268	236	208
Cr	37.84	290.00	110.00	90.00	320.00	290.00	40.00	210.00	4.12
Co	32.8	47.0	41.0	35.0	50.0	47.0	39.0	47.0	26.8
Ni	31.53	124.00	61.00	57.00	139.00	126.00	46.00	140.00	5.80
Cu	20.22	40.00	30.00	40.00	50.00	40.00	20.00	30.00	8.29
Zn	96.4	100.0	110.0	110.0	100.0	90.0	130.0	120.0	122.6
Ga	21.79	21.00	25.00	24.00	22.00	20.00	26.00	23.00	23.81
Ge		1.4	1.4	1.4	1.4	1.4	1.4	1.4	
As		7.00	5.00	17.00	5.00	9.00	28.00	19.00	
Rb	41.1	25.0	35.0	28.0	28.0	24.0	27.0	21.0	26.6
Sr	825	626	755	806	631	611	696	606	741
Y	27.6	27.4	30.1	30.5	28.7	26.3	36.8	32.4	31.0
Zr	356	206	273	300	200	202	293	254	385
Nb	76.5	34.7	52.5	54.1	35.8	33.6	52.8	42.9	67.7
Sn	2.0	2.0	2.0	2.0	2.0	2.0	3.0	2.0	2.4
Sb		0.2	0.3	0.3	0.4	0.5	0.3	0.3	
Cs	0.239	0.300	0.400	0.800	0.500	0.400	0.700	0.500	0.102
Ba	566	319	453	542	313	311	337	267	427
La	51.27	31.40	44.70	50.50	31.70	30.60	38.20	32.70	45.32
Ce	114.61	69.80	96.70	108.00	70.20	68.20	86.10	72.10	100.53
Pr	12.82	8.37	11.10	12.30	8.39	8.09	10.40	8.99	12.93
Nd	50.96	35.40	46.00	50.20	35.10	34.50	45.50	39.00	55.69
Sm	10.25	7.39	8.75	9.18	7.51	7.24	9.77	8.22	11.15
Eu	2.94	2.34	2.72	2.78	2.36	2.23	3.41	2.95	3.50
Gd	8.05	6.35	7.14	7.30	6.47	6.31	8.21	7.09	10.29
Tb	1.08	0.98	1.09	1.07	0.99	0.97	1.30	1.12	1.39
Dy	5.72	5.08	5.49	5.66	5.15	5.06	7.40	6.23	7.91
Ho	1.04	0.90	0.98	1.00	0.92	0.88	1.35	1.11	1.40
Er	2.65	2.35	2.49	2.58	2.35	2.31	3.54	2.94	3.82
Tm	0.38	0.31	0.33	0.35	0.31	0.30	0.48	0.40	0.47
Yb	2.19	1.85	2.05	2.07	1.90	1.81	2.81	2.37	2.99
Lu	0.28	0.28	0.31	0.32	0.28	0.28	0.39	0.33	0.42
Hf	9.28	5.40	6.90	7.30	5.40	5.30	7.20	6.20	8.58
Ta	5.08	2.78	4.17	4.29	2.78	2.73	4.07	3.27	4.28
W		0.80	0.70	1.60	1.00	1.40	4.30	2.30	
Tl		0.05	0.05	0.07	0.05	0.05	0.05	0.05	
Pb	3.74	5.00	5.00	5.00	5.00	5.00	5.00	5.00	2.05
Th	5.98	2.70	4.25	5.13	2.72	2.66	3.26	2.69	4.39
U	1.51	0.85	1.26	1.45	0.81	0.86	1.23	0.95	1.48
Li	6.98								9.60
Cd	0.29								0.39
$^{87}Sr/^{86}Sr$	0.704027								0.703475
$^{143}Nd/^{144}Nd$	0.512827								0.512944
$^{176}Hf/^{177}Hf$	0.282907								0.283029
$^{208}Pb/^{204}Pb$	39.0912								39.2646
$^{207}Pb/^{204}Pb$	15.6353								15.6162
$^{206}Pb/^{204}Pb$	18.9255								19.9339

	Rosais Volcanic Complex		
Location	Rosais		
Sample	SJ31	SJ99	SJ101
Lithotype	Trachybasalt	Basalt	Basalt
SiO_2	48.94	45.09	45.42
Al_2O_3	16.93	13.67	15.28
$Fe_2O_3^T$	11.41	12.66	11.66
MnO	0.19	0.17	0.17
MgO	3.84	9.89	8.68
CaO	7.6	10.98	10.23
Na_2O	4.29	2.37	2.54
K_2O	1.74	0.89	0.78
TiO_2	2.77	3.11	3.32
P_2O_5	1.01	0.43	0.64
LOI	0.50	0.52	1.12
Total	99.22	99.78	99.83
Mg#	*0.46*	*0.65*	*0.64*
Sc	12.00	31.00	26.87
Be	3.00	2.00	
V	125	292	284
Cr	20.00	370.00	325.21
Co	24.0	48.0	40.3
Ni	20.00	169.00	150.37
Cu	10.00	50.00	30.48
Zn	130.0	100.0	92.8
Ga	26.00	19.00	20.19
Ge	1.4	1.5	
As	26.00	9.00	
Rb	37.0	18.0	7.3
Sr	799	572	630
Y	42.5	27.5	25.8
Zr	418	188	289
Nb	69.4	34.0	51.4
Sn	3.0	2.0	1.9
Sb	0.3	0.2	
Cs	0.600	0.400	0.062
Ba	449	255	334
La	57.70	28.00	34.43
Ce	124.00	63.10	81.91
Pr	14.60	7.28	9.83
Nd	61.00	30.70	41.01
Sm	12.00	6.92	8.31
Eu	4.08	2.41	2.72
Gd	10.10	6.58	7.79
Tb	1.55	1.00	1.05
Dy	8.40	5.49	6.06
Ho	1.50	0.98	1.04
Er	4.10	2.59	2.87
Tm	0.56	0.35	0.40
Yb	3.38	2.11	2.34
Lu	0.47	0.29	0.33
Hf	9.30	5.00	6.96
Ta	5.40	2.83	3.36
W	2.70	2.90	
Tl	0.05	0.05	
Pb	5.00	5.00	1.61
Th	5.08	2.43	3.43
U	1.94	0.88	1.05
Li			5.30
Cd			0.32
$^{87}Sr/^{86}Sr$			0.703509
$^{143}Nd/^{144}Nd$			0.512902
$^{176}Hf/^{177}Hf$			0.282996
$^{208}Pb/^{204}Pb$			39.1998
$^{207}Pb/^{204}Pb$			15.6192
$^{206}Pb/^{204}Pb$			19.5592

	Manadas Volcanic Complex			
Location	Velas			
Sample	SJ20	SJ26	SJ32	SJ33
Lithotype	Basalt	Tefrite	Basalt	Basalt
SiO_2	45.25	44.26	44.99	45.85
Al_2O_3	15.86	16.55	16.69	16.57
$Fe_2O_3^T$	12.97	12.68	13.14	12.7
MnO	0.17	0.16	0.17	0.18
MgO	7.43	7.71	6.46	6.65
CaO	9.82	10.17	9.2	8.9
Na_2O	3.22	2.44	3.07	3.23
K_2O	1.14	0.58	1.23	1.23
TiO_2	3.72	3.70	3.96	3.56
P_2O_5	0.64	0.44	0.67	0.69
LOI	0.22	0.84	0.35	0.30
Total	100.45	99.53	99.93	99.86
Mg#	*0.57*	*0.59*	*0.53*	*0.55*
Sc	23.00	25.00	19.00	18.00
Be	2.00	2.00	2.00	2.00
V	306	290	283	249
Cr	140.00	190.00	50.00	60.00
Co	48.0	48.0	43.0	41.0
Ni	87.00	110.00	56.00	72.00
Cu	30.00	30.00	20.00	20.00
Zn	130.0	100.0	120.0	110.0
Ga	25.00	23.00	24.00	24.00
Ge	1.5	1.3	1.3	1.2
As	41.00	22.00	12.00	12.00
Rb	29.0	8.0	23.0	25.0
Sr	642	634	746	728
Y	32.5	26.6	32.9	32.7
Zr	233	218	264	288
Nb	44.6	38.5	48.1	48.2
Sn	2.0	2.0	2.0	2.0
Sb	0.3	0.2	0.2	0.2
Cs	1.400	0.500	0.600	0.500
Ba	281	267	313	332
La	32.30	27.60	34.00	36.20
Ce	72.80	63.20	77.40	81.10
Pr	9.00	7.72	9.57	9.86
Nd	39.20	33.90	41.40	42.60
Sm	8.31	7.43	8.89	8.89
Eu	2.94	2.70	3.20	3.19
Gd	7.13	6.33	7.56	7.50
Tb	1.12	1.01	1.21	1.19
Dy	6.19	5.64	6.49	6.49
Ho	1.11	1.01	1.16	1.15
Er	2.94	2.53	3.09	3.05
Tm	0.40	0.33	0.42	0.41
Yb	2.32	1.93	2.49	2.44
Lu	0.32	0.26	0.34	0.35
Hf	5.90	5.40	6.40	6.70
Ta	3.37	3.05	3.70	3.67
W	5.60	2.30	1.40	1.70
Tl	0.14	0.05	0.05	0.05
Pb	5.00	5.00	5.00	5.00
Th	2.54	2.45	2.62	2.75
U	0.90	0.82	0.87	0.96
Li				
Cd				
$^{87}Sr/^{86}Sr$				
$^{143}Nd/^{144}Nd$				
$^{176}Hf/^{177}Hf$				
$^{208}Pb/^{204}Pb$				
$^{207}Pb/^{204}Pb$				
$^{206}Pb/^{204}Pb$				

	Manadas Volcanic Complex							
Location	Velas						Fajã das Pontas	Norte Pequeno
Sample	SJ34	SJ35	SJ37	SJ38	SJ39	SJ40	SJ77	SJ78
Lithotype	Basanite	Basalt	Trachybasalt	Basalt	Basalt	mugearito	Basanite	Trachybasalt
SiO_2	44.65	46.35	46.65	46.62	45.86	51.07	43.65	48.54
Al_2O_3	15.77	16.83	16.39	16.73	16.57	16.78	14.62	16.71
$Fe_2O_3^T$	12.82	12.05	13.16	13.3	13.3	11.21	13.99	11.64
MnO	0.16	0.18	0.19	0.18	0.19	0.21	0.17	0.18
MgO	8.22	4.86	5.19	4.86	5.33	3.35	8.75	4.32
CaO	10.46	9.39	8.64	8.26	8.44	6.9	10.67	7.59
Na_2O	2.28	3.24	3.91	3.28	3.45	4.72	2.92	4.36
K_2O	0.85	1.29	1.34	1.28	1.19	1.75	0.99	1.73
TiO_2	3.59	3.32	3.52	3.43	3.53	2.47	3.91	2.96
P_2O_5	0.46	0.68	0.7	0.65	0.68	1.05	0.58	0.84
LOI	0.66	0.41	0.75	0.29	0.84	0.59	0.04	0.02
Total	99.92	98.59	100.43	98.88	99.38	100.09	100.30	98.89
Mg#	*0.60*	*0.49*	*0.50*	*0.46*	*0.48*	*0.44*	*0.59*	*0.48*
Sc	25.00	19.00	18.00	17.00	18.00	10.00	24.14	13.00
Be	2.00	2.00	2.00	2.00	2.00	3.00		3.00
V	299	260	245	230	231	121	352	181
Cr	220.00	70.00	40.00	30.00	40.00	20.00	224.11	20.00
Co	50.0	31.0	36.0	33.0	36.0	18.0	46.6	27.0
Ni	117.00	32.00	23.00	23.00	28.00	6.00	123.80	16.00
Cu	30.00	20.00	20.00	20.00	20.00	10.00	31.77	20.00
Zn	110.0	120.0	130.0	120.0	120.0	140.0	98.3	120.0
Ga	23.00	26.00	26.00	24.00	25.00	27.00	20.94	24.00
Ge	1.4	1.4	1.5	1.4	1.4	1.5		1.2
As	21.00	14.00	29.00	17.00	19.00	12.00		8.00
Rb	19.0	26.0	29.0	26.0	22.0	39.0	19.6	41.0
Sr	649	729	730	714	716	810	656	727
Y	28.9	37.1	39.0	36.1	37.9	50.5	23.7	35.2
Zr	205	335	309	302	311	404	234	406
Nb	38.2	53.8	56.2	51.5	54.5	65.6	41.0	61.7
Sn	2.0	3.0	2.0	3.0	3.0	3.0	1.7	2.0
Sb	0.2	0.3	0.4	0.3	0.3	0.2		0.2
Cs	0.800	0.500	0.600	0.600	0.900	0.700	0.187	0.400
Ba	248	368	347	375	362	493	245	429
La	27.60	41.20	41.00	40.80	41.80	58.20	27.70	50.70
Ce	61.80	90.70	91.30	89.40	92.50	126.00	64.73	114.00
Pr	7.61	11.00	11.10	10.80	11.20	15.00	8.02	13.20
Nd	33.40	47.00	47.60	46.10	47.60	64.70	34.44	54.00
Sm	7.32	9.88	9.98	9.72	10.20	13.40	7.31	10.70
Eu	2.64	3.52	3.49	3.38	3.54	4.48	2.64	3.41
Gd	6.34	8.42	8.38	8.23	8.31	11.30	7.59	9.49
Tb	1.04	1.35	1.35	1.35	1.37	1.83	1.07	1.39
Dy	5.81	7.56	7.61	7.44	7.60	10.10	5.61	6.66
Ho	1.03	1.31	1.34	1.32	1.35	1.78	0.97	1.19
Er	2.69	3.52	3.55	3.51	3.60	4.75	2.47	3.13
Tm	0.37	0.48	0.48	0.48	0.49	0.64	0.31	0.42
Yb	2.17	2.85	2.91	2.80	2.98	3.95	1.98	2.67
Lu	0.29	0.40	0.41	0.39	0.40	0.55	0.28	0.41
Hf	5.30	7.70	7.40	7.10	7.40	9.40	5.55	9.00
Ta	2.87	4.14	4.20	4.00	4.19	4.95	2.71	5.10
W	2.10	1.90	1.50	2.70	3.30	1.50		1.10
Tl	0.05	0.05	0.05	0.05	0.05	0.05		0.05
Pb	5.00	5.00	5.00	5.00	5.00	5.00	1.26	5.00
Th	2.34	3.42	3.45	3.43	3.50	4.96	2.43	4.31
U	0.84	1.17	1.19	1.24	1.26	1.50	0.79	1.62
Li							5.05	
Cd							0.30	
$^{87}Sr/^{86}Sr$							0.703396	
$^{143}Nd/^{144}Nd$							0.512933	
$^{176}Hf/^{177}Hf$							0.282996	
$^{208}Pb/^{204}Pb$							39.2935	
$^{207}Pb/^{204}Pb$							15.6175	
$^{206}Pb/^{204}Pb$							19.8352	

	Manadas Volcanic Complex							
Location	Fajã da Ribª da Areia	Fajã do Ouvidor	Calheta			Airport	Urzelina	Fajã das Almas
Sample	SJ97	SJ98	SJ79	SJ80	SJ110	SJ105	SJ106	SJ107
Lithotype	Trachybasalt	Tefrite	Basalt	Trachybasalt	Trachybasalt	Basalt	Trachybasalt	Trachybasalt
SiO_2	47.08	45.25	46.15	48.72	47.74	45.53	46.15	48.14
Al_2O_3	16.4	16.88	15.15	16.75	16.41	15.75	17.36	17.08
$Fe_2O_3^T$	12.43	12.89	12.26	11.44	12.17	12.43	11.62	11.97
MnO	0.19	0.17	0.18	0.18	0.18	0.16	0.16	0.19
MgO	5.05	5.58	7.61	4.2	5.7	7.71	5.39	4.47
CaO	8.44	8.96	9.38	7.43	8.21	9.63	9.17	7.83
Na_2O	3.76	3.92	3.5	4.42	3.94	3.36	3.88	4.31
K_2O	1.48	1.42	1.32	1.81	1.54	1.29	1.37	1.7
TiO_2	3.43	3.84	3.30	2.89	3.29	3.58	3.43	3.17
P_2O_5	0.88	0.8	0.74	0.85	0.82	0.59	0.76	0.97
LOI	0.25	0.48	0.34	0.48	0.31	0.33	0.53	0.43
Total	99.38	100.19	99.93	99.17	100.31	100.37	99.82	100.25
Mg#	*0.51*	*0.50*	*0.59*	*0.48*	*0.54*	*0.54*	*0.59*	*0.48*
Sc	16.00	19.00	20.00	12.00	17.00	24.56	18.00	13.35
Be	2.00	2.00	2.00	3.00	2.00		2.00	
V	231	291	245	175	217	257	251	200
Cr	50.00	40.00	190.00	20.00	80.00	171.70	50.00	13.41
Co	31.0	32.0	43.0	27.0	33.0	42.5	34.0	26.4
Ni	34.00	30.00	115.00	15.00	61.00	99.25	45.00	15.34
Cu	20.00	20.00	30.00	20.00	40.00	24.14	20.00	11.12
Zn	130.0	110.0	120.0	120.0	110.0	89.4	100.0	109.2
Ga	25.00	23.00	25.00	26.00	24.00	20.19	24.00	22.81
Ge	1.4	1.3	1.3	1.2	1.4		1.3	
As	14.00	6.00	5.00	9.00	59.00		6.00	
Rb	32.0	27.0	32.0	44.0	34.0	25.6	30.0	33.7
Sr	859	799	639	724	681	659	796	797
Y	40.0	33.4	34.0	36.7	36.1	25.3	32.0	27.8
Zr	327	303	311	413	321	277	295	387
Nb	60.5	51.5	50.9	63.4	54.1	47.2	49.2	70.7
Sn	3.0	2.0	2.0	3.0	2.0	1.8	2.0	2.3
Sb	0.3	0.2	0.2	0.2	0.2		0.2	
Cs	0.400	0.400	0.400	0.500	0.800	0.248	0.400	0.314
Ba	434	364	319	441	381	326	341	402
La	49.60	39.60	41.00	53.90	42.30	28.70	38.30	43.62
Ce	109.00	90.70	93.90	120.00	94.80	68.98	87.20	105.46
Pr	12.90	10.50	11.40	14.10	10.80	8.81	10.10	12.58
Nd	53.50	44.10	48.50	58.00	44.90	37.37	43.00	53.70
Sm	10.90	9.10	9.94	11.40	9.22	7.91	8.68	10.51
Eu	3.42	3.31	3.25	3.58	3.30	2.51	3.16	3.34
Gd	8.97	8.24	9.73	10.70	8.93	7.27	8.41	9.26
Tb	1.35	1.26	1.37	1.46	1.28	0.98	1.20	1.24
Dy	7.10	6.79	6.56	6.98	6.89	5.36	6.47	7.18
Ho	1.27	1.21	1.19	1.24	1.22	0.94	1.13	1.17
Er	3.26	3.16	3.12	3.28	3.28	2.60	2.99	3.34
Tm	0.43	0.42	0.41	0.44	0.44	0.38	0.39	0.42
Yb	2.62	2.49	2.56	2.82	2.69	2.15	2.38	2.87
Lu	0.40	0.35	0.39	0.43	0.39	0.29	0.34	0.35
Hf	7.70	6.90	7.50	9.60	7.20	6.91	6.70	8.89
Ta	4.69	4.41	4.18	5.33	4.45	3.38	4.20	4.44
W	2.00	1.90	2.30	1.10	1.30		1.20	
Tl	0.05	0.05	0.05	0.05	0.05		0.05	
Pb	5.00	5.00	5.00	6.00	5.00	1.75	5.00	2.18
Th	4.38	3.46	3.28	4.55	3.88	3.45	3.56	4.39
U	1.59	1.25	1.22	1.67	1.42	1.21	1.28	1.48
Li						4.84		8.12
Cd						0.23		0.39
$^{87}Sr/^{86}Sr$						0.703475		0.703442
$^{143}Nd/^{144}Nd$						0.512936		0.512932
$^{176}Hf/^{177}Hf$						0.282978		0.282999
$^{208}Pb/^{204}Pb$						39.3190		39.3155
$^{207}Pb/^{204}Pb$						15.6250		15.6242
$^{206}Pb/^{204}Pb$						19.7902		19.8539

	Submarine Pillow lavas								
Location									
Sample	**D01-001**	**D01-008**	**D01-011**	**D01-013**	**D01-014**	**D01-017**	**D01-018**	**D01-019**	**D01-020**
Lithotype	Basalt	Basalt	Basalt	Basalt	Basalt	Basalt	Basalt	Basalt	Basalt
SiO_2	46.79	47.25	46.47	46.28	46.05	46.87	47.72	46.72	46.09
Al_2O_3	15.36	15.47	14.77	15.39	15.15	14.81	15.02	14.79	14.93
$Fe_2O_3^T$	12.25	12.37	11.49	12.13	12.13	12.16	12.44	12.16	12.63
MnO	0.16	0.17	0.15	0.16	0.16	0.16	0.16	0.16	0.18
MgO	7.82	7.87	8.33	7.52	7.86	7.94	8.69	8.52	7.56
CaO	9.79	10.34	9.67	9.97	9.25	9.63	9.74	9.48	9.26
Na_2O	3.2	3.16	3.11	3.26	3.06	3.19	3.13	3.15	3.42
K_2O	0.84	0.8	0.71	0.86	0.78	0.82	0.77	0.79	0.9
TiO_2	2.86	2.90	2.78	2.83	2.83	2.85	2.83	2.78	2.94
P_2O_5	0.37	0.39	0.35	0.35	0.36	0.35	0.33	0.32	0.62
LOI	0.04	<0.01	0.41	0.07	0.77	<0.01	0.13	0.52	1.09
Total	99.48	100.72	98.23	98.83	98.40	98.78	100.96	99.39	99.62
Mg#	*0.60*	*0.60*	*0.63*	*0.59*	*0.60*	*0.60*	*0.62*	*0.62*	*0.58*
Sc	23.97	23.00	22.00	21.47	23.00	24.84	24.03	24.84	22.00
Be		2.00	2.00		2.00				2.00
V	252	259	249	237	250	258	228	238	230
Cr	188.31	200.00	300.00	156.73	190.00	215.35	222.81	229.64	290.00
Co	44.7	54.0	63.0	41.6	51.0	44.9	42.6	45.2	53.0
Ni	110.55	106.00	159.00	93.25	110.00	133.52	141.98	146.98	108.00
Cu	29.54	40.00	50.00	27.55	40.00	30.13	29.66	33.18	50.00
Zn	88.5	190.0	190.0	83.6	180.0	89.0	90.1	94.7	230.0
Ga	18.69	25.00	27.00	17.75	25.00	19.10	17.28	18.00	26.00
Ge		1.7	1.7		1.6				1.7
As		5.00	5.00		5.00				5.00
Rb	17.7	19.0	13.0	15.7	18.0	17.4	16.1	17.0	19.0
Sr	564	544	498	540	524	524	500	511	543
Y	25.3	27.9	28.8	23.3	27.1	27.3	25.8	26.4	34.3
Zr	167	190	184	155	185	169	145	154	259
Nb	32.0	32.6	31.7	31.1	32.5	31.5	26.9	29.0	45.3
Sn	1.5	2.0	3.0	1.3	2.0	1.5	1.6	2.2	3.0
Sb		0.2	0.2		0.2				0.2
Cs	0.165	0.300	0.200	0.126	0.300	0.120	0.170	0.186	0.300
Ba	230	237	243	213	223	229	204	209	308
La	22.47	23.20	21.50	20.96	22.30	21.89	20.60	22.04	31.30
Ce	42.83	49.20	45.10	41.09	46.90	42.78	39.49	42.00	66.90
Pr	5.63	5.94	5.56	5.31	5.66	5.57	5.11	5.27	8.30
Nd	24.70	24.70	23.50	23.47	23.80	24.46	22.80	23.45	34.70
Sm	5.92	6.07	5.91	5.63	5.83	6.05	5.64	5.77	8.05
Eu	2.04	2.18	2.17	1.94	2.15	2.19	2.01	2.05	2.91
Gd	6.38	6.19	6.23	5.81	6.12	6.65	6.08	6.05	8.52
Tb	0.89	1.00	1.02	0.83	0.99	0.97	0.93	0.92	1.33
Dy	5.32	5.50	5.57	4.95	5.29	5.53	5.62	5.29	6.79
Ho	0.96	0.97	0.96	0.91	0.94	1.01	0.95	0.97	1.17
Er	2.56	2.64	2.58	2.37	2.59	2.73	2.53	2.48	3.19
Tm	0.33	0.37	0.36	0.31	0.36	0.35	0.34	0.33	0.45
Yb	2.03	2.19	2.20	1.92	2.15	2.22	2.16	2.09	2.64
Lu	0.28	0.31	0.31	0.25	0.30	0.30	0.29	0.30	0.37
Hf	4.27	4.50	4.40	3.97	4.40	4.39	3.85	4.17	5.80
Ta	2.17	2.34	1.82	2.00	1.95	2.06	1.88	1.98	2.59
W		0.50	0.50		0.50				0.50
Tl		0.05	0.06		0.08				0.05
Pb	1.20	5.00	5.00	1.17	5.00	1.28	1.06	1.10	5.00
Th	2.16	2.08	1.92	2.00	2.08	2.13	2.01	2.07	2.74
U	0.74	0.77	0.52	0.68	0.76	0.68	0.66	0.70	1.01
Li	6.59			6.21		6.16	6.97	6.91	
Cd	0.12			0.11		0.11	0.12	0.14	
$^{87}Sr/^{86}Sr$	0.703728			0.703725		0.703724	0.703726	0.703069	
$^{143}Nd/^{144}Nd$	0.512982			0.512975		0.512992	0.512984	0.512988	
$^{176}Hf/^{177}Hf$	0.283102			0.283112		0.283099	0.283104	0.283110	
$^{208}Pb/^{204}Pb$	39.1709			39.1771		39.1002	39.1530	39.1538	
$^{207}Pb/^{204}Pb$	15.6243			15.6234		15.6190	15.6219	15.6216	
$^{206}Pb/^{204}Pb$	20.0476			20.0588		19.9504	20.0261	20.0236	

APPENDIX I.C Geochronological data: $^{40}Ar/^{39}Ar$ ages

Grey, crystalline portions of lava-flow interiors were separated for dating. Samples were crushed, ultrasonicated and sized to 250-425µm. The dense and clean groundmass was concentrated using a magnetic separator and careful handpicking under a binocular microscope. For irradiation, samples were packaged in Cu foil and placed in cylindrical quartz vials, together with fluence monitors of known age and K-glass and fluorite to measure interfering isotopes from K and Ca. The quartz vials were wrapped in 0.5 mm-thick Cd foil to shield samples from thermal neutrons during irradiation. The samples were irradiated for two hours in the central thimble of the U.S. Geological Survey TRIGA reactor in Denver, Colorado (Dalrymple *et al.*, 1981). The reactor vessel was rotated continuously during irradiation to avoid lateral neutron flux gradients. Reactor constants determined for these irradiations were indistinguishable from recent irradiations, and a weighted mean of constants obtained over the past five years yields $^{40}Ar/^{39}Ar_K$ = 0.000±0.004, $^{39}Ar/^{37}Ar_{Ca}$ = 0.000706±0.000051, and $^{36}Ar/^{37}Ar_{Ca}$ = 0.000281±0.000009. TCR-2 sanidine from the Taylor Creek Rhyolite (Duffield and Dalrymple, 1990) was used as a fluence monitor with an age of 27.87 Ma. This monitor is a secondary standard calibrated against the primary intralaboratory standard, SB-3, that has an age of 162.9 ± 0.9 Ma (Lanphere and Dalrymple, 2000). Fluence monitors were analyzed using a continuous laser system and a MAP 216 mass spectrometer described by Dalrymple (1989). Argon was extracted from groundmass separate using a Mo crucible in a custom resistance furnace modified from the design of Staudacher *et al*. (1978) attached to the above mass spectrometer. Heating temperatures were monitored with an optical fiber thermometer and controlled with an Accufiber Model 10 controller. Gas was purified continuously during extraction using two SAES ST-172 getters operated at 0A and 4A.

Mass spectrometer discrimination and system blanks are important factors in the precision and accuracy of $^{40}Ar/^{39}Ar$ age determinations of Pleistocene lavas because of low radiogenic yields. Discrimination is monitored by analyzing splits of atmospheric Ar from a reservoir attached to the extraction line and the MAP 216 mass discrimination is generally very stable. The mass discrimination in this study was determined before each suite of samples and varied from 1.00568±0.00016 to 1.006168±0.00022 per mass unit. Typical system blanks including mass spectrometer backgrounds were $1.5x10^{-18}$ mol of m/z 36, $9x10^{-17}$ mol of m/z 37, $3x10^{-18}$ mol of m/z 39 and $1.5x10^{-16}$ mol of m/z 40, where m/z is mass/charge ratio.

In the incremental-heating experiments, the extraction line was isolated from pumping systems and the sample was heated to a specified temperature for 5-10 minutes, cooled for 3-5 minutes, and transferred to the isolated mass spectrometer. The gas was exposed to getters during the entire extraction. Isotopic ratios were measured and corrected for extraction line and mass spectrometer blanks, mass discrimination and interfering isotopes generated in the reactor. In these experiments we separated and loaded enough material to do 12-18 steps on each unknown in order to carefully characterize the argon release. The incremental heating data and associated 1σ errors are plotted both as age spectrum and isotope correlation (isochron) diagrams. For the age spectra, apparent ages are calculated assuming that non-radiogenic Ar is atmospheric ($^{40}Ar/^{36}Ar$ = 295.5, following mass discrimination correction) in composition and are plotted against the cumulative ^{39}Ar released during the experiment. In cases with several contiguous steps yielding ages within analytical error, we calculate and report plateau ages by weighing individual ages by the inverse of their analytical error. Most groundmass age experiments do not yield identical ages across the entire spectrum due to minor alteration, recoil of ^{39}Ar and ^{37}Ar during irradiation or modest excess ^{40}Ar. Commonly accepted criteria (McDougall and Harrison, 1999) for a meaningful incremental heating age are: (1) well-defined plateau (horizontal age spectrum with no significant slope) for more than 50% of the ^{39}Ar released; (2) well-defined isochron for the plateau gas fractions; (3) concordant plateau and isochron ages; and (4) $^{40}Ar/^{36}Ar$ isochron intercept not significantly different from 295.5.

For isochron plots, data are not corrected using an atmospheric ratio. Reported isochron ages include plateau steps on well-behaved samples or a subset of data that includes the most steps yielding a reasonable goodness of fit. We often exclude the highest and lowest temperature steps because they are most strongly affected by argon recoil. We show normal isochron plots for these low-radiogenic rocks because the data are easier to visualize. Isochron ages with a high probability-of-fit regression (a low mean square of weighted deviates, MSWD ~1; York, 1969) and a $^{40}Ar/^{36}Ar$ intercept not within error of the present-day air ratio are thought to contain non-atmospheric initial argon. For these samples, we interpret the isochron age as most meaningful. Isochron ages with MSWD greater than the critical value defined by Mahon (1996) are reported with errors expanded by the square root of the MSWD (Ludwig, 1999). Full analytical results including age spectra, K/Ca, radiogenic yield, isochron and inverse isochron plots are available as a data appendix.

Supplement Table 2 – $^{40}Ar/^{39}Ar$ ages obtained in the lavas used during the present work

Location	Lava sequence	Aprox. height above sea level (m)	Aprox. distamce to Ponta dos Rosais (Km)	Sample	Lithotype	Age (Ka)
Fajã de São João lava sequence		220	46	SJ8	Tracybasalt	1309.8 ± 3.5
		290	46	SJ12	Basalt	1284.0 ± 4.8
Topo Volcanic Complex	Fajã da Caldeira do Santo Cristo	10	36.5	SJ49	Basalt	756.8 ± 5.0
	Road between Fajã da Caldeira and Fajã dos Cubres	60	34	SJ52	Basalt	743.3 ± 4.0
	Fajã dos Cubres	36	33	SJ59	Basalt	730.2 ± 4.6
	Fajã dos Cubres	410	33	SJ76	Basalt	543.3 ± 4.3
Rosais Volcanic Complex	Flow between Velas and Rosais	158	10	SJ29	Basalt	116.6 ± 2.0
	Fajã do João Dias	186	8.5	SJ87	Trachybasalt	270.1 ± 2.5
	Fajã do João Dias	200	8.5	SJ89	Basalt	215.0 ± 2.5
	Fajã do João Dias	225	8.5	SJ91	Trachybasalt	218.8 ± 3.3
Manadas Volcanic Complex	Fajã das Pontas	0	30	SJ77	Basanite	2.9 ± 10.3
	Fajã das Almas	0	25	SJ107	Trachybasalt	0.5 ± 6.9

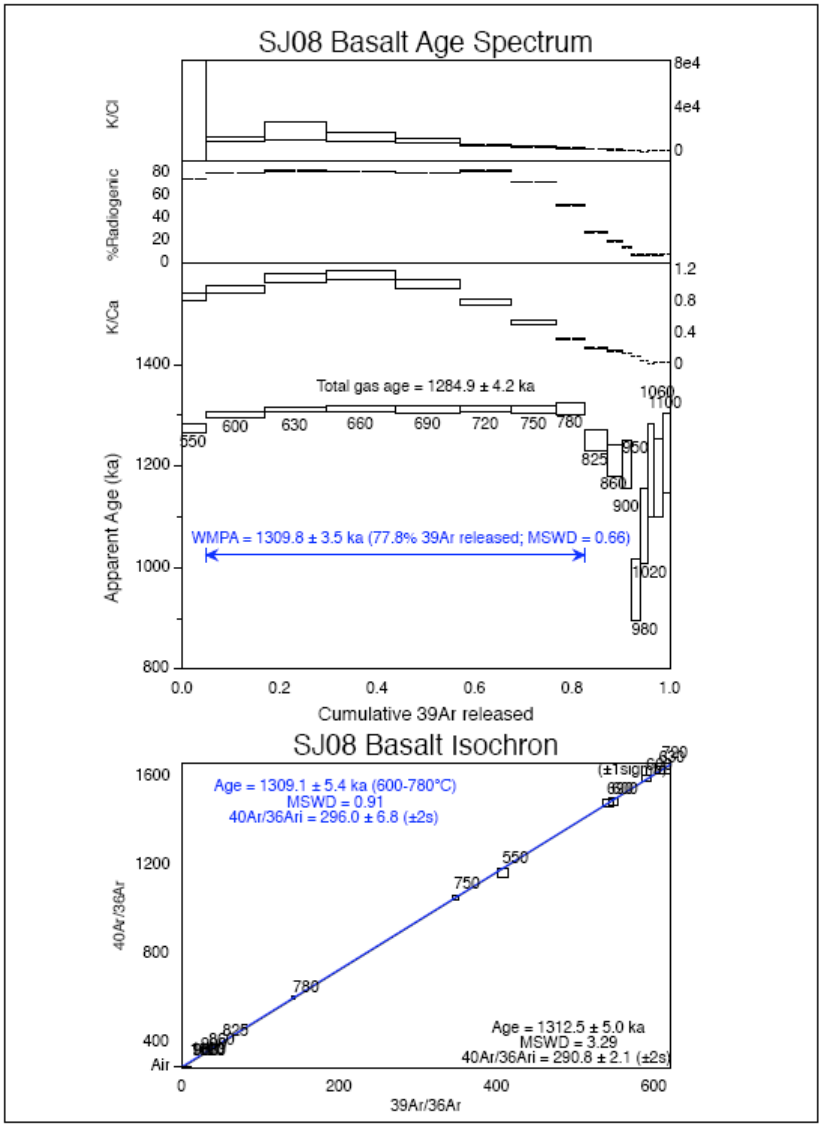
SJ08 Basalt Age Spectrum
K/Cl
%Radiogenic
K/Ca
Apparent Age (ka)
Total gas age = 1284.9 ± 4.2 ka
WMPA = 1309.8 ± 3.5 ka (77.8% 39Ar released; MSWD = 0.66)
Cumulative 39Ar released
SJ08 Basalt Isochron
Age = 1309.1 ± 5.4 ka (600-780°C)
MSWD = 0.91
40Ar/36Ari = 296.0 ± 6.8 (±2s)
Age = 1312.5 ± 5.0 ka
MSWD = 3.29
40Ar/36Ari = 290.8 ± 2.1 (±2s)
40Ar/36Ar
39Ar/36Ar

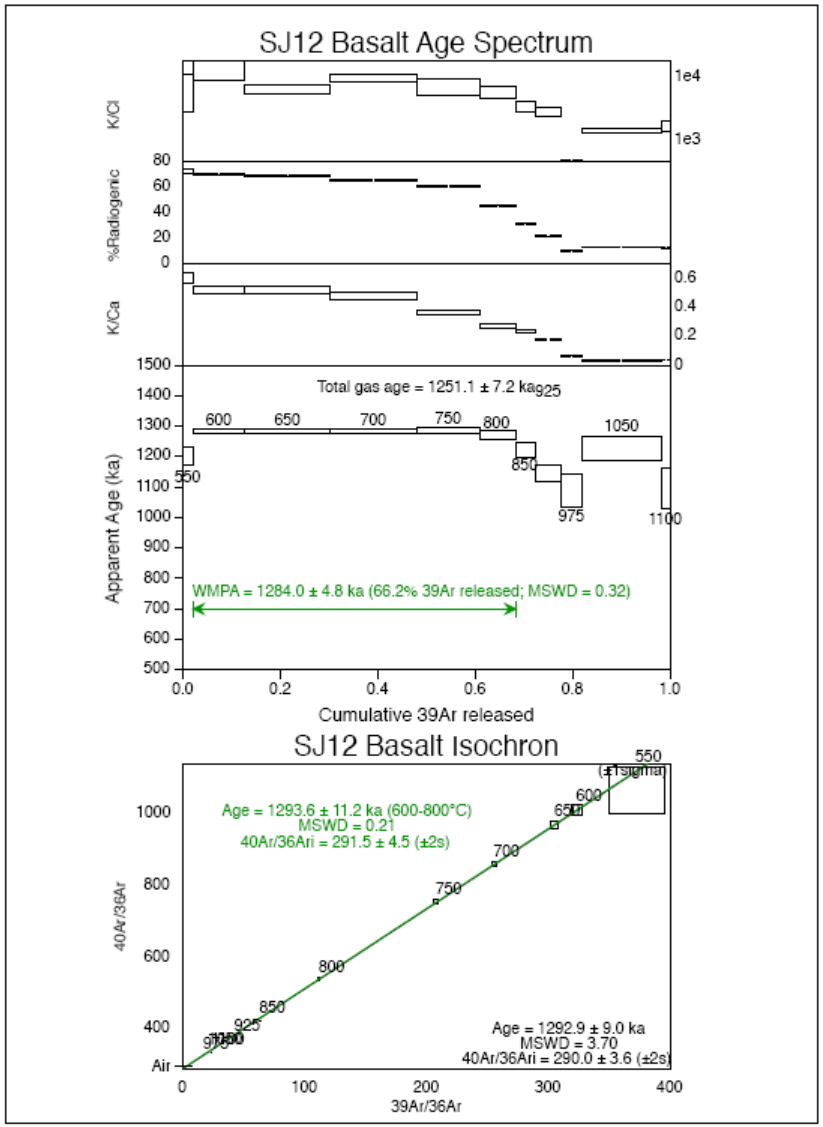
SJ12 Basalt Age Spectrum
K/Cl
%Radiogenic
K/Ca
Apparent Age (ka)
Total gas age = 1251.1 ± 7.2 ka
WMPA = 1284.0 ± 4.8 ka (66.2% 39Ar released; MSWD = 0.32)
Cumulative 39Ar released
SJ12 Basalt Isochron
Age = 1293.6 ± 11.2 ka (600-800°C)
MSWD = 0.21
40Ar/36Ari = 291.5 ± 4.5 (±2s)
Age = 1292.9 ± 9.0 ka
MSWD = 3.70
40Ar/36Ari = 290.0 ± 3.6 (±2s)
40Ar/36Ar
39Ar/36Ar

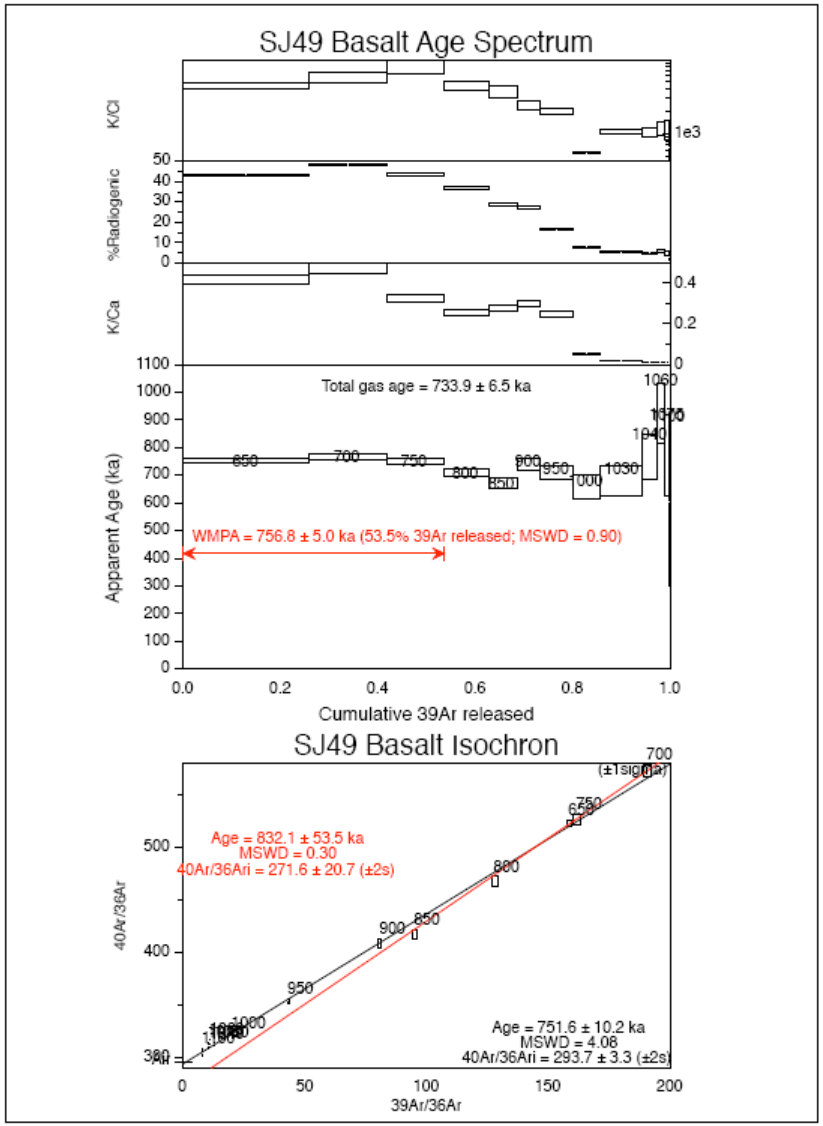
SJ49 Basalt Age Spectrum
K/Cl
%Radiogenic
K/Ca
Total gas age = 733.9 ± 6.5 ka
Apparent Age (ka)
WMPA = 756.8 ± 5.0 ka (53.5% 39Ar released; MSWD = 0.90)
Cumulative 39Ar released
SJ49 Basalt Isochron
Age = 832.1 ± 53.5 ka
MSWD = 0.30
40Ar/36Ari = 271.6 ± 20.7 (±2s)
Age = 751.6 ± 10.2 ka
MSWD = 4.08
40Ar/36Ari = 293.7 ± 3.3 (±2s)
40Ar/36Ar
39Ar/36Ar

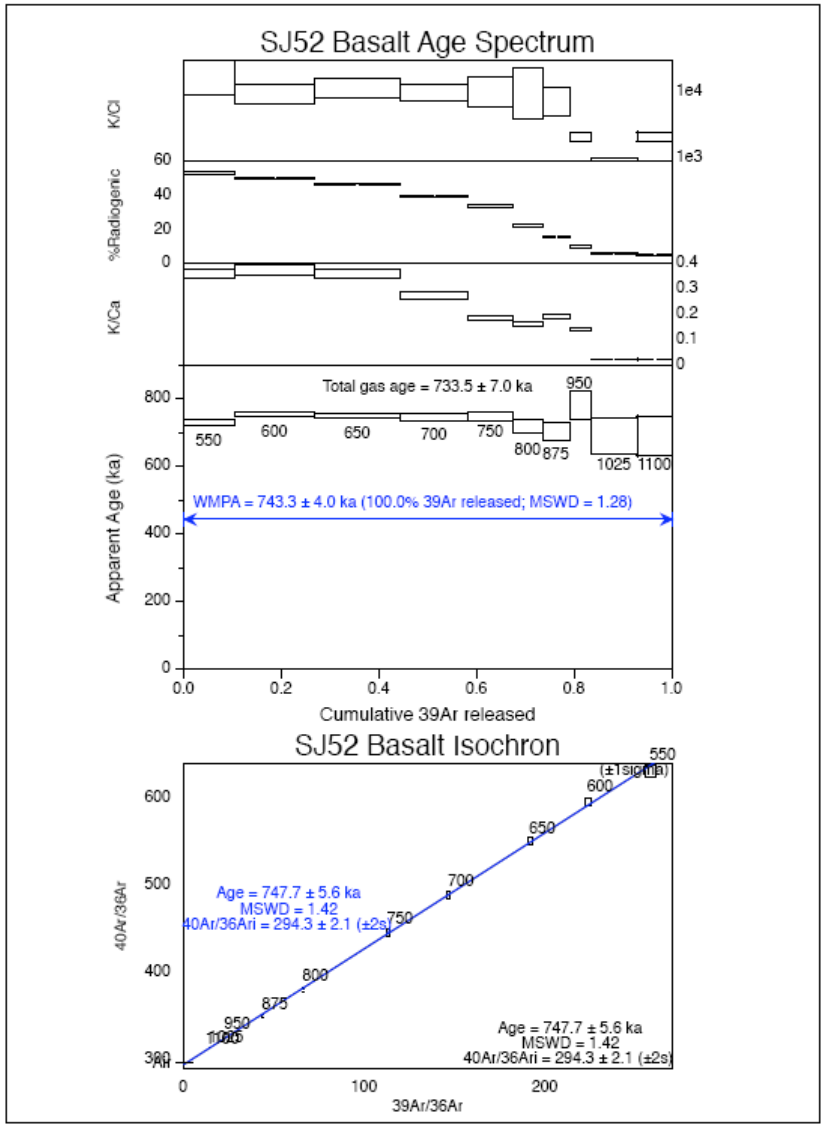
SJ52 Basalt Age Spectrum
K/Cl
%Radiogenic
K/Ca
Total gas age = 733.5 ± 7.0 ka
Apparent Age (ka)
WMPA = 743.3 ± 4.0 ka (100.0% 39Ar released; MSWD = 1.28)
Cumulative 39Ar released
SJ52 Basalt Isochron
Age = 747.7 ± 5.6 ka
MSWD = 1.42
40Ar/36Ari = 294.3 ± 2.1 (±2s)
Age = 747.7 ± 5.6 ka
MSWD = 1.42
40Ar/36Ari = 294.3 ± 2.1 (±2s)
40Ar/36Ar
39Ar/36Ar

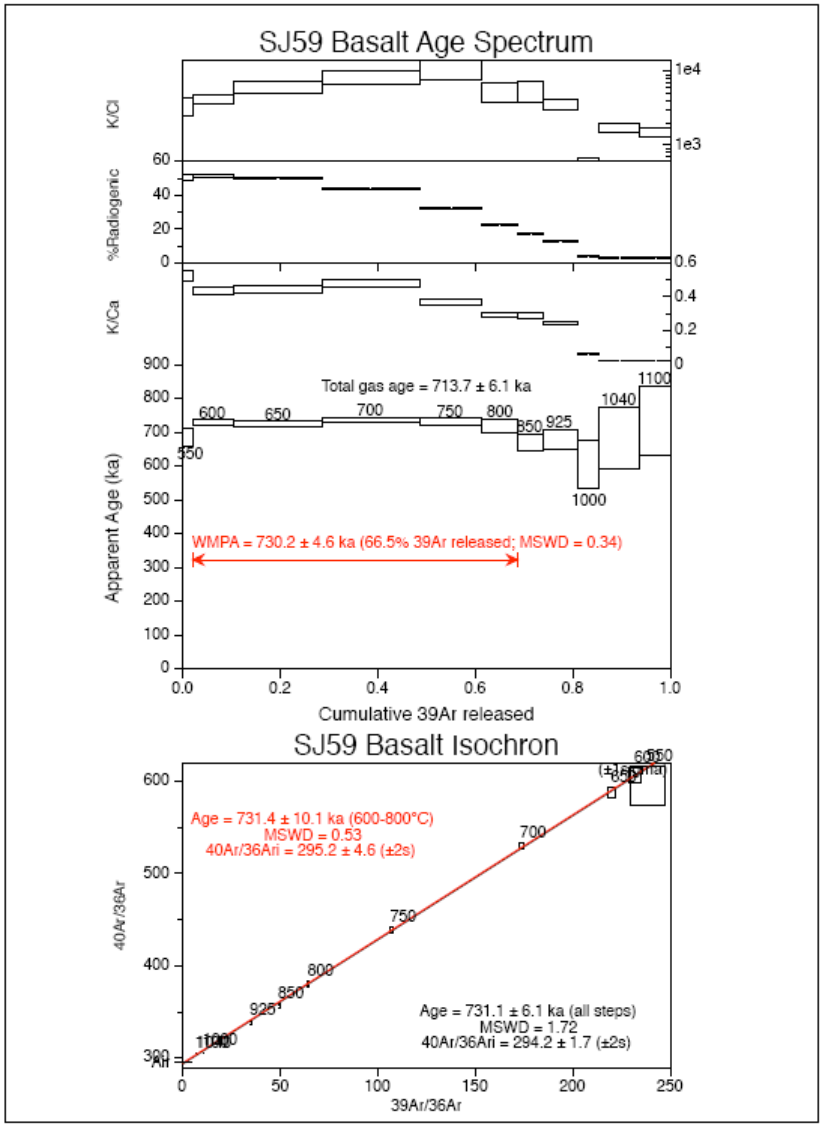
SJ59 Basalt Age Spectrum
K/Cl
%Radiogenic
K/Ca
Apparent Age (ka)
Total gas age = 713.7 ± 6.1 ka
WMPA = 730.2 ± 4.6 ka (66.5% 39Ar released; MSWD = 0.34)
Cumulative 39Ar released
SJ59 Basalt Isochron
Age = 731.4 ± 10.1 ka (600-800°C)
MSWD = 0.53
40Ar/36Ari = 295.2 ± 4.6 (±2s)
Age = 731.1 ± 6.1 ka (all steps)
MSWD = 1.72
40Ar/36Ari = 294.2 ± 1.7 (±2s)
40Ar/36Ar
39Ar/36Ar

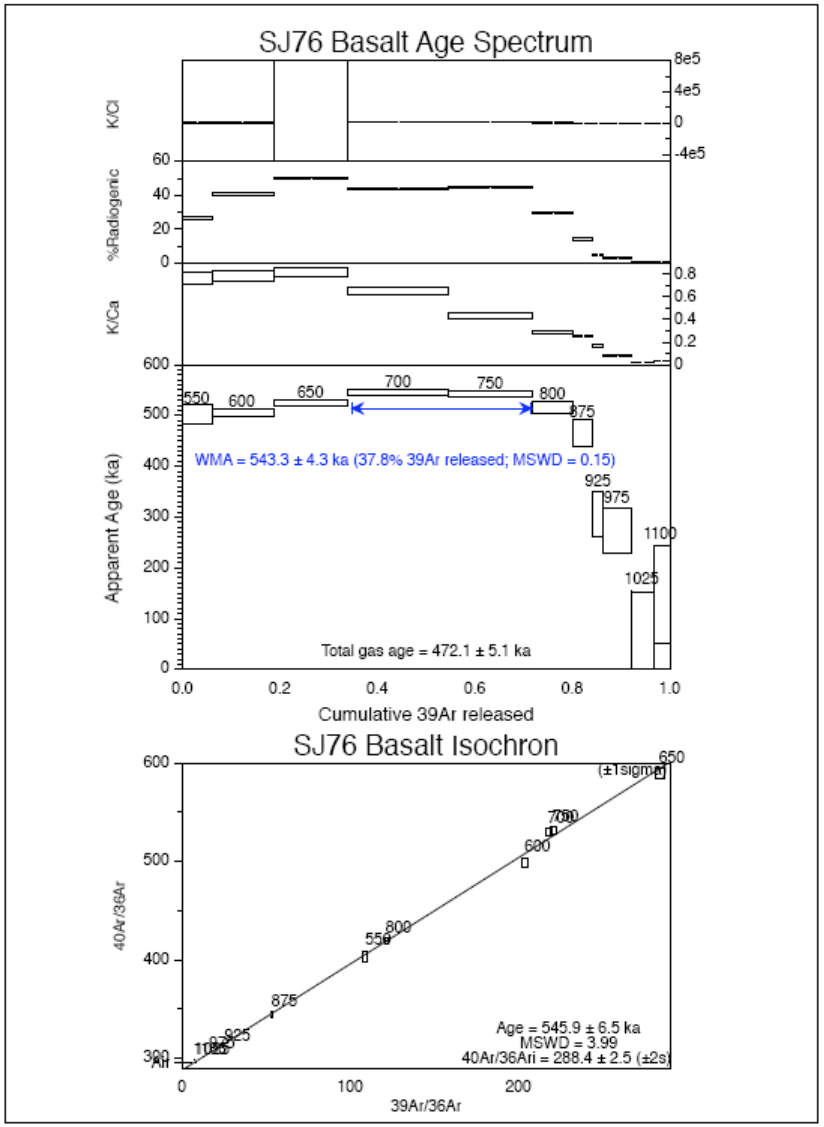
SJ76 Basalt Age Spectrum
K/Cl
%Radiogenic
K/Ca
Apparent Age (ka)
WMA = 543.3 ± 4.3 ka (37.8% 39Ar released; MSWD = 0.15)
Total gas age = 472.1 ± 5.1 ka
Cumulative 39Ar released
SJ76 Basalt Isochron
(±1sigma)
Age = 545.9 ± 6.5 ka
MSWD = 3.99
40Ar/36Ari = 288.4 ± 2.5 (±2s)
40Ar/36Ar
39Ar/36Ar

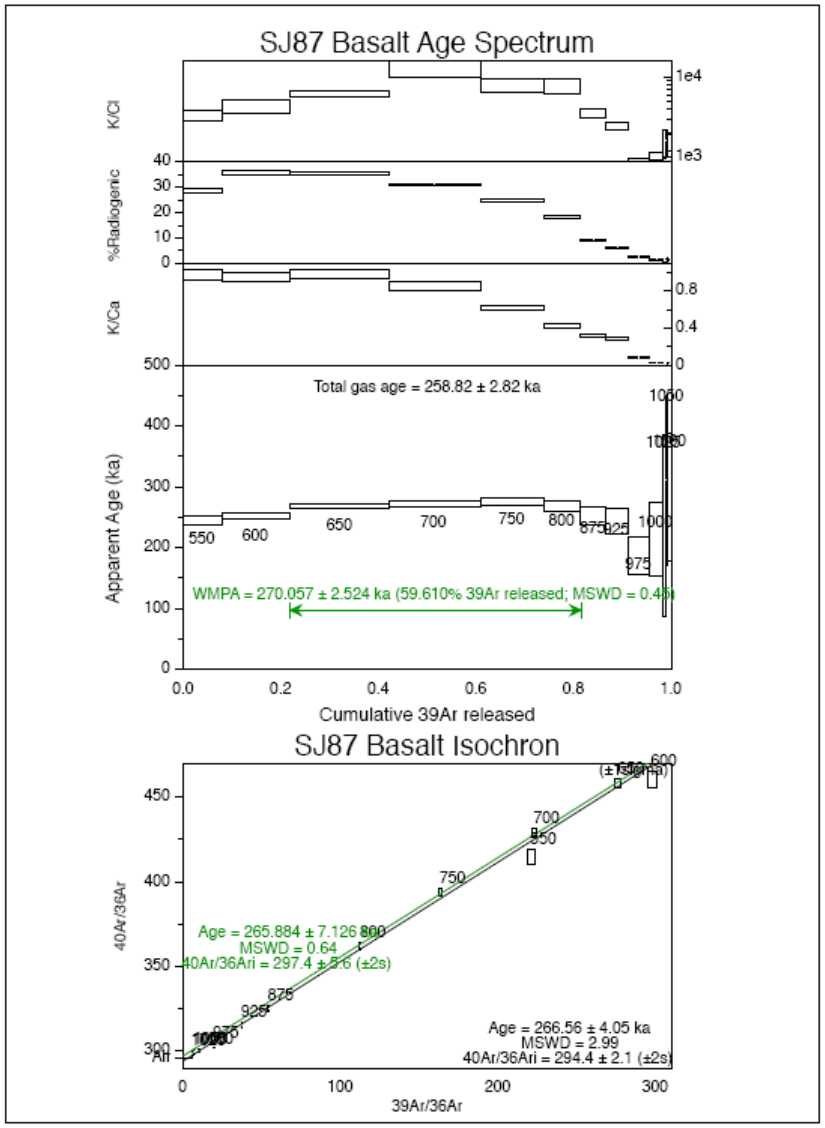
SJ87 Basalt Age Spectrum
K/Cl
%Radiogenic
K/Ca
Apparent Age (ka)
Total gas age = 258.82 ± 2.82 ka
WMPA = 270.057 ± 2.524 ka (59.610% 39Ar released; MSWD = 0.43)
Cumulative 39Ar released
SJ87 Basalt Isochron
Age = 265.884 ± 7.126
MSWD = 0.64
40Ar/36Ari = 297.4 ± 5.6 (±2s)
Age = 266.56 ± 4.05 ka
MSWD = 2.99
40Ar/36Ari = 294.4 ± 2.1 (±2s)
40Ar/36Ar
39Ar/36Ar

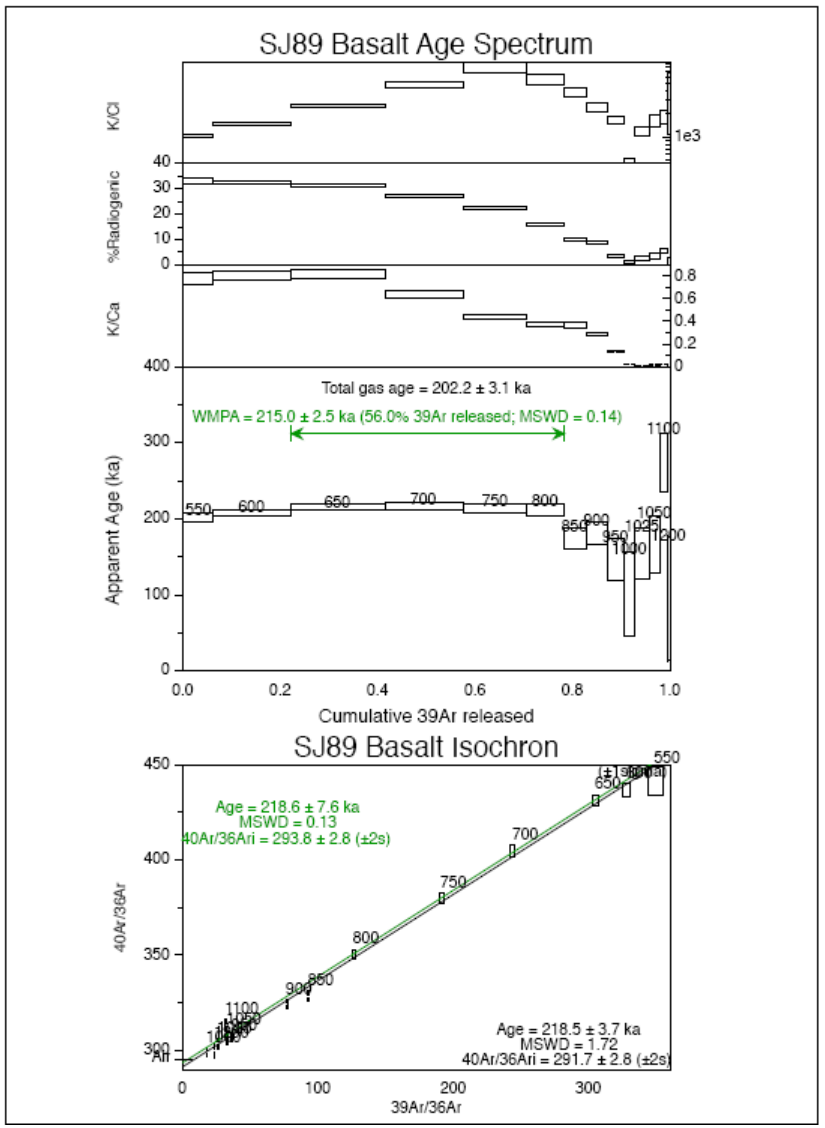
SJ89 Basalt Age Spectrum
K/Cl
%Radiogenic
K/Ca
Apparent Age (ka)
Total gas age = 202.2 ± 3.1 ka
WMPA = 215.0 ± 2.5 ka (56.0% 39Ar released; MSWD = 0.14)
Cumulative 39Ar released
SJ89 Basalt Isochron
Age = 218.6 ± 7.6 ka
MSWD = 0.13
40Ar/36Ari = 293.8 ± 2.8 (±2s)
Age = 218.5 ± 3.7 ka
MSWD = 1.72
40Ar/36Ari = 291.7 ± 2.8 (±2s)
40Ar/36Ar
39Ar/36Ar

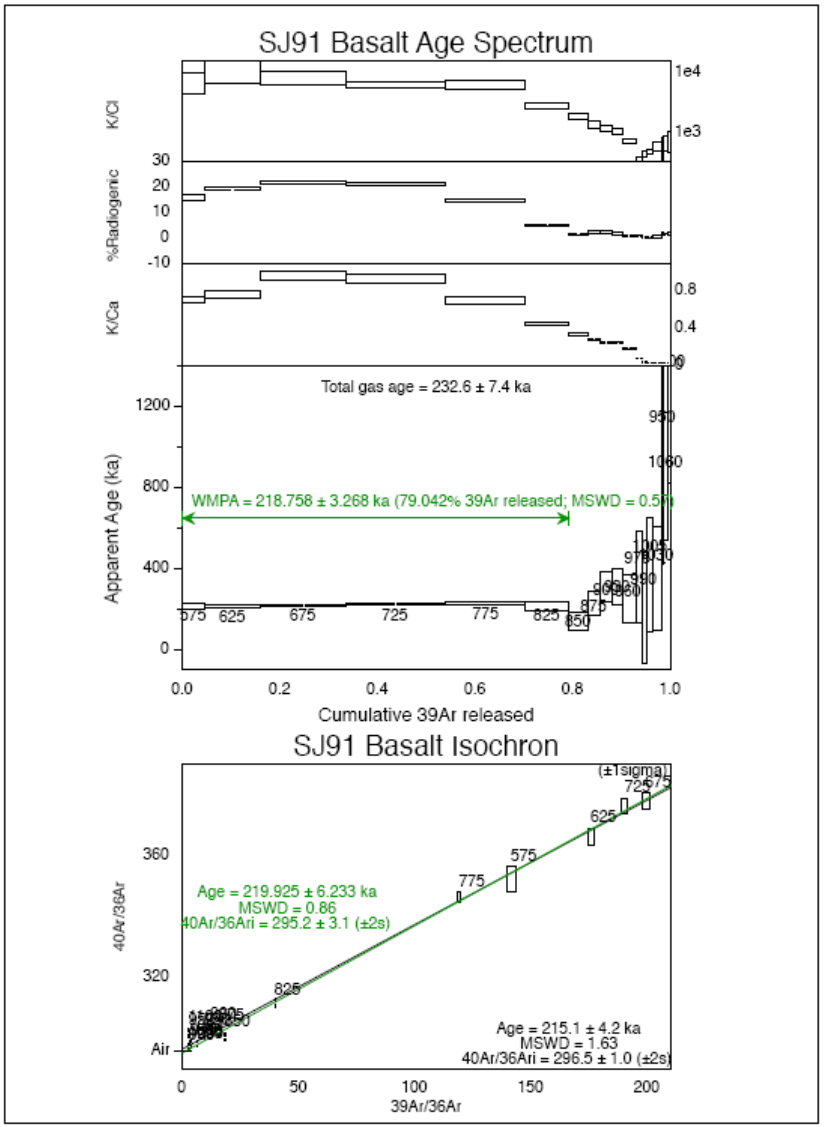
SJ91 Basalt Age Spectrum
K/Cl
%Radiogenic
K/Ca
Total gas age = 232.6 ± 7.4 ka
Apparent Age (ka)
WMPA = 218.758 ± 3.268 ka (79.042% 39Ar released; MSWD = 0.5
Cumulative 39Ar released
SJ91 Basalt Isochron
(±1sigma)
Age = 219.925 ± 6.233 ka
MSWD = 0.86
40Ar/36Ari = 295.2 ± 3.1 (±2s)
Age = 215.1 ± 4.2 ka
MSWD = 1.63
40Ar/36Ari = 296.5 ± 1.0 (±2s)
40Ar/36Ar
39Ar/36Ar

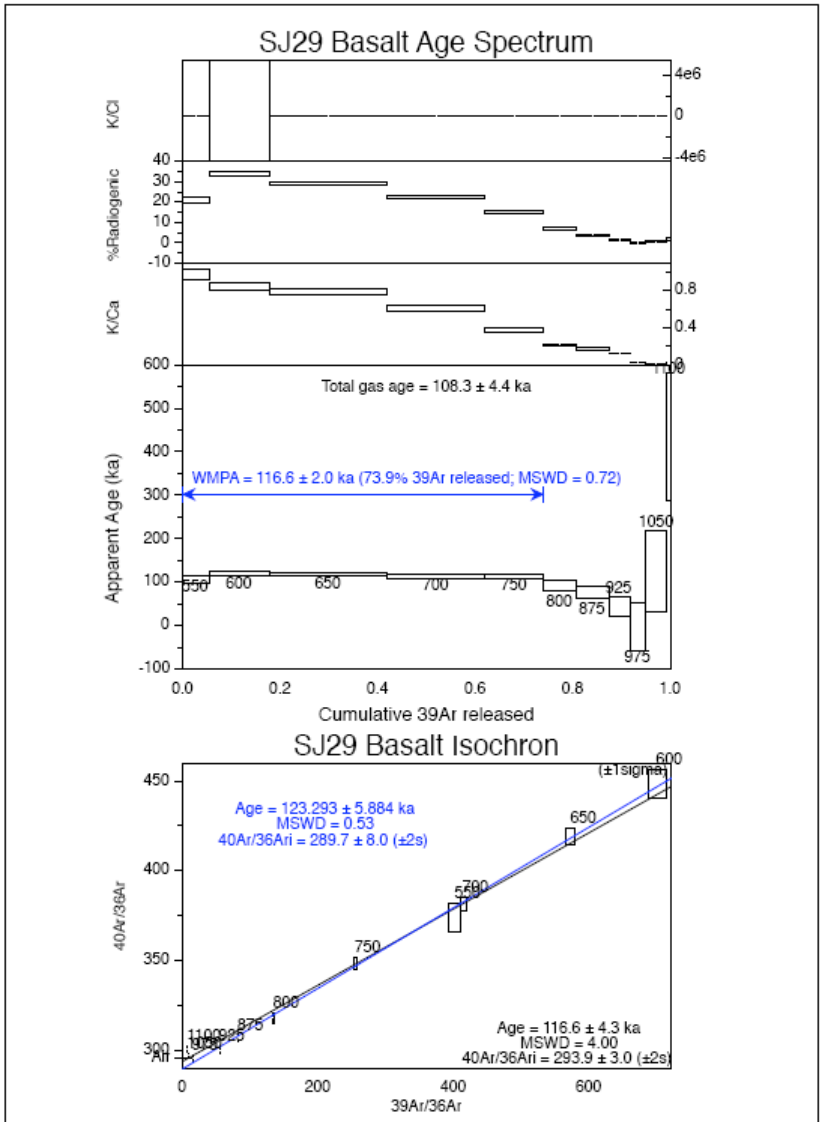
SJ29 Basalt Age Spectrum
K/Cl
%Radiogenic
K/Ca
Total gas age = 108.3 ± 4.4 ka
Apparent Age (ka)
WMPA = 116.6 ± 2.0 ka (73.9% 39Ar released; MSWD = 0.72)
Cumulative 39Ar released
SJ29 Basalt Isochron
(±1sigma)
Age = 123.293 ± 5.884 ka
MSWD = 0.53
40Ar/36Ari = 289.7 ± 8.0 (±2s)
Age = 116.6 ± 4.3 ka
MSWD = 4.00
40Ar/36Ari = 293.9 ± 3.0 (±2s)
40Ar/36Ar
39Ar/36Ar

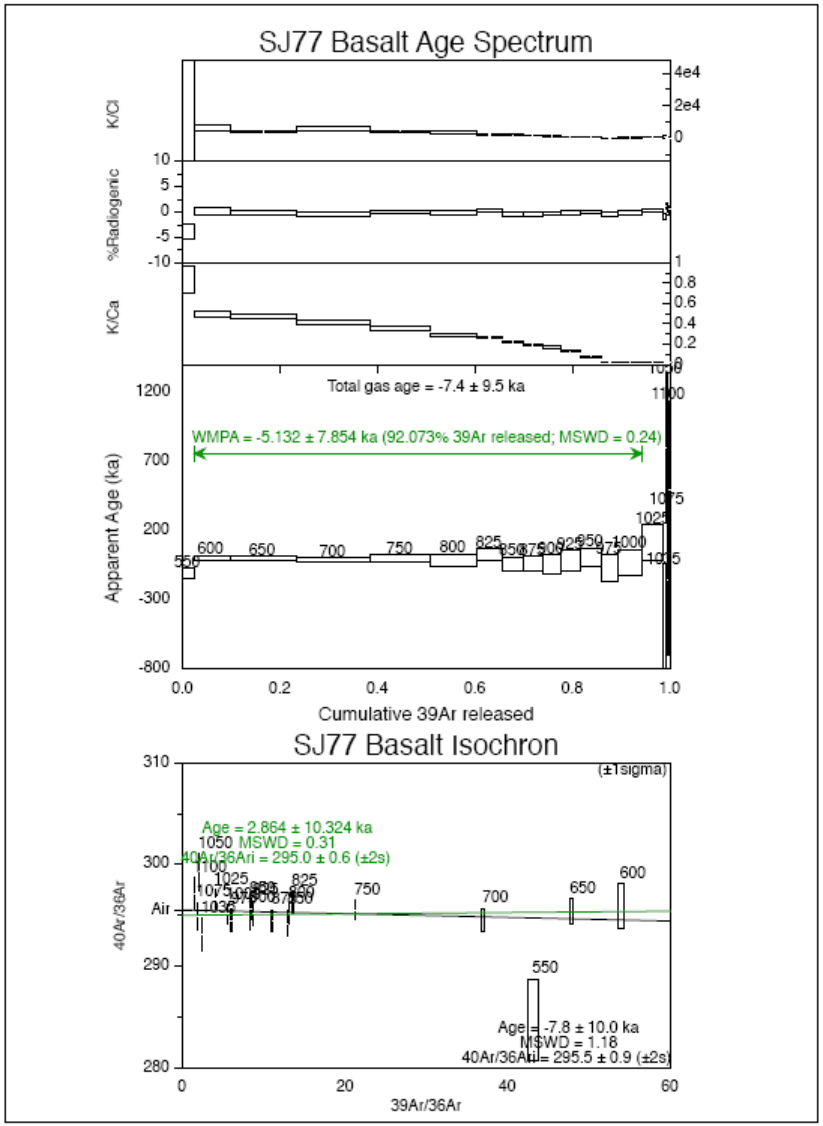
SJ77 Basalt Age Spectrum
K/Cl
%Radiogenic
K/Ca
Apparent Age (ka)
Total gas age = -7.4 ± 9.5 ka
WMPA = -5.132 ± 7.854 ka (92.073% 39Ar released; MSWD = 0.24)
Cumulative 39Ar released
SJ77 Basalt Isochron
(±1sigma)
Age = 2.864 ± 10.324 ka
1050 MSWD = 0.31
40Ar/36Ari = 295.0 ± 0.6 (±2s)
Air
Age = -7.8 ± 10.0 ka
MSWD = 1.18
40Ar/36Ari = 295.5 ± 0.9 (±2s)
40Ar/36Ar
39Ar/36Ar

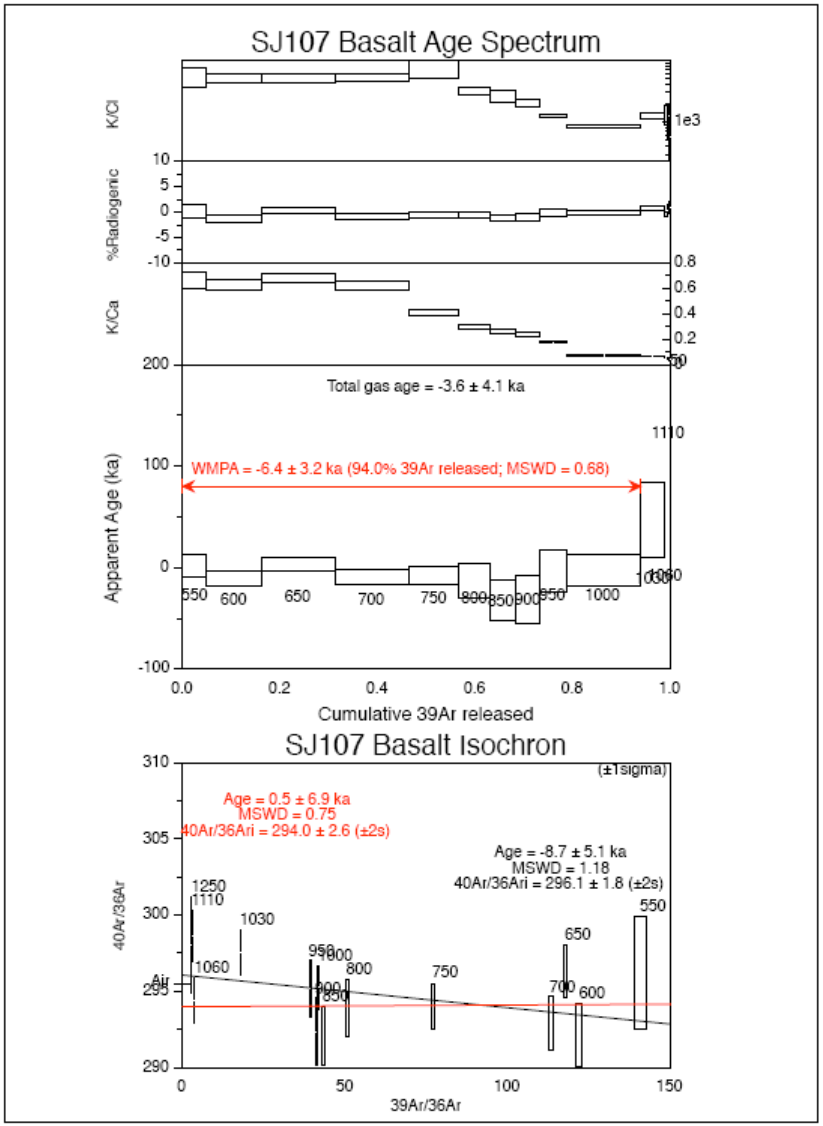
SJ107 Basalt Age Spectrum
K/Cl
%Radiogenic
K/Ca
Apparent Age (ka)
Total gas age = -3.6 ± 4.1 ka
WMPA = -6.4 ± 3.2 ka (94.0% 39Ar released; MSWD = 0.68)
Cumulative 39Ar released
SJ107 Basalt Isochron
(±1sigma)
Age = 0.5 ± 6.9 ka
MSWD = 0.75
40Ar/36Ari = 294.0 ± 2.6 (±2s)
Age = -8.7 ± 5.1 ka
MSWD = 1.18
40Ar/36Ari = 296.1 ± 1.8 (±2s)
Air
40Ar/36Ar
39Ar/36Ar

APPENDIX I.D Sample location

Sample name	Latitude	Longitude	Location	Volcanic Phase
SJ1	38.54747	-27.85607	Fajã de São João sequence	First Volcanic Phase
SJ2	38.54734	-27.85589	Fajã de São João sequence	
SJ3	38.54785	-27.85549	Fajã de São João sequence	
SJ4	38.54771	-27.85549	Fajã de São João sequence	
SJ5	38.55032	-27.85924	Fajã de São João sequence	
SJ6	38.55044	-27.85927	Fajã de São João sequence	
SJ7	38.55039	-27.85909	Fajã de São João sequence	
SJ8	38.55049	-27.85945	Fajã de São João sequence	
SJ9	38.55088	-27.85989	Fajã de São João sequence	
SJ10	38.55096	-27.86001	Fajã de São João sequence	
SJ11	38.55066	-27.85787	Fajã de São João sequence	
SJ12	38.55058	-27.85766	Fajã de São João sequence	
SJ13	38.55005	-27.85623	Fajã de São João sequence	
SJ14	38.54959	-27.85509	Fajã de São João sequence	
SJ15	38.54951	-27.85488	Fajã de São João sequence	
SJ16	38.54952	-27.85466	Fajã de São João sequence	
SJ17	38.54728	-27.85111	Fajã de São João sequence	
SJ18	38.54776	-27.84940	Fajã de São João sequence	
SJ19	38.54836	-27.84884	Fajã de São João sequence	
SJ41	38.54642	-27.85565	Fajã de São João sequence	
SJ43	38.54377	-27.85119	Fajã de São João sequence	
SJ44	38.54382	-27.85101	Fajã de São João sequence	
SJ45	38.61332	-27.92129	Ribeira east of Fajã da Caldeira	Second Volcanic Phase - Topo Volcanic Complex
SJ46	38.61353	-27.92129	Ribeira east of Fajã da Caldeira	
SJ47	38.61366	-27.92115	Ribeira east of Fajã da Caldeira	
SJ48	38.61721	-27.92118	Fajã da Caldeira sequence	
SJ49	38.62582	-27.93404	Fajã da Caldeira sequence	
SJ50	38.62588	-27.93382	Fajã da Caldeira sequence	
SJ51	38.62841	-27.94109	Fajã do Belo	
SJ52	38.63538	-27.95755	Road Fajã Caldeira-Fajã Cubres	
SJ53	38.63538	-27.95739	Road Fajã Caldeira-Fajã Cubres	
SJ54	38.63547	-27.95743	Road Fajã Caldeira-Fajã Cubres	
SJ55	38.63537	-27.95725	Road Fajã Caldeira-Fajã Cubres	
SJ56	38.63526	-27.95742	Road Fajã Caldeira-Fajã Cubres	
SJ57	38.63554	-27.95835	Road Fajã Caldeira-Fajã Cubres	
SJ58	38.63582	-27.95879	Road Fajã Caldeira-Fajã Cubres	
SJ59	38.63857	-27.96803	Fajã dos Cubres sequence	
SJ60	38.63859	-27.96824	Fajã dos Cubres sequence	
SJ61	38.63979	-27.97095	Fajã dos Cubres sequence	
SJ62	38.63974	-27.97081	Fajã dos Cubres sequence	
SJ63	38.64017	-27.97208	Fajã dos Cubres sequence	
SJ64	38.64022	-27.97248	Fajã dos Cubres sequence	
SJ65	38.64173	-27.97585	Fajã dos Cubres sequence	
SJ66	38.64269	-27.97827	Fajã dos Cubres sequence	
SJ67	38.64439	-27.98168	Fajã dos Cubres sequence	
SJ67	38.64434	-27.98192	Fajã dos Cubres sequence	
SJ68	38.64428	-27.98160	Fajã dos Cubres sequence	
SJ69	38.64440	-27.98187	Fajã dos Cubres sequence	
SJ70	38.64429	-27.98181	Fajã dos Cubres sequence	
SJ71	38.64425	-27.98228	Fajã dos Cubres sequence	
SJ72	38.64398	-27.98276	Fajã dos Cubres sequence	
SJ73	38.64390	-27.98262	Fajã dos Cubres sequence	
SJ74	38.64385	-27.98270	Fajã dos Cubres sequence	
SJ75	38.64709	-27.98780	Fajã dos Cubres sequence	
SJ76	38.64723	-27.98966	Fajã dos Cubres sequence	
SJ95	38.59357	-27.94044	Ribeira Seca dos Vimes	
SJ96	38.59814	-27.96023	Ribeira Seca dos Vimes	
SJ102	38.55065	-27.75835	Topo Village	
SJ103	38.55761	-27.78575	Topo Village	
SJ108	38.60326	-27.97603	Ribeira da Rib. Seca	
SJ109	38.54673	-27.81778	Road to Topo Village	

Sample name	Latitude	Longitude	Location	Volcanic Phase
SJ28	38.69015	-28.21850	Cliff on the football field	Second Volcanic Phase - Rosais Volcanic Complex
SJ29	38.70185	-28.22466	Road between Velas and Rosais	
SJ30	38.70413	-28.22684	Road between Velas and Rosais	
SJ31	38.70652	-28.23221	Road between Velas and Rosais	
SJ33	38.69407	-28.20233	North of Velas	
SJ34	38.69826	-28.20070	North of Velas	
SJ35	38.69409	-28.19590	North of Velas	
SJ81	38.73127	-28.23352	Fajã do João Dias sequence	
SJ82	38.73056	-28.23204	Fajã do João Dias sequence	
SJ83	38.73017	-28.23050	Fajã do João Dias sequence	
SJ84	38.73016	-28.22955	Fajã do João Dias sequence	
SJ85	38.73037	-28.22910	Fajã do João Dias sequence	
SJ86	38.72773	-28.22697	Fajã do João Dias sequence	
SJ87	38.72780	-28.22759	Fajã do João Dias sequence	
SJ88	38.72778	-28.22775	Fajã do João Dias sequence	
SJ89	38.72774	-28.22786	Fajã do João Dias sequence	
SJ90	38.72768	-28.22816	Fajã do João Dias sequence	
SJ91	38.72753	-28.22797	Fajã do João Dias sequence	
SJ92	38.72751	-28.22784	Fajã do João Dias sequence	
SJ93	38.72751	-28.22767	Fajã do João Dias sequence	
SJ94	38.72701	-28.22666	Fajã do João Dias sequence	
SJ99	38.72070	-28.23779	Pico dos Matinhos	
SJ100	38.74094	-28.28097	Road to Rosais lighthouse	
SJ101	38.74537	-28.28743	Road to Rosais lighthouse	
SJ20	38.68279	-28.21122	Flow in Velas Village	Second Volcanic Phase - Manadas Volcanic Complex
SJ26	38.68947	-28.21371	Ribeira das Velas	
SJ27	38.68940	-28.21413	Ribeira das Velas	
SJ32	38.69150	-28.21025	Ribeira near Velas	
SJ36	38.69165	-28.21007	Ribeira das Velas	
SJ37	38.69036	-28.21080	Ribeira das Velas	
SJ38	38.69062	-28.21104	Ribeira das Velas	
SJ39	38.69058	-28.21080	Ribeira das Velas	
SJ40	38.69037	-28.21107	Ribeira das Velas	
SJ77	38.65497	-27.99608	Fajã das Pontas	
SJ78	38.64964	-28.00476	Norte Pequeno	
SJ79	38.61979	-27.99753	Road Norte Pequeno-Calheta	
SJ80	38.61565	-28.00259	Road Norte Pequeno-Calheta	
SJ97	38.66666	-28.02456	Fajã da Ribeira da Areia	
SJ98	38.67885	-28.05152	Fajã do Ouvidor	
SJ104	38.67257	-28.19386	Fajã da Queimada	
SJ105	38.66473	-28.16877	Flow in the airport	
SJ106	38.64439	-28.11047	Historic eruption 1808	
SJ107	38.62937	-28.08223	Fajã das Almas	
SJ110	38.61003	-27.99883	Calheta	

APPENDIX II: Mineral Chemistry

The microprobe analyses, which results are presented in the following tables, were performed in a JEOL equipment (JXA – 8500F) that belongs to the Laboratório Nacional de Energia e Geologia located in S. Mamede de Infesta. This equipment has five wavelength dispersive spectrometers (WDS) and an energy dispersive X-ray microanalysis (EDS).

The silicate minerals analyses were obtained using a current of 10nA at accelerating potentials of 15kV. The count rates for each element were approximately of 20s and the diameter of the beam was 1μm.

The patterns used were: Fluorite (F Kα); Vanadinite (Cl Kα); Albite (Na Kα); Orthoclase (Al Kα, Si Kα, K Kα); Apatite (P Kα, Ca Kα); MgO (Mg Kα); Barite (Ba Kα); $MnTiO_3$ (Mn Kα, Ti Kα); Cr_2O_3 (Cr Kα); Fe_2O_3 (Fe Kα); Esfalerite (Zn Kα, S Kα); Volastonite (Ca Kα, Si Kα); ZrO_2 (Zr Lα); Ni (Kα).

In the flowchart is explained the meaning of the reference given to each microprobe analysis.

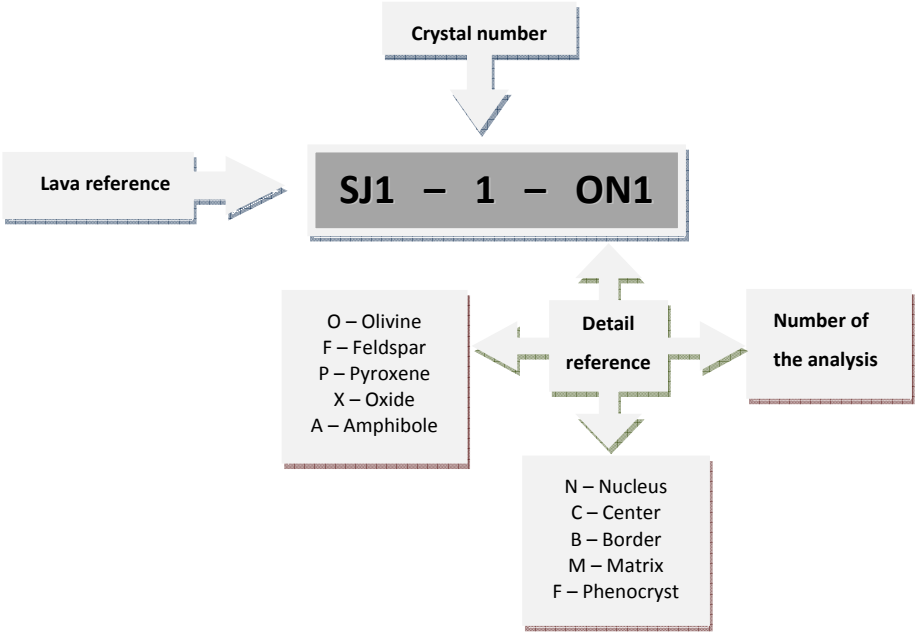

APPENDIX II.A: OLIVINE

Sample	SJ7					SJ8				SJ9		SJ18		
Lithotype	Plagioclase-bearing basalt					Trachybasalt				Basalt		Basalt Trachyandesite		
Ref.	SJ7-2-ON7	SJ7-2-OB9	SJ7-2-ON10	SJ7-5-ON-14	SJ7-5-OB-15	SJ8-3-OB8	SJ8-3-ON9	SJ8-4-OC10	SJ8-4-OB11	SJ9-2-ON7	SJ9-2-OB8	SJ18-2-ON5	SJ18-2-OB8	SJ18-2-OC9
SiO_2 (%)	38.00	38.33	38.38	39.04	38.82	38.89	39.62	38.96	38.30	38.86	38.03	32.90	33.49	33.04
TiO_2	0.019	0.005	0.000	0.112	0.046	0.020	0.018	0.055	0.066	0.049	0.070	0.177	0.091	0.130
Al_2O_3	0.017	0.011	0.053	0.042	0.004	0.082	0.037	0.027	0.081	0.022	0.050	0.066	0.152	0.180
NiO	0.000	0.021	0.000	0.051	0.037	0.099	0.074	0.114	0.049	0.054	0.089	0.000	0.024	0.000
FeO	24.23	23.88	24.28	22.95	23.35	22.32	17.89	16.31	20.92	17.22	20.88	50.97	51.63	50.72
MnO	0.336	0.345	0.318	0.291	0.247	0.381	0.178	0.321	0.301	0.142	0.417	1.760	1.550	1.540
MgO	38.03	38.03	38.13	39.23	39.18	39.17	43.68	43.63	40.49	44.65	40.61	13.09	12.18	13.06
CaO	0.193	0.201	0.236	0.175	0.173	0.189	0.221	0.175	0.258	0.212	0.261	0.440	0.347	0.366
Cr_2O_3	0.000	0.000	0.000	0.000	0.000	0.000	0.000	0.000	0.000	0.000	0.000	0.000	0.000	0.000
ZnO	0.000	0.000	0.000	0.000	0.000	0.000	0.000	0.000	0.000	0.000	0.000	0.000	0.000	0.000
V_2O_3	0.000	0.000	0.000	0.000	0.000	0.000	0.000	0.000	0.000	0.000	0.000	0.000	0.000	0.000
Total	100.8	100.8	101.4	101.9	101.9	101.1	101.7	99.6	100.5	101.2	100.4	99.4	99.5	99.0
Number of ions on the basis of 4 O														
Si	0.990	0.996	0.993	0.998	0.995	1.000	0.991	0.991	0.987	0.976	0.982	1.010	1.027	1.015
Al^{IV}	0.001	0.000	0.002	0.001	0.000	0.000	0.001	0.001	0.002	0.001	0.002	0.000	0.000	0.000
Al^{VI}	0.000	0.000	0.000	0.000	0.000	0.002	0.000	0.000	0.000	0.000	0.000	0.002	0.005	0.007
Ti	0.000	0.000	0.000	0.002	0.001	0.000	0.000	0.001	0.001	0.001	0.001	0.004	0.002	0.003
Ni	0.000	0.000	0.000	0.001	0.001	0.002	0.001	0.002	0.001	0.001	0.002	0.000	0.001	0.000
Fe^{2+}	0.528	0.519	0.526	0.491	0.500	0.480	0.374	0.347	0.451	0.362	0.451	1.309	1.324	1.303
Mn	0.007	0.008	0.007	0.006	0.005	0.008	0.004	0.007	0.007	0.003	0.009	0.046	0.040	0.040
Mg	1.477	1.474	1.472	1.495	1.497	1.501	1.630	1.654	1.555	1.673	1.563	0.599	0.557	0.598
Ca	0.005	0.006	0.007	0.005	0.005	0.005	0.006	0.005	0.007	0.006	0.007	0.014	0.011	0.012
Fo%	73.7	74.0	73.7	75.3	74.9	75.8	81.3	82.7	77.5	82.2	77.6	31.4	29.6	31.5

APPENDIX II.A: OLIVINE

Sample	SJ20 - Basalt								SJ29			SJ32 - Basalt
Lithotype	Lava	Lava	Lava	Nodule	Nodule	Nodule	Nodule	Nodule	Basalt			Lava
Ref.	SJ21B-3-ON1	SJ21B-3-OC2	SJ21B-4-OC3	SJ20A-2-OB3	SJ20A-2-OC4	SJ20A-5-ON13	SJ20A-5-OB15	SJ20A-2-ON16	SJ29-4-OB15	SJ29-4-ON17	SJ29-OM18	SJ32-2-ON1
SiO_2 (%)	37.48	36.39	38.43	38.95	38.22	37.58	38.15	38.30	38.27	40.16	37.46	37.98
TiO_2	0.078	0.278	0.042	0.068	0.099	0.048	0.048	0.058	0.033	0.017	0.055	0.034
Al_2O_3	0.076	2.580	0.030	0.044	0.059	0.015	0.034	0.049	0.000	0.061	0.078	0.051
NiO	0.083	0.097	0.176	0.049	0.000	0.058	0.000	0.044	0.039	0.053	0.000	0.000
FeO	19.58	18.44	18.01	19.14	20.77	21.92	20.16	20.62	23.35	15.31	32.52	25.81
MnO	0.201	0.297	0.236	0.417	0.328	0.218	0.462	0.340	0.348	0.063	0.891	0.529
MgO	43.29	41.51	43.19	42.62	41.29	40.54	41.52	40.89	38.03	44.76	29.60	36.23
CaO	0.137	0.250	0.177	0.225	0.164	0.162	0.193	0.184	0.237	0.182	0.376	0.165
Cr_2O_3	0.000	0.000	0.000	0.000	0.000	0.000	0.000	0.000	0.000	0.000	0.000	0.068
ZnO	0.000	0.000	0.000	0.000	0.000	0.000	0.000	0.000	0.000	0.000	0.000	0.080
V_2O_3	0.000	0.000	0.000	0.000	0.000	0.000	0.000	0.000	0.000	0.000	0.000	0.000
Total	100.9	99.8	100.3	101.5	100.9	100.5	100.6	100.5	100.3	100.6	101.0	100.9
Number of ions on the basis of 4 O												
Si	0.958	0.935	0.979	0.984	0.979	0.973	0.979	0.985	0.998	1.002	1.015	0.997
Al^{IV}	0.002	0.065	0.001	0.001	0.002	0.000	0.001	0.001	0.000	0.000	0.000	0.002
Al^{VI}	0.000	0.013	0.000	0.000	0.000	0.000	0.000	0.000	0.000	0.002	0.002	0.000
Ti	0.001	0.005	0.001	0.001	0.002	0.001	0.001	0.001	0.001	0.000	0.001	0.001
Ni	0.002	0.002	0.004	0.001	0.000	0.001	0.000	0.001	0.001	0.001	0.000	0.000
Fe^{2+}	0.418	0.396	0.384	0.405	0.445	0.475	0.433	0.444	0.509	0.320	0.737	0.567
Mn	0.004	0.006	0.005	0.009	0.007	0.005	0.010	0.007	0.008	0.001	0.020	0.012
Mg	1.650	1.590	1.641	1.606	1.578	1.566	1.589	1.568	1.479	1.666	1.196	1.419
Ca	0.004	0.007	0.005	0.006	0.004	0.004	0.005	0.005	0.007	0.005	0.011	0.005
Fo%	79.8	80.1	81.0	79.9	78.0	76.7	78.6	78.0	74.4	83.9	61.9	71.5

APPENDIX II.A: OLIVINE

Sample	SJ32 - Basalt						SJ49				SJ52	
Lithotype	Lava	Lava	Nodule	Nodule	Nodule	Nodule	Basalt				Basalt	
Ref.	SJ32-2-ON2	SJ32-5-ON8	SJ32A-4-ON10	SJ32A-4a-ON11	SJ32AOM12	SJ32A-5-ON13	SJ49-1-ON5	SJ49-1-OB6	SJ49-3-ON7	SJ49-3-OB8	SJ52-2-ON5	SJ52-5-ON6
SiO_2 (%)	37.85	37.98	39.42	39.10	39.43	39.27	39.68	38.61	39.93	38.37	39.64	39.13
TiO_2	0.007	0.091	0.038	0.032	0.067	0.067	0.022	0.052	0.032	0.099	0.056	0.070
Al_2O_3	0.074	0.063	0.057	0.086	0.017	0.036	0.054	0.035	0.049	0.000	0.062	0.016
NiO	0.049	0.000	0.075	0.070	0.080	0.075	0.100	0.035	0.145	0.104	0.139	0.010
FeO	25.3	24.94	19.61	19.6	17.73	19.97	18.07	23.42	14.57	24.33	17.67	20.72
MnO	0.485	0.600	0.320	0.169	0.286	0.231	0.223	0.363	0.260	0.460	0.196	0.320
MgO	36.06	36.51	41.35	41.25	42.48	40.64	42.59	37.14	44.23	36.39	42.42	40.33
CaO	0.142	0.171	0.164	0.166	0.189	0.193	0.172	0.250	0.239	0.357	0.160	0.173
Cr_2O_3	0.000	0.034	0.035	0.000	0.082	0.000	0.000	0.000	0.047	0.000	0.070	0.000
ZnO	0.120	0.016	0.000	0.000	0.000	0.000	0.000	0.000	0.065	0.000	0.057	0.177
V_2O_3	0.000	0.000	0.000	0.007	0.000	0.000	0.000	0.000	0.000	0.000	0.000	0.000
Total	100.1	100.4	101.1	100.5	100.4	100.5	100.9	99.9	99.6	100.1	100.5	100.9
Number of ions on the basis of 4 O												
Si	1.000	0.998	1.001	0.998	1.000	1.004	1.001	1.010	1.006	1.007	1.004	1.001
Al^{IV}	0.000	0.002	0.000	0.002	0.000	0.000	0.000	0.000	0.000	0.000	0.000	0.000
Al^{VI}	0.002	0.000	0.002	0.001	0.001	0.001	0.002	0.001	0.001	0.000	0.002	0.000
Ti	0.000	0.002	0.001	0.001	0.001	0.001	0.000	0.001	0.001	0.002	0.001	0.001
Ni	0.001	0.000	0.002	0.001	0.002	0.002	0.002	0.001	0.003	0.002	0.003	0.000
Fe^{2+}	0.559	0.548	0.416	0.418	0.376	0.427	0.381	0.512	0.307	0.534	0.374	0.443
Mn	0.011	0.013	0.007	0.004	0.006	0.005	0.005	0.008	0.006	0.010	0.004	0.007
Mg	1.421	1.431	1.565	1.570	1.607	1.549	1.602	1.448	1.662	1.425	1.602	1.539
Ca	0.004	0.005	0.004	0.005	0.005	0.005	0.005	0.007	0.006	0.010	0.004	0.005
Fo%	71.8	72.3	79.0	79.0	81.0	78.4	80.8	73.9	84.4	72.7	81.1	77.6

APPENDIX II.A: OLIVINE

Sample	SJ52						SJ55					SJ70
Lithotype	Basalt						Tefrite					Basalt
Ref.	SJ52-5-OB7	SJ52-6-ON8	SJ52-6-OB9	SJ52-3-ON10	SJ52-3-OB11	SJ52-4-ON13	SJ55-3-ON6	SJ55-3-OC7	SJ55-3-OB8	SJ55-OM9	SJ55-OM10	SJ70-1-ON5
SiO_2 (%)	37.62	39.39	38.34	38.80	37.54	39.46	38.67	39.00	36.75	34.20	38.82	39.44
TiO_2	0.059	0.014	0.084	0.035	0.075	0.017	0.060	0.025	0.107	0.169	0.082	0.045
Al_2O_3	0.052	0.066	0.058	0.040	0.040	0.004	0.067	0.080	0.031	0.086	0.016	0.000
NiO	0.084	0.139	0.069	0.050	0.035	0.159	0.232	0.200	0.000	0.000	0.000	0.135
FeO	28.72	20.43	25.02	20.77	28.97	17.98	22.52	19.97	34.89	42.82	23.09	19.5
MnO	0.465	0.231	0.406	0.328	0.562	0.302	0.407	0.310	0.564	0.994	0.380	0.290
MgO	33.56	40.74	36.68	40.40	33.89	42.27	38.73	41.64	28.09	22.46	38.70	39.37
CaO	0.249	0.158	0.217	0.169	0.241	0.173	0.140	0.232	0.355	0.472	0.223	0.129
Cr_2O_3	0.112	0.000	0.000	0.058	0.000	0.012	0.000	0.000	0.000	0.000	0.000	0.000
ZnO	0.024	0.000	0.000	0.040	0.000	0.153	0.000	0.000	0.000	0.000	0.000	0.000
V_2O_3	0.000	0.011	0.000	0.014	0.000	0.029	0.000	0.000	0.000	0.000	0.000	0.000
Total	100.9	101.2	100.9	100.7	101.4	100.6	100.8	101.5	100.8	101.2	101.3	98.9
Number of ions on the basis of 4 O												
Si	1.002	1.002	1.001	0.996	0.996	1.002	0.999	0.990	1.009	0.981	0.999	1.021
Al^{IV}	0.000	0.000	0.000	0.001	0.001	0.000	0.001	0.002	0.000	0.003	0.000	0.000
Al^{VI}	0.002	0.002	0.002	0.000	0.000	0.000	0.001	0.000	0.001	0.000	0.000	0.000
Ti	0.001	0.000	0.002	0.001	0.002	0.000	0.001	0.000	0.002	0.004	0.002	0.001
Ni	0.002	0.003	0.001	0.001	0.001	0.003	0.005	0.004	0.000	0.000	0.000	0.003
Fe^{2+}	0.640	0.435	0.546	0.446	0.643	0.382	0.487	0.424	0.801	1.027	0.497	0.422
Mn	0.010	0.005	0.009	0.007	0.013	0.007	0.009	0.007	0.013	0.024	0.008	0.006
Mg	1.333	1.545	1.428	1.546	1.341	1.600	1.492	1.575	1.150	0.961	1.486	1.520
Ca	0.007	0.004	0.006	0.005	0.007	0.005	0.004	0.006	0.010	0.015	0.006	0.004
Fo%	67.6	78.0	72.3	77.6	67.6	80.7	75.4	78.8	58.9	48.3	74.9	78.3

APPENDIX II.A: OLIVINE

Sample	SJ70							SJ77					
Lithotype	Basalt							Basanite					
Ref.	SJ70-1-OC6	SJ70-1-OB7	SJ70-OM9	SJ70-2-ON18	SJ70-2-OB19	SJ70-2A-ON20	SJ70-2A-OB21	SJ77-6-ON1	SJ77-5-ON6	SJ77-5-OB7	SJ77-OM8	SJ77-4-ON9	SJ77-4-OB11
SiO_2 (%)	40.21	39.06	40.45	38.49	40.67	40.61	39.12	40.46	40.13	37.94	37.59	40.38	38.80
TiO_2	0.043	0.071	0.063	0.012	0.026	0.054	0.052	0.003	0.030	0.083	0.150	0.009	0.079
Al_2O_3	0.067	0.080	0.076	0.025	0.072	0.002	0.058	0.030	0.091	0.000	0.129	0.034	0.108
NiO	0.271	0.122	0.149	0.197	0.211	0.212	0.205	0.137	0.155	0.000	0.038	0.272	0.224
FeO	13.49	23.45	14.54	20.43	12.26	13.23	20.85	14.39	18.44	27.59	30	14.48	23.1
MnO	0.213	0.318	0.213	0.262	0.291	0.132	0.298	0.000	0.221	0.489	0.634	0.223	0.342
MgO	46.47	36.06	45.47	39.18	46.36	46.54	40.27	45.43	41.88	35.04	31.66	45.76	38.51
CaO	0.288	0.426	0.282	0.155	0.309	0.316	0.352	0.240	0.176	0.271	0.353	0.224	0.232
Cr_2O_3	0.000	0.000	0.000	0.000	0.000	0.000	0.000	0.000	0.000	0.000	0.000	0.000	0.000
ZnO	0.000	0.000	0.000	0.000	0.000	0.000	0.000	0.000	0.000	0.000	0.000	0.000	0.000
V_2O_3	0.000	0.000	0.000	0.000	0.000	0.000	0.000	0.000	0.000	0.000	0.000	0.000	0.000
Total	101.1	99.6	101.2	98.8	100.2	101.1	101.2	100.7	101.1	101.4	100.6	101.4	101.4
Number of ions on the basis of 4 O													
Si	0.994	1.024	1.001	1.006	1.006	1.000	0.999	1.004	1.011	0.998	1.010	0.998	0.999
Al^{IV}	0.002	0.000	0.000	0.000	0.000	0.000	0.001	0.000	0.000	0.000	0.000	0.001	0.001
Al^{VI}	0.000	0.002	0.002	0.001	0.002	0.000	0.000	0.001	0.003	0.000	0.004	0.000	0.002
Ti	0.001	0.001	0.001	0.000	0.000	0.001	0.001	0.000	0.001	0.002	0.003	0.000	0.002
Ni	0.005	0.003	0.003	0.004	0.004	0.004	0.004	0.003	0.003	0.000	0.001	0.005	0.005
Fe^{2+}	0.279	0.514	0.301	0.446	0.254	0.273	0.445	0.299	0.388	0.607	0.674	0.299	0.497
Mn	0.004	0.007	0.004	0.006	0.006	0.003	0.006	0.000	0.005	0.011	0.014	0.005	0.007
Mg	1.712	1.410	1.677	1.526	1.711	1.709	1.533	1.682	1.573	1.375	1.268	1.687	1.478
Ca	0.008	0.012	0.007	0.004	0.008	0.008	0.010	0.006	0.005	0.008	0.010	0.006	0.006
Fo%	86.0	73.3	84.8	77.4	87.1	86.2	77.5	84.9	80.2	69.4	65.3	84.9	74.8

APPENDIX II.A: OLIVINE

Sample	SJ83						SJ91					
Lithotype							Trachybasalt					
Ref.	SJ83-3-ON1	SJ83-3-OB2	SJ83-3-OC3	SJ83-4-ON4	SJ83-1-ON11	SJ83-OM17	SJ91-4-OC1	SJ91-4-OB2	SJ91-4-OB3	SJ91-3-OC12	SJ91-3-OB13	SJ91-OM14
SiO_2 (%)	39.44	39.53	39.83	39.63	38.48	39.22	40.03	37.62	38.59	39.26	37.53	36.95
TiO_2	0.022	0.036	0.035	0.000	0.121	0.070	0.075	0.066	0.059	0.034	0.151	0.116
Al_2O_3	0.009	0.025	0.007	0.078	0.048	0.011	0.063	0.022	0.036	0.060	0.030	0.077
NiO	0.094	0.069	0.094	0.000	0.069	0.000	0.104	0.026	0.064	0.175	0.000	0.038
FeO	17.1	18.73	17.24	18.67	20.15	19.52	19.43	28.59	26.92	22.38	31.72	34.96
MnO	0.098	0.151	0.249	0.240	0.355	0.418	0.231	0.418	0.263	0.301	0.457	0.594
MgO	43.22	42.27	43.12	41.71	41.16	41.52	39.10	31.69	33.69	37.38	29.05	27.28
CaO	0.194	0.207	0.181	0.134	0.231	0.186	0.177	0.231	0.182	0.116	0.249	0.259
Cr_2O_3	0.000	0.000	0.058	0.035	0.023	0.000	0.000	0.000	0.000	0.000	0.000	0.000
ZnO	0.000	0.024	0.056	0.000	0.121	0.032	0.000	0.000	0.000	0.000	0.000	0.000
V_2O_3	0.000	0.000	0.010	0.000	0.004	0.000	0.000	0.000	0.000	0.000	0.000	0.000
Total	100.2	101.0	100.9	100.5	100.8	101.0	99.2	98.7	99.8	99.7	99.2	100.3
Number of ions on the basis of 4 O												
Si	0.998	0.999	1.003	1.006	0.986	0.997	1.031	1.023	1.025	1.022	1.029	1.020
Al^{IV}	0.000	0.001	0.000	0.000	0.001	0.000	0.000	0.000	0.000	0.000	0.000	0.000
Al^{VI}	0.000	0.000	0.000	0.002	0.000	0.000	0.002	0.001	0.001	0.002	0.001	0.002
Ti	0.000	0.001	0.001	0.000	0.002	0.001	0.001	0.001	0.001	0.001	0.003	0.002
Ni	0.002	0.001	0.002	0.000	0.001	0.000	0.002	0.001	0.001	0.004	0.000	0.001
Fe^{2+}	0.362	0.396	0.363	0.396	0.432	0.415	0.419	0.650	0.598	0.487	0.728	0.807
Mn	0.002	0.003	0.005	0.005	0.008	0.009	0.005	0.010	0.006	0.007	0.011	0.014
Mg	1.631	1.593	1.618	1.579	1.573	1.574	1.502	1.284	1.335	1.451	1.188	1.123
Ca	0.005	0.006	0.005	0.004	0.006	0.005	0.005	0.007	0.005	0.003	0.007	0.008
Fo%	81.8	80.1	81.7	79.9	78.5	79.1	78.2	66.4	69.1	74.9	62.0	58.2

APPENDIX II.A: OLIVINE

Sample	SJ107				D17					
Lithotype	Trachybasalt				Basalt					
Ref.	SJ107-6-OC26	SJ107-6-OB29	SJ107-8-OC28	SJ107-8-OB27	D17-1-ON1	D17-1-OB2	D17-1A-ON3	D17-OM4	D17-OM5	D17-OM18
SiO_2 (%)	39.08	37.56	38.85	37.36	39.77	38.70	39.94	37.39	38.11	39.91
TiO_2	0.094	0.159	0.040	0.096	0.000	0.097	0.000	0.205	0.205	0.042
Al_2O_3	0.000	0.076	0.024	0.064	0.076	0.045	0.029	0.115	0.086	0.103
NiO	0.010	0.000	0.000	0.034	0.205	0.057	0.294	0.000	0.000	0.196
FeO	20.54	28.63	19.95	27.14	16.25	22.15	16.29	25.53	27.82	16.15
MnO	0.168	0.745	0.327	0.649	0.185	0.385	0.158	0.401	0.350	0.152
MgO	39.28	32.01	39.30	33.34	43.93	38.62	43.76	35.68	33.66	44.11
CaO	0.179	0.351	0.190	0.330	0.211	0.319	0.181	0.439	0.461	0.200
Cr_2O_3	0.000	0.000	0.000	0.000	0.000	0.000	0.000	0.000	0.000	0.000
ZnO	0.000	0.000	0.022	0.008	0.000	0.000	0.000	0.000	0.000	0.000
V_2O_3	0.032	0.183	0.000	0.175	0.000	0.000	0.000	0.000	0.000	0.000
Total	99.4	99.7	98.7	99.2	100.6	100.4	100.7	99.8	100.7	100.9
Number of ions on the basis of 4 O										
Si	1.012	1.014	1.012	1.008	0.999	1.002	1.002	0.993	1.010	0.999
Al^{IV}	0.000	0.000	0.000	0.000	0.001	0.000	0.000	0.004	0.000	0.001
Al^{VI}	0.000	0.002	0.001	0.002	0.001	0.001	0.001	0.000	0.003	0.002
Ti	0.002	0.003	0.001	0.002	0.000	0.002	0.000	0.004	0.004	0.001
Ni	0.000	0.000	0.000	0.001	0.004	0.001	0.006	0.000	0.000	0.004
Fe^{2+}	0.445	0.646	0.435	0.612	0.341	0.480	0.342	0.567	0.617	0.338
Mn	0.004	0.017	0.007	0.015	0.004	0.008	0.003	0.009	0.008	0.003
Mg	1.517	1.288	1.526	1.341	1.645	1.491	1.638	1.413	1.330	1.646
Ca	0.005	0.010	0.005	0.010	0.006	0.009	0.005	0.012	0.013	0.005
Fo%	77.3	66.6	77.8	68.7	82.8	75.7	82.7	71.4	68.3	83.0

APPENDIX II.B: FELDSPAR

Sample	SJ7										SJ8		
Lithotype	Plagioclase-bearing basalt										Trachybasalt		
Ref.	SJ7-3-FN1	SJ7-3-FC2	SJ7-3-FB3	SJ7-3 MF5	SJ7-4-FN12	SJ7-4-FB13	SJ7-1-FN16	SJ7-1-FNC17	SJ7-1-FCB18	SJ7-1-FB19	SJ8-6-FN12	SJ8-6-FB13	SJ8-5-FN14
SiO_2 (%)	49.46	51.52	57.76	53.81	47.72	49.12	49.24	50.09	49.42	52.53	48.50	53.45	50.37
TiO_2	0.070	0.059	0.145	0.233	0.066	0.078	0.063	0.057	0.051	0.155	0.031	0.070	0.053
Al_2O_3	30.67	29.62	24.96	27.04	31.89	31.47	30.91	30.84	31.20	29.06	31.77	28.21	30.30
FeO	0.438	0.574	0.393	0.711	0.309	0.196	0.292	0.473	0.420	0.345	0.250	0.582	0.338
MnO	0.000	0.044	0.009	0.000	0.000	0.079	0.035	0.035	0.026	0.000	0.096	0.000	0.009
MgO	0.178	0.143	0.181	0.209	0.143	0.141	0.158	0.147	0.139	0.146	0.148	0.220	0.121
CaO	15.04	13.31	7.92	11.19	16.37	15.17	15.15	14.86	15.30	12.58	15.75	11.94	14.49
Na_2O	2.91	3.86	6.21	5.03	2.23	2.83	2.78	3.11	2.76	4.22	2.47	4.59	3.33
K_2O	0.142	0.225	0.943	0.340	0.057	0.125	0.153	0.155	0.096	0.215	0.109	0.239	0.122
BaO	0.081	0.052	0.201	0.051	0.093	0.029	0.064	0.078	0.000	0.089	0.096	0.036	0.094
SrO	0.000	0.000	0.000	0.000	0.000	0.000	0.698	0.759	0.853	0.789			
Total	99.0	99.4	98.7	98.6	98.9	99.2	99.5	100.6	100.3	100.1	99.2	99.3	99.2
Number of ions on the basis of 32 O													
Si	9.14	9.44	10.52	9.89	8.86	9.05	9.11	9.18	9.09	9.60	8.96	9.75	9.27
Ti	0.01	0.01	0.02	0.03	0.01	0.01	0.01	0.01	0.01	0.02	0.00	0.01	0.01
Al	6.68	6.40	5.36	5.86	6.98	6.84	6.74	6.66	6.76	6.26	6.92	6.07	6.57
Fe^{3+}	0.07	0.09	0.06	0.11	0.05	0.03	0.05	0.07	0.06	0.05	0.04	0.09	0.05
Mn	0.00	0.01	0.00	0.00	0.00	0.01	0.01	0.01	0.00	0.00	0.02	0.00	0.00
Mg	0.05	0.04	0.05	0.06	0.04	0.04	0.04	0.04	0.04	0.04	0.04	0.06	0.03
Ca	2.98	2.61	1.55	2.20	3.26	3.00	3.00	2.92	3.02	2.46	3.12	2.33	2.86
Na	1.04	1.37	2.19	1.79	0.80	1.01	1.00	1.10	0.98	1.50	0.89	1.62	1.19
K	0.03	0.05	0.22	0.08	0.01	0.03	0.04	0.04	0.02	0.05	0.03	0.06	0.03
An	73.5	64.7	39.0	54.1	80.0	74.2	74.4	71.9	75.0	61.4	77.4	58.2	70.1
Ab	25.7	34.0	55.4	44.0	19.7	25.1	24.7	27.2	24.5	37.3	22.0	40.5	29.2
Or	0.83	1.30	5.55	1.96	0.33	0.73	0.90	0.89	0.56	1.25	0.64	1.39	0.70

APPENDIX II.B: FELDSPAR

Sample	SJ8					SJ9							
Lithotype	Trachybasalt					Basalt							
Ref.	SJ8-5-FNC15	SJ8-5-FCB16	SJ8-5-FB17	SJ8-5-MF18	SJ8-5-MF19	SJ9-4-FC2	SJ9-4-FN3	SJ9-4-FCB4	SJ9-4-FB5	SJ9-5-MF6	SJ9-3-FN9	SJ9-3-FC10	SJ9-3-FB11
SiO_2 (%)	50.29	48.10	51.78	61.58	54.67	48.50	48.66	49.32	49.21	54.32	48.61	49.22	52.73
TiO_2	0.063	0.071	0.088	0.202	0.285	0.084	0.053	0.027	0.047	0.147	0.033	0.065	0.143
Al_2O_3	30.33	31.37	29.05	22.23	27.64	31.51	32.64	31.18	31.21	27.53	31.23	31.51	28.42
FeO	0.361	0.488	0.421	0.650	0.808	0.378	0.363	0.219	0.423	0.506	0.308	0.435	0.571
MnO	0.000	0.017	0.000	0.009	0.069	0.035	0.000	0.000	0.044	0.009	0.000	0.000	0.044
MgO	0.158	0.152	0.204	0.152	0.218	0.133	0.091	0.137	0.212	0.193	0.172	0.203	0.275
CaO	14.18	16.07	13.16	4.54	10.73	15.82	15.99	14.87	15.52	11.26	15.70	15.60	12.34
Na_2O	3.30	2.45	4.00	6.99	5.31	2.50	2.42	2.99	2.75	5.02	2.45	2.67	4.41
K_2O	0.140	0.070	0.187	3.050	0.178	0.057	0.085	0.071	0.086	0.357	0.062	0.113	0.231
BaO	0.042	0.072	0.014	0.068	0.081	0.099	0.000	0.004	0.151	0.000	0.037	0.044	0.022
SrO						0.000	0.000	0.000	0.000	0.000	0.709	0.750	0.812
Total	98.9	98.9	98.9	99.5	100.0	99.1	100.3	98.8	99.7	99.3	99.3	100.6	100.0
Number of ions on the basis of 32 O													
Si	9.28	8.94	9.52	11.11	9.90	8.97	8.89	9.11	9.05	9.90	9.02	9.03	9.66
Ti	0.01	0.01	0.01	0.03	0.04	0.01	0.01	0.00	0.01	0.02	0.00	0.01	0.02
Al	6.59	6.87	6.30	4.73	5.90	6.87	7.03	6.79	6.77	5.91	6.83	6.81	6.13
Fe^{3+}	0.06	0.08	0.06	0.10	0.12	0.06	0.06	0.03	0.07	0.08	0.05	0.07	0.09
Mn	0.00	0.00	0.00	0.00	0.01	0.01	0.00	0.00	0.01	0.00	0.00	0.00	0.01
Mg	0.04	0.04	0.06	0.04	0.06	0.04	0.02	0.04	0.06	0.05	0.05	0.06	0.07
Ca	2.80	3.20	2.59	0.88	2.08	3.14	3.13	2.94	3.06	2.20	3.12	3.07	2.42
Na	1.18	0.88	1.43	2.44	1.86	0.90	0.86	1.07	0.98	1.77	0.88	0.95	1.57
K	0.03	0.02	0.04	0.70	0.04	0.01	0.02	0.02	0.02	0.08	0.01	0.03	0.05
An	69.8	78.1	63.8	21.8	52.2	77.5	78.1	73.0	75.3	54.2	77.7	75.9	59.9
Ab	29.4	21.5	35.1	60.7	46.8	22.2	21.4	26.6	24.2	43.7	21.9	23.5	38.7
Or	0.82	0.41	1.08	17.47	1.03	0.33	0.49	0.42	0.50	2.05	0.36	0.65	1.34

APPENDIX II.B: FELDSPAR

Sample	SJ18				SJ20- Basalt						SJ32		
Lithotype	Basalt trachyandesite				Lava	Lava	Lava	Lava	Nodule	Nodule	Nodule	Lava	Nodule
Ref.	SJ18-3-FC10	SJ18-4-FN11	SJ18-5-MF12	SJ18-5-MF13	SJ20-1-FB4	SJ20-1-FC5	SJ20-1-FN6	SJ20-1-MF7	SJ20A-1-FC1	SJ20A-3-FC7	SJ32-n-M12	SJ32-M21	SJ32A-1-PN1
SiO_2 (%)	57.11	59.31	66.00	63.45	49.57	55.45	53.54	49.56	51.66	48.07	53.08	51.75	50.34
TiO_2	0.027	0.000	0.172	0.141	0.131	0.032	0.034	0.176	0.096	0.085	0.033	0.166	0.059
Al_2O_3	26.70	25.47	18.91	20.69	30.64	26.84	28.51	30.94	29.44	32.03	28.49	28.64	30.15
FeO	0.190	0.152	0.409	0.243	0.438	0.201	0.371	0.439	0.227	0.409	0.359	0.420	0.283
MnO	0.000	0.000	0.018	0.000	0.000	0.095	0.000	0.009	0.070	0.000	0.000	0.000	0.018
MgO	0.121	0.099	0.040	0.074	0.165	0.119	0.092	0.199	0.120	0.151	0.132	0.186	0.158
CaO	9.22	7.40	1.34	2.74	14.98	10.35	11.62	14.92	13.60	15.90	12.10	12.87	13.94
Na_2O	5.68	6.78	6.08	8.04	2.87	5.22	4.77	2.87	3.74	2.36	4.17	3.88	3.06
K_2O	0.510	0.623	6.750	3.400	0.178	0.318	0.276	0.112	0.193	0.110	0.219	0.275	0.126
BaO	0.041	0.140	0.071	0.221	0.008	0.027	0.084	0.076	0.086	0.000	0.092	0.119	0.402
SrO	0.000	0.000	0.000	0.000	0.728	1.091	0.996	0.697	0.757	0.000	0.468	0.431	0.120
Total	99.6	100.0	99.8	99.0	99.7	99.7	100.3	100.0	100.0	99.1	99.1	98.7	98.7
Number of ions on the basis of 32 O													
Si	10.29	10.61	11.87	11.47	9.16	10.12	9.77	9.13	9.48	8.89	9.74	9.58	9.33
Ti	0.00	0.00	0.02	0.02	0.02	0.00	0.00	0.02	0.01	0.01	0.00	0.02	0.01
Al	5.67	5.37	4.01	4.41	6.67	5.78	6.13	6.72	6.37	6.98	6.16	6.25	6.59
Fe^{3+}	0.03	0.02	0.06	0.04	0.07	0.03	0.06	0.07	0.03	0.06	0.06	0.07	0.04
Mn	0.00	0.00	0.00	0.00	0.00	0.01	0.00	0.00	0.01	0.00	0.00	0.00	0.00
Mg	0.03	0.03	0.01	0.02	0.05	0.03	0.03	0.05	0.03	0.04	0.04	0.05	0.04
Ca	1.78	1.42	0.26	0.53	2.96	2.02	2.27	2.94	2.67	3.15	2.38	2.55	2.77
Na	1.98	2.35	2.12	2.82	1.03	1.85	1.69	1.02	1.33	0.85	1.48	1.39	1.10
K	0.12	0.14	1.55	0.79	0.04	0.07	0.06	0.03	0.05	0.03	0.05	0.07	0.03
An	45.9	36.3	6.6	12.8	73.5	51.3	56.5	73.7	66.0	78.3	60.8	63.7	71.0
Ab	51.1	60.1	53.9	68.2	25.5	46.8	41.9	25.7	32.9	21.0	37.9	34.7	28.2
Or	3.03	3.64	39.48	19.00	1.04	1.88	1.60	0.66	1.12	0.65	1.31	1.62	0.76

APPENDIX II.B: FELDSPAR

Sample	SJ32						SJ49		SJ52				
Lithotype	Nodule	Nodule	Nodule	Nodule	Nodule	Nodule	Basalt		Basalt				
Ref.	SJ32A-1-PN2	SJ32A-4-PINC6	SJ32A-4-PC8	SJ32A-4-PM9	SJ32A-8-PN14	SJ32A-8-PB15	SJ49-PM4	SJ49-PM14	SJ52-1-FC1	SJ52-1-FB2	SJ52-M3	SJ52-2-FC4	SJ52-M12
SiO_2 (%)	50.09	51.12	51.37	51.87	53.66	51.12	52.87	53.57	51.69	51.74	50.98	52.28	52.36
TiO_2	0.051	0.116	0.098	0.159	0.096	0.200	0.555	0.125	0.055	0.108	0.133	0.092	0.120
Al_2O_3	30.40	29.86	29.34	28.99	28.55	29.30	29.17	28.71	29.86	29.99	30.49	29.70	29.06
FeO	0.304	0.261	0.313	0.588	0.418	0.530	0.277	0.165	0.284	0.583	0.410	0.269	0.328
MnO	0.027	0.000	0.054	0.000	0.000	0.000	0.000	0.090	0.000	0.063	0.009	0.063	0.080
MgO	0.135	0.136	0.166	0.203	0.189	0.187	0.103	0.106	0.178	0.132	0.094	0.151	0.117
CaO	13.98	13.42	13.05	12.88	11.72	13.10	11.45	11.53	12.93	13.20	13.22	12.61	11.96
Na_2O	3.01	3.33	3.61	3.64	4.44	3.67	4.56	4.57	3.74	3.39	3.34	3.93	4.23
K_2O	0.156	0.231	0.228	0.205	0.229	0.170	0.395	0.225	0.204	0.267	0.244	0.205	0.355
BaO	0.425	0.386	0.423	0.433	0.449	0.416	0.011	0.113	0.023	0.033	0.071	0.075	0.000
SrO	0.076	0.054	0.097	0.097	0.021	0.052	0.461	0.521	0.422	0.337	0.353	0.335	0.429
Total	98.7	98.9	98.7	99.1	99.8	98.7	99.9	99.7	99.4	99.8	99.3	99.7	99.0
Number of ions on the basis of 32 O													
Si	9.29	9.43	9.50	9.55	9.77	9.46	9.64	9.77	9.48	9.45	9.36	9.54	9.63
Ti	0.01	0.02	0.01	0.02	0.01	0.03	0.08	0.02	0.01	0.01	0.02	0.01	0.02
Al	6.64	6.49	6.39	6.29	6.13	6.39	6.27	6.17	6.45	6.45	6.60	6.39	6.30
Fe^{3+}	0.05	0.04	0.05	0.09	0.06	0.08	0.04	0.03	0.04	0.09	0.06	0.04	0.05
Mn	0.00	0.00	0.01	0.00	0.00	0.00	0.00	0.01	0.00	0.01	0.00	0.01	0.01
Mg	0.04	0.04	0.05	0.06	0.05	0.05	0.03	0.03	0.05	0.04	0.03	0.04	0.03
Ca	2.78	2.65	2.59	2.54	2.29	2.60	2.24	2.25	2.54	2.58	2.60	2.47	2.36
Na	1.08	1.19	1.29	1.30	1.57	1.32	1.61	1.62	1.33	1.20	1.19	1.39	1.51
K	0.04	0.05	0.05	0.05	0.05	0.04	0.09	0.05	0.05	0.06	0.06	0.05	0.08
An	71.3	68.0	65.7	65.3	58.5	65.7	56.8	57.5	64.8	67.2	67.6	63.2	59.7
Ab	27.8	30.6	32.9	33.4	40.1	33.3	40.9	41.2	33.9	31.2	30.9	35.6	38.2
Or	0.95	1.40	1.37	1.24	1.37	1.02	2.34	1.34	1.22	1.62	1.49	1.23	2.11

APPENDIX II.B: FELDSPAR

Sample	SJ55					SJ70					SJ77		
Lithotype	Tefrite					Basalt					Basanite		
Ref.	SJ55-1-PB3	SJ55-1-PC4	SJ55-1-PN5	SJ55-PM16	SJ55-PM17	SJ70-PM13	SJ70-PM14	SJ70-PM15	SJ70-PM16	SJ70-PM17	SJ77-1-PB12	SJ77-1-PC13	SJ77-PM14
SiO_2 (%)	48.79	53.62	53.20	53.57	52.83	52.18	53.61	52.22	54.33	55.89	50.35	47.93	55.89
TiO_2	0.038	0.092	0.110	0.086	0.142	0.124	0.234	0.176	0.232	0.200	0.199	0.018	0.317
Al_2O_3	31.62	29.92	29.92	29.76	29.39	30.04	29.43	29.99	27.63	28.38	30.53	32.77	27.26
FeO	0.427	0.263	0.347	0.634	0.701	0.421	0.582	0.382	0.591	0.565	0.494	0.414	0.896
MnO	0.072	0.073	0.073	0.000	0.000	0.000	0.000	0.000	0.000	0.000	0.054	0.072	0.000
MgO	0.103	0.137	0.151	0.194	0.199	0.240	0.196	0.261	0.119	0.132	0.165	0.121	0.064
CaO	14.41	12.22	12.12	11.66	11.81	12.72	11.18	12.90	10.36	10.28	13.49	15.34	9.57
Na_2O	2.58	3.69	3.58	3.75	3.69	3.44	3.74	3.50	4.30	3.97	3.23	1.95	4.95
K_2O	0.127	0.149	0.171	0.234	0.248	0.284	0.292	0.225	0.487	0.392	0.196	0.080	0.333
BaO	0.070	0.000	0.047	0.020	0.028	0.007	0.077	0.062	0.026	0.107	0.088	0.080	0.105
SrO	0.347	0.433	0.436	0.450	0.439	0.360	0.402	0.339	0.354	0.396	0.348	0.356	0.412
Total	98.6	100.6	100.2	100.4	99.5	99.8	99.7	100.1	98.4	100.3	99.1	99.1	99.8
Number of ions on the basis of 32 O													
Si	9.06	9.66	9.63	9.67	9.64	9.50	9.72	9.50	9.97	10.03	9.28	8.87	10.11
Ti	0.01	0.01	0.01	0.01	0.02	0.02	0.03	0.02	0.03	0.03	0.03	0.00	0.04
Al	6.92	6.35	6.38	6.33	6.32	6.45	6.29	6.43	5.98	6.00	6.63	7.15	5.81
Fe^{3+}	0.07	0.04	0.05	0.10	0.11	0.06	0.09	0.06	0.09	0.08	0.08	0.06	0.14
Mn	0.01	0.01	0.01	0.00	0.00	0.00	0.00	0.00	0.00	0.00	0.01	0.01	0.00
Mg	0.03	0.04	0.04	0.05	0.05	0.07	0.05	0.07	0.03	0.04	0.05	0.03	0.02
Ca	2.87	2.36	2.35	2.26	2.31	2.48	2.17	2.51	2.04	1.98	2.66	3.04	1.85
Na	0.93	1.29	1.26	1.31	1.31	1.21	1.32	1.23	1.53	1.38	1.15	0.70	1.74
K	0.03	0.03	0.04	0.05	0.06	0.07	0.07	0.05	0.11	0.09	0.05	0.02	0.08
An	74.9	64.1	64.5	62.3	62.9	66.0	61.1	66.1	55.3	57.3	68.9	80.9	50.6
Ab	24.3	35.0	34.5	36.2	35.6	32.3	37.0	32.5	41.6	40.1	29.9	18.6	47.3
Or	0.79	0.93	1.09	1.49	1.57	1.76	1.91	1.37	3.10	2.61	1.20	0.51	2.10

APPENDIX II.B: FELDSPAR

Sample	SJ77			SJ83							SJ91	
Lithotype	Basanite										Trachybasalt	
Ref.	SJ77-PM15	SJ77-2-PC16	SJ77-2-PB17	SJ83-2 - PN5	SJ83-2 - PC6	SJ83-2 - PB7	SJ83-1 - PN8	SJ83-1 - PC9	SJ83-1 - PB10	SJ83-M18	SJ91-1PC15	SJ91-1PB16
SiO_2 (%)	52.13	48.10	51.32	47.59	50.94	54.07	52.47	50.87	54.11	51.82	47.88	51.98
TiO_2	0.183	0.022	0.149	0.045	0.134	0.164	0.097	0.116	0.130	0.114	0.023	0.104
Al_2O_3	30.27	32.60	30.82	32.33	30.21	27.88	28.98	30.36	27.94	29.68	33.04	29.57
FeO	0.801	0.316	0.578	0.208	0.431	0.431	0.357	0.387	0.290	0.478	0.356	0.541
MnO	0.000	0.027	0.000	0.000	0.000	0.027	0.036	0.000	0.000	0.063	0.000	0.100
MgO	0.110	0.139	0.148	0.163	0.144	0.202	0.146	0.167	0.132	0.198	0.089	0.146
CaO	12.76	15.41	13.41	15.84	13.57	10.87	12.35	13.92	10.93	13.07	15.59	12.74
Na_2O	3.18	2.16	3.37	2.05	3.30	4.75	3.91	3.19	4.75	3.64	2.03	3.68
K_2O	0.132	0.097	0.220	0.092	0.203	0.482	0.251	0.174	0.530	0.226	0.100	0.218
BaO	0.030	0.066	0.059	0.000	0.117	0.107	0.089	0.000	0.072	0.124	0.013	0.031
SrO	0.397	0.386	0.433	0.391	0.399	0.390	0.458	0.472	0.382	0.427	0.420	0.536
Total	100.0	99.3	100.5	98.7	99.4	99.4	99.1	99.7	99.3	99.8	99.5	99.6
Number of ions on the basis of 32 O												
Si	9.47	8.89	9.33	8.86	9.36	9.88	9.64	9.33	9.89	9.48	8.83	9.52
Ti	0.03	0.00	0.02	0.01	0.02	0.02	0.01	0.02	0.02	0.02	0.00	0.01
Al	6.48	7.10	6.60	7.09	6.54	6.01	6.27	6.56	6.02	6.40	7.18	6.38
Fe^{3+}	0.12	0.05	0.09	0.03	0.07	0.07	0.05	0.06	0.04	0.07	0.05	0.08
Mn	0.00	0.00	0.00	0.00	0.00	0.00	0.01	0.00	0.00	0.01	0.00	0.02
Mg	0.03	0.04	0.04	0.05	0.04	0.05	0.04	0.05	0.04	0.05	0.02	0.04
Ca	2.49	3.05	2.61	3.16	2.67	2.13	2.43	2.74	2.14	2.56	3.08	2.50
Na	1.12	0.77	1.19	0.74	1.18	1.68	1.39	1.13	1.68	1.29	0.73	1.31
K	0.03	0.02	0.05	0.02	0.05	0.11	0.06	0.04	0.12	0.05	0.02	0.05
An	68.3	79.3	67.8	80.6	68.6	54.2	62.6	70.0	54.2	65.6	80.4	64.8
Ab	30.8	20.1	30.8	18.9	30.2	42.9	35.9	29.0	42.6	33.1	19.0	33.9
Or	0.85	0.59	1.33	0.56	1.22	2.87	1.52	1.04	3.14	1.35	0.62	1.32

APPENDIX II.B: FELDSPAR

Sample	SJ91	SJ91						SJ107			
Lithotype	Trachybasalt	Trachybasalt						Trachybasalt			
Ref.	SJ91-PM17	SJ91-PM18	SJ91-2-PN19	SJ91-2-PC20	SJ91-2-PB21	SJ91-PM22	SJ91-PM23	SJ91-PM24	SJ107-4-FN16	SJ107-4-FC17	SJ107-4-FB18	SJ107-5-FN19
SiO_2 (%)	52.46	52.28	47.32	48.17	48.85	54.41	53.91	52.52	60.63	59.65	52.67	58.66
TiO_2	0.132	0.098	0.008	0.047	0.051	0.140	0.190	0.181	0.000	0.037	0.156	0.045
Al_2O_3	29.36	30.28	32.59	32.33	32.38	28.55	28.46	29.64	23.97	25.11	29.04	25.08
FeO	0.769	0.547	0.430	0.415	0.414	0.491	0.459	0.680	0.306	0.157	0.342	0.030
MnO	0.100	0.000	0.000	0.127	0.063	0.009	0.009	0.000	0.018	0.036	0.053	0.089
MgO	0.101	0.090	0.129	0.140	0.124	0.079	0.105	0.114	0.093	0.093	0.157	0.059
CaO	11.79	12.44	15.54	15.28	14.29	10.81	10.70	11.59	6.24	6.82	11.94	7.13
Na_2O	4.11	3.69	2.10	2.18	2.86	4.71	4.22	4.13	7.53	7.34	4.18	6.91
K_2O	0.209	0.228	0.126	0.184	0.182	0.274	0.229	0.236	0.572	0.483	0.219	0.491
BaO	0.060	0.000	0.041	0.103	0.091	0.017	0.105	0.117	0.117	0.077	0.121	0.194
SrO	0.456	0.456	0.369	0.376	0.434	0.408	0.420	0.466	0.541	0.493	0.425	0.589
Total	99.5	100.1	98.7	99.4	99.7	99.9	98.8	99.7	100.0	100.3	99.3	99.3
Number of ions on the basis of 32 O												
Si	9.59	9.50	8.82	8.91	8.98	9.86	9.87	9.59	10.87	10.67	9.65	10.63
Ti	0.02	0.01	0.00	0.01	0.01	0.02	0.03	0.02	0.00	0.00	0.02	0.01
Al	6.33	6.48	7.16	7.05	7.02	6.10	6.14	6.38	5.06	5.30	6.27	5.36
Fe^{3+}	0.12	0.08	0.07	0.06	0.06	0.07	0.07	0.10	0.05	0.02	0.05	0.00
Mn	0.02	0.00	0.00	0.02	0.01	0.00	0.00	0.00	0.00	0.01	0.01	0.01
Mg	0.03	0.02	0.04	0.04	0.03	0.02	0.03	0.03	0.02	0.02	0.04	0.02
Ca	2.31	2.42	3.10	3.03	2.82	2.10	2.10	2.27	1.20	1.31	2.34	1.38
Na	1.46	1.30	0.76	0.78	1.02	1.66	1.50	1.46	2.62	2.55	1.49	2.43
K	0.05	0.05	0.03	0.04	0.04	0.06	0.05	0.06	0.13	0.11	0.05	0.11
An	60.5	64.2	79.7	78.6	72.6	55.0	57.5	59.9	30.4	33.0	60.4	35.3
Ab	38.2	34.4	19.5	20.3	26.3	43.4	41.0	38.6	66.3	64.2	38.3	61.8
Or	1.28	1.40	0.77	1.13	1.10	1.66	1.47	1.46	3.32	2.78	1.32	2.89

APPENDIX II.B: FELDSPAR

Sample	SJ107				D17					
Lithotype	Trachybasalt				Basalt					
Ref.	SJ107-5-FNC20	SJ107-5-FCB21	SJ107-5-FB22	SJ107-M23	D17-2-PN6	D17-2-PB7	D17-PM8	D17-PM9	D17-PM16	D17-PM17
SiO_2 (%)	61.57	61.07	53.15	54.22	51.68	53.61	54.08	53.76	53.57	53.37
TiO_2	0.000	0.006	0.110	0.139	0.072	0.079	0.145	0.152	0.176	0.122
Al_2O_3	23.15	23.62	28.27	28.30	29.93	29.54	28.88	28.93	29.02	28.66
FeO	0.164	0.112	0.306	0.470	0.356	0.397	0.388	0.318	0.449	0.500
MnO	0.000	0.018	0.000	0.063	0.000	0.054	0.027	0.000	0.000	0.018
MgO	0.090	0.101	0.170	0.175	0.214	0.235	0.142	0.223	0.259	0.241
CaO	5.26	5.53	11.72	11.17	12.59	11.74	11.84	11.49	11.67	11.58
Na_2O	7.96	7.86	4.40	4.67	3.27	3.75	3.53	3.87	4.57	4.36
K_2O	0.708	0.663	0.274	0.315	0.132	0.231	0.211	0.237	0.275	0.253
BaO	0.178	0.143	0.112	0.061	0.094	0.042	0.086	0.079	0.134	0.049
SrO	0.459	0.530	0.396	0.449	0.368	0.348	0.302	0.343	0.419	0.373
Total	99.5	99.7	98.9	100.0	98.7	100.0	99.6	99.4	100.5	99.5
Number of ions on the basis of 32 O										
Si	11.06	10.97	9.77	9.84	9.51	9.70	9.81	9.78	9.70	9.74
Ti	0.00	0.00	0.02	0.02	0.01	0.01	0.02	0.02	0.02	0.02
Al	4.90	5.00	6.13	6.06	6.49	6.30	6.18	6.21	6.19	6.16
Fe^{3+}	0.02	0.02	0.05	0.07	0.05	0.06	0.06	0.05	0.07	0.08
Mn	0.00	0.00	0.00	0.01	0.00	0.01	0.00	0.00	0.00	0.00
Mg	0.02	0.03	0.05	0.05	0.06	0.06	0.04	0.06	0.07	0.07
Ca	1.01	1.06	2.31	2.17	2.48	2.28	2.30	2.24	2.26	2.26
Na	2.77	2.74	1.57	1.64	1.17	1.32	1.24	1.37	1.60	1.54
K	0.16	0.15	0.06	0.07	0.03	0.05	0.05	0.06	0.06	0.06
An	25.6	26.9	58.6	55.9	67.5	62.4	64.1	61.2	57.6	58.6
Ab	70.2	69.2	39.8	42.3	31.7	36.1	34.6	37.3	40.8	39.9
Or	4.12	3.85	1.63	1.88	0.84	1.46	1.36	1.51	1.62	1.53

APPENDIX II.C: PYROXENE

Sample	SJ8					SJ18		SJ49					
Lithotype	Trachybasalt					Basalt trachyandesite		Basalt					
Ref.	SJ8-1-PC1	SJ8-1-PB2	SJ8-1-PN3	SJ8-2-PB6	SJ8-2-PN7	SJ18-1-PN1	SJ18-1-PB2	SJ49-4-PN1	SJ49-4-PC2	SJ49-4-PB3	SJ49-5-PN10	SJ49-6-PN11	SJ49-6-PN12
SiO_2 (%)	51.41	48.74	50.59	50.07	52.58	51.91	49.76	47.18	52.24	51.01	49.28	51.90	49.42
TiO_2	1.030	2.270	0.423	1.680	0.540	0.628	1.616	3.300	0.718	2.150	1.870	0.981	2.390
Al_2O_3	0.67	4.70	0.87	4.07	1.67	1.54	3.60	6.32	3.17	3.26	6.23	3.79	4.51
Cr_2O_3	0.008	0.005	0.000	0.051	0.000	0.000	0.010	0.315	1.004	0.000	0.435	0.332	0.204
FeO	12.75	7.55	17.88	7.57	8.81	13.00	8.70	7.24	4.28	7.17	5.34	4.15	6.45
Fe_2O_3	0.646	0.848	0.000	0.639	0.000	0.000	1.559	0.138	0.000	0.000	0.000	0.000	0.000
MnO	0.679	0.099	0.852	0.261	0.333	0.332	0.324	0.145	0.154	0.118	0.172	0.000	0.100
MgO	10.92	13.37	7.80	13.90	13.85	11.27	12.81	12.20	16.66	13.25	14.21	16.04	12.86
CaO	21.37	20.82	19.92	20.66	21.08	20.51	20.79	21.60	20.40	21.46	21.20	21.31	21.89
Na_2O	0.455	0.466	0.491	0.489	0.480	0.394	0.522	0.553	0.453	0.628	0.494	0.410	0.725
K_2O	0.002	0.000	0.028	0.015	0.000	0.019	0.021	0.006	0.004	0.000	0.000	0.010	0.010
Total	99.94	98.86	98.85	99.41	99.34	99.60	99.71	98.99	99.08	99.05	99.23	98.92	98.56
Number of ions on the basis of 4 cations													
Si	1.963	1.836	1.992	1.871	1.970	1.979	1.871	1.779	1.924	1.915	1.828	1.915	1.861
Al^{IV}	0.030	0.164	0.008	0.129	0.030	0.021	0.129	0.221	0.076	0.085	0.172	0.085	0.139
Ti	0.030	0.064	0.013	0.047	0.015	0.018	0.046	0.094	0.020	0.061	0.052	0.027	0.068
Al^{VI}	0.000	0.045	0.033	0.050	0.043	0.048	0.031	0.060	0.062	0.060	0.100	0.080	0.061
Cr	0.000	0.000	0.000	0.002	0.000	0.000	0.000	0.009	0.029	0.000	0.013	0.010	0.006
Fe^{3+}	0.005	0.024	0.000	0.018	0.000	0.000	0.044	0.004	0.000	0.000	0.000	0.000	0.000
Fe^{2+}	0.421	0.238	0.589	0.237	0.276	0.414	0.274	0.228	0.132	0.225	0.166	0.128	0.203
Mn	0.022	0.003	0.028	0.008	0.011	0.011	0.010	0.005	0.005	0.004	0.005	0.000	0.003
Mg	0.622	0.751	0.458	0.775	0.774	0.641	0.718	0.686	0.915	0.742	0.786	0.883	0.722
Ca	0.874	0.840	0.841	0.827	0.846	0.838	0.838	0.873	0.805	0.863	0.843	0.843	0.883
Na	0.034	0.034	0.038	0.035	0.035	0.029	0.038	0.040	0.032	0.046	0.036	0.029	0.053
K	0.000	0.000	0.001	0.001	0.000	0.001	0.001	0.000	0.000	0.000	0.000	0.000	0.000
En (Mg)	**32.4**	**40.5**	**23.9**	**41.5**	**40.6**	**33.7**	**38.1**	**38.2**	**49.3**	**40.4**	**43.7**	**47.6**	**39.9**
Wo (Ca)	**45.6**	**45.3**	**43.9**	**44.4**	**44.4**	**44.0**	**44.5**	**48.6**	**43.4**	**47.1**	**46.8**	**45.5**	**48.8**
Fs (Fe)	**22.0**	**14.3**	**32.2**	**14.1**	**15.0**	**22.3**	**17.4**	**13.2**	**7.4**	**12.5**	**9.5**	**6.9**	**11.4**

APPENDIX II.C: PYROXENE

Sample	SJ55				SJ70				SJ83				
Lithotype	Tefrite				Basanite								
Ref.	SJ55-6-PN11	SJ55-6-PB12	SJ55-PM13	SJ55-PM14	SJ70-1-PN11	SJ70-1-PB12	SJ70-PM22	SJ70-PM23	SJ83-5-PN12	SJ83-5-PC13	SJ83-5-PB14	SJ83-6-PC15	SJ83-6-PB16
SiO_2 (%)	47.99	49.94	51.71	51.75	51.95	45.68	46.44	45.89	46.50	49.21	50.77	48.87	48.96
TiO_2	2.330	2.280	1.655	1.750	1.364	3.880	3.180	4.000	2.580	1.575	1.910	1.810	2.320
Al_2O_3	7.43	3.79	2.21	2.24	2.81	7.12	7.95	6.83	9.02	6.36	3.14	6.11	4.62
Cr_2O_3	0.116	0.000	0.016	0.016	0.358	0.008	1.056	0.008	0.106	0.003	0.000	0.198	0.000
FeO	7.55	8.63	10.36	9.71	5.56	10.89	5.57	8.32	6.85	6.46	7.32	6.15	7.49
Fe_2O_3	0.572	0.000	0.000	0.000	0.000	0.459	0.000	0.586	0.130	0.000	0.000	0.019	0.331
MnO	0.027	0.171	0.244	0.090	0.117	0.205	0.072	0.250	0.090	0.216	0.199	0.090	0.153
MgO	12.95	13.21	13.53	13.65	15.62	10.20	12.87	11.56	12.61	14.17	14.08	14.06	13.28
CaO	19.85	20.27	19.89	19.44	20.79	20.01	21.41	20.62	19.98	20.00	20.98	20.90	21.11
Na_2O	0.727	0.511	0.462	0.476	0.249	0.664	0.356	0.613	0.620	0.486	0.393	0.419	0.486
K_2O	0.009	0.000	0.042	0.014	0.008	0.075	0.002	0.014	0.014	0.034	0.018	0.020	0.004
Total	99.55	98.80	100.12	99.14	98.83	99.19	98.90	98.69	98.50	98.51	98.81	98.65	98.76
Number of ions on the basis of 4 cations													
Si	1.788	1.886	1.935	1.952	1.935	1.746	1.743	1.746	1.747	1.839	1.908	1.827	1.845
Al^{IV}	0.212	0.114	0.065	0.048	0.065	0.254	0.257	0.254	0.253	0.161	0.092	0.173	0.155
Ti	0.065	0.065	0.047	0.050	0.038	0.112	0.090	0.114	0.073	0.044	0.054	0.051	0.066
Al^{VI}	0.114	0.055	0.033	0.052	0.059	0.067	0.095	0.053	0.146	0.119	0.047	0.096	0.050
Cr	0.003	0.000	0.000	0.000	0.011	0.000	0.031	0.000	0.003	0.000	0.000	0.006	0.000
Fe^{3+}	0.016	0.000	0.000	0.000	0.000	0.013	0.000	0.017	0.004	0.000	0.000	0.001	0.009
Fe^{2+}	0.235	0.273	0.324	0.306	0.173	0.348	0.175	0.265	0.215	0.202	0.230	0.192	0.236
Mn	0.001	0.005	0.008	0.003	0.004	0.007	0.002	0.008	0.003	0.007	0.006	0.003	0.005
Mg	0.719	0.744	0.755	0.768	0.868	0.581	0.720	0.656	0.706	0.790	0.789	0.784	0.746
Ca	0.792	0.820	0.798	0.786	0.830	0.820	0.861	0.841	0.804	0.801	0.845	0.837	0.852
Na	0.053	0.037	0.033	0.035	0.018	0.049	0.026	0.045	0.045	0.035	0.029	0.030	0.035
K	0.000	0.000	0.002	0.001	0.000	0.004	0.000	0.001	0.001	0.002	0.001	0.001	0.000
En (Mg)	**40.8**	**40.4**	**40.1**	**41.2**	**46.3**	**32.9**	**41.0**	**36.7**	**40.8**	**43.9**	**42.2**	**43.1**	**40.4**
Wo (Ca)	**44.9**	**44.5**	**42.3**	**42.2**	**44.3**	**46.3**	**49.0**	**47.1**	**46.4**	**44.5**	**45.2**	**46.1**	**46.1**
Fs (Fe)	**14.3**	**15.1**	**17.6**	**16.6**	**9.4**	**20.8**	**10.1**	**16.2**	**12.8**	**11.6**	**12.6**	**10.8**	**13.5**

APPENDIX II.C: PYROXENE

Sample	SJ91						SJ20 - Basalt					
Lithotype	Trachybasalt						Lava	Lava	Nodule	Nodule	Nodule	Nodule
Ref.	SJ91-5-PN4	SJ91-4-PC5	SJ91-4-PB8	SJ91-6-PC9	SJ91-6-PB10	SJ91-6-PN11	SJ21B-5-PN8	SJ21B-5-PB11	SJ21A-4-PB9	SJ21A-4-PC10	SJ21A-6-PC11	SJ21A-6-PB12
SiO_2 (%)	48.50	49.21	46.83	52.20	47.72	48.22	47.41	46.23	44.59	48.03	47.78	42.66
TiO_2	2.030	1.740	2.950	0.915	3.000	2.100	2.130	3.070	4.000	2.550	2.520	4.710
Al_2O_3	7.31	6.69	6.90	3.59	5.57	6.53	6.86	8.09	8.28	6.00	5.51	10.29
Cr_2O_3	0.302	0.219	0.000	0.302	0.044	0.412	0.024	0.063	0.055	0.000	0.000	0.000
FeO	7.00	6.49	7.76	5.28	8.30	6.24	6.75	6.47	6.35	6.68	5.33	5.68
Fe_2O_3	0.000	0.000	0.772	0.000	0.751	0.516	1.990	1.253	1.926	0.930	1.920	2.715
MnO	0.135	0.199	0.125	0.118	0.224	0.108	0.136	0.255	0.080	0.142	0.212	0.168
MgO	13.87	14.52	12.62	16.33	12.93	13.71	12.55	12.35	11.76	13.35	13.71	10.97
CaO	19.51	19.70	20.29	19.94	20.18	20.42	20.13	21.02	21.18	21.07	21.24	21.15
Na_2O	0.605	0.528	0.490	0.470	0.492	0.560	0.763	0.507	0.514	0.446	0.466	0.584
K_2O	0.000	0.017	0.000	0.039	0.023	0.000	0.009	0.005	0.000	0.020	0.022	0.022
Total	99.26	99.31	98.73	99.18	99.24	98.81	98.75	99.32	98.73	99.22	98.71	98.95
Number of ions on the basis of 4 cations												
Si	1.803	1.823	1.769	1.924	1.798	1.804	1.787	1.734	1.691	1.799	1.796	1.618
Al^{IV}	0.197	0.177	0.231	0.076	0.202	0.196	0.213	0.266	0.309	0.201	0.204	0.382
Ti	0.057	0.048	0.084	0.025	0.085	0.059	0.060	0.087	0.114	0.072	0.071	0.134
Al^{VI}	0.123	0.115	0.077	0.079	0.045	0.092	0.091	0.092	0.062	0.064	0.041	0.078
Cr	0.009	0.006	0.000	0.009	0.001	0.012	0.001	0.002	0.002	0.000	0.000	0.000
Fe^{3+}	0.000	0.000	0.022	0.000	0.021	0.015	0.056	0.035	0.055	0.026	0.054	0.078
Fe^{2+}	0.218	0.201	0.245	0.163	0.262	0.195	0.213	0.203	0.201	0.209	0.168	0.180
Mn	0.004	0.006	0.004	0.004	0.007	0.003	0.004	0.008	0.003	0.004	0.007	0.005
Mg	0.769	0.802	0.711	0.897	0.726	0.765	0.705	0.691	0.665	0.746	0.769	0.621
Ca	0.777	0.782	0.821	0.787	0.815	0.819	0.813	0.845	0.861	0.846	0.856	0.860
Na	0.044	0.038	0.036	0.034	0.036	0.041	0.056	0.037	0.038	0.032	0.034	0.043
K	0.000	0.001	0.000	0.002	0.001	0.000	0.000	0.000	0.000	0.001	0.001	0.001
En (Mg)	**43.5**	**44.8**	**39.4**	**48.5**	**39.7**	**42.6**	**39.4**	**38.8**	**37.3**	**40.7**	**41.5**	**35.6**
Wo (Ca)	**44.0**	**43.7**	**45.5**	**42.5**	**44.5**	**45.6**	**45.4**	**47.4**	**48.2**	**46.2**	**46.2**	**49.3**
Fs (Fe)	**12.6**	**11.6**	**15.0**	**9.0**	**15.8**	**11.9**	**15.3**	**13.8**	**14.5**	**13.1**	**12.3**	**15.1**

APPENDIX II.C: PYROXENE

Sample	SJ29				SJ77				SJ32 - Basalt				
Lithotype	Basalt				Basanite				Lava	Lava	Nodule	Nodule	Nodule
Ref.	SJ29-5-PC4	SJ29-5-PC5	SJ29-PM6	SJ29-PM7	SJ77-6-PN2	SJ77-6-PB3	SJ77-PM4	SJ77-PM5	SJ32-3-PN17	SJ32-3-PC18	SJ32-2-PN5	SJ32-5-PM6	SJ32-5-PM7
SiO_2 (%)	46.75	47.22	50.36	47.13	48.48	46.32	48.16	49.84	49.41	48.21	51.94	49.25	48.74
TiO_2	2.610	2.620	2.060	2.820	2.240	3.460	2.890	2.640	1.750	2.220	0.361	1.760	1.740
Al_2O_3	8.36	8.11	3.63	6.66	6.81	7.42	4.74	4.04	5.48	6.72	3.99	5.57	5.66
Cr_2O_3	0.005	0.074	0.008	0.037	0.063	0.080	0.051	0.000	0.050	0.037	1.101	0.029	0.000
FeO	7.21	8.28	8.38	7.06	8.44	7.84	7.84	8.39	7.87	7.06	6.33	7.64	6.21
Fe_2O_3	1.263	0.049	0.000	0.967	0.000	0.000	0.472	0.000	0.000	0.000	0.000	0.000	2.183
MnO	0.045	0.289	0.209	0.127	0.118	0.137	0.037	0.135	0.200	0.055	0.136	0.172	0.198
MgO	12.65	12.73	14.19	12.72	12.79	12.05	12.90	13.50	13.01	12.80	17.52	13.25	13.56
CaO	19.68	19.07	19.85	20.68	19.64	20.79	20.65	20.18	19.82	20.46	16.64	20.20	20.44
Na_2O	0.693	0.668	0.388	0.545	0.710	0.449	0.616	0.542	0.694	0.690	0.592	0.623	0.662
K_2O	0.003	0.016	0.000	0.000	0.003	0.016	0.000	0.037	0.010	0.000	0.020	0.002	0.002
Total	99.27	99.12	99.07	98.75	99.29	98.56	98.35	99.30	98.29	98.25	98.63	98.50	99.39
Number of ions on the basis of 4 cations													
Si	1.749	1.770	1.890	1.778	1.814	1.756	1.827	1.871	1.865	1.817	1.918	1.853	1.820
Al^{IV}	0.251	0.230	0.110	0.222	0.186	0.244	0.173	0.129	0.135	0.183	0.082	0.147	0.180
Ti	0.073	0.074	0.058	0.080	0.063	0.099	0.082	0.075	0.050	0.063	0.010	0.050	0.049
Al^{VI}	0.118	0.128	0.051	0.074	0.114	0.087	0.039	0.049	0.109	0.116	0.092	0.100	0.069
Cr	0.000	0.002	0.000	0.001	0.002	0.002	0.002	0.000	0.001	0.001	0.032	0.001	0.000
Fe^{3+}	0.036	0.001	0.000	0.027	0.000	0.000	0.013	0.000	0.000	0.000	0.000	0.000	0.061
Fe^{2+}	0.226	0.259	0.263	0.223	0.264	0.249	0.249	0.263	0.248	0.223	0.195	0.240	0.194
Mn	0.001	0.009	0.007	0.004	0.004	0.004	0.001	0.004	0.006	0.002	0.004	0.005	0.006
Mg	0.706	0.711	0.794	0.715	0.714	0.681	0.730	0.756	0.732	0.719	0.965	0.743	0.755
Ca	0.789	0.766	0.798	0.836	0.787	0.844	0.839	0.812	0.802	0.826	0.658	0.814	0.818
Na	0.050	0.049	0.028	0.040	0.052	0.033	0.045	0.039	0.051	0.050	0.042	0.045	0.048
K	0.000	0.001	0.000	0.000	0.000	0.001	0.000	0.002	0.000	0.000	0.001	0.000	0.000
En (Mg)	**40.2**	**40.7**	**42.6**	**39.6**	**40.3**	**38.3**	**39.8**	**41.2**	**40.9**	**40.6**	**52.9**	**41.2**	**41.2**
Wo (Ca)	**44.9**	**43.8**	**42.9**	**46.3**	**44.5**	**47.5**	**45.8**	**44.2**	**44.8**	**46.7**	**36.1**	**45.2**	**44.6**
Fs (Fe)	**14.9**	**15.5**	**14.5**	**14.1**	**15.1**	**14.2**	**14.4**	**14.6**	**14.2**	**12.7**	**11.0**	**13.6**	**14.3**

APPENDIX II.C: PYROXENE

Sample	SJ32 - Basalt		
Lithotype	Nodule	Nodule	Nodule
Ref.	SJ32-1-PN14	SJ32-1-PB15	SJ32A-2a-PN4
SiO_2 (%)	51.95	51.65	49.86
TiO_2	0.859	0.703	1.335
Al_2O_3	4.04	3.91	4.54
Cr_2O_3	0.515	0.914	0.000
FeO	4.44	6.33	7.73
Fe_2O_3	0.000	0.000	0.256
MnO	0.046	0.109	0.251
MgO	16.33	14.74	13.73
CaO	20.66	19.66	19.75
Na_2O	0.275	0.655	0.658
K_2O	0.000	0.000	0.000
Total	99.11	98.67	98.11
	Number of ions on the basis of 4 cations		
Si	1.915	1.927	1.882
Al^{IV}	0.085	0.073	0.118
Ti	0.024	0.020	0.038
Al^{VI}	0.090	0.099	0.084
Cr	0.015	0.027	0.000
Fe^{3+}	0.000	0.000	0.007
Fe^{2+}	0.137	0.198	0.244
Mn	0.001	0.003	0.008
Mg	0.897	0.820	0.773
Ca	0.816	0.786	0.799
Na	0.020	0.047	0.048
K	0.000	0.000	0.000
En (Mg)	**48.5**	**45.4**	**42.2**
Wo (Ca)	**44.1**	**43.5**	**43.6**
Fs (Fe)	**7.5**	**11.1**	**14.2**

APPENDIX II.D1: OXIDE – SPINEL

Sample	SJ7	SJ8	SJ18		SJ20	SJ29		SJ32			
Lithotype	Plagioclase-bearing basalt	Trachybasalt	Basalt trachyandesite		Basalt	Basalt		Basalt			
Ref.	SJ7-11-XM	SJ8-4-XF	SJ18-3-XF	SJ18-4-XF	SJ21b-12-XM	SJ29-1-XM	SJ29-3-XM	SJ32-9-XFnod	SJ32-16-XFnod	SJ32-20-XM	SJ32a-5-XF
Spinel:	Ti-Mag	Ti-Mag	Ti-Mag	Ti-Mag	Ti-Mag	Ti-Mag	Ti-Mag	Ti-Mag	Ti-Mag	Ti-Mag	Ti-Mag
TiO_2 (%)	19.17	18.76	25.96	24.34	23.73	23.32	23.03	16.76	16.48	21.62	16.24
Al_2O_3	5.940	2.110	2.270	2.190	5.840	1.700	1.950	5.690	7.630	6.050	10.240
MgO	6.450	1.418	2.160	1.660	5.390	3.340	3.350	5.570	5.850	4.930	7.560
MnO	0.4094	0.6431	0.7821	0.7326	0.4743	0.7264	0.6161	0.2919	0.4057	0.4390	0.3193
V_2O_3	0.0000	0.0000	0.0000	0.0000	0.0000	0.0000	0.0000	0.0000	0.0000	0.0000	0.0000
ZnO	0.2358	0.1304	0.0000	0.1391	0.3748	0.1373	0.0244	0.0000	0.1843	0.0000	0.1116
NiO	0.0000	0.0000	0.0000	0.0000	0.0000	0.0263	0.0000	0.0000	0.0122	0.0000	0.0000
FeO	39.70	44.90	51.75	49.97	44.13	47.35	46.31	38.95	38.39	43.80	35.86
Fe_2O_3	27.81	27.50	17.19	17.99	16.34	23.11	21.00	31.81	28.05	20.71	28.24
Cr_2O_3	0.1087	0.0186	0.0000	0.0000	0.1249	0.3251	0.5058	0.0700	2.4800	0.2684	0.0406
Total	99.83	95.49	100.10	97.02	96.40	100.03	96.79	99.14	99.48	97.81	98.61
			Number of ions on the basis of 32 O								
Ti	4.04	4.37	5.70	5.54	5.18	5.11	5.20	3.59	3.47	4.68	3.37
Al	1.96	0.77	0.78	0.78	2.00	0.58	0.69	1.91	2.52	2.05	3.33
Mg	2.69	0.65	0.94	0.75	2.33	1.45	1.50	2.36	2.44	2.11	3.11
Mn	0.097	0.169	0.193	0.188	0.117	0.179	0.157	0.070	0.096	0.107	0.075
V	0.000	0.000	0.000	0.000	0.000	0.000	0.000	0.000	0.000	0.000	0.000
Zn	0.049	0.030	0.000	0.031	0.080	0.030	0.005	0.000	0.038	0.000	0.023
Ni	0.000	0.000	0.000	0.000	0.000	0.006	0.000	0.000	0.003	0.000	0.000
Fe^{2+}	9.30	11.63	12.63	12.64	10.71	11.53	11.62	9.28	9.00	10.54	8.27
Fe^{3+}	5.87	6.41	3.78	4.10	3.57	5.07	4.74	6.82	5.91	4.48	5.86
Cr	0.024	0.005	0.000	0.000	0.029	0.075	0.120	0.016	0.549	0.061	0.009

APPENDIX II.D1: OXIDE – SPINEL

Sample	SJ49	SJ55	SJ70				SJ77		SJ91	D17	
Lithotype	Basalt	Tefrite	Basalt				Basanite		Trachybasalt	Basalt	
Ref.	SJ49-13-XM	SJ55-2-XM	SJ70-1-XM	SJ70-2-XM	SJ70-3-XM	SJ70-4-XM	SJ77-18-XM	SJ77-19-XM	SJ91-25-XF	D17-19-X(ol)	D17-20-XM
Spinel:	Ti-Mag	Ti-Mag	Ti-Mag	Ti-Mag	Crom	Crom	Ti-Mag	Ti-Mag	Mag	Crom	Crom
TiO_2 (%)	21.37	24.10	21.10	21.70	1.98	1.53	21.97	23.17	1.58	8.11	6.83
Al_2O_3	2.560	1.181	2.590	3.000	19.700	13.590	2.070	2.040	1.726	17.710	19.800
MgO	2.910	1.292	1.350	1.980	13.630	8.990	3.600	4.090	4.080	9.480	9.310
MnO	0.5751	0.6501	0.6775	0.6290	0.2359	0.2692	0.6602	0.5849	1.0374	0.3631	0.3090
V_2O_3	0.0000	0.0000	0.0000	0.0000	0.0000	0.0229	0.0000	0.0000	0.6154	0.0000	0.0000
ZnO	0.1031	0.2572	0.0406	0.0488	0.1163	0.0246	0.0731	0.0403	0.1122	0.0166	0.2757
NiO	0.0141	0.0161	0.0628	0.0000	0.1357	0.0204	0.0426	0.0000	0.1445	0.0951	0.0000
FeO	45.11	50.00	45.96	47.14	15.17	20.71	45.72	45.42	26.81	26.37	26.12
Fe_2O_3	22.50	19.00	19.80	21.38	10.30	7.66	25.07	21.16	65.36	16.28	14.25
Cr_2O_3	0.3046	0.1571	0.0888	0.2768	37.3300	44.6300	0.2663	0.5432	0.4508	19.0600	21.8400
Total	95.44	96.66	91.67	96.16	98.60	97.45	99.47	97.05	101.91	97.49	98.74
Number of ions on the basis of 32 O											
Ti	4.90	5.55	5.08	4.96	0.37	0.31	4.83	5.18	0.35	1.61	1.33
Al	0.92	0.43	0.98	1.07	5.85	4.31	0.71	0.72	0.59	5.52	6.05
Mg	1.32	0.59	0.64	0.90	5.12	3.61	1.57	1.81	1.77	3.74	3.60
Mn	0.148	0.169	0.184	0.162	0.050	0.061	0.163	0.147	0.255	0.081	0.068
V	0.000	0.000	0.000	0.000	0.000	0.005	0.000	0.000	0.143	0.000	0.000
Zn	0.023	0.058	0.010	0.011	0.022	0.005	0.016	0.009	0.024	0.003	0.053
Ni	0.003	0.004	0.016	0.000	0.027	0.004	0.010	0.000	0.034	0.020	0.000
Fe^{2+}	11.49	12.81	12.31	11.97	3.19	4.66	11.17	11.30	6.52	5.83	5.66
Fe^{3+}	5.16	4.38	4.77	4.89	1.95	1.55	5.51	4.74	14.30	3.24	2.78
Cr	0.073	0.038	0.022	0.066	7.431	9.495	0.061	0.128	0.104	3.983	4.476

APPENDIX II.D1: OXIDE – SPINEL

Sample	SJ107				
Lithotype	Trachybasalt				
Ref.	SJ107-7-X(anf)	SJ107-8-XM	SJ107-9-XC	SJ107-10-XC	SJ107-11-XM
Spinel:	Ti-Mag	Ti-Mag	Ti-Mag	Ti-Mag	Ti-Mag
TiO_2 (%)	16.85	17.54	21.31	21.42	22.03
Al_2O_3	6.390	6.510	5.790	3.980	4.040
MgO	8.050	5.160	5.950	5.400	4.910
MnO	0.4548	0.5578	0.5723	1.0622	0.6232
V_2O_3	0.0000	0.0000	0.0000	0.0000	0.0000
ZnO	0.0000	0.0000	0.0320	0.3031	0.0559
NiO	0.0000	0.0223	0.0223	0.0000	0.0000
FeO	34.68	40.05	40.67	41.08	43.22
Fe_2O_3	30.96	28.94	20.10	22.72	21.60
Cr_2O_3	0.1929	0.1210	0.0518	0.0206	0.0103
Total	97.58	98.90	94.50	95.98	96.49
Number of ions on the basis of 32 O					
Ti	3.58	3.76	4.73	4.75	4.88
Al	2.13	2.18	2.01	1.38	1.40
Mg	3.39	2.19	2.62	2.38	2.15
Mn	0.109	0.135	0.143	0.265	0.155
V	0.000	0.000	0.000	0.000	0.000
Zn	0.000	0.000	0.007	0.066	0.012
Ni	0.000	0.005	0.005	0.000	0.000
Fe^{2+}	8.20	9.54	10.04	10.14	10.64
Fe^{3+}	6.59	6.20	4.46	5.04	4.79
Cr	0.043	0.027	0.012	0.005	0.002

APPENDIX II.D2: OXIDE – ILMENITE

Sample	SJ20		SJ29	SJ32	SJ55	SJ91	
Lithotype	Basalt		Basalt	Basalt	Tefrite	Trachybasalt	
Ref.	SJ21A-5-XF(nod)	SJ21A-6-XF(nod)	SJ29-2-XM	SJ32-19-XF	SJ55-1-XM	SJ91-26-XF	SJ91-27-XF
SiO_2 (%)	0.003	0.053	0.093	0.032	0.075	0.098	0.130
TiO_2	49.360	49.610	49.440	46.390	50.510	34.930	37.260
Al_2O_3	0.975	0.886	0.147	0.921	0.041	0.322	0.267
MgO	7.720	8.180	4.920	6.010	1.635	5.620	2.330
MnO	0.261	0.306	0.710	0.406	0.888	1.152	0.316
V_2O_3	0.000	0.000	0.000	0.000	0.000	0.000	0.000
ZnO	0.000	0.138	0.065	0.113	0.000	0.041	0.000
NiO	0.000	0.000	0.047	0.000	0.000	0.000	0.004
FeO	30.375	29.672	33.662	30.540	40.532	20.314	28.559
Fe_2O_3	10.819	9.511	10.133	15.369	5.377	36.370	28.618
Cr_2O_3	0.119	0.140	0.000	0.067	0.000	0.146	0.052
CaO	0.000	0.000	0.230	0.000	0.203	0.000	0.110
Na_2O	0.000	0.000	0.000	0.000	0.000	0.000	0.000
Total	99.63	98.50	99.45	99.85	99.26	98.99	97.65
Number of ions on the basis of 4 cations							
Si	0.000	0.003	0.005	0.002	0.004	0.005	0.007
Ti	1.83	1.85	1.88	1.77	1.95	1.47	1.59
Al	0.06	0.05	0.01	0.06	0.00	0.02	0.02
Mg	0.57	0.60	0.37	0.46	0.12	0.47	0.20
Mn	0.011	0.013	0.030	0.017	0.039	0.055	0.015
V	0.000	0.000	0.000	0.000	0.000	0.000	0.000
Zn	0.000	0.005	0.002	0.004	0.000	0.002	0.000
Ni	0.000	0.000	0.002	0.000	0.000	0.000	0.000
Fe^{2+}	1.26	1.23	1.43	1.30	1.74	0.95	1.35
Fe^{3+}	0.40	0.35	0.39	0.59	0.21	1.53	1.22
Cr	0.005	0.005	0.000	0.003	0.000	0.006	0.002
Ca	0.000	0.000	0.012	0.000	0.011	0.000	0.007
Na	0.000	0.000	0.000	0.000	0.000	0.000	0.000

APPENDIX II.E: AMPHIBOLE

Sample	SJ107							SJ32		
Lithotype	Trachybasalt							Basalt		
Ref.	SJ107-2-AN1	SJ107-2-AB2	SJ107-2-AC3	SJ107-2-AC4	SJ107-2-AN5	SJ107-1-AN12	SJ107-1-AB13	SJ32-4-A10	SJ32-4-A11	SJ32-4-A13
SiO_2 (%)	40.38	40.08	40.29	40.16	40.15	40.27	40.74	40.32	40.50	40.28
TiO_2	5.52	5.73	5.76	5.78	5.36	5.72	5.65	5.54	5.82	5.47
Al_2O_3	12.51	12.96	12.95	13.00	12.83	12.85	12.97	12.66	12.75	12.55
Cr_2O_3	0.00	0.00	0.00	0.00	0.00	0.00	0.00	0.00	0.00	0.00
Fe_2O_3	1.91	1.81	0.00	0.00	1.97	0.00	0.96	0.00	0.54	0.00
FeO	11.02	9.98	9.26	9.09	11.58	9.69	11.61	9.76	9.46	9.86
MnO	0.11	0.08	0.12	0.15	0.11	0.19	0.13	0.11	0.14	0.23
MgO	12.24	12.46	12.32	11.97	11.81	11.67	11.80	12.62	12.37	12.76
CaO	10.64	10.36	10.86	11.12	10.58	10.77	10.71	10.94	11.05	10.91
Na_2O	2.74	2.80	2.68	2.75	2.85	2.77	2.78	2.68	2.66	2.71
K_2O	0.78	0.77	0.78	0.80	0.77	0.77	0.76	0.72	0.73	0.71
Total	97.85	97.03	95.02	94.82	98.00	94.69	98.12	95.35	96.02	95.48
Number of ions on the basis of 23 O										
Si	5.97	5.95	6.05	6.05	5.95	6.08	6.00	6.05	6.06	6.02
Al^{IV}	2.03	2.05	1.95	1.95	2.05	1.92	2.00	0.00	1.95	1.94
Al^{VI}	0.19	0.25	0.35	0.36	0.23	0.37	0.28	0.29	0.31	0.25
Ti	0.61	0.64	0.65	0.65	0.60	0.65	0.63	0.63	0.66	0.62
Cr	0.00	0.00	0.00	0.00	0.00	0.00	0.00	0.00	0.00	0.00
Fe^{3+}	0.21	0.20	0.00	0.00	0.22	0.00	0.11	0.00	0.00	0.06
Fe^{2+}	1.36	1.24	1.16	1.15	1.43	1.22	1.43	1.23	1.18	1.23
Mn	0.014	0.010	0.015	0.019	0.013	0.024	0.017	0.014	0.018	0.030
Mg	2.70	2.76	2.76	2.69	2.61	2.63	2.59	2.82	2.76	2.84
Ca	1.69	1.65	1.75	1.80	1.68	1.74	1.69	1.76	1.77	1.75
Na(M4)	0.18	0.23	0.25	0.20	0.19	0.26	0.24	0.24	0.23	0.22
Na(A)	0.61	0.58	0.53	0.60	0.64	0.55	0.55	0.54	0.54	0.57
K	0.15	0.15	0.15	0.15	0.14	0.15	0.14	0.14	0.14	0.14
#Mg	0.66	0.69	0.70	0.70	0.65	0.68	0.64	0.70	0.70	0.70

APPENDIX III: Isotope Formula

An isotope of an element is an atom whose nucleus contains the same number of protons but a different number of neutrons. The unstable or radiogenic isotopes form due to unstable nucleus of a parent element that stabilizes itself by emitting ionizing radiation during decay to a daughter element.

The isotope pairs used in this study are Rb-Sr, Sm-Nd, Th-U-Pb and Lu-Hf and their composition can be expressed by the following equations:

(III. 1) $$\left(\frac{^{87}Sr}{^{86}Sr}\right)=\left(\frac{^{87}Sr}{^{86}Sr}\right)_0+\frac{^{87}Rb}{^{86}Sr}\left(e^{\lambda t}-1\right)$$

(III. 2) $$\left(\frac{^{143}Nd}{^{144}Nd}\right)=\left(\frac{^{143}Nd}{^{144}Nd}\right)_i+\frac{^{147}Sm}{^{144}Nd}\left(e^{\lambda t}-1\right)$$

(III. 3) $$\left(\frac{^{206}Pb}{^{204}Pb}\right)=\left(\frac{^{206}Pb}{^{204}Pb}\right)_i+\frac{^{238}U}{^{204}Pb}\left(e^{\lambda_1 t}-1\right)$$

(III. 4) $$\left(\frac{^{207}Pb}{^{204}Pb}\right)=\left(\frac{^{207}Pb}{^{204}Pb}\right)_i+\frac{^{235}U}{^{204}Pb}\left(e^{\lambda_2 t}-1\right)$$

(III. 5) $$\left(\frac{^{208}Pb}{^{204}Pb}\right)=\left(\frac{^{208}Pb}{^{204}Pb}\right)_i+\frac{^{232}Th}{^{204}Pb}\left(e^{\lambda_3 t}-1\right)$$

(III. 6) $$\left(\frac{^{176}Hf}{^{177}Hf}\right)=\left(\frac{^{176}Hf}{^{177}Hf}\right)_i+\frac{^{176}Lu}{^{177}Hf}\left(e^{\lambda t}-1\right)$$

The previous equations have the same format, so using Rb-Sr isotopic system as an example, the members of the equations are: $\left(\frac{^{87}Sr}{^{86}Sr}\right)$, the present isotopsic composition of the lava, $\left(\frac{^{87}Sr}{^{86}Sr}\right)_i$, the isotopic composition of the lava at the time of formation and $\left(\frac{^{87}Rb}{^{86}Sr}\right)$ is the parent/daughter isotope ratio of the lava at present time. The λ is the constant decay of each isotope and t is the time since the formation of the lava, which are presented in Supplement Table 3.

Supplement Table 3 – Constant decays and halflives of the isotopes foucoused in theis study.

Father	Daughter	decay constant (y^{-1})	Half-live (y)
^{87}Rb	^{87}Sr	$\lambda=1.42*10^{-11}$	$48.800*10^{9}$
^{147}Sm	^{143}Nd	$\lambda=6.54*10^{-12}$	$1.06*10^{11}$
^{238}U	^{206}Pb	$\lambda_1=1.55125*10^{-10}$	$4.4680*10^{9}$
^{235}U	^{207}Pb	$\lambda_2=9.84850*10^{-10}$	$0.7038*10^{9}$
^{232}Th	^{208}Pb	$\lambda_3=4.94750*10^{-11}$	$14.010*10^{9}$
^{176}Lu	^{176}Hf	$\lambda=1.94*10^{-11}$	$35.7*10^{9}$

The north Hemisphere Reference Line (NHRL) is presented in the text and plotted in the lead diagrams. This line is defined by the equations:

(III. 7) $$^{207}Pb/^{204}Pb = 0.1084 *(^{206}Pb/^{204}Pb) + 13.491$$

(III. 8) $$^{208}Pb/^{204}Pb = 1.209 *(^{206}Pb/^{204}Pb) + 15.627$$

The deviation of the isotopic composition of the lavas in relation with the NHRL is given by:

(III. 9) $$\Delta 7/4 = \left[\left(^{207}Pb/^{204}Pb\right)_{sample} - \left(^{207}Pb/^{204}Pb\right)_{NHRL}\right] * 100$$

(III. 10) $$\Delta 8/4 = \left[\left(^{208}Pb/^{204}Pb\right)_{sample} - \left(^{208}Pb/^{204}Pb\right)_{NHRL}\right] * 100$$

The μ value is $\mu_{206} = \frac{^{238}U}{^{204}Pb}$ but it can be calculated by transforming equation (III. 3) into:

(III. 11) $$\mu_{206} = \frac{\left(^{206}Pb/^{204}Pb\right)_{sample} - \left(^{206}Pb/^{204}Pb\right)_{primeval}}{e^{\lambda_1 T} - e^{\lambda_1 t}}$$

Where $\left(^{206}Pb/^{204}Pb\right)_{primeval}$ is the isotopic composition of Canyon Diablo meteorite, considered to have the primeval isotopic composition of the earth (Tatsumoto *et al*., 1973, in Feaure & Mensing, 1995), according with the values in Supplement Table 4

Supplement Table 4 – Isotope ratios of Primeval lead in Troilite of the iron Meteorite Canyon Diablo (Tatsumoto *et al*., 1973, *in* Feaure & Mensing, 1995).

Canyon del Diablo		
$\left(^{206}Pb/^{204}Pb\right)$	$\left(^{207}Pb/^{204}Pb\right)$	$\left(^{208}Pb/^{204}Pb\right)$
9,307	10,294	29,487

The time integrated value of Th/U ratio is estimated for the age of the earth i.e. T=4.55Ga, combining equations (III. 3) and (III. 5):

(III. 12) $$\kappa_{Pb} = \left(\frac{^{208}Pb}{^{206}Pb}\right)^{*} * \frac{\left(e^{\lambda_1 t} - 1\right)}{\left(e^{\lambda_3 t} - 1\right)}$$

where

(III. 13) $$\left(\frac{^{208}Pb}{^{206}Pb}\right)^{*} = \frac{\left(^{208}Pb/^{204}Pb\right)_{sample} - \left(^{208}Pb/^{204}Pb\right)_{primeval}}{\left(^{206}Pb/^{204}Pb\right)_{sample} - \left(^{206}Pb/^{204}Pb\right)_{primeval}}$$

APPENDIX IV: Modeling Isotopes

In this appendix are presented the parameters and the method used to model Hf, Nd and Pb isotopes, which were presented in Chapter 10.

The first model combines the geochemical composition and isotope signature of Sm, Nd, Lu and Hf, of MORB with three different sediments during a subduction event at 1 Ga ago.

The second model shows the evolution of an ancient magmatic liquid that fertilized the mantle beneath the region located west and southwest of Ponta dos Rosais. Signals of this fertilization are present on the lavas located on the west side of São Jorge island and become diluted towards the east side. This model uses Hf and Nd geochemical and isotopic composition of an ancient primitive mantle that produces a melt at 3 (or 2) Ga ago, which mixes with a depleted source that should correspond to the common mantle component. The third model uses Th, U and Pb isotopic compositions to model the ancient magmatic liquid, in order to see if these isotope systems are coupled with Hf and Nd.

APPENDIX IV.A: Hf-Nd Model for Subducted Sediments

Model for subduction of MORB and terrigenous sediments at 1Ga ago.

MORB present day

$^{176}Hf/^{177}Hf$= 0.283267

$^{143}Nd/^{144}Nd$= 0.513151

Composition

Nd=9.550ppm; Sm=3.113ppm;

Hf=2.284ppm; Lu=0.454ppm

Bulk crust (25%N-MORB+25%altered MORB+50%gabbro)

Turbidite present day

$^{176}Hf/^{177}Hf$= 0.281471

$^{143}Nd/^{144}Nd$= 0.511320

Composition

Nd=16.000ppm; Sm=2.540ppm;

Hf=5.110ppm; Lu=0.170ppm

(V29-20-S (cc10-S), Vervoort *et al.*, 1999)

Subduction at 1 Ga

MORB alteration (after Kogiso et al., 1997)

Sediment-melt alteration (Johnson and Plank, 1999).

MORB

$^{176}Hf/^{177}Hf$= 0.282714

$^{143}Nd/^{144}Nd$= 0.511857

Composition

Nd=7.449ppm; Sm=2.690ppm;

Hf=1.781ppm; Lu=0.449ppm

Turbidite

$^{176}Hf/^{177}Hf$= 0.281378

$^{143}Nd/^{144}Nd$= 0.510690

Composition

Nd=12.68ppm; Sm=2.02ppm;

Hf=2.80ppm; Lu=0.140ppm

Subducted MORB mixes with different proportions of sediments (0%, 2%, 4%, 6%, 8%, 10%, 20%, 100%)

Present day Isotopic Composition

Percentage of sediments	εNd	εHf
0%	12.717	22.760
2%	11.427	20.666
4%	10.173	18.619
6%	8.953	16.618
8%	7.765	14.661
10%	6.609	12.746
20%	1.254	3.764
100%	-25.671	-44.488

APPENDIX 4.2: Model for subduction of MORB and pelagic sediments at 1Ga ago.

MORB present day

$^{176}Hf/^{177}Hf$= 0.283267

$^{143}Nd/^{144}Nd$= 0.513151

Composition

Nd=9.550ppm; Sm=3.113ppm;

Hf=2.284ppm; Lu=0.454ppm

Bulk crust (25%N-MORB+25%altered MORB+50%gabbro)

Shale present day

$^{176}Hf/^{177}Hf$= 0.281795

$^{143}Nd/^{144}Nd$= 0.511231

Composition

Nd=32.48ppm; Sm=6.00ppm;

Hf=3.71ppm; Lu=0.32ppm

(BW-SA.1, Vervoort *et al.*, 1999)

Subduction at 1 Ga

MORB alteration (after Kogiso et al., 1997)

Sediment-melt alteration (Johnson and Plank, 1999).

MORB

$^{176}Hf/^{177}Hf$= 0.282714

$^{143}Nd/^{144}Nd$= 0.511857

Composition

Nd=7.449ppm; Sm=2.690ppm;

Hf=1.781ppm; Lu=0.449ppm

Shale

$^{176}Hf/^{177}Hf$= 0.281555

$^{143}Nd/^{144}Nd$= 0.510498

Composition

Nd=25.75ppm; Sm=4.77ppm;

Hf=2.04ppm; Lu=0.26ppm

Subducted MORB mixes with different proportions of sediments (0%, 2%, 4%, 6%, 8%, 10%, 20%, 100%)

Present day Isotopic Composition

Percentage of sediments	εNd	εHf
0%	12.717	22.760
2%	10.073	21.543
4%	7.666	20.333
6%	5.465	19.130
8%	3.445	17.934
10%	1.584	16.745
20%	-5.881	10.897
100%	-27.401	-30.608

Model for subduction of MORB and GLOSSb at 1Ga ago.

MORB present day

$^{176}Hf/^{177}Hf$= 0.283267

$^{143}Nd/^{144}Nd$= 0.513151

Composition

Nd=9.550ppm; Sm=3.113ppm;

Hf=2.284ppm; Lu=0.454ppm

Bulk crust (25%N-MORB+25%altered MORB+50%gabbro)

GLOSS present day

$^{176}Hf/^{177}Hf$= 0.282283

$^{143}Nd/^{144}Nd$= 0.51218

Composition

Nd=27.00ppm; Sm=5.78ppm;

Hf=4.06ppm; Lu=0.41ppm

(Plank & Langmuir 1998)

Subduction at 1 Ga

MORB alteration (after Kogiso et al., 1997)

Sediment-melt alteration (Johnson and Plank, 1999).

MORB

$^{176}Hf/^{177}Hf$= 0.282714

$^{143}Nd/^{144}Nd$= 0.511857

Composition

Nd=7.449ppm; Sm=2.690ppm;

Hf=1.781ppm; Lu=0.449ppm

GLOSS

$^{176}Hf/^{177}Hf$= 0.282000

$^{143}Nd/^{144}Nd$= 0.511331

Composition

Nd=21.40ppm; Sm=4.60ppm;

Hf=2.23ppm; Lu=0.33ppm

Subducted MORB mixes with different proportions of sediments (0%, 2%, 4%, 6%, 8%, 10%, 20%, 100%)

Present day Isotopic Composition

Percentage of sediments	εNd	εHf
0%	12.717	22.760
2%	11.520	21.879
4%	10.407	21.006
6%	9.369	20.142
8%	8.399	19.286
10%	7.490	18.439
20%	3.687	14.324
100%	-27.401	-30.608

APPENDIX IV.B: H-Nd Model for an Ancient Source (3 to 2Ga)

Model using Hf and Nd isotopes for an ancient melting liquid, which was generated during a melting event at 2 or 3 Ga ago, from a depleted residue. In this, flowchart is presented the melting parameters and source compositions and in the next is presented the isotopic evolution.

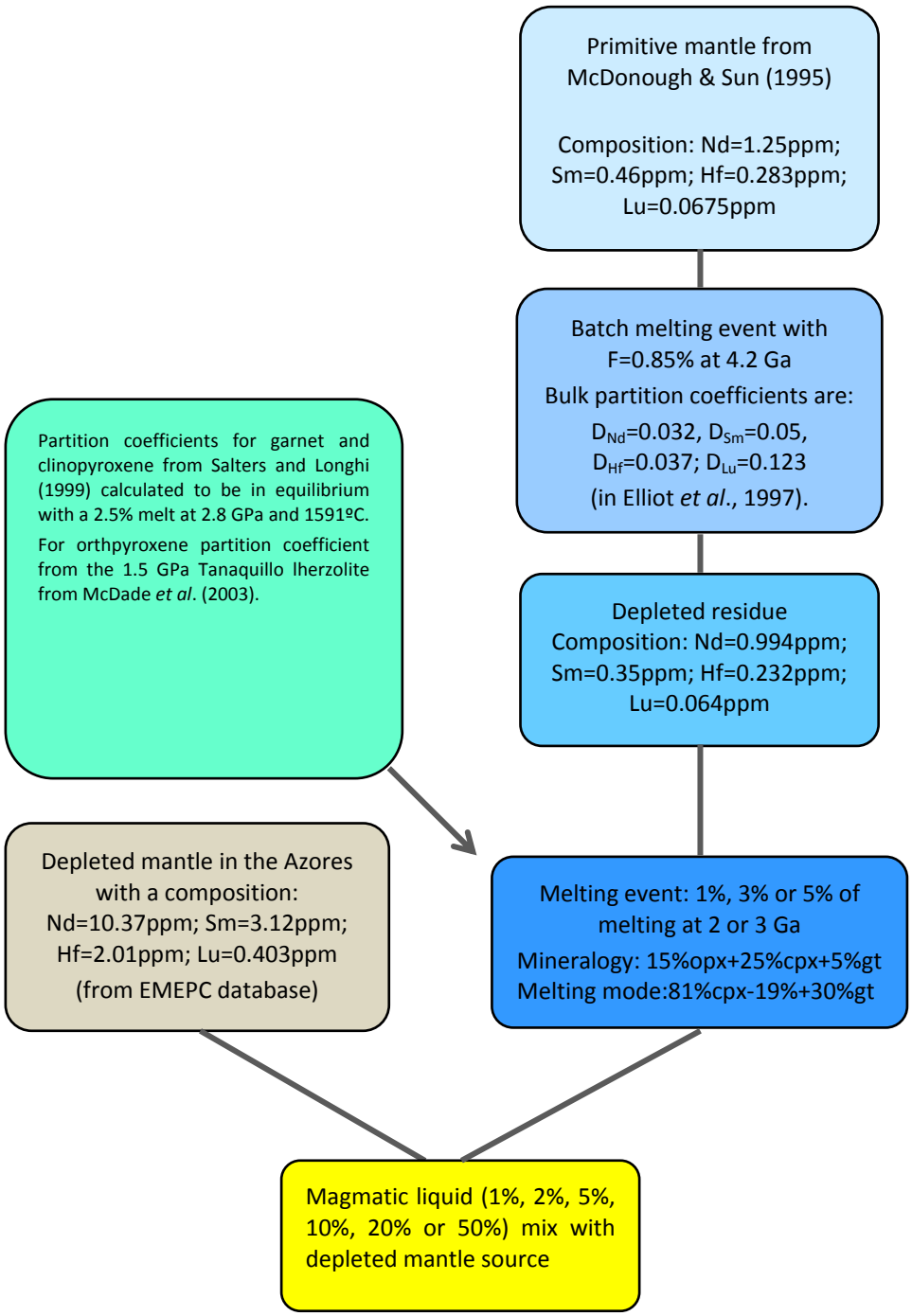

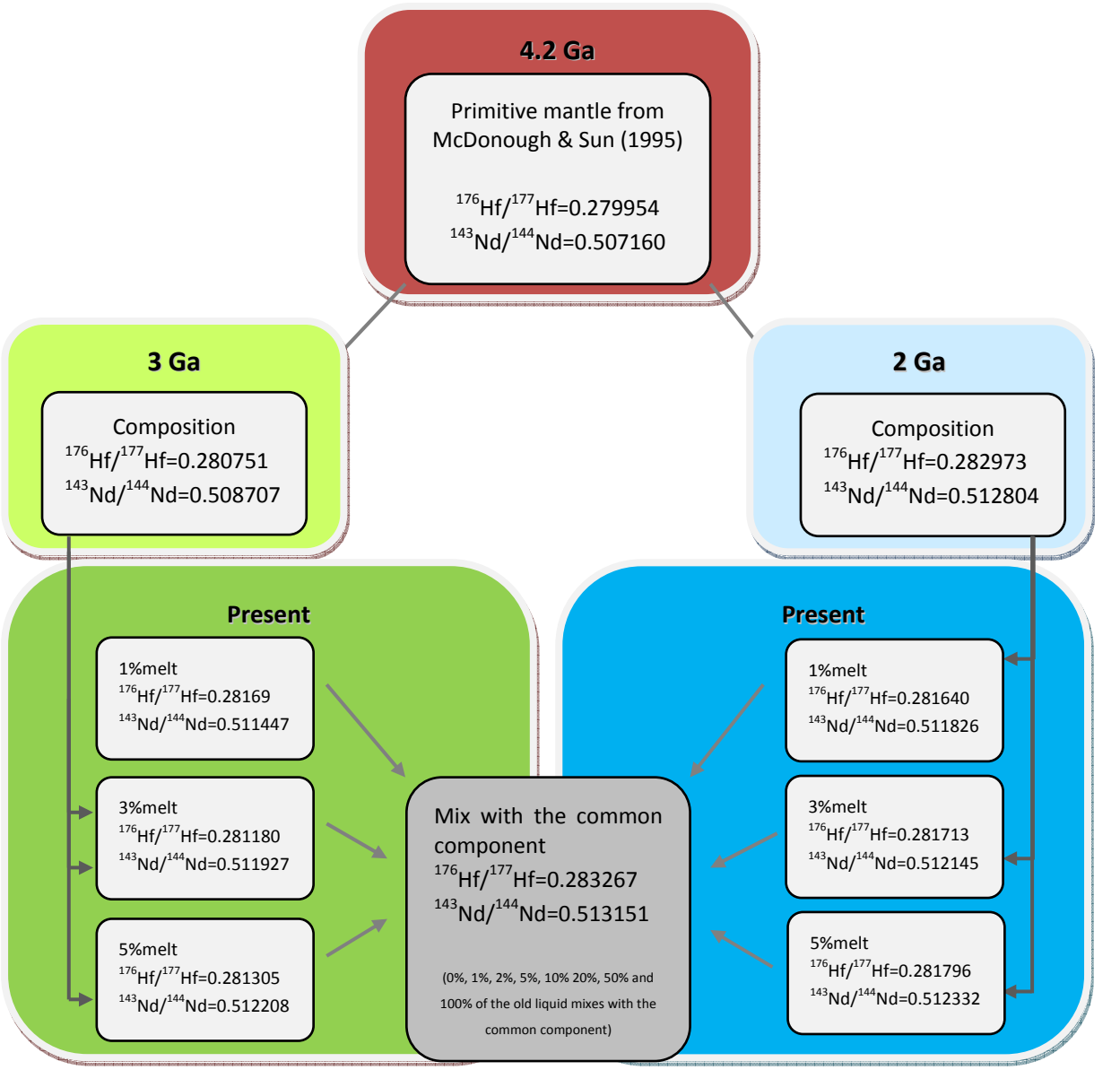

3Ga (1% melt)		3Ga (3% melt)		3Ga (5% melt)	
εNd	εHf	εNd	εHf	εNd	εHf
10.00	17.50	10.00	17.50	10.00	17.50
9.01	16.02	9.55	16.38	9.76	16.67
8.05	14.57	9.10	15.28	9.52	15.84
5.40	10.36	7.81	12.04	8.80	13.37
1.58	3.83	5.80	6.84	7.65	9.33
-4.38	-7.72	2.26	-2.81	5.43	1.48
-15.03	-33.61	-5.70	-27.01	-0.47	-20.36
-23.23	-60.22	-13.88	-56.31	-8.39	-51.87

2Ga (1% melt)		2Ga (3% melt)		2Ga (5% melt)	
εNd	εHf	εNd	εHf	εNd	εHf
10.00	17.50	10.00	17.50	10.00	17.50
9.23	16.40	9.63	16.67	9.78	16.85
8.49	15.33	9.26	15.85	9.56	16.20
6.42	12.22	8.20	13.43	8.90	14.28
3.46	7.38	6.55	9.57	7.85	11.13
-1.18	-1.16	3.64	2.38	5.86	5.08
-9.46	-20.33	-2.90	-15.63	0.68	-11.45
-15.83	-40.02	-9.61	-37.44	-5.97	-34.51

APPENDIX IV.C: Th-U-Pb model for the ancient source (3 to 2Ga)

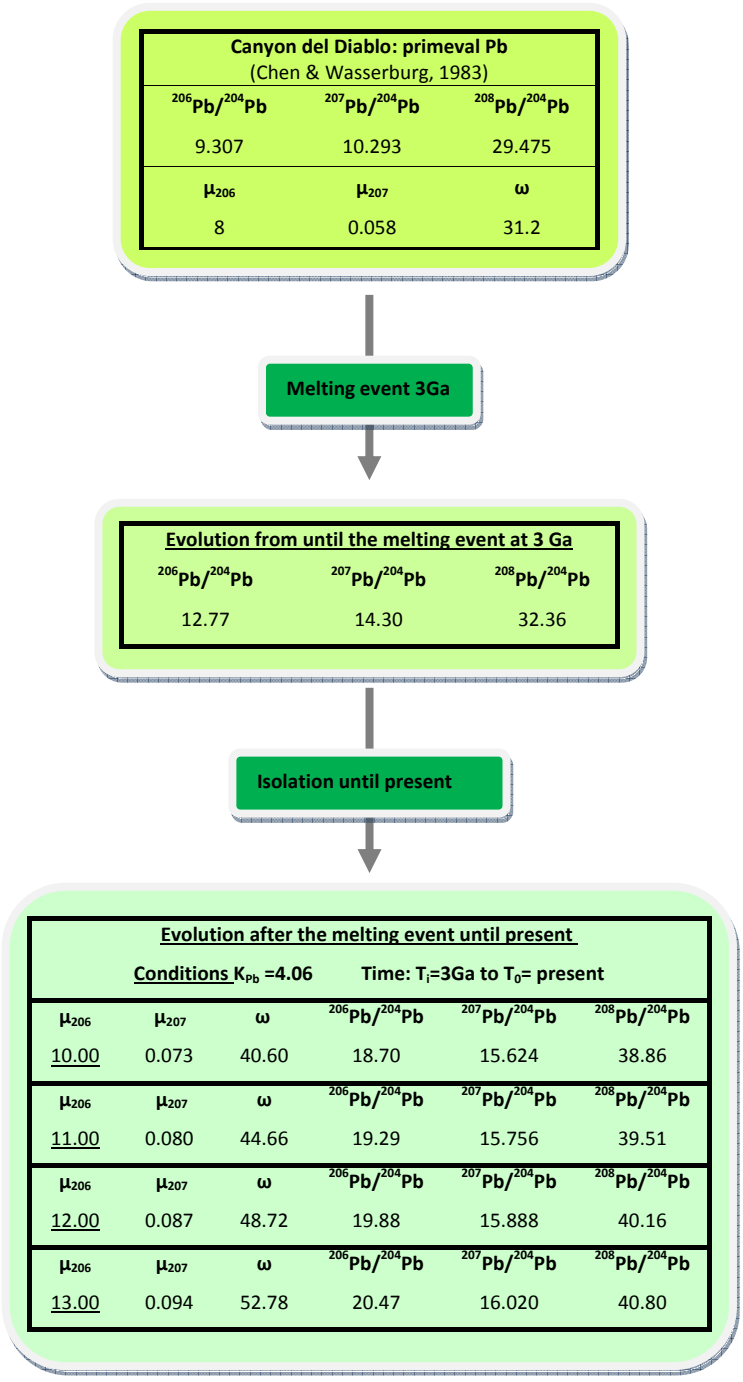

Evolution after the melting event until present

Conditions K_{Pb} =4.06 **Time: T_i=3Ga to T_0= present**

μ_{206}	μ_{207}	ω	$^{206}Pb/^{204}Pb$	$^{207}Pb/^{204}Pb$	$^{208}Pb/^{204}Pb$
10.00	0.073	40.60	18.70	15.624	38.86
μ_{206}	μ_{207}	ω	$^{206}Pb/^{204}Pb$	$^{207}Pb/^{204}Pb$	$^{208}Pb/^{204}Pb$
11.00	0.080	44.66	19.29	15.756	39.51
μ_{206}	μ_{207}	ω	$^{206}Pb/^{204}Pb$	$^{207}Pb/^{204}Pb$	$^{208}Pb/^{204}Pb$
12.00	0.087	48.72	19.88	15.888	40.16
μ_{206}	μ_{207}	ω	$^{206}Pb/^{204}Pb$	$^{207}Pb/^{204}Pb$	$^{208}Pb/^{204}Pb$
13.00	0.094	52.78	20.47	16.020	40.80

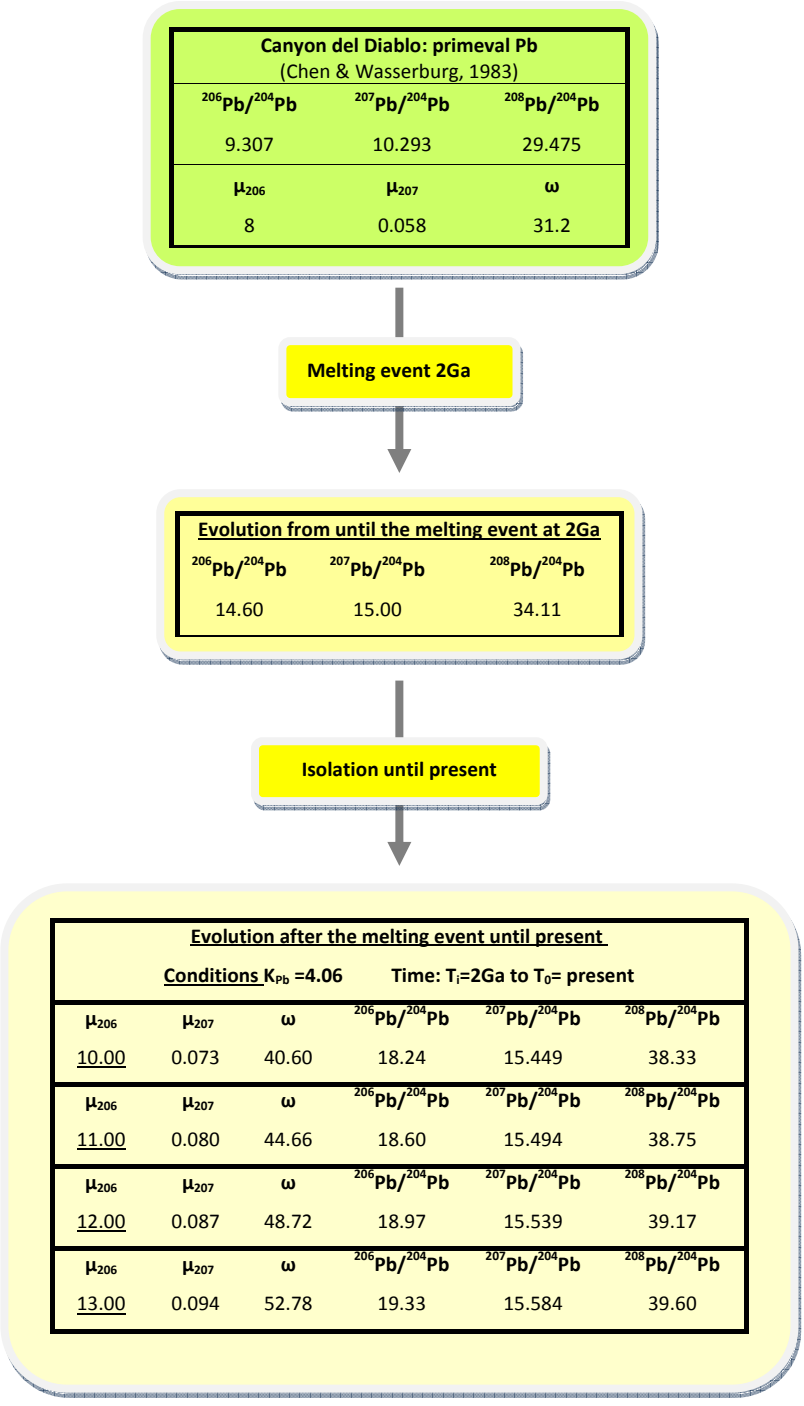
Canyon del Diablo: primeval Pb
(Chen & Wasserburg, 1983)
206Pb/204Pb
207Pb/204Pb
208Pb/204Pb
9.307
10.293
29.475
μ206
μ207
ω
8
0.058
31.2
Melting event 2Ga
Evolution from until the melting event at 2Ga
206Pb/204Pb
207Pb/204Pb
208Pb/204Pb
14.60
15.00
34.11
Isolation until present
Evolution after the melting event until present
Conditions KPb =4.06
Time: Ti=2Ga to T0= present
μ206 μ207 ω 206Pb/204Pb 207Pb/204Pb 208Pb/204Pb
10.00 0.073 40.60 18.24 15.449 38.33
μ206 μ207 ω 206Pb/204Pb 207Pb/204Pb 208Pb/204Pb
11.00 0.080 44.66 18.60 15.494 38.75
μ206 μ207 ω 206Pb/204Pb 207Pb/204Pb 208Pb/204Pb
12.00 0.087 48.72 18.97 15.539 39.17
μ206 μ207 ω 206Pb/204Pb 207Pb/204Pb 208Pb/204Pb
13.00 0.094 52.78 19.33 15.584 39.60

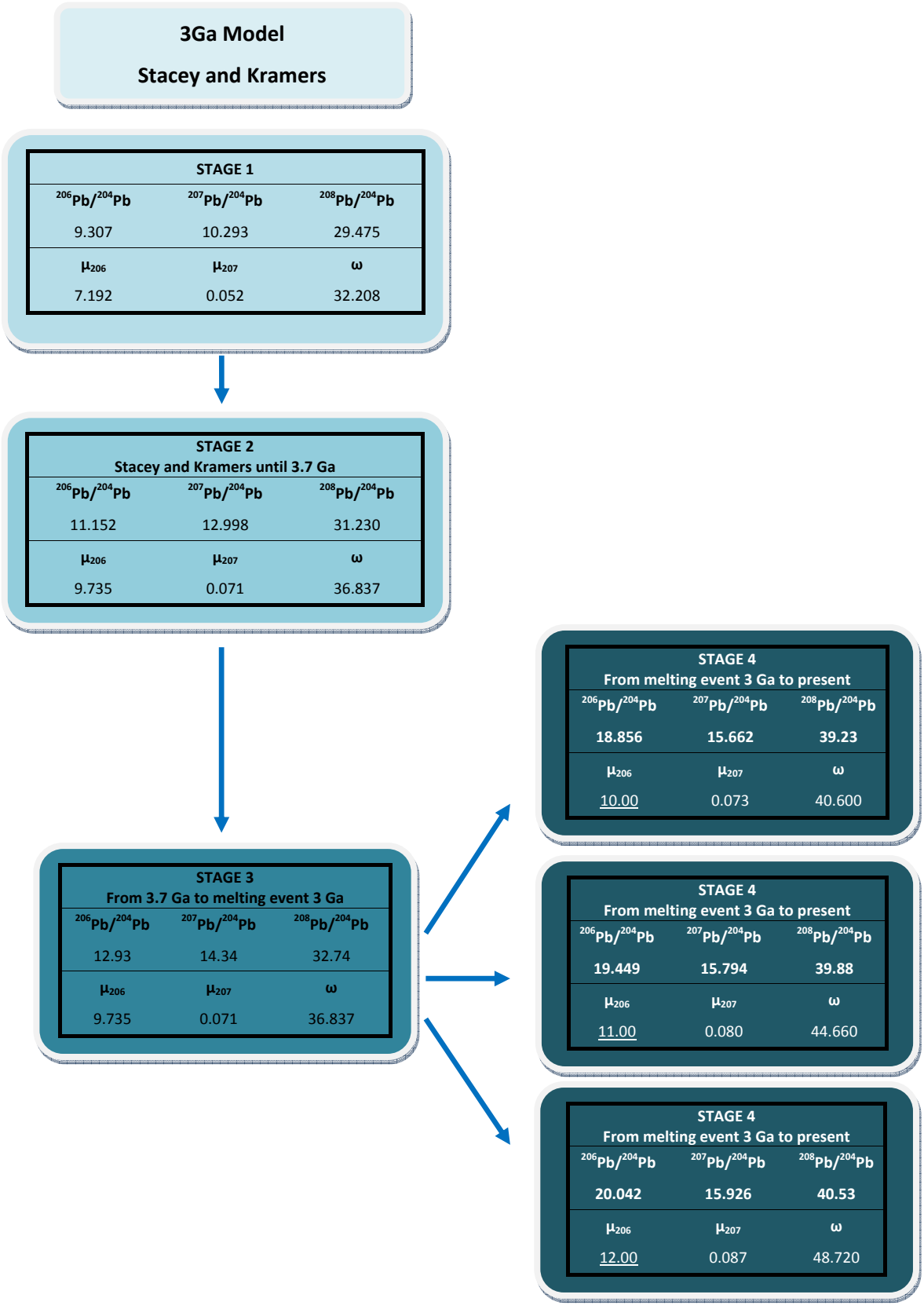
3Ga Model
Stacey and Kramers
STAGE 1
206Pb/204Pb 207Pb/204Pb 208Pb/204Pb
9.307 10.293 29.475
μ206 μ207 ω
7.192 0.052 32.208
STAGE 2
Stacey and Kramers until 3.7 Ga
206Pb/204Pb 207Pb/204Pb 208Pb/204Pb
11.152 12.998 31.230
μ206 μ207 ω
9.735 0.071 36.837
STAGE 3
From 3.7 Ga to melting event 3 Ga
206Pb/204Pb 207Pb/204Pb 208Pb/204Pb
12.93 14.34 32.74
μ206 μ207 ω
9.735 0.071 36.837
STAGE 4
From melting event 3 Ga to present
206Pb/204Pb 207Pb/204Pb 208Pb/204Pb
18.856 15.662 39.23
μ206 μ207 ω
10.00 0.073 40.600
STAGE 4
From melting event 3 Ga to present
206Pb/204Pb 207Pb/204Pb 208Pb/204Pb
19.449 15.794 39.88
μ206 μ207 ω
11.00 0.080 44.660
STAGE 4
From melting event 3 Ga to present
206Pb/204Pb 207Pb/204Pb 208Pb/204Pb
20.042 15.926 40.53
μ206 μ207 ω
12.00 0.087 48.720

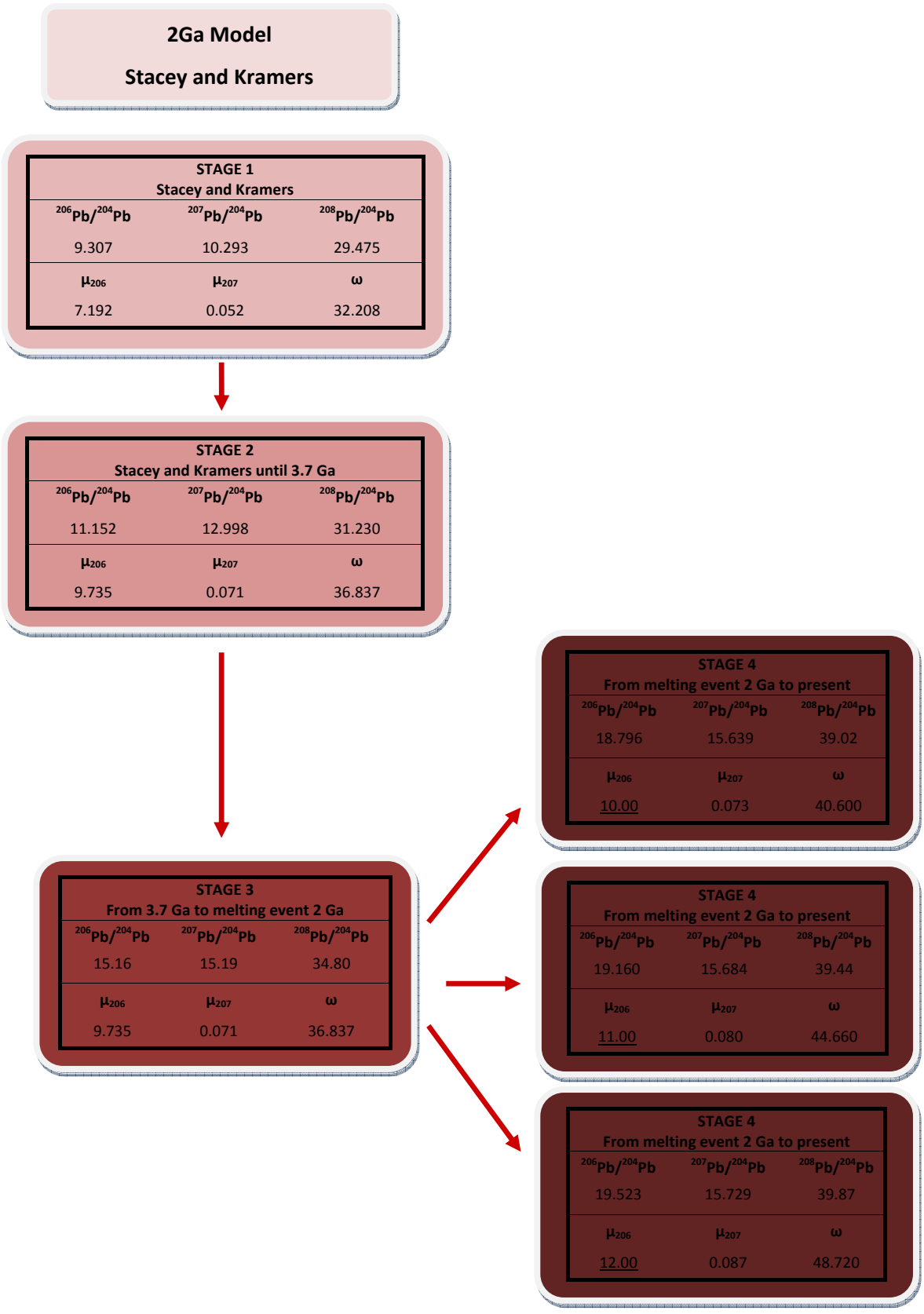
2Ga Model
Stacey and Kramers
STAGE 1
Stacey and Kramers
206Pb/204Pb
207Pb/204Pb
208Pb/204Pb
9.307
10.293
29.475
μ206
μ207
ω
7.192
0.052
32.208
STAGE 2
Stacey and Kramers until 3.7 Ga
206Pb/204Pb
207Pb/204Pb
208Pb/204Pb
11.152
12.998
31.230
μ206
μ207
ω
9.735
0.071
36.837
STAGE 3
From 3.7 Ga to melting event 2 Ga
206Pb/204Pb
207Pb/204Pb
208Pb/204Pb
15.16
15.19
34.80
μ206
μ207
ω
9.735
0.071
36.837
STAGE 4
From melting event 2 Ga to present
206Pb/204Pb
207Pb/204Pb
208Pb/204Pb
18.796
15.639
39.02
μ206
μ207
ω
10.00
0.073
40.600
STAGE 4
From melting event 2 Ga to present
206Pb/204Pb
207Pb/204Pb
208Pb/204Pb
19.160
15.684
39.44
μ206
μ207
ω
11.00
0.080
44.660
STAGE 4
From melting event 2 Ga to present
206Pb/204Pb
207Pb/204Pb
208Pb/204Pb
19.523
15.729
39.87
μ206
μ207
ω
12.00
0.087
48.720

REFERENCES

Abdel-Monem, A.A., Fernandez, L.A., and Boone, G.A. (**1975**). K-Ar-Ages from the eastern Azores group (Santa Maria, São Miguel and the Formigas islands). *Lithos 8: 247–254*.

Agostinho, J. (**1927**). The earthquake in the Azores islands on 31st August 1926. *Vulkanologie 10: 268-272.*

Albarède, F. (**1992**). How deep do common basaltic magmas form and differentiate? *J. Geophys. Res. 97 (87): 10997-11009*.

Albarède, F., Telouk, P., Blichert-Toft J., Boyet, M., Agranier, A., Nelson B.K. (**2004**). Precise and accurate isotopic measurements using multiple-collector MC-ICP-MS. *Geochim. Cosmochim. Acta 68: 2725–2744.*

Andersen, D.J., Lindsley, D.H., Davidson, P.M. (**1993**). QUILF: a PASCAL program to assess equilibria among Fe-Mg-Ti oxides, pyroxenes, olivine, and quartz. *Computers in Geosciences 19: 1333-1350.*

Ave'Lallemant, H., Carter, N. (**1970**). Syntectonic recrystallization of olivine and modes of flow in the upper mantle. *GSA Bulletin 81: 2203-2220.*

Azevedo, J.M.M., Ferreira, M.P. (**1995**). As grandes Formações Vulcânicas da ilha das Flores, Açores. *Proceedings do IV Congresso Nacional de Geologia, M.L.M.G. Universidade do Porto. 3p*.

Azevedo, J.M., Ferreira, M.R.P. (**2006**). The volcanotectonic evolution of Flores Island, Azores (Portugal). *Journ. Vulcanol. Geother. Res. 156: 90–102*.

Azevedo, J.M.M., Ferreira, M.P., Martins, J.A. (**1991**). The emergent volcanism of Flores Island, Azores, (Portugal). Arquipél., *Rev. Univ. Açores (Sér, Ciên. Nat.) 9: 37–46*.

Bard, J. P. (**1986**). Microtextures of igneous and metamorphic rocks. *D. Reidel Publishing Company, 264 p.*

Beattie, P. (**1993**). Olivine-melt and and orthopyroxene-melt equilibria. *Contrib. Mineral. Petrol. 115: 103-111.*

Beattie, P., Drake, M., Jones, J., Leeman, W., Longhi, J., McKay, G., Nielsen, R., Palme, H., Shaw, D., Takahashi, E., Watson, B. (**1993**). Terminology for trace-element partitioning. *Geochim. Cosmochim. Acta 57: 1605-1606.*

Beattie, P., Ford, C., Russell, D. (**1991**). Partition coefficients for olivine-melt and orthopyroxene-melt systems. *Contrib. Mineral. Petrol., 109: 212-224*.

Beier, C. (**2006**). The magmatic evolution of oceanic plateaus: a case study from the Azores. *PhD dissertation presented to the Christian-Albrechts University in Kiel, 175p*.

Beier, C. Haaser, K., Hansteen, T.H. (**2006**). Magma evolution of the Sete Cidades Volcano, São Miguel, Azores. *J. Petrol. 47: 1375-1411.*

Beier, C., Stracke, A., Haase, K.M. (**2007**). The peculiar geochemical signatures of São Miguel lavas: metasomatised or recycled mantle sources?. *Earth Planet. Sci Lett. 259: 186-199*.

Beier, C., Haase, K., Abouchami, W., Krienitz, M-S., Hauff, F. (**2008**). Magma genesis by rifting of oceanic lithosphere above anomalous mantle: Terceira Rift, Azores. *G^3. doi: 10.1029/2008GC002112.*

Bennett, S., Elliott, T., Blundy, J. (**2003**). New insights into magma source compositions: constraints from combined Zr/Hf and Nb/Ta systematic. *Geophys. Res. Abstr. 2878*.

Best, M. (**1982**). Igneous and Metamorphic Petrology. *Freeman: 630p.*

Best, M., Christiansen, E. (**2001**). Igneous Petrology. *Blackwell Science, Inc.: 458p*.

Blundy, J.D., Falloon, T.J., Wood, B.J., Dalton J.A. (**1995**). Sodium partitioning between clinopyroxene and silicate melts. *J Geophys. Res-Solid, 100: 15501-15515*.

Bonatti, E., (**1990**). Not so hot hotspot in the oceanic mantle. *Science, 250: 107- 111.*

Borges, P. (**2003**) Ambientes Litorais nos Grupos Central e Oriental do Arquipélago dos Açores: Conteúdos e Dinâmica de Microescala. *PhD thesis presented to the Azores University, 412p*.

Borges, J.F., Bezzeghoud, M., Buforn, E., Pro, C., Fitas, A. (**2007**). The 1980, 1997 and 1998 Azores earthquakes and some seismo-tectonic implications. *Tectonophysics 435: 37-54.*

Bourdon, B., Langmuir, C.H., Zindler, A. (**1996**). Ridge-hotspot interaction along the Mid-Atlantic ridge between 37º30 and 40º30 N: the U-Th disequilibrium evidence. *Earth Planet. Sci. Lett., 142: 175-190.*

Bourdon, B., Turner, S., Ribe, N.M., (**2005**). Partial melting and upwelling rates beneath the Azores from a U-series isotope perspective. *Earth Planet. Sci. Lett. 239: 42-56.*

Cannat, M., Briais, A., Deplus, C., Escartín, J., Georgen, J., Lin, J., Mercouriev, S., Meyzen, C., Muller, M., Pouliquen, G., Rabain, A., Silva, P. (**1999**). Mid-Atlantic Ridge-Azores hotspot interactions: along-axis migration of a hotspot-derived event of enhanced magmatism 10 to 4Ma ago. *Earth Planet. Sci. Lett., 173: 257-269*.

Carvalho, A., Sousa, M.L., Oliveira, C.S., Campos-Costa, A., Nunes, J.C., Forjaz, V.H. (**2001**). Seismic hazard for the Central Group of the Azores Islands. *Bollettino di Geofisica Teorica ed Applicata 42: 89-105*.

Cas, R.A.F., Wright, J.V. (**1993**). Volcanic Sucessions: modern and ancient. *Chapman & Hall: 528p*.

Chauvel, C., Blichert-Toft, J. (**2001**). A hafnium isotope and trace element perspective on melting of the depleted mantle. *Earth Planet. Sci. Lett., 190: 137–151.*

Chauvel, C., Lewin, E., Carpentier, M., Arndt, N. and Marini, J.C., (**2008**). Role of recycled oceanic basalt and sediment in generating the Hf-Nd mantle array. *Nature Geoscience, 1: 64-67.*

Clague, D.A., Frey, F.A. (**1982**). Petrology and trace element geochemistry of the Honolulu volcanics, Oahu: Implications for the oceanic mantle below Hawaii. *J. Petrology, 23: 447-504*.

Costa Nunes, J. (**1986**). Sismicidade histórica e instrumental do Arquipélago dos Açores. *Catálogo Preliminar: 1444-1980. Not published (computer file for the São Miguel hazard study of Oliveira et al., 1990).*

Costa Nunes, J., Costa, P.T., Senos, M.L. (**1998**). Estudos de sismicidade no Arquipélago dos Açores – Aplicação ao sismo de 9 de Julho de 1998. *Actas do "I Simpósio de Meteorologia e Geofísica".*

Cox, K.G., Bell, J.D., Pankurst, R.J. (**1979**). The interpretation of igneous rocks. *George Allen Unwin, 450 p.*

Davies, G.R., Norry, M.J., Gerlach, D.C., Cliff, R.A. (**1989**). A combined chemical and Pb-Sr-Nd isotope study of the Azores and Cape Verde hot-spots: The geodynamic implications. *In: Saunders, A.D. & Norry, M.J. (eds) – Magmatism in the ocean basins. Geol. Soc. Special Publication, 42: 231-235.*

Dalrymple, G.B. (**1989**). The GLM continuous laser system for $^{40}Ar/^{39}Ar$ dating; description and performance characteristics. *U.S. Geol. Surv. Bull. 189: 89-96*.

Dalrymple, G.B., Alexander, Jr.E.C., Lanphere, M.A., Kraker, G.P. (**1981**). Irradiation of samples for $^{40}Ar/^{39}Ar$ dating using the Geological Survey TRIGA reactor. *U.S. Geol. Surv. Prof. Paper 1176: 5 p*.

Danyushevsky, L.V. (**2000**). The effect of small amounts of H_2O on crystallisation of mid-ocean ridge and backarc basin magmas. *J. Volcanol. Geotherm. Res., 110: 265-280*.

Deer, W.A., Howie, R.A., Zussman, J. (**1992**). An Introduction to the Rock Forming Minerals. *2º Edition Logman Scientifical Technical, 696p.*

Demand, J., Fabriol, R., Gerad, F., Lundt, F., Chovelon, P. (**1982**). Prospection géothermique, íles de Faial et de Pico (Açores): rapport geologique, geochimique et gravimetrique. *Rapport B.R.G.M. 82S.G.N.003 G.H.T. 65p*.

Dobosi, G., Fodor, R.V. (**1992**). Magma fractionation replenishment, and mixing as inferred from green-core clinopyroxenes in Pliocene basanite, Southern Slovakia. *Lithos, 28: 133-150*.

Dosso, L., Bougault, H., Joron, J.L. (**1993**). Geochemical morphology of the North Atlantic Ridge, 10°-24°N: trace element-isotope complementarity. *Earth Planet. Sci. Lett., 120: 443-462*.

Dosso, L., Bougault, H., Langmuir, C., Bollinger, C., Bonnier, O., Etoubleau, J. (**1999**). The age and distribution of mantle heterogeneity along the Mid-Atlantic Ridge (31–41 degrees N). *Earth Planet. Sci. Lett., 170: 269–286*.

Duffield, W.A., Dalrymple, G.B. (**1990**). The Taylor Creek Rhyolite of New Mexico, a rapidly emplaced field of lava domes and flows. *Bull. Volc. 52 (6): 475-487*.

Dupré, B., Lambret, B., Allégre, C-J. (**1982**). Isotopic variations within a single oceanic island: the Terceira case. *Nature, 299: 620-622*.

Eggler, D.H. (**1978**). The effect of CO_2 upon partial melting of peridotite in the system Na_2O-CaO-Al_2O_3-MgO-SiO_2-CO_2 to 35 kb, with an analysis of melting in a peridotite-H_2O-CO_2 system. *Am. J. Sci. 278: 305-343*.

Elkins, L.J., Gaetani, G.A., Sims., K.W.W. (**2008**). Partitioning of U and Th during garnet pyroxenite partial melting: Constraints on the source of alkaline ocean island basalts. *Earth Planet. Sci. Lett., 265, 270-286.*

Elliott, T., Blichert-Toft, J., Heumann, A., Koetsier, G., Forjaz, V.H. (**2007**). The origin of enriched mantle beneath Sao Miguel, Azores. *Geochim. Cosmochim. Acta, 71(1): 219-240*.

Escartín, J., Cannat, M., Pouliquen, G., Rabain, A., Lin, J. (**2001**). Constraints on the interaction between the Mid-Atlantic Ridge and the Azores hotspot from bathymetry and gravity (36-39°N). *J. Geophys. Res. 106: 21719-21736*.

Eugster, H.P., Wones, D.R. (**1962**). Stability relations of the ferruginous biotite, annite. *J. Petrology 3: 82-125.*

Faure, G., Mensing, T.M. (**2005**). Isotopes: Principles and applications (3rd ed.). *Hoboken, New Jersey, John Wiley & Sons, Inc., 897p.*

Féraud, G., Kaneoka, I., Allègre, C.J. (**1980**). K/Ar ages and stress pattern in the Azores: Geodynamic implications. *Earth Planet. Sci. Lett., 46: 275-286*.

Feraud, G., Schmincke, H.U., Lietz, J., Gostaud, J., Pritchard, G., Bleil, U. (**1984**). New K-Ar ages, chemical analyses and magnetic data of rocks from the islands of Santa Maria (Azores), Porto Santo (Madeira Archipelago) and Gran Canaria (Canary Islands). *Arquipél., Rev. Univ. Açores (Sér, Ciên. Nat.) 5: 213–240*.

Ferreira, M.P., Azevedo, J.M., (**1995**). Evolução geológica do arquipélago dos Açores baseada na geocronologia. *Seminar Geologia Atlântica, A.P.G., 9, Ponta Delgada (São Miguel, Açores).*

Flower, M.F.J., Schmincke, H-U., Bowman, H. (**1976**). Rare earth and other trace elements in historic Azorean lavas. *J. Volcanol. Geotherm. Res., 1: 127-147*.

Ford, C.E., Russell, D.G., Craven, J.A., Fisk, M.R. (**1983**). Olivine-liquid equilibria: temperature, pressure and composition dependence of crystal/liquid cation partition coefficients for Mg, Fe^{2+}, Ca and Mn. *J. of Petrology, 24 (5): 256-265.*

Forjaz, V.H. (**1983**). Azores tectonic sketch. *Centro de Vulcanologia, Universidade dos Açores. Unpublished Research Report: 1 pp.*

Forjaz, V.H. (**1997**) – Vulcão dos Capelinhos, Retrospectivas. *Observatório Vulcanológico e Geotérmico dos Açores, I: 259p*.

Forjaz, V.H., Fernandes, N.S.M. (**1970**). Folha "B"da ilha de S. Jorge (Açores) da Carta Geológica de Portugal na escala 1:50 000. *Serv. Geol. Portugal*.

Forjaz, V.H., Fernandes, N.S.M. (**1975**). Carta Geológica de Portugal na escala de 1:50000. Noticia explicativa das Folhas "A" e "B", Ilha de São Jorge (Açores). *Serv. Geol. Portugal, 32p*.

Forjaz, V.H., França, Z.T., Nunes, J.C. (**2001**). Serretian, a new type of submarine eruptions. *Abstracts, "Cities on Volcanoes 2" Auckland. New Zeland: 39p*.

Forjaz, V.H, França, Z.T., Ribeiro, L.P. (**2008**). 1808 – Mistério do Vulcão da Urzelina da ilha de São Jorge dos Açores: Documentos e anotações do Observatório Vulcanológico e Geotérmico dos Açores, 200 anos após a sua ocorrência. *OVGA, 80p.*

Forjaz, V.H., Monjadirno, J., Fernandes, N.S.M. (**1970**). Folha "A"da ilha de S. Jorge (Açores) da Carta Geológica de Portugal na escala 1:50 000. *Serv. Geol. Portugal*.

Forjaz, H.H., Macedo, J.R., Serralheiro, A. (**1974**). Crise seismovulcânica do Faial-Pico (Novembro-Dezembro 1973). *Rel. Int. DGFCUL, Lisboa 7p.*

Forjaz, V.H., Serralheiro, A., Nunes, J.C. (**1990**). Carta Vulcanologica dos Açores – Grupo Central na escala 1:200000. *Ed. from the Regional Civil Protection and the Volcanology Center (INIC)*.

Forjaz, V.H., Rocha, F.M., Medeiros, J.M., Meneses, L.F., Sousa, C. (**2000**). Notícias sobre o Vulcão Oceânico da Serreta, Ilha Terceira dos Açores. *Ed. OGVA*.

França, Z. (**2000**). Origem e evolução Petrológica e Geoquímica do Vulcanismo da Ilha do Pico, Açores. *PhD thesis presented to the Azores University, 391p*.

França, Z., Almeida, M.H., Wallenstein, N. (**1995**). Ocorrência de xenólitos mantélicos numa lava da ilha do Pico. *Gaia 11: 47-52*.

França, Z., Colombo, T.M., Tassinari, C.G., Cruz, J.V., Aparicio, A.Y., Araña, V., Rodrigues, B.N. (**2006**). Petrology, geochemistry and Sr-Nd-Pb isotopes of the volcanic rocks from Pico Island-Azores (Portugal). *Journ. Vulcanol. Geother. Res. 156: 71-89*.

França, Z., Cruz, J., Nunes, J.C., Forjaz, V.H. (**2005**). Geologia dos Açores: Uma perspectiva actual. *Revista Açoreana, 10: 140p*.

França, Z., Forjaz, V.H., Tilling, R., Kuentz, D., Widom, E., Lago, L. (**2009**). Volcanic History of Pico and Faial Islands, Azores: an Overview. *270p*.

França, Z.T., Lago, M., Galé, C., Ubide, T., Widom, E., Arranz, E., Forjaz, V.H. (**2008**). Composition of Gabbroic Xenoliths in Flores Island (Azores, Portugal). *Revista de la sociedad española de mineralogia, 9: 103-104.*

França, Z.T., Lago, M., Nunes, J.C., Galé, C., Forjaz, V.H., Pueyo, O., Arranz, E. (**2006a**). Geochemistry of Alkaline Basalts of Corvo Island (Azores, Portugal): Preliminary Data. *Geogaceta 40: 87–90*.

Frey, F.A., Green, D.H., Roy, S.D. (**1978**). Integrated models of basalt petrogenesis: A study of quartz tholeiites to olivine melilites from South Eastern Australia utilizing geochemical and experimental petrological data. *J. Petrology, 19:, 463-513*.

Galer, S.J.G., Abouchami, W. (**1998**). Practical application of lead triple spiking for correction of instrumental mass discrimination. *Mineral. Mag., 62A: 491–492*.

Galer, S.J.G., O'Nions, R.K. (**1985**). Residence times of thorium, uranium and lead in the mantle with implications for mantle convection. *Nature, 316: 778-782*.

Geldmacher, J., Hoernle, K., Bogaard, P.V.D., Duggen, S., Werner, R. (**2005**). New $^{40}Ar/^{39}Ar$ age and geochemical data from seamounts in the Canary and Madeira volcanic provinces: Support for the mantle plume hypothesis. *Earth Planet. Sci. Lett. 237: 85-101*.

Gente, P., Dyment, J., Maia, M., Goslin, J. (**2003**). Interaction between the Mid-Atlantic Ridge and the Azores hotspot during the last 85 Myr: Emplacement and rifting of the hotspot-derived plateaus. G^3 *(4) 10, 8514*.

Green, D.H. (**1973**). Conditions of melting of basanite magma from garnet peridotite. *Earth Planet. Sci. Lett., 17: 456-465*.

Greenough, J.D. (**1988**). Minor phases in the earth's mantle. Evidence from trace - and minor - element patterns in primitive alkaline magmas. *Chem. Geol., 69: 177-192*.

Gribble, C.D., Hall, A.J. (**1992**). Optical Mineralogy: Principles and Practice. *UCL Press: 303p*.

Gonzaga, R., Lowry, D., Jacob, D.E., LeRoex, A., Schulze, D., Menzies, M.A. (**2010**). Eclogites and garnet pyroxenites : similarities and differences. *J. Volcan. Geother. Res., 190: 235-247*.

Haase, K.M. (**1996**). The relationship between the age of the lithosphere and the composition of oceanic magmas: Constraints on partial melting, mantle sources and the thermal structure of the plates. *Earth Planet. Sci. Lett., 144: 75-92*.

Halliday, A.N., Davies, G.R., Lee, D-C., Tommasini, S., Paslick, C.R., Fitton, J.G., James, D.E. (**1992**). Lead isotope evidence for young trace element enrichment in the oceanic upper mantle. *Nature, 359: 623-627*.

Halliday, A.N., Lee, D-C., Tommasini, S., Davies, R.G., Paslick, C.R., Fitton, J.G., James, E.D. (**1995**). Incompatible trace elements in OIB and MORB and source enrichment in the sub-oceanic mantle. *Earth Planet. Sci. Lett., 133: 379-395*.

Hawkesworth, C.J., Norry, M.J., Roddick, J.C., Vollmer, R. (**1979**). $^{143}Nd/^{144}Nd$ and $^{87}Sr/^{86}Sr$ ratios from the Azores and their significance in LIL-element enriched mantle. *Nature, 280: 28-31*.

Hildenbrand, A., Madureira, P., Marques, F.O., Cruz, I., Henry, B., Silva, P. (**2008**). Multi-stage evolution of a sub-aerial volcanic ridge over the last 1.3 Myr: S. Jorge Island, Azores Triple Junction. *Earth Planet. Sci. Lett,. 273: 289-298*.

Hirn, A., Haessler, H., Trong, P.H., Wittlinger, G., Victor, L.A.M. (**1980**). Aftershock Sequence Of the January 1st, 1980, Earthquake and Present-Day Tectonics in the Azores. *Geophys. Res. Lett. 7: 501-504*.

Hirschmann, M.M., Ghiorso, M.S. (**1994**). Activities of nickel, cobalt, and manganese silicates in magmatic liquids and applications to olivine/liquid and to silicate/metal partitioning. *Geochim. Cosmochim. Acta, 58: 4109-4126*.

Hirschmann, M.M., Stolper, E.M. (**1996**). A possible role for garnet pyroxenite in the origin of the "garnet signature" in MORB. *Contrib. Mineral. Petrol. 124: 185-208*.

Jiménez-Munt, I., Fernàndez, M.M.T., Bird, P. (**2001**). The transition from linear to diffuse plate boundary in the Azores-Gibraltar region: results from a thin-sheet model. *Earth Planet. Sci. Lett., 192: 175-189.*

Jochum, K.P., Hofmann, A.W. (**1997**). Constraints on Earth evolution from antimony in mantle-derived rocks. *Chem. Geol. 139: 39-49*.

Johnson, M.C., Plank, T. (**1999**). Dehydration and melting experiments constrain the fate of subducted sediments. *G^3, 1, doi: 1999GC000014*.

Kogiso T., Tatsumi Y., Nakano, S. (**1997**). Trace element transport during dehydration processes in the subducted oceanic crust; 1. Experiments and implications for the origin of ocean island basalts. *Earth Planet. Sci. Lett., 148: 193-205*.

Krause, D., Watkins, N. (**1970**). North Atlantic crustal genesis in the vicinity of the Azores. *Geophys. J. R. Astron. Soc., 19: 261-283*.

Lanphere, M.A., Dalrymple, G.B. (**2000**). First-principles calibration of ^{38}Ar tracers: Implications for the ages of $^{40}Ar/^{39}Ar$ fluence standards. *U.S. Geol. Surv. Prof. Paper 1621: 10p*.

Lourenço, N. (**2007**). Tectono-magmatic processes at the Azores triple junction. *PhD Thesis presented to the Algarve University, 239pp*.

Lourenço, N., Miranda, J.M., Mendes-Victor, L.A., Madeira, J., Needham, H.D. (**1998**). Morpho-tectonic analyses on the Azores Volcanic Plateau from new bathymetric compilation of the area. *Marine Geophys Res. 20: 141-156*.

Ludwig, K.R. (**1999**). User's Manual for Isoplot/Ex Version 2, A Geochronological Toolkit for Microsoft Excel. *Berkeley Geochronology Center Spec. Pub. 1a, Berkeley, CA: 47p*.

Luis, J.F., Miranda, J.M., Galdeano, A., Patriat. P. (**1998**). Constraints on The Structure of the Azores Spreading Center from Gravity Data. *Marine Geophysical Research, 20: 157-170.*

Luis, J.F., Miranda, J.M., Galdeano, A., Patriat, P., Rossignol, J.C., Mendes-Victor, L.A. (**1994**). The Azores triple junction evolution since 10 Ma from aeromagnetic survey of the Mid-Atantic Ridge. *Earth Planet. Sci. Lett., 125: 439-459.*

Machado, A., Azevedo, J.M.M., Almeida, D.P.M., Chemale, F. (**2008**). Geochemistry of Volcanic Rocks from Faial Island (Azores). *Lisbon: e-Terra, GEOTIC – Sociedade Geológica de Portugal: 1–14*.

Machado, F. (**1949**). O terramoto de S. Jorge de 1757. *Açoreana, 4 (4): 1-14*.

Machado, F. (**1957**). Caldeiras Vulcânicas dos Açores. *Atlântida, 1(5): 275-278*.

Machado, F. (**1973**). Periodicidade sísmica nos Açores. *Com. Serv. Geol. Port., 56: 475-487*.

Machado, F., Forjaz, V.H. (**1965**). A crise sísmica de São Jorge, de Fevereiro de 1964. *Bol. Soc. Geol. de Portugal, 16: 19-36.*

Machado, F., Forjaz, V.H. (**1968**). A actividade vulcânica na ilha do Faial (1957-67). *Ed da Comisão de Turismo da Horta, 89p.*

Machado, F., Trêpa, M.V., Férin, C., Nunes, J.C. (**1974**). Crise sísmica do Pico (Açores), Nov 1973. *Açoreana, 6: 155-170*.

Madeira, J. (**1998**). Estudos de neotectónica nas ilhas do Faial, Pico e S. Jorge: uma contribuição para o conhecimento geodinâmico da junção tripla dos Açores. *PhD thesis presented to the University of Lisbon, 481p*.

Madeira, J., Silveira, A.B.D., Serralheiro, A. (**1998**). Efeitos geológicos do Sismo do Faial de 9 de Julho de 1998. *Protecção Civil, II (14): 12-20*.

Madureira, P. (**2006**). Geoquímica elementar e isotópica (He e Ne) das lavas máficas da ilha Terceira: evidências para uma origem profunda da pluma dos Açores. *PhD Thesis presented to the Evora University, 230 pp.*

Madureira, P., Moreira, M., Mata, J., Allègre, C.-J. (**2005**). Primitive neon isotopes in Terceira Island (Azores Archipelago). *Earth Planet. Sci. Lett., 233: 429-440.*

Mahon, K. (**1996**). The New "York" Regression: Application of an improved statistical method to geochemistry. *Inter. Geology Rev. 38: 293-303*.

Mata, J. (**1996**). Petrologia e Geoquímica das Lavas da Ilha da Madeira: implicações para os modelos de evolução do manto terrestre. *PhD Thesis presented to the University of Lisbon, 471 pp*.

McDade, P., Blundy, J.D., Wood, B.J., (**2003**). Trace element partitioning on the Tinaquillo lherzolite solidus at 1.5 GPa. *Phys. Earth Planet. Int., 139: 129-147.*

McDonough, W.F., Sun, S.S. (**1995**). Composition of the Earth. *Chem. Geology, 120: 223-253*.

McDougall, I., Harrison, T.M. (**1999**). Geochronology and thermochronology by the $^{40}Ar/^{39}Ar$ method. *2nd Edition, Oxford University Press: 269p*.

McKenzie, D.P. (**1972**). Active tectonics of the Mediterranean region. *Geophys. J.R. Astro. Soc., 30: 109-185.*

Middlemost, E.A.K. (**1989**). Iron oxidation ratios, norms and the classification of volcanic rocks. *Chem. Geology, 77: 19-26*.

Millet, M-A., Doucelance, R., Baker, J.A., Schiano, P. (**2009**). Reconsidering the origins of isotopic variations in Ocean Island Basalts: Insights from fine-scale study of São Jorge Island, Azores archipelago. *Chem. Geol. 265: 289-302.*

Minster, J.F., Allègre, J-C, (**1978**). Systematic use of trace elements in igneous processes: Part III, Inverse problem of batch melting in volcanic suites. *Contrib. Mineral. Petrol., 68: 37-52*.

Mitchell, N., Beier, C., Rosin, P., Quartau, R., Tempera, F. (**2008**). Lava penetrating water: Submarine lava flows around the coasts of Pico Island, Azores. *G^3 9 (3): 1-29*.

Moreira, M., Doucelance, R., Kurz, M.D., Dupre, B., Allegre, C-J. (**1999**). Helium and lead isotope geochemistry of the Azores Archipelago. *Earth Planet. Sci. Lett., 169: 189-205*.

Morimoto, N., Fabries, J., Ferguson, A.K., Ginzburg, I.V., Ross, M., Seifert, F.A., Zussman, J., Aoki, K., Gottardi, G. (**1988**). Nomenclature of pyroxenes. *Am. Mineral. 73: 1123–1133*.

Nicholis, M.G., Rutherford, M.J. (**2004**). Experimental constrains on magma ascent rate for the Crater Flat volcanic zone hawaiite. *Geology, 32: 489-492*.

Nunes, J.C. (**1991**). Microssismos e Neotectónica: contribuição para o seu estudo nos Açores. *Provas de Aptidão Pedagógica e Capacidade Científica. Azores University, 245p*.

Nunes, J.C., Forjaz, V.H., França, Z. (**1997**). Novos elementos sobre a crise sísmica de 1973, Ilha do Pico (Açores). *In Instituto Superior Técnico (Ed) 3º Encontro Sobre Sismologia e Engenharia Sísmica – Proceedings. Lisboa. Instituto de Estruturas, Território e Construção – DECivil: 39-48*.

Nunes, J.C., Forjaz, V.H., Oliveira, C. S. (**2000**). Catalogo sísmico da Região dos Açores, vol. I (1980-88), vol. II (1989-98). *PPERCAS Project, Azores University*.

Nunes, J.C., Forjaz, V.H., Oliveira, C.S., (**2004**). Catálogo sísmico da Região dos Açores 1850 – 1998. *VULCMAC Project, Azores University*.

Nunes, J.C., França, Z., Malheiro, A.M. (**1998**). Distribuição das intensidades sísmicas da ilha do Pico referentes ao sismo de 9 de Julho de 1998: condicionantes morfológicas, geológicas e tectónicas. *Actas do "I Simpósio de Meteorologia e Geofísica", Lagos*.

Oliveira, C.S., Lucas, A.R., Guedes, J.H.C. (**1992**). 10 anos após o sismo dos Açores de 1 de Janeiro de 1980. *Monografia, LNEC, 1: 356pp*.

Oliveira, C.S., Sousa, M.L., Guedes, J.H.C., Martins, A., Campos-Costa, A. (**1998**). A crise sísmica do Faial/Pico/São Jorge iniciada com o sismo de 9 de Julho de 1998 vista na rede acelerográfica dos Açores. *Actas do "I Simpósio de Meteorologia e Geofísica", Lagos.*

Oversby, V.M. (**1971**). Lead in Ocean Islands: Faial, Azores and Trindade. *Earth Plan. Sci. Lett., 11: 401-406.*

Patchett, P.J., White, W.M., Feldmann, H., Kielinczuk S., Hofmann, A.W. (**1984**). Hafnium/rare earth element fractionation in the sedimentary system and crustal recycling into the Earth's mantle. *Earth Planet. Sci. Lett. 69: 365-378*.

Pearce, J.A., Kempton, P.D., Nowell, G.M., Noble, S.R. (**1999**). Hf–Nd element and isotope perspective on the nature and provenance of mantle and subduction components inWestern Pacific arc-basin systems. *J. Petrol. 40: 1579–1611.*

Pfänder, J.A., Münker, C., Stracke, A. & Mezger, K. (**2007**). Nb/Ta and Zr/Hf in ocean island basalts - implications for crust - mantle differentiation and the fate of Niobium. *Earth Planet. Sci. Lett., 254: 158-172*.

Plank, T., Langmuir, C.H. (**1998**). The geochemical composition of subducting sediments and its consequences for the crust and mantle. *Chemical Geology 145: 325–394.*

Pretorius, W., Weis, D., Williams, G.A., Hanano, D., Kieffer, B., Scoates, J.S. (**2006**). Complete Trace Elemental Characterisation of Granitoid (USGS G-2, GSP-2) Reference Materials by High Resolution Inductively Coupled Plasma-Mass Spectrometry. *Geostandards and Geoanalytical Research 30(1): 39-54*.

Prytulak, J., Elliott, T.R. (**2007**). TiO_2 enrichment in ocean island basalts. *Earth Planet. Sci. Lett., 263: 388-403.*

Putirka, K., Johnson, M., Kinzler, R., Longhi, J., Walker, D. (**1996**). Thermometry of mafic igneous rocks based on clinopyroxene-liquid equilibria, 0-30 kbar. *Contrib. Min. Petrol., 123: 92-108*.

Putirka, K., Mikaelian, H., Ryerson, F., Shaw, H. (**2003**). New clinopyroxene-liquid thermobarometers for mafic, evolved, and volatile-bearing lava compositions, with applications to lavas from Tibet and the Snake River Plain, Idaho. *Am. Mineral., 88: 1542-1554*.

Ribeiro, A. (**1982**). Tectónica de placas: aplicação à sismotectónica e à evolução da fronteira de placas Açores-Gibraltar. *Geonovas, 4: 87-96*.

Ribeiro, L.P. (**2001**). Estudo petrológico e geoquímico de três sequências lávicas da ilha da Madeira: implicações petrogenéticas. *Master thesis presented to the University of Lisbon, 170p.*

Ribeiro, L.P., Calvert, A., França, Z., Rodrigues, B., Abreu, M.P. (**2010**). New $^{40}Ar/^{39}Ar$ and geochemical constraints on São Jorge Island, Azores. *GCA, A867.*

Ribeiro, L.P., França, Z., Forjaz, V.H., Abreu, M.P. (**2008**). Estimated pressure and temperature during magma extraction beneath São Jorge Island, Azores. *EGU 2008-A-10548*.

Ribeiro, L.P., França, Z., Rodrigues, B., Forjaz, V.H. (**2007**). First approach to geochemical study of São Jorge lavas, Azores. *Geophys. Research Abstr., 9: 09998*.

Ribeiro, L.P., França, Z., Rodrigues, B., Forjaz, V.H. (**2007a**). Preliminary characterization of São Jorge island mantle source (Azores). *GCA A836*.

Rock, N.M.S., Leake, B.E. (**1984**). The International Mineralogical Association amphibole nomenclature scheme: computerization and its consequences. *Mineralogical Magazine, 48: 211-227*.

Rodrigues, B., Alves, C.M.A, Serralheiro, A., Vorjaz, V.H. (**1995**). Nota prévia sobre a petrologia e geoquímica da ilha de Santa Maria, Açores. *Memórias da Academia das Ciências, 46: 71-91*.

Roeder, P.L., Emslie, R.F. (**1970**). Olivine-liquid equilibrium. *Contrib. Mineral. Petrol., 29: 275-289*.

Rollinson, H. (**1993**). Using Geochemical data: evaluation, presentation, interpretation. *Longman: 352p*.

Rosman, K.J.R., Taylor, P.D.P. (**1998**). Isotopic composition of elements. *Pure Appl. Chem., 70: 217–235*.

Salters, V.J.M., Longhi, J. (**1999**). Trace element partitioning during the initial stages of melting beneath mid-ocean ridges. *Earth Planet. Sci. Lett., 166: 15-30.*

Salters, V.J.M., Zindler, A. (**1995**). Extreme $^{176}Hf/^{177}Hf$ in the sub-oceanic mantle. *Earth Planet. Sci. Lett. 129: 13-30*.

Schaefer, B.F., Turner, S., Parkinson, I., Rogers, N., Hawkesworth, C. (**2002**). Evidence for recycled Archean oceanic mantle lithosphere in the Azores plume. *Nature, 42: 304-307*.

Schilling, J-G., Bergeron, M.B., Evans, R., Smith, J.V. (**1980**). Halogens in the mantle beneath the North Atlantic. *Phil. Trans. R. Soc. Lond. A 297: 147–178*.

Schilling, J-G. (**1975**). Azores mantle blob: rare-earth evidence. *Earth Planet. Sci. Lett., 25: 103-115*.

Schmincke, H-U. (**1973**). Magmatic evolution and tectonic regime in the Canary, Madeira, and Azores island groups. *Geol. Soc. America Bull., 84: 633-648*.

Schmincke, H-U., Weibel, M. (**1972**). Chemical study of rocks from Madeira, Porto Santo and São Miguel, Terceira (Azores). *Neues Jahrbuch für Mineralogie Abhandlungen, 117: 253-281*.

Searle, R. (**1980**). Tectonic pattern of the Azores spreading centre and triple junction. *Earth Planet. Sci. Lett. 51: 415-434.*

Shaw, D. (**2006**). Trace elements in magmas: a theoretical treatment. *Cambridge University Press, 242p*.

Sigmarsson, O., Carn, S., Carracedo, J.C. (**1995**). Systematics of U-series nuclides in primitive lavas from the 1730-36 eruption in Lanzarote, Canary Islands and the implication for the role of garnet pyroxenite during oceanic basalt formation. *Earth. Planet. Sci. Lett., 270: 1337-1351*.

SIVISA, (**1998**). Boletim sismológico preliminar dos Açores. Centro de Coordenação do Sistema de Vigilância Sismológica dos Açores. *Inst. de Meteorologia e Univ. Açores*.

Smith, W.H.F., Sandwell, D.T. (**1997**). Global sea floor topography from satellite altimetry and ship depth soundings. *Science, 277: 1957-1962*

Snyder, D.C., Widom, E., Pietruszka, A.J., Carlson, R.W. (**2004**). The role of open-system processes in the development of silicic magma chambers: a chemical and isotopic investigation of the Fogo A trachyte deposit, São Miguel, Azores. *J. Petrology 45: 723-738*.

Staudacher, T., Jessberger, E.K., Dorflinger, J., Kiko, J. (**1978**). A refined ultrahigh-vacuum furnace for rare gas analysis. *J. Phys. E: Sci. Instru. 11: 781-784*.

Stracke A., Bizimis M., Salters V.J.M. (**2003**). Recycling oceanic crust: Quantitative constraints. G^3, 4: doi:10.1029/2001GC000223.

Stracke, A., Hofmann, A.W., Hart, S.R. (**2005**). FOZO, HIMU and the rest of the mantle zoo. G^3*, 6: doi:10.1029/2004GC000824.*

Stracke, A., Salters, V.J.M., Sims, K.W.W. (**1999**). Assessing the presence of garnet-pyroxenite in the mantle sources of basalts through combined hafnium-neodymium-thorium isotope systematic. G^3*, 1: doi:10.1029/1999GC000013*.

Sun, S-S. (1980). Lead isotopic study of young volcanic rocks from mid-ocean ridges, ocean islands and island arcs. *Philos. Trans. R. Soc. London A, 297: 409-445*

Tracy, R.J., Robinson, P. (**1977**). Zoned titanian augite in alkali olivine basalt from Tahiti and the nature of titanium substitutions in augite. *Am. Mineral., 62: 634-645*.

Tuff, J., Gibson, S.A. (**2007**). Trace-element partitioning between garnet, clinopyroxene and Fe-rich picritic melts at 3 to 7 GPa. *Contrib. Mineral. Petrol., 153 : 369-387*.

Turner, S., Hawkesworth, C., Rogers, N., King, P. (**1997**). U-Th isotope disequilibria and ocean island basalt generation in the Azores. *Chem. Geology, 139 (1-4): 145-164*.

Ulmer, P. (**1989**). The dependence of the Fe^{2+}-Mg cation-partitioning between olivine and basaltic liquid on pressure, temperature and composition: an experimental study to 30 Kbars. *Contrib. Mineral. Petrol., 101: 261-273*.

Vervoort, J.D., Blichert-Toft, J. (**1999**). Evolution of the depleted mantle: Hf isotope evidence from juvenile rocks through time. *Geochim. Cosmochim. Acta, 63: 533–556.*

Vogt, P., Jung, W. (**2004**). The Terceira Rift as hyper-slow, hotspot-dominated oblique spreading axis: A comparison with other slow-spreading plate boundaries. *Earth Planet. Sci. Lett., 218: 77-90*.

Wass, S.Y. (**1979**). Multiple origins of clinopyroxenes in alkali basaltic rocks. *Lithos,12: 115-132*.

Weis, D., Kieffer, B., Hanano, D., Silva, I.N., Barling, J., Pretorius, W., Maerschalk, C., Mattielli, N. (**2007**). Hf isotope compositions of U. S. Geological Survey reference materials. G^3*, 8(6): 1-15*.

Weis, D., Kieffer, B., Maerschalk, C., Barling, J., Jong, J.D., Williams, G.A., Hanano, D., Pretorius, W., Mattielli, N., Scoates, J.S., Goolaerts, A., Friedman, R.M., Mahoney, J.B. (**2006**). High-precision isotopic characterization of USGS reference materials by TIMS and MC-ICP-MS. G^3*, 7(8): 1-30*.

White, W.M. (**2010** last update). *http://www.imwa.info/white-geochemistry.html*.

White, W.M., Schilling, J-G. (**1978**). The nature and origin of geochemical variation in Mid-Atlantic Ridge basalts from the central north Atlantic. Geochim. Cosmochim. Acta, 42: 1501-1516.

White, W.M., Schilling, J-G., Hart, S.R. (**1976**). Evidence for the Azores mantle plume from strontium isotopes geochemistry of the central North Atlantic. *Nature, 263: 659–663*.

White, W.M., Tapia, M.D.M., Schilling, J-G. (**1979**). The Petrology and Geochemistry of the Azores Islands. *Contrib. Mineral. Petrol., 69: 201-213*.

Widom, E., Carlson, R.W., Gill, J.B., Schmincke, H.U. (**1997**). Th-Sr-Nd-Pb isotope and trace element evidence for the origin of the Sao Miguel, Azores, enriched mantle source. *Chem. Geology, 140 (1-2): 49-68.*

Widom, E., Farquhar, J. (**2003**). Oxygen isotope signature in olivines from Sao Miguel, Azores: Implications for crustal and mantle processes. *Chemical Geology, 193: 237-255*.

Widom, E., Shirey, S.B. (**1996**). Os isotope systematics in the Azores: implications for mantle plume sources. *Earth Planet. Sci. Lett., 142: 451-465.*

Wilson, M. (**1989**). Igneous Petrogénesis: A global tectonic approach. *Ed. Unwin Hyman: 446p*.

Yoder, H.S., Tilley, C.E. (**1962**). Origin of basaltic magmas: An experimental study of natural and synthetic rock systems. *J. Petrology, 3: 342-532*.

York, D. (**1969**). Least squares fitting of a straight line with correlated errors. *Earth Planet. Sci. Lett. 5: 320-324*.

Yu, D., Fontignie, D., Schilling, J-G. (**1997**). Mantle plume-ridge interactions in the Central North Atlantic: a Nd isotope study of Mid-Atlantic Ridge basalts from 30°N to 50°N. *Earth Planet. Sci. Lett., 146: 259-272*.

Zellmer, G.F., Sparks, R.S.J., Hawkesworth, C.J., Wiedenbeck, M. (**2003**). Magma emplacement and remobilization timescales beneath Montserrat: Insight from Sr and Ba zonation in plagioclase phenocrysts. *J. Petrology, 44: 1413-1431*.

Zindler, A., Hart, S. (**1986**). Chemical Geodynamics. *Ann. Rev. Earth Planet. Sc., 14: 493-571*.